Summer 2014

Fundamental design principles of novel MEMS based "Landau" switches, sensors, and actuators : Role of electrode geometry and operation regime

Ankit Jain
Purdue University

Graduate School ETD Form 9
(Revised 12/07)

PURDUE UNIVERSITY
GRADUATE SCHOOL
Thesis/Dissertation Acceptance

This is to certify that the thesis/dissertation prepared

By Ankit Jain

Entitled

Fundamental Design Principles of Novel MEMS Based "Landau" Switches, Sensors, and Actuators
: Role of Electrode Geometry and Operation Regime

For the degree of Doctor of Philosophy

Is approved by the final examining committee:

MUHAMMAD A. ALAM
Chair

ARVIND RAMAN

MARK S. LUNDSTROM

RASHID BASHIR

To the best of my knowledge and as understood by the student in the *Research Integrity and Copyright Disclaimer (Graduate School Form 20)*, this thesis/dissertation adheres to the provisions of Purdue University's "Policy on Integrity in Research" and the use of copyrighted material.

Approved by Major Professor(s): MUHAMMAD A. ALAM

Approved by: M. R. Melloch 08-06-2014
Head of the Graduate Program Date

FUNDAMENTAL DESIGN PRINCIPLES OF NOVEL MEMS BASED "LANDAU" SWITCHES, SENSORS, AND ACTUATORS : ROLE OF ELECTRODE GEOMETRY AND OPERATION REGIME

A Dissertation

Submitted to the Faculty

of

Purdue University

by

Ankit Jain

In Partial Fulfillment of the

Requirements for the Degree

of

Doctor of Philosophy

December 2014

Purdue University

West Lafayette, Indiana

To

my parents, grandparents,

and

high school math teacher.

ACKNOWLEDGMENTS

When I look back, I had just finished my undergraduation in 2008 and had decided to join PhD program at Purdue University. To be honest, at that time, I had no idea how PhD will turn out to be? Moreover, I was not sure whether I will be able to finish it or not. Since I have made it, I must admit that this journey has been made possible by support, guidance, and inspiration of many people and I want to take this opportunity to acknowledge their contributions.

First and foremost, I want to express my sincere gratitude towards my PhD advisor Prof. M. A. Alam. He is the best advisor undoubtedly. If I have to do my PhD again, I would still like to do under his guidance only. From him, I have learnt: (i) to learn, (ii) to simplify complex problems, (iii) to focus on the essentials of a problem and not on unnecessary details, (iv) to see new problems in one's mistakes. The chapter 5 of this thesis started as a result of my mistake. Since my code did not include the full physics, I was observing hysteresis-free abrupt switching in MEMS. In the beginning, I did not realize the importance of that abrupt jump. It was Prof. Alam's vision to see that this could lead to ideal switching in a FET and it did eventually. Therefore, I will carry these learnings such as "seeing new problems in one's mistakes" for the rest of my life.

I am very grateful to all my committee members for serving in my PhD committee. More than that, I must say that teachings from each of my committee members have had a huge impact on the work presented in this thesis. For example, although I learnt about transistors and its mathematics during my undrgraduation, my deeper understanding of transistors is due to Prof. Mark Lundstrom. Since chapter 5 is all about transistors, I don't think it would have been possible without taking his classes and watching his online lectures.

Since I did my undergraduation in Electrical Engineering, I was not exposed to beam mechanics and spring-mass systems. It is impossible to understand MEMS without understanding these concepts. In this regard, Prof. Arvind Raman's nicely written papers on AFM and his class on AFM made my life a lot easier. My understanding of spring-mass systems or cantilevers is due to his papers and classes and without which chapters 3 & 4 would not have been in good shape.

When I started my PhD, I was only looking into RF-MEMS capacitive switches. The idea that MEMS can be used as biosensors and most importantly that adsorption of biomolecules on a cantilever surface can increase its stiffness, came only after reading Prof. Rashid Bashir's work on biosensors. In this sense, chapter 6 is inspired by his work. I am really thankful to him for giving me time for discussions and serving in my PhD committee.

Special thanks to all my collaborators: Prof. Dimitrios Peroulis and his group for providing RF-MEMS devices, Prof. Marisol Koslowski for creep models, Prof. Alina Alexeenko for damping models, and Prof. Jayathi Murthy for coarse grained modeling of RF-MEMS devices. They all have been very good collaborators and very good mentors as well.

I am also thankful to Ms. Vicki Johnson and Mr. Matt Golden for taking care of all administrative things and making my life easy at many occasions. I also want to acknowledge the support from funding agencies such as PRISM and MIT-MSD center for providing me the necessary resources, which made this work possible.

I also want to thank my past and present group members for making my stay at Purdue wonderful. I feel lucky that I was surrounded by not only great minds, but also inspiring and motivating people who kept me going whenever I felt demotivated. I must mention Abdul Wahab, Ryyan Khan, Piyush Dak, Raghu Vamsi, Aida Ebrahimi, Sang Hoon Shin, Reza Asadpour, Xin Jin, Dr. Sambit Palit, Dr. Sourabh Dongaonkar, Dr. Biswajit Ray, Dr. M. Masuduzzaman, Dr. Ahmad Ehteshamul Islam, and Dr. Pradeep R. Nair for their constant help throughout the course of my PhD.

I am also thankful to all my friends outside lab who made my stay at Purdue very enjoyable and memorable. In particular, I must mention Rohit Jain, Nitin Sharma, Nitish Sihag, Dr. Gururaj Naik, and Dr. Dooshaye Moonshiram. I will always cherish the moments spent with you all.

I am also delighted to mention about my non Purdue friends who have always supported me even from long distance. I have shared several moments of not only joy but also sadness with them. They include Dr. Nishant Kumar, Pradeep Kumar, Megha Girdhar, Mayank Sachan, Harsh Vardhan, Chandra Mohan, Tapish Agarwal, Prashant Kumar, Ashish Lodh, and Pallavi Raonka.

Finally, like many other things in my life, this PhD would also not have been possible without the constant support, guidance, inspiration, and love of my mother, father, and sister. Thanks for always being there!

TABLE OF CONTENTS

Page

Page

Page

Page

LIST OF TABLES

LIST OF FIGURES

Figure Page

Figure Page

Figure Page

Figure Page

Figure Page

Figure Page

Figure Page

Figure Page

Figure Page

Figure Page

ABSTRACT

Jain, Ankit Ph.D., Purdue University, December 2014. Fundamental Design Principles of Novel MEMS based "Landau" Switches, Sensors, and Actuators : Role of Electrode Geometry and Operation Regime. Major Professor: M. A. Alam.

Microelectromechanical systems (MEMS) are considered as potential candidates for "More-Moore" and "More-than-Moore" applications due to their versatile use as sensors, switches, and actuators. Examples include accelerometers for sensing, RF-MEMS capacitive switches in communication, suspended-gate (SG) FETs in computation, and deformable mirrors in optics. In spite of the wide range of applications of MEMS in diverse fields, one of the major challenges for MEMS is their instability. Instability divides the operation into stable and unstable regimes and poses fundamental challenges for several applications. For example: Tuning range of deformable mirrors is fundamentally limited by pull-in instability, RF-MEMS capacitive switches suffer from the problem of hard landing, and intrinsic hysteresis of SG-FETs puts a lower bound on the minimum power dissipation.

In this thesis, we provide solutions to the application specific problems of MEMS and utilize operation in or close to unstable regime for performance enhancement in several novel applications. Specifically, we propose the following: (i) novel device concepts with nanostructured electrodes to address the aforementioned problems of instability, (ii) a switch with hysteresis-free ideal switching characteristics based on the operation in unstable regime, and (iii) a Flexure biosensor that operates at the boundary of the stable and unstable regimes to achieve improved sensitivity and signal-to-noise ratio. In general, we have advocated electrode geometry as a design variable for MEMS, and used MEMS as an illustrative example of "Landau" systems to advocate operation regime as a new design variable.

1. INTRODUCTION

This thesis is about microelectromechanical systems (MEMS) and has two parts. The first part focuses on specific applications of MEMS and associated problems; whereas in second part, MEMS are identified and used as an illustrative example of a broader class of bi-stable "Landau" systems. The specific contributions include:

- **Role of Electrode Geometry in MEMS:** Classical MEMS based applications have relied on planar electrodes. In this thesis, we for the first time, use electrode geometry as a new design variable to address several problems associated with classical planar electrodes (details in chapters 3 and 4).

- **Using Operation Regime as a New Design Variable:** Classical MEMS actuators are associated with an intrinsic instability that divides the operation regime into stable and unstable regimes. Traditionally, this instability and associated unstable regime have always been considered as a problem to be mitigated. In this thesis, we advocate using operation regime as a design variable and show that operation in the unstable or close to unstable regime can give rise to extraordinary performance enhancement. The concepts associated with the use of "operation regime" as a design variable are not limited to MEMS only, but belong to a general class of bi-stable Landau systems (details in chapters 5 and 6).

- **Potential of Integration of MEMS and FETs:** The first MEMS device invented in 1967 was a resonant gate transistor [1] and was based on the integration of MEMS and an FET. After that, the two fields (namely, MEMS and FET) evolved separately without realizing the true potential of their integration. In this thesis, we demonstrate the full potential of integration of MEMS

with FET and show that integrating two different technologies can enable applications that are not possible by individual technologies (details in chapters 5 and 6).

The rest of the chapter is organized as follows. In section 1.1, we briefly discuss the history of electromechanical systems. We highlight the prospects of MEMS for both More-Moore and More-than-Moore applications in section 1.2. We discuss different types of MEMS and give examples of each type in section 1.3. In section 1.4, we highlight various design variables that can help tune the performance. We present the outline of thesis in section 1.5. In section 1.6, we list all the published papers based on the work presented in this thesis.

1.1 History of Electromechanical Systems

Electromechanical systems have impacted our society in an unparalleled way. In the last two centuries, the world has seen the phenomenal growth of electromechanical systems at all length scales. In the mid- 1800's to early 1900's, it was electromechanical systems at macro length scales (few centimeters to few meters) in the form of electromagnetically actuated motors and generators, which are now ubiquitous. Electric motors and generators enabled conversion of electrical energy to mechanical energy and vice versa, and are now indispensable for power generation and rail transport. In the early to mid- 1900's, electromechanical relays were used in communication and computation much before the adoption of vacuum tubes. For example, electromechanical relays were used in telegraphy and the first digital computer by Konrad Zuse (invented in late 1930's) was also based on electromechanical relays. It is only after 1950's that electromechanical systems at micron length scales, widely known as microelectromechanical systems (MEMS), started to emerge. Pressure sensors were the first MEMS devices, which were invented after the discovery of piezoresistive effect in silicon and germanium in 1954, and eventually commercialized in 1970's [2]. In the mid- 1960's, the first MEMS actuator known as resonant gate transistor was

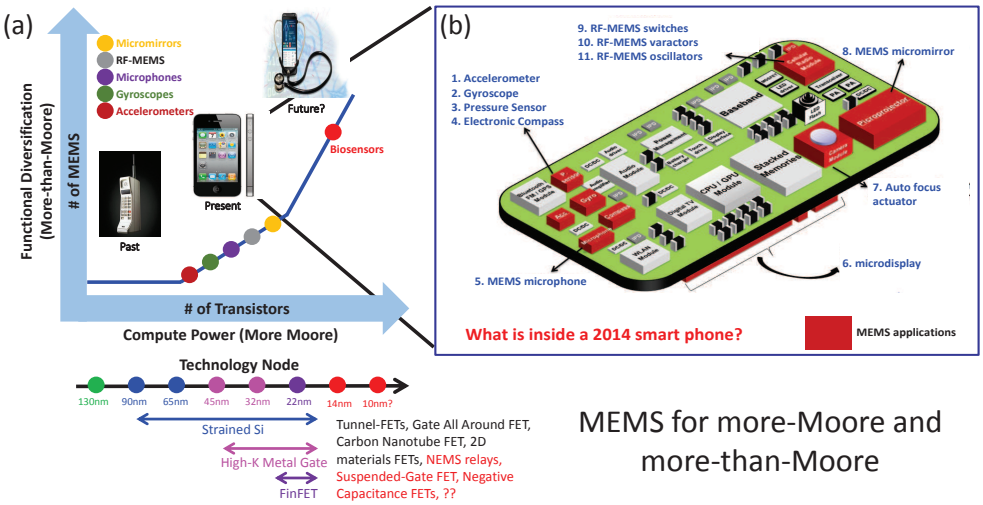

Fig. 1.1. MEMS for both More-Moore and More-than-Moore applications. (a) Evolution of the mobile phones in last three decades highlights both the continuously increasing number of MEMS components adding functional diversity and increasing number of transistors for information processing. (b) Significant board area of the most advanced 2014 smart phone is taken by MEMS components enabling new applications. (image courtesy: google images, Apple, Qualcomm X Prize, and Yole development)

invented [1], eventually leading to many more applications based on the concept of MEMS actuation. It should be stressed that MEMS actuators are electrostatically actuated; electromechanical systems at macro length scales are actuated electromagnetically . This is because magnetic forces are much weaker compared to electrostatic forces at small length scales [3]. Note that, MEMS contain moving parts, e.g., cantilevers, membranes, and diaphragms, which are made by micro-fabrication techniques such as surface and bulk micro-machining in contrast to standard machining techniques such as lathe machining [4]. With this historical background, in the next section, we highlight the potential of MEMS for More-than-Moore and More-Moore applications.

1.2 MEMS for More-Moore and More-than-Moore

Since 1970's, MEMS have been creating new applications in diverse fields, which would not be possible otherwise. For example, they are widely used in automobile, gaming, chemical, health, and display industries [5, 6]. In automobile industry, they are used as accelerometers in crash sensors [7], pressure sensors in tyre pressure monitoring systems (TPMS) [7], and gyroscopes in vehicle stability control system [6]. The replacement of joystick by Wii in gaming industry has been enabled by MEMS based accelerometers [7]. In health industry, they are used as pressure sensors in blood pressure measuring unit; whereas chemical industry requires pressure sensors for monitoring of gas leakage. Other applications of MEMS include digital micromirror devices (DMD) [8] in projectors, optical switches [7], ink-jet printers head [7], and micro-fludics [7]. Beyond this industrial use of MEMS, in recent years, they are gradually entering in the field of consumer electronics e.g., smart phones [9, 10].

Figure 1.1 uses the example of mobile phones to highlight the commercialization of MEMS in consumer electronics. Since 1980's, mobile phones have evolved from being a very rudimentary and bulky to highly sophisticated and lightweight (Fig. 1.1 a). This continuing evolution may eventually embed bio-sensors in smart phones to enable medical diagnosis. This evolution is not only driven by the increasing number of transistors (following well-known Moore's law of transistor industry), but also continuously increasing number of MEMS [9, 10]. Although the total number of MEMS components in any electronic gadgets is much smaller than the number of transistors, it should be appreciated that each MEMS component enables a new function. Note that, increasing number of transistors can only increase the brain power of the system; whereas components such as MEMS enable senses and muscles. Considering these two aspects, two research directions have emerged: The More-Moore strategy focuses on integrating more number of transistors in a given area to sustain the Moore's law; and the More-than-Moore approach focuses on creating new applications (Figs. 1.1-1.2).

Figure 1.1 b shows different MEMS components that are inside the most advanced phone of today, which include inertial sensors e.g., accelerometer and gyroscope, RF-MEMS, microphone, and microdisplays. New MEMS are being added in each generation [9,10]. The addition of these MEMS components enable new applications adding functional diversity. MEMS are therefore identified as ideal candidates for creating More-than-Moore applications [11,12], and is reflected in their inclusion in 2011 ITRS (International Technology Roadmap for Semiconductors) [6].

It is interesting to note that MEMS are traditionally known for creating new applications. But, in recent years, they are being considered for More-Moore applications also. Since scaling of transistors is becoming more and more difficult every generation, sustaining the growth has become a fundamental challenge of enormous scientific and economic importance. The scaling of transistors in past few technology nodes have required new breakthroughs (Fig. 1.1 a). These breakthroughs have involved engineering both the material and device geometry. Examples of material engineering include use of strained Si and high-κ metal gate (HKMG); whereas adoption of Fin-FET [13] is an example of device geometry engineering (Fig. 1.1 a). Next technology generations will also require similar innovations. Various alternatives to the current transistors include multi-gate FET [14], nanowire based gate all around (GAA) FET [15], carbon nanotube FET [16], 2D materials such as graphene or MoS2 based FET [17], tunnel FET [18], and negative capacitance FET [19]. MEMS, or rather, nanoelectromechanical systems (NEMS) such as NEMS relays [20] and suspended-gate field effect transistors (SG-FETs) [21] are also being considered as an alternative of transistor due to their extraordinary performance to be discussed in section 1.3 and we will discuss them in detail in subsequent chapters. In this thesis, we will show that MEMS based switches provide us a unique platform to realize ideal switching characteristics that are not possible by other existing alternatives of transistors. Therefore, MEMS are not only good candidates for More-than-Moore applications, but also find applications along More-Moore direction (Fig. 1.2). In the next section, we discuss application space of MEMS and show specific examples for sensing, switching, and

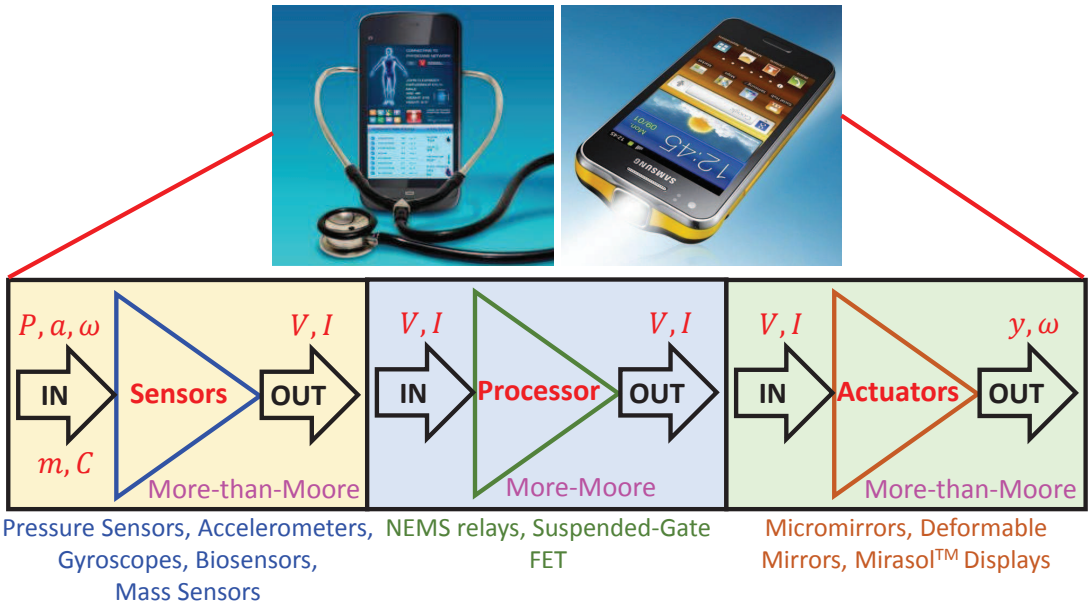

Fig. 1.2. Sensor, information processor, and an actuator are the three essential pieces of any electronic gadget. MEMS find applications in each of them. The key differences among them and corresponding devices in each category are shown schematically.

actuation. We also identify some of the bottlenecks of existing MEMS devices and point out our proposal of novel MEMS devices to address those bottlenecks.

1.3 Application Space of MEMS

In the previous section, we pointed out that MEMS are potential candidates for enabling both More-Moore and More-than-Moore applications. We now discuss specific applications of MEMS in broad range of fields. Broadly, MEMS can be categorized as sensors, switches, and actuators (Fig. 1.2). They differ in the following ways. The input to sensors is some physical quantity e.g., pressure (P), acceleration (a), rotation (ω), mass (m), or some chemical concentration (C) and the output is an electrical quantity like voltage (V) or current (I). In contrast, input to MEMS

actuators is an electrical quantity like voltage (V) or current (I) and the output is some displacement (y) or rotation (ω). In MEMS based switches, input is V or I and the output is also V or I. Note that, MEMS based switches differ from classical field effect transistors as the latter do not involve any mechanical movement; whereas MEMS based switches are just specific examples of MEMS actuators in which y or ω is converted to electrical quantities for output. Also, classical MEMS sensors such as pressure sensors and accelerometers are micro-mechanical systems relying on the mechanical movement due to some external stimuli e.g., pressure (P) or acceleration (a) to be sensed. The readout based on either capacitance change (capacitive detection) or resistance change (piezoresistive detection) is the only electrical part in classical MEMS sensors. In contrast, MEMS actuators or switches are electromechanical systems that rely on the interaction between the electrostatic and mechanical forces. The mechanical movement induced by electrostatic force enables novel applications. We illustrate these points in details through following examples:

1.3.1 MEMS Sensors for More-than-Moore

A typical MEMS based sensor consists of a movable or a bendable element such as a cantilever, fixed-fixed beam, or a diaphragm. Based on the interaction of stimuli (to be detected) with the movable element, MEMS sensors can broadly be divided into following three categories: (i) Force sensors, (ii) Elastic sensors, and (iii) Stress sensors. In force sensors, the stimuli exerts an external force on the movable element and causes it to move. The movement is then used as the signature for detection. In elastic sensors, the interaction of stimuli with the movable element results in modification of the elastic properties such as mass or the stiffness, resulting in the change in the resonance frequency. This change in the resonance frequency is measured for detection. Finally, in stress sensors, the stimuli introduces a stress in the movable element resulting in either bending of the movable element or change in the resonance frequency or both. Either of which can then be measured for detection. Note that,

Interaction → / Operation ↓	Force	Elastic		Stress
	Force	Mass	Stiffness	Stress
Static	Deflection	NA	Deflection	Deflection
Dynamic	NA	Resonance Frequency	Resonance Frequency	Resonance Frequency

Fig. 1.3. Classification of MEMS sensors based on the operation mode and the interaction between stimuli and movable element.

based on the operation mode of sensor, they are further classified in two categories: (i) Static sensors and (ii) Dynamic Sensors. The static sensors are based on the measurement of static deflection of movable element; whereas the dynamic sensors rely on the change in resonance frequency. Force sensors are operated in static mode; whereas elastic sensors are classically operated in dynamic mode. In this thesis, in chapter 6, we will introduce a new class of elastic sensors that operate in static mode. Interestingly, stress sensors can be operated in both modes. Figure 1.3 summarizes this classification of MEMS sensors. Below, we illustrate each of the above points using specific example of MEMS sensor.

Pressure Sensors: Static Force Sensors

Classical pressure sensors consist of a diaphragm suspended above a fixed electrode (Fig.1.4 A). It is an example of a force sensor operated in static mode. When a pressure is exerted on the diaphragm, it deflects downward towards the fixed electrode changing the gap y between the two electrodes [22]. The change in capacitance due to change in the gap (y) is then measured using electronic circuits. Another approach for pressure sensing involves a diaphragm of a piezoresistive material, in which pressure on the diaphragm creates a strain in the diaphragm and changes its resistance [22]. This

change in the resistance can then be read electrically. Note that, the capacitive sensors do not require any specific material, but piezoresistive sensors require a piezoresistive material for sensing.

Accelerometer (Inertial Sensor): Static Force Sensor

Inertial sensors are used for the sensing of inertial quantities such as acceleration and rotation [2,5]. Inertial sensors (e.g., accelerometers) are employed in automobiles as crash sensors, smart phones for the rotation of screens, and Wii games [7]. Figure 1.4 B shows the schematic of an accelerometer. It consists of an inertial mass (M) attached to the springs, a movable electrode, and two fixed electrodes as shown in Fig. 1.4 B. It is also an example of a force sensor operated in static mode. In presence of an acceleration (a), inertial mass experiences a force of (Ma) opposite to the direction of acceleration. The movement due to this acceleration changes the gap (y_1 & y_2) between the movable and the fixed electrodes, and therefore changes the differential capacitance. This change in the differential capacitance is then measured electrically for the detection of acceleration. Note that, Fig. 1.4 B shows one movable and two fixed electrodes, however, in practice there are multiple electrodes to amplify the change in differential capacitance.

Vapor/Gas and Biomolecule Sensors

MEMS based vapor/gas and biomolecule sensors share the same structure that consists of a cantilever (Fig. 1.4 C-D). In case of vapor/gas sensing [23], a vapor/gas sensitive material such as a polymer is attached to the cantilever; whereas biomolecule sensing [24] requires decorating the cantilever surface by receptor molecules. Note that, vapor/gas or biomolecule sensor can be either elastic sensor or stress sensor and can be operated in either static or dynamic mode. In static mode stress sensor, addition of vapor/gas to the polymer or target-receptor binding creates a surface stress and results in the bending of the cantilever. The displacement of the tip of the

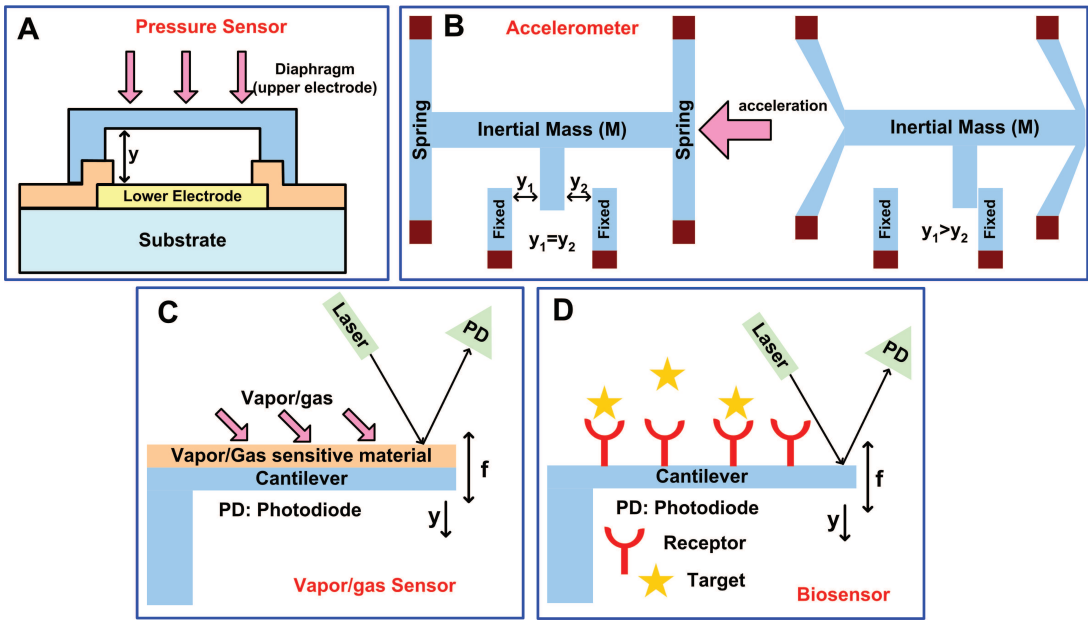

Fig. 1.4. Examples of MEMS sensors. (A) Classical pressure sensors and (B) accelerometer with capacitive read out. In both cases, change in the capacitance due to change in the gap between the two electrodes is used for detection. Cantilever based emerging (C) vapor/gas and (D) bio-molecule sensors. Both sensors rely on change in the surface stress or mass of the cantilever for detection. Note that, all these sensors solely rely on mechanical movement of a cantilever or diaphragm, and electrical part is only for the read out. There is no interaction between mechanical or electrostatic forces.

cantilever (y) is then measured using optical instruments. In contrast, dynamic mode elastic sensors require observing the change in the resonance frequency (f) due to the addition of mass to the cantilever due to the capture of vapor/gas or biomolecules.

Proposed Sensors in this Thesis

As mentioned above, classical MEMS based sensors are only micromechanical systems. There is no interaction between electrostatic and mechanical forces. The electrical part in classical MEMS sensors is only for readout. In chapter 6, we will propose a new class of electromechanical sensors in which a voltage is applied to the

movable element. The interaction between electrical and mechanical forces divides the operation regime into stable and unstable regimes (details in chapter 2). We will show that operation at the boundary of stable and unstable regimes enhances both the sensitivity and signal-to-noise ratio of the sensor.

1.3.2 MEMS Actuators for More-than-Moore

We now discuss examples of MEMS actuators in which electrostatic force induces displacement in a movable electrode and thus controls the gap (y) between the two electrodes (one movable and one fixed). Note that, this ability to control the gap (y) between the two electrodes enables many applications in diverse fields ranging from communication to computation to optics (Fig. 1.5). Broadly, MEMS actuators can be categorized as capacitive (Fig. 1.5 A) and FET actuators (Figs. 1.5 A - B). Both capacitive and FET actuators share the same mechanical structure i.e., one movable electrode M_1 or gate suspended in air. Electrically, capacitive actuators have a fixed bottom electrode; whereas FET actuators have a semiconducting channel to enable transistor action (Figs.1.5 A-B). Note that, both type of actuators can be operated in two modes:(i) tunable (or analog) and (ii) switching (or digital). Tunable mode requires continuous change of the gap (y) between the two electrodes with continuous change of applied voltage. In contrast, only two states of the gap (y) i.e., up state ($y = y_0$) and down state ($y = 0$) are used in switching mode. Note that, MEMS switches for More-Moore applications to be discussed below are special case of MEMS actuators. The description of both tunable and switching applications enabled by these actuators is discussed below:

Optics: Deformable Mirrors (Tunable Capacitive Actuator)

Deformable mirrors employ an array of MEMS actuators to change the shape of a mirror. They are widely used in adaptive optics for enhanced imaging [25, 29]. They consist of an array of tiny (micron size) mirrors each of which is mounted on a

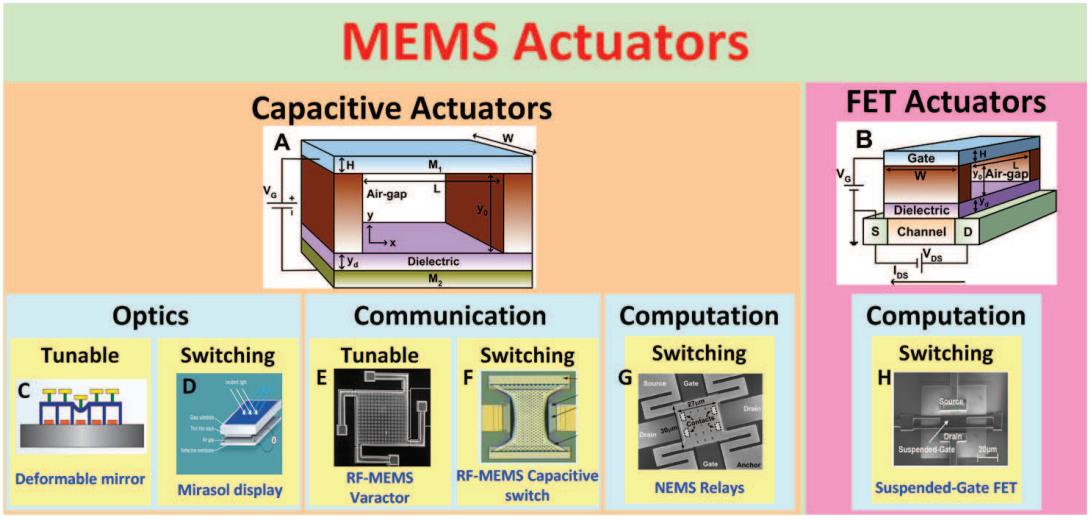

Fig. 1.5. Examples of MEMS actuators used in the fields ranging from communication to computation to optics. Schematic of (A) capacitive and (B) FET actuators. MEMS actuators are used as (C) deformable mirrors [25] and (D) Mirasol displays [26] in optics, (E) RF-MEMS varactors [27] and (F) capacitive switches [28] in communication, (G) NEMS relays [20] and (H) SG-FET [21] in computation.

movable electrode of MEMS actuator as shown in Fig. 1.6 A. Controlling the position of the movable electrode in each actuator enables adjusting the relative position of the mirrors as shown in Fig. 1.6 B. This relative adjustment of the position of mirrors allows to tune the shape of the mirror and thus enable corrective optics applications. The key performance metric of deformable mirrors is the tuning range and a large tuning range is desired. As we will see in chapter 2, the intrinsic instability of MEMS actuators, however, limits the tuning range. In chapter 4, we will propose design of novel tunable MEMS actuators with improved tuning range.

Optics: Mirasol Displays (Switching Capacitive Actuator)

Mirasol displays [26] are reflective interferrometric displays and work based on the principle of thin film interference. These displays do not require any external light source, instead use the ambient light for display. Each pixel in these displays consists

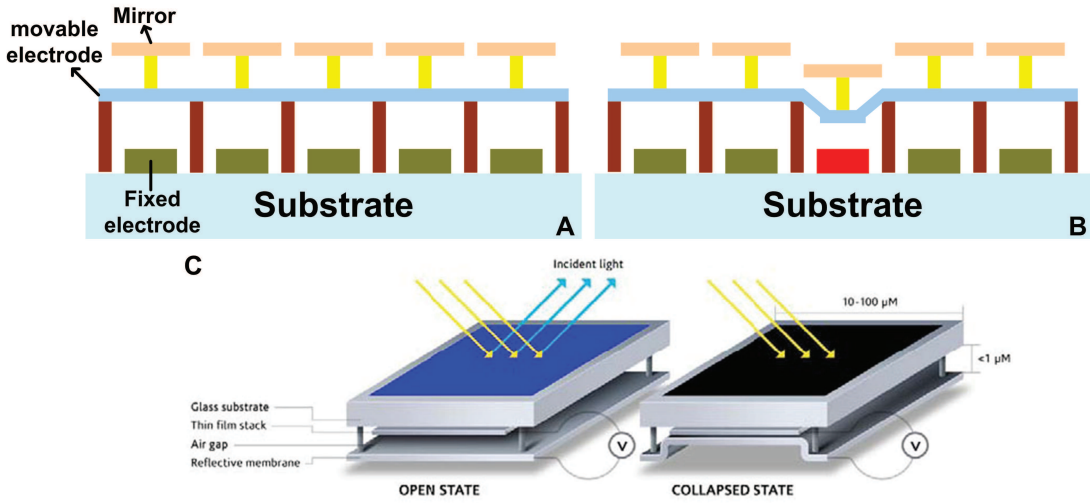

Fig. 1.6. Application of capacitive MEMS actuators in optics. (A)-(B) Tunable deformable mirrors which are used in adaptive optics. The relative position of individual mirror mounted on the movable electrode can be controlled through the application of voltage between movable and fixed electrode, thus enabling tuning of the shape of the mirror. (C) Operation of Mirasol displays which are a reflective interferrometric low power displays.

of three MEMS actuators (each for different color red, green, and blue). Figure 1.6 C shows the schematic and operation of Mirasol displays. The constructive interference of reflected light from thin film stack and bottom reflective membrane gives rise to a particular color, which depends on the gap between thin film stack and the reflective membrane. When a voltage is applied between thin film stack and reflective membrane, they collapse and the pixel appears black. Note that, the operation of Mirasol displays rely on the structure and MEMS actuation rather than any specific properties of a material as in LED or LCD based displays. Moreover, their standby power is very small, and power is consumed only during switching between different states of color e.g., blue to black.

Communication: RF-MEMS Varactors (Tunable Capacitive Actuator)

Radio frequency (RF)-MEMS varactors are tunable capacitors. Capacitance is tuned by applying the voltage between movable and the bottom fixed electrode (Fig. 1.5 E). Schematically, they have the same structure as shown in Fig. 1.5 A. Dielectric need not be present in some cases. RF-MEMS varactors [30] are used in low noise parametric amplifiers (LNA), harmonic frequency generators, and voltage controlled oscillators (VCOs) [30]. Note that, classical varactors based on Si or GaAs p-n or Schottky junction diodes do not provide adequate tuning, sufficient RF linearity, high enough quality factor, and higher self-resonance frequency as compared to RF-MEMS varactors [30].

Communication: RF-MEMS Capacitive Switches (Switching Capacitive Actuator)

RF-MEMS capacitive switches (Fig. 1.5 F) are used for signal routing, impedance matching networks, and adjustable gain amplifiers [28, 30, 31]. Figure 1.7 A shows the use of an RF-MEMS capacitive switch in a transmission line to pass or block an RF signal. In the up state of the movable electrode, impedance is high due to low capacitance, and therefore signal is transmitted (Fig. 1.7 B). In contrast, when electrode is in the down position, impedance is low due to high capacitance, and therefore signal is reflected (Fig. 1.7 C). Note that, RF-MEMS capacitive switches have lower power consumption, lower insertion loss, lower return loss, higher RF linearity, and better isolation compared to their semiconductor counterparts such as Si FETs, GaAs MESFETs (Metal Semiconductors Field Effect Transistors), and p-i-n (PIN) diodes [28, 30, 31]. Since the operation of the switch requires switching the movable electrode between up and down position, the movable electrode hits the bottom dielectric with high velocity during switching and causes dielectric surface to degrade. This is one of the key reliability concerns of RF-MEMS switches. We

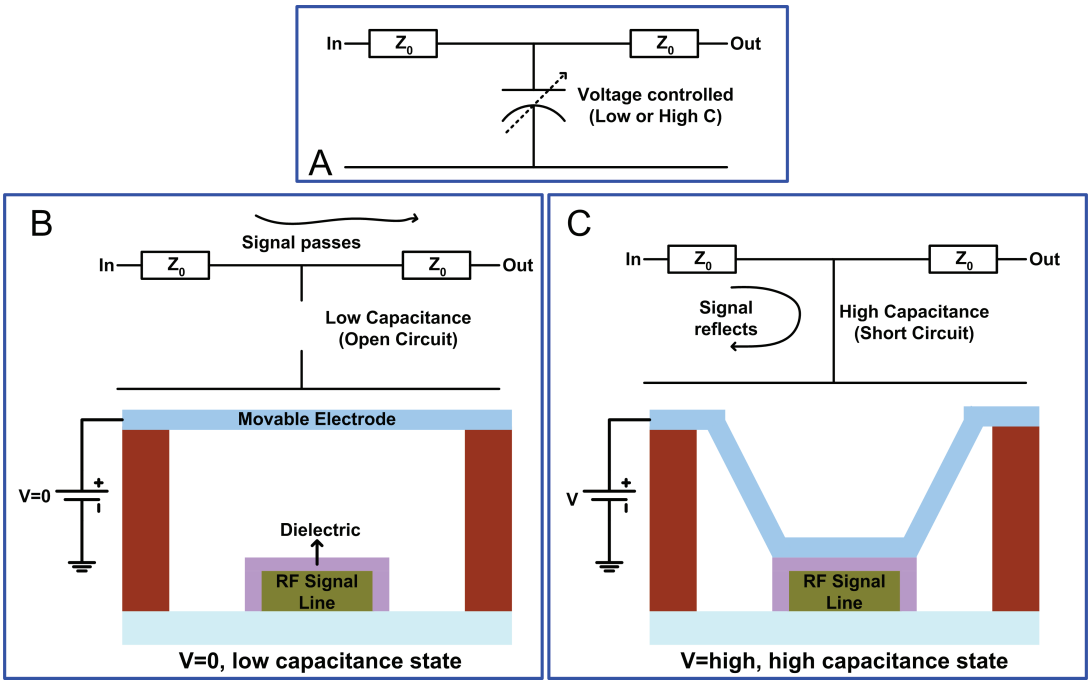

Fig. 1.7. Operation of an RF-MEMS capacitive switch which utilizes the switching mode of a capacitive MEMS actuator. (A) Equivalent circuit model which shows the use of a capacitve switch. (B) When voltage is not applied, capacitance is low and impedance is high, signal passes. (C) In contrast, when voltage is high, capacitance is high and impedance is low, signal reflects. Z_0 is the impedance of transmission line itself.

will discuss the physics of hard-landing in chapter 2 and provide novel strategies of soft-landing in chapter 4.

Proposed Actuators in this Thesis

We will show in chapter 2 that the interaction between the electrostatic and mechanical forces in MEMS actuators results in an intrinsic instability. This instability poses application specific problems in several of MEMS applications. In chapter 4, we propose novel design of MEMS actuators that rely on the use of electrode geometry

as a design variable. The proposed actuators use nanostructured electrodes (instead of classical planar) to circumvent the problems associated with instability.

1.3.3 MEMS Switches for More-Moore

In the previous section, we discussed More-than-Moore applications of MEMS actuators. Here, we illustrate some of the emerging MEMS actuators namely MEMS switches for More-Moore applications. As mentioned above, MEMS switches are specific examples of MEMS actuators with voltage or current as the output.

Computation: NEMS Relays (Switching Capacitive Actuator)

Figure 1.8 shows the schematic of NEMS relays, which are examples of MEMS capacitive actuators. They consist of a cantilever (called source) and two fixed electrodes (called gate and drain, respectively). The terminology of source, gate, and drain has been borrowed from transistors. In the OFF state, source is separated from the drain and no current flows between them (Fig. 1.8 a). In ON state, application of voltage between gate and source pulls the source down to contact drain and a direct current path is created between them (Fig. 1.8 b). The major advantage of NEMS relays over current FETs is their superior OFF state performance. NEMS relays have very low off current (compared to classical FETs) due to the presence of an air-gap between source and drain. Since turning on of NEMS relays require mechanical movement, they are slower than classical FETs. The cascading of NEMS relays at circuit level will make the circuit run even slower due to large mechanical delays. Therefore, NEMS relays based circuits employ different circuit architectures in which no operation relies on cascading of NEMS relays. Instead, during any operation, corresponding NEMS relays are turned on simultaneously. Further details can be found in reference [32] and references therein. Note that, hard-landing during switching is also one of the reliability concerns in NEMS relays and will be discussed further in chapter 4.

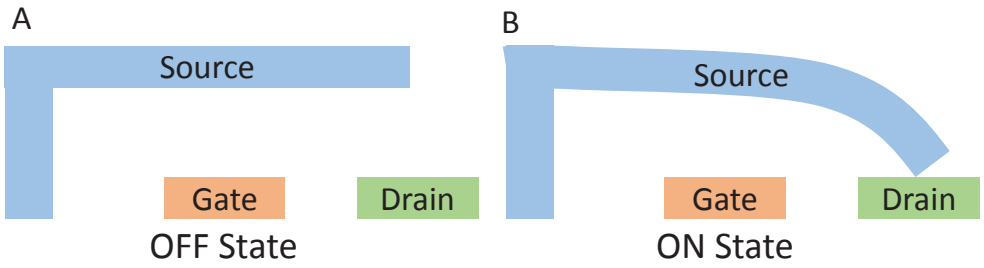

Fig. 1.8. Operation of a nanoelectromechanical system relays for More-Moore applications. (A) In off state, source is separated from the drain by an air-gap; whereas (B) in on state metallic source and drain are shorted to create a direct current path.

Computation: Suspended-Gate FET (Switching FET Actuator)

Suspended-Gate Field Effect Transistor (SG-FET) [21] combines both MEMS actuation and FET behavior. It is a FET with a movable gate (Figs. 1.5 B & H). The movement of the gate due to the application of gate voltage gives rise to unique FET characteristics. Like NEMS relays, SG-FET also has very low sub-threshold leakage compared to classical FETs because of the separation of gate from the channel by an air-gap. Therefore, SG-FET can also be used as a sleep transistor. However, the inherent pull-in instability of MEMS actuators gives rise to abrupt switching equivalent to sub-threshold swing of $0mV/dec$ [21]. Because of such sharp switching characteristics, SG-FET is considered as an ideal candidate for the replacement of classical FETs. However, the intrinsic hysteresis of SG-FET poses a fundamental challenge for the reduction of power supply voltage. We will discuss the issue of hysteresis in chapter 2 and address it in chapter 5. Also, in SG-FET, gate is separated from the channel by a large distance in off state, one should address the issue of drain induced barrier lowering (DIBL), which is supposed to be worse than classical FETs.

1.4 Design Variables

In this chapter, we have so far focused on potential of MEMS from an application point of view. We discussed several MEMS devices both for More-Moore and More-than-Moore applications. We now discuss what are the different design variables that can be optimized to tune the performance of any electronic or MEMS based device. In general, there are three key ingredients of a device: (i) material, (ii) geometry, and (iii) operation regime (Fig. 1.9). The performance of a device can be tuned through tuning of any of the variable. Note that, the unique physics of MEMS provide a platform to advocate "operation regime" as a new design variable for performance enhancement (details in chapter 2). We also show in chapter 4, how the use of electrode geometry as a design variable can address some of the problems associated with planar electrodes. We discuss several examples to further highlight the role of each of the design variable.

1.4.1 Material

The first design variable is "material". The performance of any device (whether for More-Moore applications or More-than-Moore applications) can be improved by choosing a better material. For example, the resistance of a metal wire can be decreased by choosing a material with high conductivity. The wires made of gold have low resistance compared to wires made of copper. Also, pull-in voltage in RF-MEMS capacitive switches can be lowered by having a membrane of low Young's modulus [33]. Also, channel materials such as GaAs [34] or CNT [16] (instead of Si) can improve the on current due to higher mobility of charge carriers. One can cite more examples, but it has been observed that the discovery of new materials with better property keep replacing old materials. That is the reason that the world moved from stone age to bronze age to iron age. The bottom line is adoption of materials with better properties can lead to better device performance.

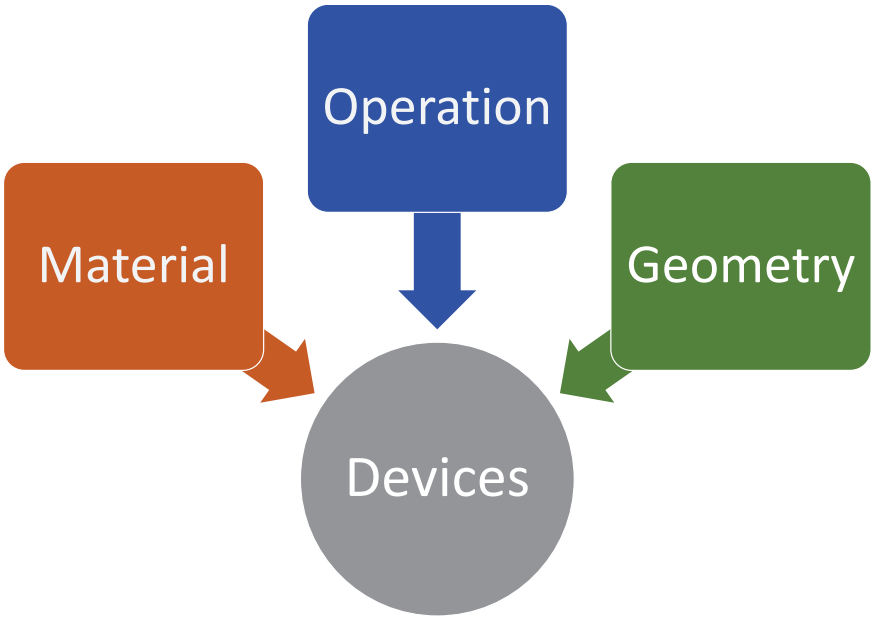

Fig. 1.9. Material, geometry, and operation regime are the three key components of any electronic or electromechanical device.

1.4.2 Geometry

The second design variable is "geometry". In certain cases, the device performance can be modified/improved by changing the device geometry (keeping material the same). For example, the resistance of a wire can be modified by changing its length or cross-sectional area. We will also show in chapters 3-4 how modifying the electrode geometry helps address some of the problems associated with classical planar electrodes based MEMS. The other example of modifying the geometry includes antenna, where the geometry of antenna determines the directivity and the radiation pattern [35]. Similarly, in biosensors, the geometry of the sensor surface determines the response time [36]. The density of states of classical materials such as Si depends on the dimensionality of the material. For example, $D(E) \propto E^{\frac{D_F-2}{2}}$ with $D_F = 3$ for bulk semiconductors, $D_F = 2$ for a sheet, and $D_F = 1$ for a wire, where $D(E)$ is the density of states at energy E. Also, the electric field due to a charge source depends again on the dimensionality of the source. For example, $\xi \propto \frac{1}{r^{2-D_F}}$ with $D_F = 0$ for

a point source, $D_F = 1$ for a line source, and $D_F = 2$ for a planar source, where ξ is the electric field at a distance r from the source. All these examples therefore suggest that geometry can be used to tune the device performance.

1.4.3 Operation Regime

The third variable is "operation regime", which is very different from conventional design variables such as material and geometry. Traditionally, electronic devices were operated in stable regimes only. But, recently it has been proposed that operation in or close to unstable regime can lead to performance enhancement. For example, negative capacitance FETs operate in the unstable regime to provide necessary voltage amplification leading to lower sub-threshold swing [19]. In section 1.3, we also saw that inherent pull-in instability of SG-FET leads to $0mV/decade$ sub-threshold swing characteristics [21]. We will show several such examples in chapters 5 & 6, where modifying the operation regime or utilizing instability will lead to performance enhancement.

The role of the three design variables can be easily understood by the following analogy. Consider, material and geometry of a device are represented by numbers as shown in Fig. 1.10. The higher number represents better material quality or better geometry. The arithmetic operation (addition or multiplication) between these two numbers represents the "operation regime" of the device. Performance is the output of this arithmetic operation. We consider addition as the classical operation in the stable regime; whereas multiplication represents operation in or close to the unstable regime. This analogy clearly highlights that the improvement in material or device geometry improves the performance. However, an extraordinary gain in performance is possible only by changing the operation regime. We will demonstrate this using specific examples of MEMS in chapters 5 and 6.

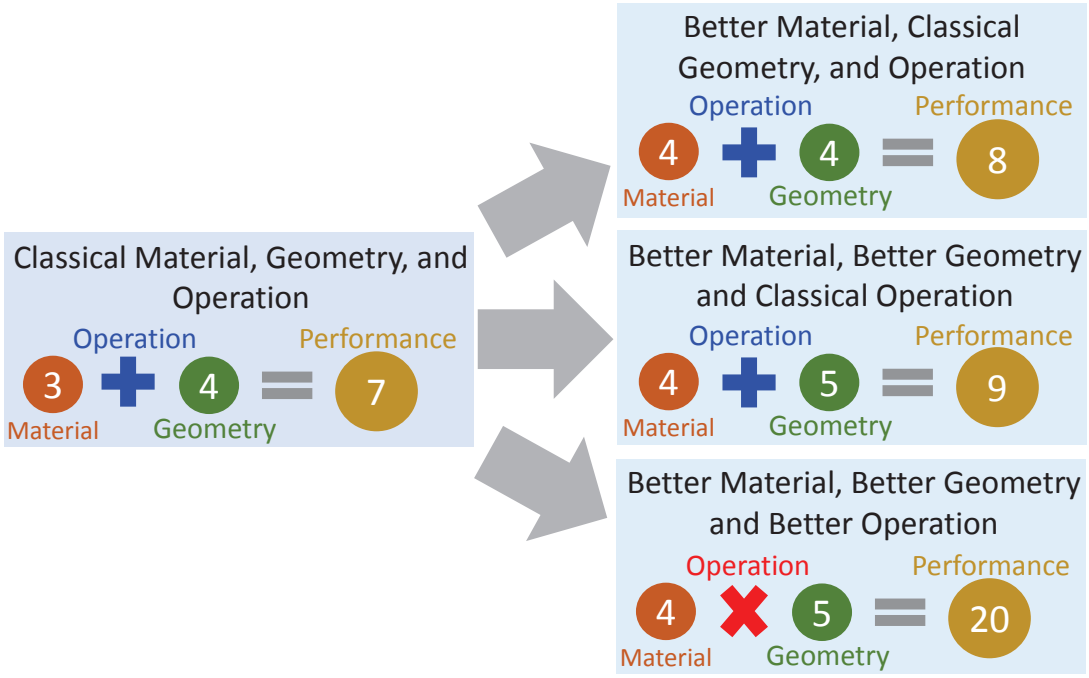

Fig. 1.10. Explaining the role of various design variables using simple example of arithmetic operations.

1.5 Outline of the Thesis

The focus of this thesis is on electronic/electromechanical systems with intrinsic instability. We call such systems "Landau" systems (details in chapter 2). Landau systems are bi-stable in nature and are characterized by a two well energy landscape. The presence of instability (or bi-stable nature) naturally divides the operation regime in two regimes: stable and unstable. The goal of the thesis is to understand instability and its consequences, provide solutions to the problems that arise because of instability, and utilize it (operation in or close to the unstable regime) for performance enhancement. In this thesis, we have used MEMS capacitive actuators as an illustrative example of Landau systems. For the specific applications of MEMS, we have proposed use of electrode geometry as a design variable to address the problems arising because of instability. We have then used MEMS as a platform to advocate

the "operation regime" as a new design variable. For the sake of generality, we have considered ferroelectric materials as another example of Landau systems. We show that the concepts derived from the analysis of MEMS are general enough to be applicable to ferroelectric materials. The analysis presented in this thesis is based on experimentally validated detailed numerical simulations and analytical calculations. Note that, the chapters 3 & 4 are specific to MEMS applications; whereas chapters 5 & 6 only use MEMS as a platform to advocate the role of operation regime. The outline of the thesis is as follows (Fig. 1.11):

- In chapter 2, we introduce the concept of Landau systems using MEMS capacitive actuators and ferroelectric materials. Using the evolution of energy landscapes, we discuss the origin of instability and point out its consequences on the static/dynamic response of the system. We then point out which features of instability are important in which applications. We highlight the problems that arise because of the instability. We also discuss the applications where instability can be used for performance enhancement.

- The focus of chapter 3 is on the development of a universal framework for the instability in MEMS capacitive actuators. We provide compact analytical formulas for instability and related characteristics that can explain a broad range of experimental data in a single theoretical framework. We also illustrate the usefulness of the developed scaling relationships by using them for the characterization of novel MEMS actuators.

- In chapter 4, we focus on applications of MEMS capacitive actuators in which instability lead to a fundamental problem. Specifically, we propose novel solutions to address the problem of limited travel range in tunable gap electromechanical actuators and hard-landing in MEMS switches. The proposed solutions are based on utilizing the electrode geometry as a design variable.

- In chapter 5, we harness instability or use operation regime as a design variable for performance enhancement in field effect transistors (FETs). We utilize the

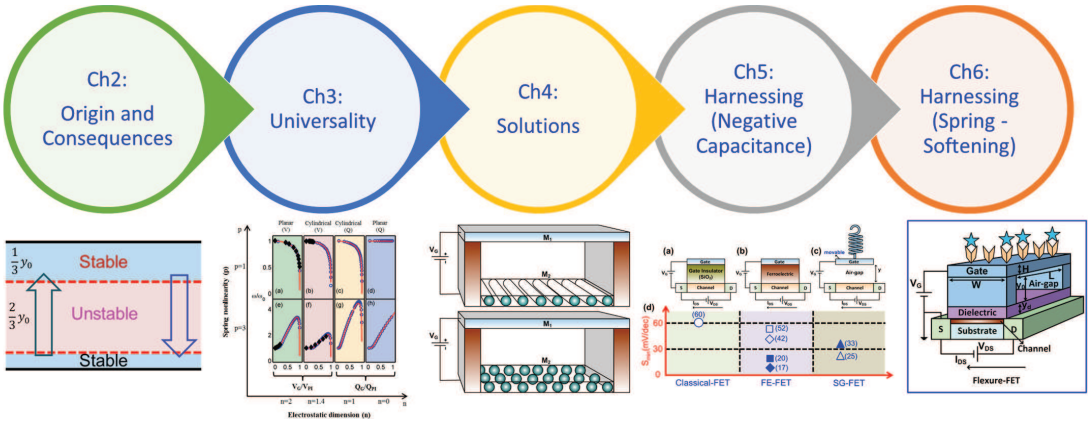

Fig. 1.11. Schematically showing the outline of the thesis. Each chapter focuses on one key aspect of the instability.

negative capacitance behavior in the unstable regime for voltage amplification in suspended-gate FET and ferroelectric FET for sub-60$mV/decade$ switching characteristics. We then establish that there is a fundamental lower limit of sub-threshold swing associated with each negative capacitance FET. We find that the limit depends on the type of negative capacitor and channel type. We then propose a novel device concept that uses series combination of two different types of negative capacitors as gate insulator of a FET. We then show that the proposed device with constant channel capacitance has the potential to achieve hysteresis-free $0mV/decade$ (ideal) switching characteristics.

- In chapter 6, we continue with the philosophy of using operation regime as a design variable. We propose a new class of Flexure biosensors that operate close to the boundary between stable and unstable regime to not only improve the sensitivity but also amplify signal-to-noise ratio.

- In chapter 7, we summarize the findings of this thesis and propose some possible future directions.

1.6 List of Associated Publications

Following is the list of publications based on the work presented in this thesis.

Chapter 3:

- **A. Jain** and M. A. Alam, "Generalized Theory of Electro-Mechanical Resonators With Fractal Electrodes," in Volume 5: 6th International Conference on Micro- and Nanosystems, 2012.
- **A. Jain** and M. A. Alam, "Universal Resonant and Pull-in Characteristics of Tunable-Gap Electromechanical Actuators," IEEE Transactions on Electron Devices, vol. 60, no. 12, p. 4240-4247, 2013.

Chapter 4:

- **A. Jain**, P. R. Nair, and M. A. Alam, "Strategies for Dynamic Soft-Landing in Capacitive Microelectromechanical Switches," Applied Physics Letters, vol. 98, no. 23, p. 234104:1-3, 2011.
- **A. Jain**, P. R. Nair, and M. A. Alam, "Capacitive Microelectromechanical Switches with Dynamic Soft-Landing," U.S. Patent 13/46600607, 2012.
- **A. Jain** and M. A. Alam, "Extending and Tuning the Travel Range of Microelectromechanical Actuators Using Electrically Reconfigurable Nano-Structured Electrodes," Journal of Microelectromechanical Systems, vol. 22, no. 5, p. 1001-1003, 2013.

Chapter 5:

- **A. Jain** and M. A. Alam, "Prospects of Hysteresis-Free Abrupt Switching (0 mV/decade) in Landau Switches," IEEE Transactions on Electron Devices, vol. 60, no. 12, p. 4269-4276, 2013.
- **A. Jain** and M. A. Alam, "Stability Constraints Define the Minimum Subthreshold Swing of a Negative Capacitance Field-Effect Transistor," IEEE Transactions on Electron Devices, vol. 61, no. 7, p. 2235-2242, 2014.
- **A. Jain** and M. A. Alam, "Proposal of a Hysteresis-Free Zero Sub-threshold Swing Field Effect Transistor (ZSubFET)," (Conditionally Accepted in TED), 2014.
- M. Masuduzzaman, **A. Jain**, and M. A. Alam, "NEMS Devices with Series Ferroelectric Negative Capacitor," U.S. Provisional Patent 66696-01, 2014.

Chapter 6:

- **A. Jain**, P. R. Nair, and M. A. Alam, "Transistor-based particle detection systems and methods," U.S. Patent 13/748171, Jul. 2013.
- **A. Jain**, P. R. Nair, and M. A. Alam, "Flexure-FET Biosensor to Break the Fundamental Sensitivity Limits of Nanobiosensors Using Nonlinear Electromechanical Coupling," Proceedings of the National Academy of Sciences of the United States of America, vol. 109, no. 24, p. 9304-9308, 2012.
- **A. Jain** and M. A. Alam, "Signal-to-Noise Ratio Improves in Critical Point Flexure Sensors," (Under Review), 2014.

Appendix G:

- **A. Jain**, S. Palit, and M. A. Alam, "A Physics Based Predictive Modeling Framework for Dielectric Charging and Creep in RF MEMS Capacitive Switches and Varactors," Journal of Microelectromechanical Systems, vol. 21, no. 2, p. 420-429, 2012.

Appendix H:

- **A. Jain**, A. E. Islam, and M. A. Alam, "A Theoretical Study of Negative Bias Temperature Instability in p-Type NEMFET," in 18th Biennial University/Government/Industry Micro/Nano Symposium, 2010.
- **A. Jain**, A. E. Islam, and M. A. Alam, "On the Electro-Mechanical Reliability of NEMFET as an Analog/Digital Switch," in IEEE International Reliability Physics Symposium, 2012.

Other publications (during academic program) not discussed in this thesis:

- S. Palit, **A. Jain**, and M. A. Alam, "A non-obtrusive technique to characterize dielectric charging in RF-MEMS capacitive switches," in IEEE International Reliability Physics Symposium, 2012.
- S. Palit, **A. Jain**, and M. Ashraful Alam, "Universal Scaling and Intrinsic Classification of Electro-Mechanical Actuators," Journal of Applied Physics, vol. 113, no. 14, p. 144906:1-8, 2013.
- S. Mahapatra, A. E. Islam, S. Deora, V. D. Maheta, K. Joshi, **A. Jain**, and M. A. Alam, "A Critical Re-evaluation of the Usefulness of R-D Framework in Predicting NBTI Stress and Recovery," in IEEE International Reliability Physics Symposium, 2011.

- S. Gupta, B. Jose, K. Joshi, **A. Jain**, M. A. Alam, and S. Mahapatra, "A Comprehensive and Critical Re-assessment of 2-stage Energy Level NBTI Model," in IEEE International Reliability Physics Symposium, 2012.

- S. Mahapatra, N. Goel, S. Desai, S. Gupta, B. Jose, S. Mukhopadhyay, K. Joshi, **A. Jain**, A. E. Islam, and M. A. Alam,"A Comparative Study of Different Physics-Based NBTI Models," IEEE Transactions on Electron Devices, vol. 60, no. 3, p. 901-916, 2013.

2. ELEMENTARY PHYSICS OF INSTABILITY

In the previous chapter, we mentioned about using instability and operation regime as a design variable. In this chapter, we illustrate the physics of instability and how does that lead to stable and unstable regimes, using MEMS capacitive actuators as an example case. For MEMS capacitive actuators, we show that its operation and instability can be understood using a simple spring-mass system. We establish the connection between the so called two well "Landau" energy landscape and the energy landscape of MEMS capacitive actuators. Once this connection is established, we find that the phenomenon of instability is a key characteristic feature of all Landau systems and we use ferroelectric material as another example to justify it. Our approach is very general: It explains both the static and dynamic characteristics, as well as provide techniques to control device operation. This chapter is organized as follows. We start with the discussion of instability in MEMS in section 2.1. We discuss ferroelectrics in section 2.2. We comment on the general features of Landau systems in section 2.3 and conclude in section 2.4.

2.1 Instability in MEMS/NEMS

2.1.1 Spring-Mass Model of MEMS Capacitive Actuators

Figure 2.1 shows the schematic of a typical voltage actuated MEMS capacitive actuator. As explained in chapter 1, it consists of a movable electrode M_1 and a fixed electrode M_2, separated by an air-gap and a thin dielectric (Fig. 2.1 a). The application of voltage V_G causes M_1 to deflect toward the fixed dielectric and reduced gap between M_1 and M_2 increases the capacitance. This tuning of the gap and the

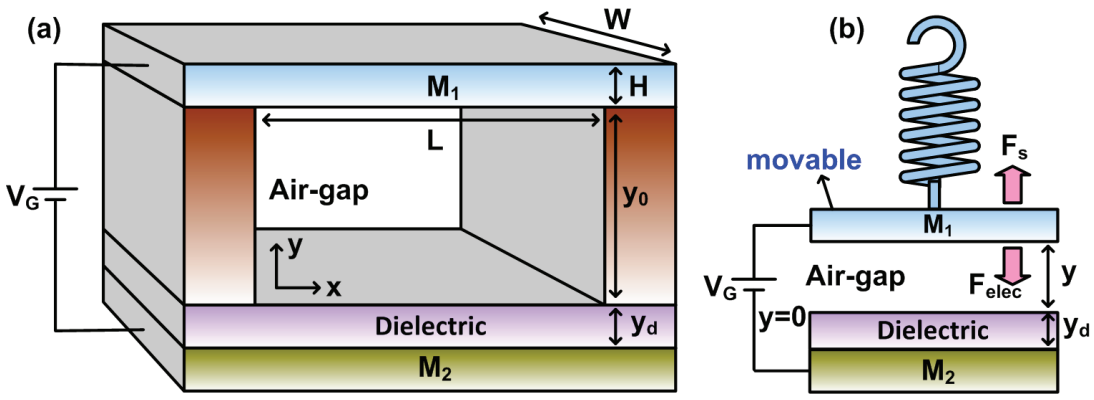

Fig. 2.1. (a) Schematic of a MEMS capacitive actuator, representative of many applications such as, RF-MEMS switches, varactors, deformable mirrors, and Mirasol displays. (b) Lumped parameter spring-mass model of the same.

capacitance with V_G is the basis of many applications such as, RF-MEMS capacitive switches [30], varactors [30], deformable mirrors [25], and Mirasol displays [26].

The behavior of MEMS capacitive actuator can be modeled using a simple spring-mass system (Fig. 2.1 b), which is characterized by a single displacement y assuming all the points on M_1 move together. In spring-mass model, we assume that electrode M_1 is suspended from a spring above the fixed electrode M_2. And, the operation is governed by the interaction between mechanical energy (or force) and electrostatic energy (or force), and are discussed below-

Energy Landscapes : Spring and Electrostatic Energy

The spring energy (derived from the mechanical energy in Euler-Bernoulli framework, refer to appendix A) consists of two parts: (i) linear spring energy and (ii) non-linear spring energy corresponding to a spring of cubic non-linearity. The expression for each components is given by-

$$U_s^L = \frac{1}{2}\left(\frac{\alpha EI}{L^3} - \frac{\beta P}{L}\right)(y_0 - y)^2 = \frac{1}{2}k\,(y_0 - y)^2\,, \tag{2.1}$$

$$U_s^{NL} = \frac{\gamma EA}{4L^3}\left(y_0 - y\right)^4 = \frac{1}{4}k'\left(y_0 - y\right)^4, \tag{2.2}$$

where α, β, and γ are the geometrical constants that depend on the specific boundary conditions of electrode M_1 (refer to Eqs. A.1 - A.2 for fixed-fixed case). Note that, $k = \left(\frac{\alpha EI}{L^3} - \frac{\beta P}{L}\right)$ is the linear spring constant, whereas $k' \equiv \frac{\gamma EA}{L^3}$ corresponds to a spring of cubic non-linearity. Here, E is the Young's modulus of the electrode material, I is the second moment of area, L is the length, and P is the axial load M_1. For a rectangular cross-sectional beam, second moment of area I is given as $I \equiv \frac{WH^3}{12}$ [37], where W is the width and H is the thickness of M_1. It should be stressed that the term $\frac{1}{2}\frac{\alpha EI}{L^3}\left(y_0 - y\right)^2$ in U_s^L corresponds to bending energy of M_1 (Eq. A.3 in appendix A) and $-\frac{\beta P}{2L}\left(y_0 - y\right)^2$ energy component corresponds to the stress in M_1 (Eq. A.5). Moreover, the quadratic dependence of U_s^L on the stretching of spring (i.e., $(y_0 - y)$) is the consequence of quadratic dependence of $U_{Bending}$ & U_{Stress} on $y(x)$ (Eqs. A.3 - A.5). Similarly, U_s^{NL} corresponds to $U_{Stretching}$ (Eq. A.4) and quadruple dependence of $U_{Stretching}$ on $y(x)$ is reflected in the quadruple dependence of U_s^{NL} on $(y_0 - y)$. Note that, the equations 2.1-2.2 governs the mechanical aspect of the actuator.

The other energy component is the electrostatic energy and consists of two parts: (i) energy stored in the capacitor ($\frac{Q^2}{2C(y)}$) and (ii)decrease in the energy of the voltage source ($-QV_G$), and is given by-

$$U_{elec} = \frac{Q^2}{2C(y)} - QV_G, \tag{2.3}$$

where $C(y)$ is the total capacitance of the MEMS actuator and Q is the charge on M_1.

The static operation of the actuator is simply governed by minimization of total energy, $U = U_s^L + U_s^{NL} + U_{elec}$, with respect to Q and y. Minimizing U with respect

to Q, i.e., $\frac{dU}{dy} = 0$, yields well-known capacitor equation i.e., $Q = C(y)V_G$. The total energy of the system thus reduces to-

$$U = U_s^L + U_s^{NL} - \frac{1}{2}C(y)V_G^2. \tag{2.4}$$

Further minimization of U with respect to y, i.e., $\frac{dU}{dy} = 0$, yields the following force balance equation [38]-

Force Balance : Spring and Electrostatic Forces

$$F_s = F_{elec}, \tag{2.5}$$

where F_s is the total restoring spring force and is given by-

$$F_s \equiv k\left(y_0 - y\right) + k'\left(y_0 - y\right)^3. \tag{2.6}$$

In equation 2.6, the linear term corresponds to U_s^L and cubic term to U_s^{NL}. And, F_{elec} is the total electrostatic force acting on M_1 and is given by-

$$F_{elec} = -\frac{1}{2}\frac{dC}{dy}V_G^2. \tag{2.7}$$

The electrostatic force is governed by the capacitance (C) of the actuator. For a parallel-plate capacitive actuator, total capacitance is $C = \frac{\epsilon_0 WL}{y + \frac{y_d}{\epsilon_d}}$. Here, ϵ_0 is the permittivity of free space, y_d is the dielectric thickness, and ϵ_d is the corresponding dielectric constant. Therefore, for parallel-plate capacitive actuator, the electrostatic force reduces to-

$$F_{elec} = \frac{1}{2}\frac{\epsilon_0 WL}{\left(y + \frac{y_d}{\epsilon_d}\right)^2}V_G^2. \tag{2.8}$$

Similarly, once C is known, F_{elec} can easily be calculated for other geometries also. Equations 2.5-2.7 govern the static behavior of MEMS actuators. Dynamics of the spring-mass system in response to V_G is dictated by Newton's law-

Equation of Motion

$$m\frac{d^2y}{dt^2} + b\frac{dy}{dt} + F_s = F_{elec}. \tag{2.9}$$

Equation 2.9 is similar to Eq. A.13. Here, m is the total mass of M_1 and b is the damping coefficient, which is governed by squeeze-film gas damping in MEMS actuators [39].

Conditions of Stability/Instability

So far, we have discussed equations, such as, force balance (Eq. 2.5) that can be used to find the equilibrium points. We now discuss how to determine whether an equilibrium point is an stable equilibrium point or an unstable equilibrium point. For that, we re-write Eq. 2.9 (for $b = 0$), as follows-

$$\frac{dy}{dt} = v, \quad m\frac{dv}{dt} = F_{elec} - F_s; \tag{2.10}$$

where v is the velocity. Now, using the conditions of equilibrium, which requires all time derivatives to be zero, i.e., $\frac{dy}{dt} = 0$ and $\frac{dv}{dt} = 0$, we get back the equation of force balance (Eq. 2.5). Therefore, at equilibrium $v = 0 \equiv v_{eq}$ and $F_s(y_{eq}) = F_{elec}(y_{eq})$, where y_{eq} and v_{eq} define the points of equilibrium. In order to check the stability/instability of points defined by y_{eq} and v_{eq}, consider small perturbations

around the equilibrium point by letting $y = y_{eq} + \Delta y$ and $v = v_{eq} + \Delta v$. With these values of y and v, Eq. 2.10 reduces to -

$$\frac{d\Delta y}{dt} = \Delta v, \quad m\frac{d\Delta v}{dt} = \frac{d\left(F_{elec} - F_s\right)}{dy}\Delta y \equiv k_{eff}\Delta y \tag{2.11}$$

where $k_{eff} \equiv \frac{d(F_{elec}-F_s)}{dy} = \frac{d^2U}{dy^2}$ is the local (or effective) stiffness at $y = y_{eq}$. Note that, the new system has trivial equilibrium point at $(0, 0)$ and it's stability depends only on the value of k_{eff}. One may now seek solutions to Eq. 2.11 by setting $\Delta y = Ae^{\lambda t}$ and $\Delta v = Be^{\lambda t}$. For nontrivial solutions, the following equations must be satisfied [40]-

$$\lambda^2 + k_{eff} = 0. \tag{2.12}$$

Equation 2.12 suggests that if λ is real and positive, the corresponding equilibrium point will be unstable; whereas if λ is imaginary, equilibrium point will be stable. Therefore, based on linear stability analysis, following are the conditions of stable and unstable equilibrium-

$$Stable : k_{eff} \equiv \frac{d^2U}{dy^2} > 0 \tag{2.13}$$

$$Unstable : k_{eff} \equiv \frac{d^2U}{dy^2} < 0 \tag{2.14}$$

Note that, if $\frac{d^2U}{dy^2} = 0$, linear stability analysis cannot be applied, one will need to consider higher order terms in the series expansion of F_{elec} and F_s. We must emphasize that there is a rich literature on the classification of stability/instability of equilibrium points such as Lyapunov's stability or Structural stability criteria [40], we have however restricted ourselves to linear stability analysis, relevant for the discussion in

this thesis. For more rigorous discussion on instability, the reader may refer to the following references [40, 41].

2.1.2 Origin of Instability in MEMS Capacitive Actuators

We now illustrate how does instability arise in a simple spring-mass system. Origin of the instability can be understood by looking at the evolution of (i) total system's energy landscape or (ii) spring and electrostatic forces in response to the applied V_G. Although, both approaches capture the essential physics and explain the MEMS behavior, some may find one approach more convenient than the other.

Evolution of Energy Landscapes

Figure 2.2 a shows U-y (Eq. 2.4) profile for a linear spring (i.e., $k' = 0$ in Eq. 2.4) and parallel plate capacitive actuator, when V_G is increasing. At each V_G, M_1 is stabilized at the minimum of U. When V_G is low, U-y profile exhibits only one minima. But, with increasing V_G, U-y profile exhibits two minima corresponding to two stable equilibrium points (one at $y \approx y_0$ and other at $y = 0$, see open and filled circles in Fig. 2.2 a) and one maxima corresponding to unstable equilibrium point (open square in Fig. 2.2 a). M_1 is stabilized at one of the two equilibrium points ($y \approx y_0$ when V_G is increasing from zero). Note that, with increasing V_G, the stable and unstable equilibrium points approach each other to annihilate at $V_G = V_{PI}$ and making MEMS capacitive actuator inherently unstable. Beyond, $V_G > V_{PI}$, U-y profile exhibits only one minima at $y = 0$. Therefore, when V_G exceeds the pull-in voltage (V_{PI}), M_1 can no longer be stabilized in air. Instead, it gets pulled-in to stabilize at $y = 0$, corresponding to the global minima of U. This is the well-known pull-in instability of voltage actuated MEMS actuators [1] and occurs at $y = y_c$, where

$$y_c = \frac{2}{3} y_0 - \frac{y_d}{3\epsilon_d}. \tag{2.15}$$

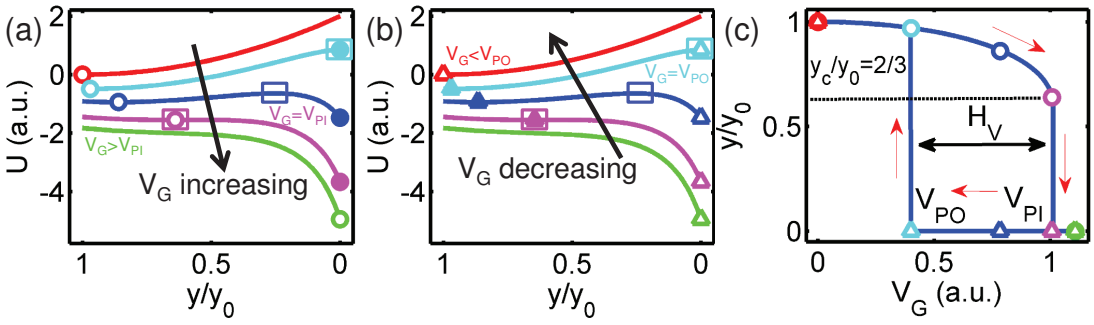

Fig. 2.2. Evolution of energy landscapes when (a) V_G is increasing and (b) V_G is decreasing. Open circle and open triangle denote the position where M_1 is stabilized when V_G is increasing or decreasing, respectively. Filled symbols denote the other minima in energy landscape. Open square denote the unstable equilibrium point which separates the two stable equilibrium points by an energy barrier. (c) The corresponding hysteretic y-V_G characteristics.

Equation 2.15 implies that (i) $y_c = \frac{2}{3}y_0$ for $y_d = 0$ and (ii) y_c does not depend on the stiffness of M_1 and always occurs at two third of the initial air-gap for a parallel-plate actuator [1].

Once M_1 is pulled in, it cannot be pulled back at the same V_G due to the presence of an energy barrier (Figs. 2.2 a-b). As V_G is reduced below V_{PI}, U-y profile is modified and unstable equilibrium moves towards $y = 0$ as shown in Fig. 2.2 b. M_1 however remains stuck at $y = 0$ until unstable equilibrium occurs at $y = 0$ at $V_G = V_{PO}$. Any further reduction in V_G below pull-out voltage (V_{PO}), makes M_1 to swing back to air. Figure 2.2 c shows the corresponding y-V_G hysteretic characteristics showing the abrupt change in y at $V_G = V_{PI}$ and $V_G = V_{PO}$.

Balance of the Two Forces

The energy landscape in Fig. 2.2 described the combined effect of the integrated system. The analysis of individual components provides further insights as follows. We now look at the evolution of spring and electrostatic forces in response to the

applied V_G to understand the operation of MEMS capacitive actuator. Figure 2.3 a shows the two forces for a linear spring (i.e., $k' = 0$ in Eq. 2.6) and parallel plate actuator, when V_G is increasing. As expected from Eq. 2.6, F_s is independent of V_G; whereas F_{elec} increases as V_G^2 (Eq. 2.8). The forces are balanced at two points (open circle and open square in Fig. 2.3 a) in the air-gap and M_1 is stabilized at points denoted by open circles. The points denoted by open squares corresponds to an unstable equilibrium point. As V_G increases, the two points come closer and merge at $V_G = V_{PI}$. Beyond V_G exceeding V_{PI}, F_{elec} overwhelmes F_s and they cannot be balanced at any point in the air. Therefore, M_1 is pulled in to rest on the dielectric at $y = 0$. As evident from Fig. 2.3 a, at $V_G = V_{PI}$, F_s and F_{elec} are tangent to each other. In other words, mechanical ($-\frac{dF_s}{dy}$) and electrical ($\frac{dF_{elec}}{dy}$) stiffness match at pull-in i.e.,

$$k = \frac{\epsilon_0 W L}{\left(y_c + \frac{y_d}{\epsilon_d}\right)^3} V_G^2. \tag{2.16}$$

Equations 2.5-2.8 together with Eq. 2.16 yield Eq. 2.15. Corresponding analytical formula for pull-in voltage is given by-

$$V_{PI} = \sqrt{\frac{8}{27} \frac{k\left(y_0 + \frac{y_d}{\epsilon_d}\right)^3}{\epsilon_0 W L}}. \tag{2.17}$$

Once M_1 is pulled in, it cannot be pulled back at the same V_G due to much higher F_{elec} than F_s at $y = 0$ (Fig. 2.3 a). When V_G is reduced below V_{PI}, M_1 remains stuck at $y = 0$ until F_{elec} becomes equal to F_s. This occurs at pull-out voltage (V_{PO}), which is given by-

$$V_{PO} = \sqrt{\frac{2k y_0 y_d^2}{\epsilon_0 \epsilon_d^2 W L}}. \tag{2.18}$$

As soon as V_G is reduced below V_{PO}, F_s exceeds F_{elec} at $y = 0$ and M_1 comes back

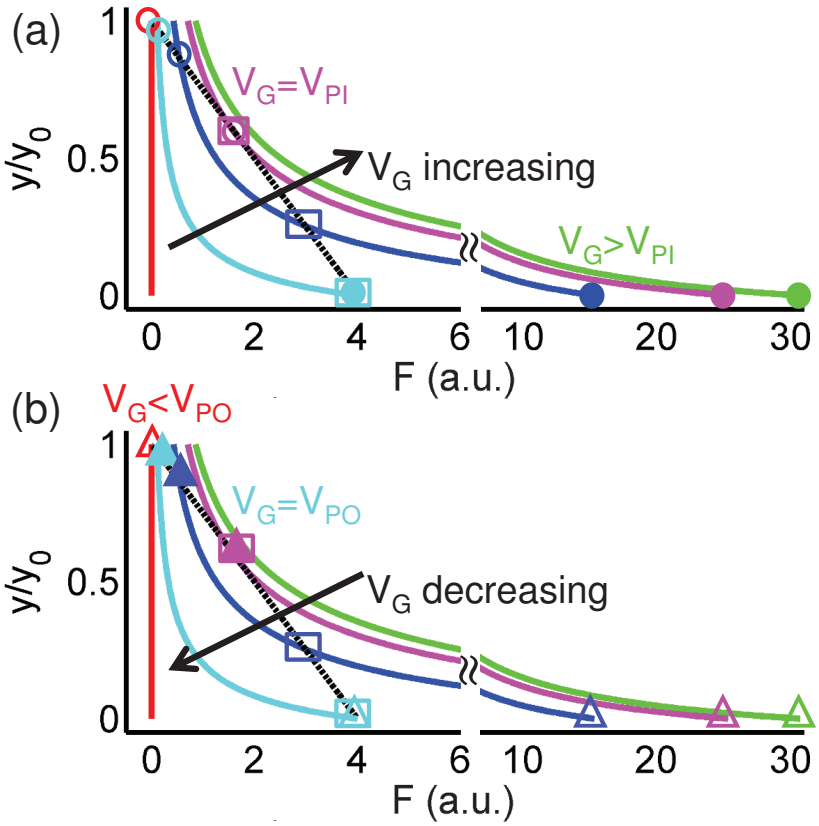

Fig. 2.3. The evolution of the spring and electrostatic forces, when (a) V_G is increasing and (b) V_G is decreasing. Dotted straight line corresponds to the spring force; whereas solid curved lines correspond to the electrostatic force. Open circle and open triangle denote the position where M_1 is stabilized when V_G is increasing or decreasing, respectively. Filled symbols denote the other position where M_1 can also be stabilized. Open squares denote the points where the two forces balance, but M_1 cannot be stabilized.

in air. This asymmetry between pull-in and pull-out leads to the hysteretic y-V_G characteristics as shown in Fig. 2.2 c.

2.1.3 Consequences of Pull-in Instability

In the previous section 2.1.2, we showed how the interaction between mechanical and electrostatic energy (or forces) leads to pull-in instability and hysteresis in capac-

itive MEMS actuators. We now carefully examine the consequences of this instability on the static and dynamic response.

Static Response

(i) Stable and Unstable Regimes:

First obvious consequence of pull-in instability is that M_1 can only be stabilized in certain region of the air-gap, while rest of the region is inherently unstable. Beyond pull-in, M_1 is stabilized at $y = 0$, provided a thin dielectric is present (i.e., $y_d \neq 0$). The bottom line is that there are two stable regimes (corresponding to open/filled circles in Figs. 2.2-2.3) separated by an inherently unstable regime (corresponding to open squares in Figs. 2.2-2.3) as shown in Fig. 2.4 (characteristics of a typical bistable system). We will later see that all bi-stable Landau systems are characterized by this property and may lead to many novel applications.

In the literature, region of the air-gap in which M_1 can be stabilized is termed as travel range of M_1 and is equal to $y_0 - y_c$ (Fig. 2.4). Travel range is a very important performance metric for tunable-gap electromechanical actuators and a large value is desired. But, as we saw, pull-in instability limits it to only one third of the air-gap for parallel-plate actuators (Fig. 2.4). We will come back to this issue in chapter 4 and discuss various ways of extending the travel range.

(ii) Spring-Softening Effect:

We saw that the application of V_G not only changes y, but also modifies the curvature of $U - y$ profile at the stable and unstable equilibrium points (Fig. 2.2). This change in the curvature can be captured by defining an effective stiffness of M_1 and is given by-

$$\frac{k_{eff}}{k} \equiv \frac{d^2U}{dy^2} = -\frac{d\left(F_s - F_{elec}\right)}{y} = 3 - 2\frac{y_0}{y}. \tag{2.19}$$

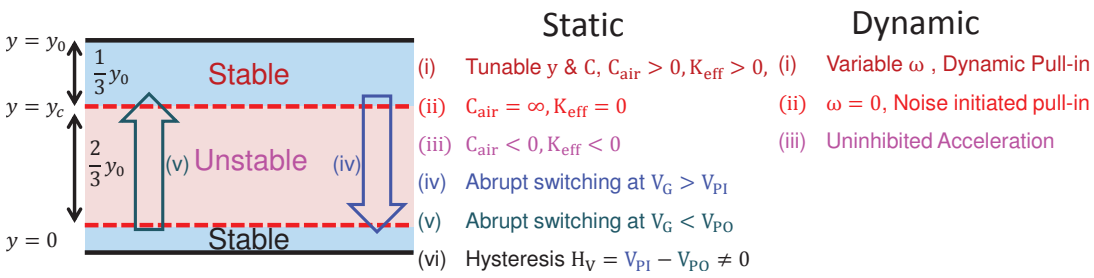

Fig. 2.4. Schematically showing the effect of instability in MEMS capacitive actuators on its static and dynamic response.

Figure 2.5 a shows k_{eff} as a function of y. k_{eff} decreases with decrease in y (or equivalent increase in V_G)and becomes zero at pull-in, i.e., $y = \frac{2y_0}{3}$. Intuitively, this behavior can be understood as follows. The system is characterized by two stiffness: mechanical and electrical. Mechanical stiffness ($k_m = -dF_s/dy = k$) is positive and independent of V_G; whereas electrical stiffness ($k_e = dF_e/dy = -\frac{\epsilon_0 WLV_G^2}{y^3}$ for $y_d = 0$) is negative. As a result, effective stiffness $k_{eff} = k_m + k_e$ continues to decrease with increasing V_G and eventually becomes zero at pull-in. This is the well known spring-softening effect [1]. k_{eff} is negative for $y < \frac{2y_0}{3}$ and is signature of unstable regime. This spring-softening effect have important consequences for sensing applications and will be discussed in detail in chapter 6.

(iii) Negative Capacitance:

In the upper stable regime, MEMS capacitive actuator behaves like a regular tunable capacitor. With the increase in V_G, y decreases and capacitance ($C = \epsilon_0/y$) increases. However, in the unstable regime, the effective air-gap capacitance ($C_{air} \equiv WL\left(\frac{d^2U}{dQ^2}\right)^{-1} = \frac{dQ}{dV_{air}}$) becomes negative (Fig. 2.5 b). Here, V_{air} is the voltage drop in air and $Q = \epsilon_0 V_{air}/y$ is the per unit area charge on M_1. Note that, C_{air} is the differential capacitance and only signifies the curvature of U-Q curve. Although, this

behavior is similar to the negative effective stiffness in the unstable regime, it has not been much appreciated in MEMS literature.

This strange behavior can be understood in a more transparent way if we look at $U-Q$ profile instead of $U-y$ profile. For that, we first minimize total energy $U = U_s^L + U_s^{NL} + U_{elec}$ with respect to y i.e., $dU/dy = 0$. This yields the force balance equation $k\,(y_0 - y) = \frac{Q^2 WL}{2\epsilon_0}$. The total energy is now simplified to-

$$\frac{U}{WL} = \frac{1}{2}\alpha_0^{'} Q^2 + \frac{1}{4}\beta_0^{'} Q^4 - QV_G, \tag{2.20}$$

where $\alpha_0^{'} = y_0/\epsilon_0$ and $\beta_0^{'} = -WL/2\epsilon_0^2 k$ are material/geometrical constant of the actuator. In Equation 2.20, the first term ($\frac{1}{2}\alpha_0^{'} Q^2$) and the third term ($-QV_G$) correspond to the normal capacitor energy and the decrease in the energy of the voltage source, respectively. The second term ($-\frac{1}{4}\beta_0^{'} Q^4$) however is unusual and is responsible for the negative capacitance in the unstable regime. One can now look at the evolution of $U-Q$ profiles with applied V_G to understand the operation of MEMS capacitive actuator. Using Eq. 2.20, effective air-gap capacitance is given by-

$$C_{air}^{-1} \equiv \frac{1}{WL}\frac{d^2U}{dQ^2} = \alpha_0^{'} + 3\beta_0^{'} Q^2 = \frac{3y - 2y_0}{\epsilon_0}. \tag{2.21}$$

Equation 2.21 suggests that C_{air} is positive when $y > \frac{2y_0}{3}$, negative when $0 < y < \frac{2y_0}{3}$, and infinite at $y = \frac{2y_0}{3}$ (Fig. 2.5 b). The charges Q_{c1} and Q_{c2} in Fig. 2.5 b corresponds to $y = \frac{2y_0}{3}$ and $y = 0$, respectively, and are given by-

$$Q_{c1}^2 = \frac{2\epsilon_0 k y_0}{3WL}, Q_{c2}^2 = \frac{2\epsilon_0 k y_0}{WL}. \tag{2.22}$$

This negative capacitance behavior cannot typically be observed because system is unstable in that regime. However, if the device is stabilized in the negative capacitance regime using feedback mechanisms, it can lead to voltage amplification. We will discuss this effect and its consequences in field effect transistors in chapter 5.

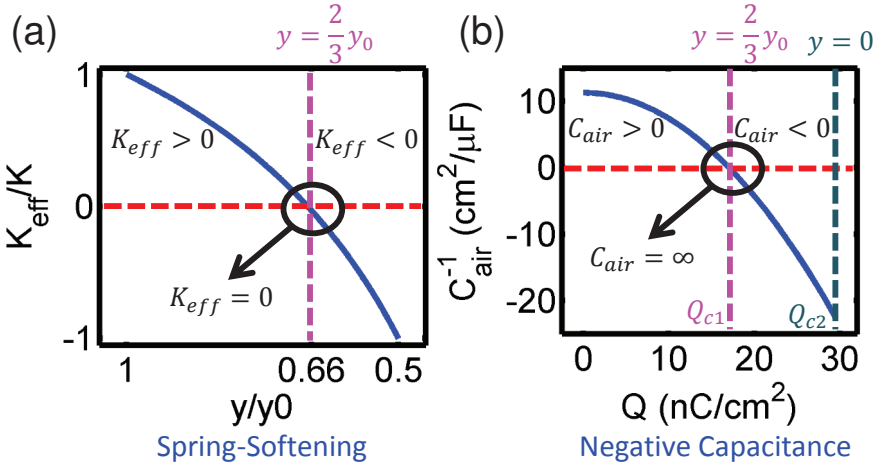

Fig. 2.5. (a) Effective stiffness (k_{eff}) and (b) effective air-gap capacitance (C_{air}) as a function of the gap (y) between the two electrodes and charge (Q) on M_1, respectively.

(iv) Transition Boundary:

We just saw that MEMS exhibit normal behavior with positive stiffness and capacitance; whereas unusual behavior such as negative capacitance and negative stiffness in the unstable regime. However, at the transition boundary (which occurs at $y = \frac{2y_0}{3}$ for parallel-plate geometry) of stable and unstable regime, effective stiffness is zero i.e., $k_{eff} = 0$ and effective air-gap capacitance is infinite i.e., $C_{air}^{-1} = 0$. We will see in chapter 5 that infinite air-gap capacitance at the transition boundary will lead to a fundamental result of negative capacitance field effect transistors; whereas zero stiffness at the transition boundary will become the basis of novel critical-point Flexure sensors in chapter 6.

(v) Abrupt Transition:

In the previous subsections, we looked at what happens in the stable/unstable regimes and at the corresponding transiton boundary. Another important thing to note is the abrupt transition from one stable regime to another stable regime at

$V_G = V_{PI}$ and $V_G = V_{PO}$, respectively (Fig. 2.4). Note that, increasing V_G infinitesimally above V_{PI} or decreasing it infinitesimally below V_{VPO} causes y to change by large amount (Fig. 2.2 c). This abrupt transition is responsible for ultra sharp switching characteristics in suspended-gate field effect transistors [21] and nanoelectromechanical relays [20]. We will discuss this abrupt transition in more detail in chapter 5.

(vi) Hysteresis:

Abrupt transition discussed above is always associated with an intrinsic hysteresis (H_V) (Fig. 2.4). It means that going and coming from one stable branch to another branch occurs at different voltages i.e., $V_{PI} \neq V_{PO}$. The value of hysteresis can be obtained from analytical expressions of V_{PI} & V_{PO} (Eqs. 2.17 - 2.18), and is given by-

$$H_V \equiv V_{PI} - V_{PO} = \frac{2k}{3\epsilon_0 WL} \frac{y_0 + 4\frac{y_d}{\epsilon_d}}{V_{PI} + V_{PO}} y_c^2. \tag{2.23}$$

Equation 2.23 suggests that hysteresis and pull-in instability are correlated. As soon as y_c becomes zero, H_V also becomes zero. As abrupt transition is associated with y_c, hysteresis-free abrupt transition seems impossible in the MEMS capacitive actuator. We will come back to this issue of hysteresis-free abrupt transition in chapter 5 and address the possibility or impossibility of hysteresis-free abrupt transition.

Dynamic Response

In the previous section, we looked at the consequences of pull-in instability on the static response. We pointed out that effective air-gap capacitance and effective stiffness becomes negative in the unstable regime. We now look at the dynamic response and try to understand movement of M_1 when it transitions from one stable regime to another.

(i) Variable Resonance Frequency:

MEMS capacitive actuators, which we are discussing, are also tunable oscillators with resonance frequency given by $\omega_0 = \sqrt{k/m}$ at $V_G = 0$. We saw that k_{eff} changes with the application of V_G. Therefore, resonance frequency, which is directly related to k_{eff} (Figs. 2.2 a - b), i.e., $\omega = \sqrt{k_{eff}/m}$, changes as well. Therefore, MEMS capacitive actuator can also serve as a tunable oscillator with ω being tuned by the application of V_G. Using Eq. 2.19, one can obtain an analytical expression for ω as follows-

$$\frac{\omega}{\omega_0} = \sqrt{\frac{k_{eff}}{k}} = \sqrt{3 - 2\frac{y_0}{y}}. \tag{2.24}$$

Equation 2.24 suggests that ω decreases continuously from ω_0 to zero as y changes from y_0 to $y = \frac{2y_0}{3}$. In chapter 6, we will see that ultra low frequency close to pull-in is responsible for the improvement of signal-to-noise ratio in Flexure sensors.

(ii) Pull-in below Pull-in Voltage:

When we discussed the static response, we saw that M_1 transitions from upper stable regime to lower stable regime, when $V_G > V_{PI}$ is applied. Surprisingly, M_1 can dynamically transition for $V_G < V_{PI}$ in the following ways:

Dynamic Pull-in

Dynamic pull-in can occur when V_G is suddenly changed from zero to $V_G < V_{PI}$, such that $U(y_0)$ is greater than the value of U at the top of the energy barrier (Fig. 2.6 a). Now, M_1 starts from $y = y_0$ at $t = 0$ and moves down hill to gain kinetic energy. If damping is very small, M_1 can get sufficient kinetic energy to surmount the energy barrier as shown in Fig. 2.6 a. Figure 2.6 b shows the corresponding position of M_1 as a function of time. The chances of such dynamic pull-in are higher when damping

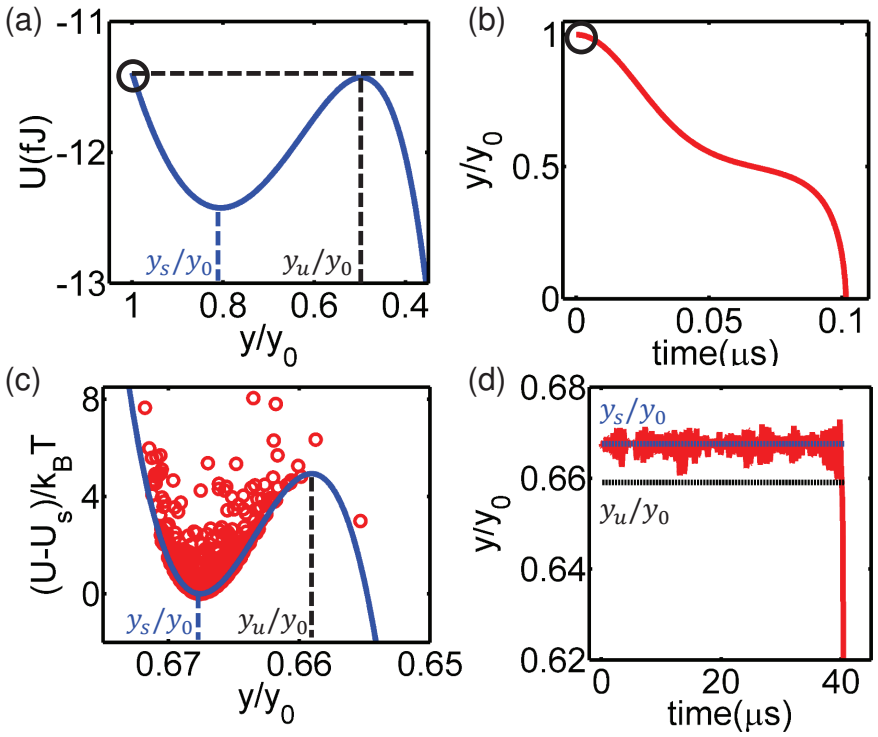

Fig. 2.6. Pull-in can occur even when $V_G < V_{PI}$ due to: (a)-(b) Dynamic pull-in or (c)-(d) noise initiated pull-in. Open circle in (a)-(b) denotes the initial starting point for M_1 and dotted line denotes $U(y_0)$. y_s denote stable equilibrium point and y_u unstable equilibrium point. Dynamic pull-in requires that $U(y_0) > U(y_u)$. In (c)-(d) open circles denote total energy (sum of potential and kinetic) and $U_s = U(y_s)$.

is small. If the damping is very high, dynamic pull-in will not occur. However, M_1 may still get pulled-in for $V_G < V_{PI}$ due to thermomechanical fluctuations as follows.

Noise Initiated Pull-in

Figure 2.6 c shows potential energy landscape when $V_G < V_{PI}$. Ideally, M_1 should stabilize at $y = y_s$ and remain there. However, due to M_1 being in thermal equilibrium with the surroundings, it exchanges energy continuously in units of k_BT, where k_B is the Boltzmann constant and T is the absolute temperature. As a result, M_1

vibrates randomly around its stable equilibrium position as shown in Figs. 2.6 c-d. These random vibrations are the source of noise in MEMS. If the energy barrier $(U(y_u) - U(y_s))$ is couple of k_BT as shown in Fig. 2.6 c, M_1 can get the required energy from the surroundings to surmount the barrier leading to noise initiated pull-in. This noise initiated pull-in puts a fundamental limit on how close we can operate close to pull-in. This will therefore play a critical role in Flexure sensors that achieve maximum sensitivity close to pull-in only (chapter 6 for further discussion).

(iii) Uninhibited Acceleration During Pull-in:

In the previous subsection, we looked at the unintended pull-in, which occurs even when $V_G < V_{PI}$. For regular operation, when $V_G > V_{PI}$ is applied, $U - y$ profile as shown in Fig. 2.7 a, suggests that M_1 will experience a large acceleration in unstable regime. Figures 2.7 b - c show position and velocity of M_1 as a function of time during pull-in. Sudden increase in the velocity towards the end is due to this large acceleration. This uninhibited acceleration will cause M_1 to gain huge kinetic energy $(KE = \frac{1}{2}mv^2)$ (Fig. 2.7 a). M_1 will therefore land on the dielectric surface with very high velocity and cause dielectric to degrade. This hard-landing of M_1 is one of the major reliability concerns in MEMS switches. In chapter 4, we will discuss various strategies to reduce impact velocity of M_1 during pull-in.

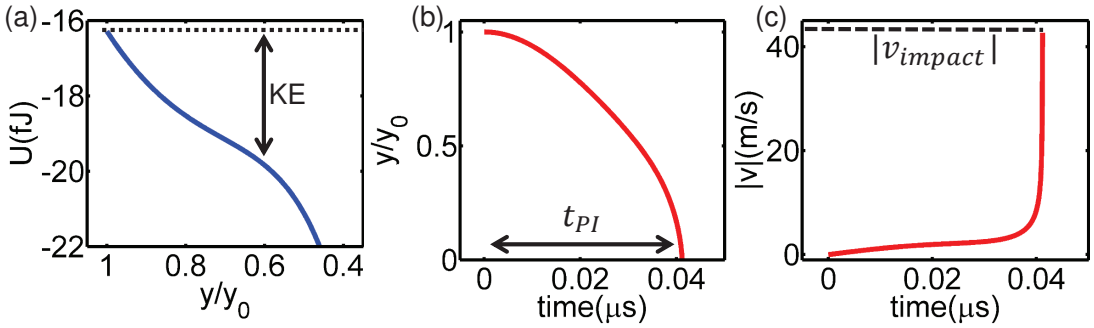

Fig. 2.7. Uninhibited acceleration during pull-in. (a) Potential energy landscape for $V_G > V_{PI}$. (b) Position and (c) velocity of M_1 as a function of time. t_{PI} is the pull-in time and v_{impact} is the impact velocity with which M_1 reaches $y = 0$.

2.2 Instability in a Ferroelectric Material

In the previous section, we discussed the origin and consequences of instability in MEMS capacitive actuators. We now look at the behavior of ferroelectric materials, which also show similar instability characteristics, in-spite of their completely different physics.

2.2.1 Origin of Instability in Ferroelectric Materials

Figure 2.8 a shows the schematic of a ferroelectric based capacitor structure in which a ferroelectric insulator is sandwiched between two metal electrodes M_1 & M_2. This capacitor behaves very differently compared to regular capacitors (with traditional dielectrics such as SiO_2) that follows simple linear charge-voltage relationship. In order to understand the operation of ferroelectric based capacitor, we look at the evolution of energy landscapes as a function of the applied V_G. We consider a single crystalline ferroelectric material. The total energy U of a ferroelectric material is related to the charge Q on M_1 by Landau's energy landscape and is given by-

$$\frac{U}{WLy_{FE}} = \frac{1}{2}\alpha_0 Q^2 + \frac{1}{4}\beta_0 Q^4 + \frac{1}{6}\gamma_0 Q^6 - Q\frac{V_G}{y_{FE}}, \tag{2.25}$$

where α_0, β_0, and γ_0 are material dependent constants. y_{FE} is the thickness of the ferroelectric dielectric. Note that, the first $(\alpha_0 Q^2/2)$ and the fourth term $(-QV_G/y_{FE})$ in Eq. 2.25 are similar to a regular capacitor. The second $(Q^4/4\beta_0)$ and the fourth terms $(\frac{1}{6}\gamma_0 Q^6)$ are extra for a ferroelectric material. If all the coefficients α_0, β_0, and γ_0 are positive, qualitatively, nothing interesting or unusual happens. Capacitor behaves normally, but with a nonlinear charge-voltage characteristics. However, a ferroelectric has $\alpha_0 < 0, \beta_0 > 0, \gamma_0 >$ or $\alpha_0 < 0, \beta_0 < 0, \gamma_0 > 0$ and therefore exhibits a completely different charge-voltage characteristics.

Figure 2.8 a shows $U - Q$ profiles for a ferroelectric with $\alpha_0 < 0, \beta_0 > 0, \gamma_0 = 0$, when V_G is increasing. Ferroelectric is stabilized at the minimum of U. At $V_G = 0$, $U - Q$ profiles exhibits two local minima (stable equilibrium points are denoted by open and filled circles in Fig. 2.8 a) separated by a local maxima (unstable equilibrium is denoted by open square in Fig. 2.8 a). As V_G increases, $U - Q$ profile changes such that value of Q at equilibrium increases (though keeping the same negative sign, we have assumed that ferroelectric is negatively polarized at $V_G = 0$). With the increase in V_G, left stable equilibrium point and unstable equilibrium point approach each other to annihilate at $V_G = V_{sp}$. Therefore, as soon as V_G exceeds V_{sp}, Q has to abruptly change from a negative value $Q = -Q_c$ to a positive value as shown in Fig. 2.8 c.

If V_G is now reduced below V_{sp}, Q can not switch back from a positive value to a negative value, because of the presence of an energy barrier (Figs. 2.8 a - b). V_G has to be reduced below V_{sn} for switching back the ferroelectric to a negative value. When V_G is decreasing, ferroelectric switches at $Q = Q_c$. Value of Q_c can be obtained by requiring that $\frac{d^2U}{dQ^2} = 0$ i.e., $\alpha_0 + 3\beta_0 Q_c^2 + 5\gamma_0 Q_c^4 = 0$. If $\gamma_0 = 0$, an analytical solution for Q_c exists and is given by-

$$Q_c = \sqrt{\frac{-\alpha_0}{3\beta_0}}. \tag{2.26}$$

Figure 2.8 c shows the corresponding hysteretic $Q - V_G$ characteristics. There are two sharp jump in $Q - V_G$ characteristics at $V_G = V_{sp}$ and $V_G = V_{sn}$. Mathematically, $Q - V_G$ profile can be obtained by requiring $\frac{dU}{dQ} = 0$ i.e.,

$$\frac{V_{FE}}{y_{FE}} = \alpha_0 Q + \beta_0 Q^3 + \gamma_0 Q^5, \tag{2.27}$$

where $V_{FE} = V_G$ for capacitor structure in Fig. 2.8 a. The values of corresponding V_{sp} or V_{sn} are obtained from Eq. 2.27 with $Q = -Q_c$ and $Q = Q_c$, respectively, and are given by (for $\gamma_0 = 0$)-

$$V_{sp} = -V_{sn} = -\frac{2\alpha_0 Q_c y_{FE}}{3}. \tag{2.28}$$

Note that, V_{sp}/V_{sn} are analogous to V_{PI}/V_{PO} of MEMS capacitive actuators; whereas Q_c is similar to y_c.

2.2.2 Consequences of Instability in Ferroelectrics

We saw that the qualitative operation and behavior of a ferroelectric material is very similar to a MEMS capacitive actuator. Both of them exhibit instability. In MEMS capacitive actuator, instability arises due to interaction between spring and electrostatic forces; whereas in ferroelectrics, it arises due to the internal atmoic structure of ferroelectric materials [42]. We therefore expect that qualitative consequences of instability in ferroelectric materials should also be similar to MEMS capacitive actuators. We briefly highlight them below.

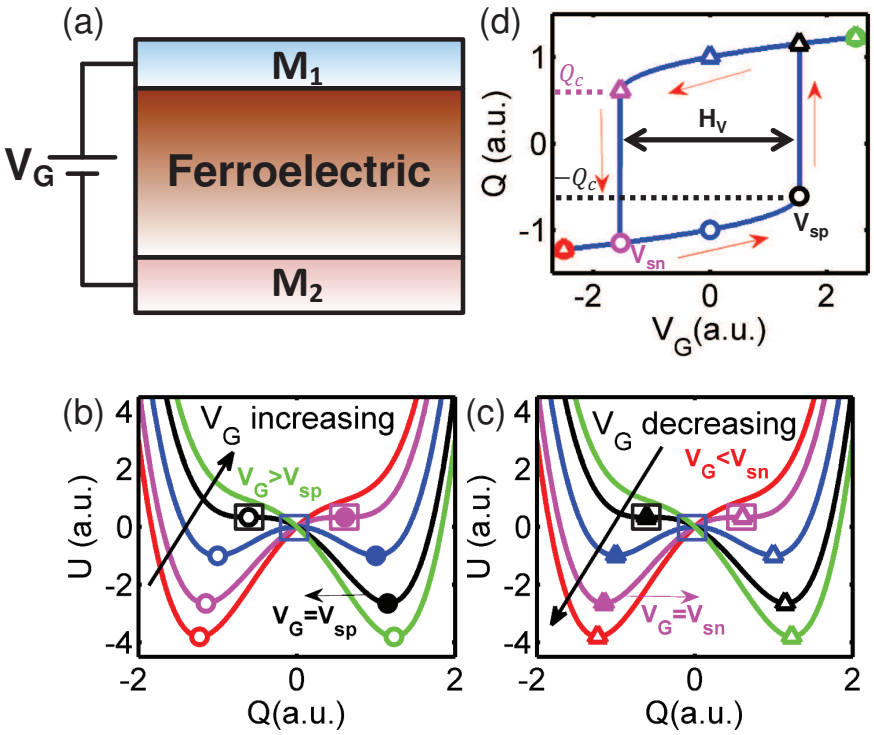

Fig. 2.8. (a) Schematic of a ferroelectric material based capacitor structure. Evolution of the energy landscapes of ferroelectric material when (b) V_G is increasing and (c) V_G is decreasing. Open circle and open triangle denote the equilibrium points where ferroelectric is stabilized when V_G is increasing and decreasing, respectively. Filled circles and triangles denote other equilibrium points. Open squares denote unstable equilibrium points.(C) Corresponding hysteretic $Q - V_G$ characteristics of the ferroelectric material showing abrupt jump in charge at $V_G = V_{sp}$ and $V_G = V_{sn}$.

Static Response

(i) Stable and Unstable Regimes: Similar to the stable/unstable regimes of a MEMS capacitive actuator, ferroelectric dielectric exhibits stable/unstable regimes as shown in Fig. 2.9. Ferroelectric is stable only for $Q < -Q_c$ & $Q > Q_c$. It cannot be stabilized for charge values ranging from $Q = -Q_c$ to $Q = Q_c$. The key point is that two stable regimes are separated by an unstable regime (typical characteristics of a bi-stable system).

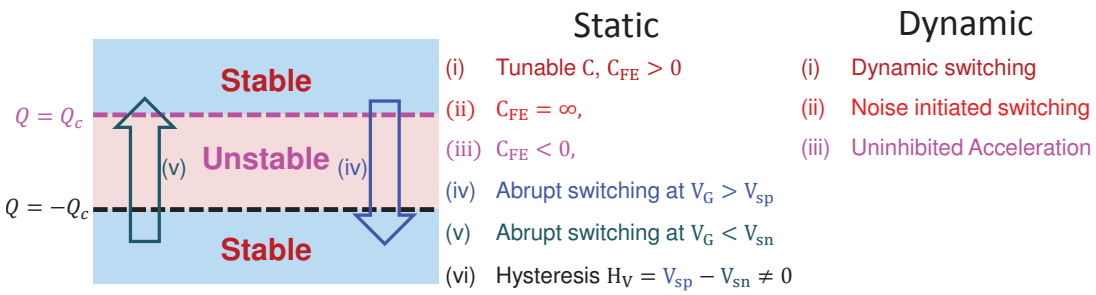

Fig. 2.9. Schematically showing the instability related characteristics of a ferroelectric material.

(ii) Negative Capacitance: Voltage drop across the ferroelectric material (Eq. 2.27) increases with Q in the stable regimes and decreases with Q in the unstable regimes (2.10 a). As a result, the capacitance of ferroelectric, given by-

$$C_{FE}^{-1} \equiv \frac{1}{WL}\frac{d^2U}{dQ^2} = y_{FE}\left(\alpha_0 + 3\beta_0 Q^2 + 5\gamma_0 Q^4\right), \tag{2.29}$$

is positive in the stable regimes and negative in the unstable regime (2.10 b). This negative capacitance behavior of ferroelectric has been utilized in field effect transistors for voltage amplification. We will discuss it in detail in chapter 5.

(iii) Transition Boundary: The boundary between stable and unstable regimes occur at $Q = \pm Q_c$. Like MEMS capacitive actuators, capacitance C_{FE} is infinite at the transition boundary (Fig. 2.10 b). The capacitance being infinite at the transition boundary have very important consequences for field effect transistors and will discuss further in chapter 5.

(iv) Abrupt Transition: The transition from one stable regime to another stable regime is abrupt as shown in Fig. 2.8 c. As soon as V_G is infinitesimally increased or decreased above V_{sp} or below V_{sn}, Q changes abruptly. This abrupt transition is similar to the abrupt transition in MEMS capacitive actuator.

(v) Hysteresis: Going from one stable regime (say $Q < -Q_c$ in Fig. 2.9) to another ($Q > Q_c$ in Fig. 2.9) and coming back to the same regime occurs at different

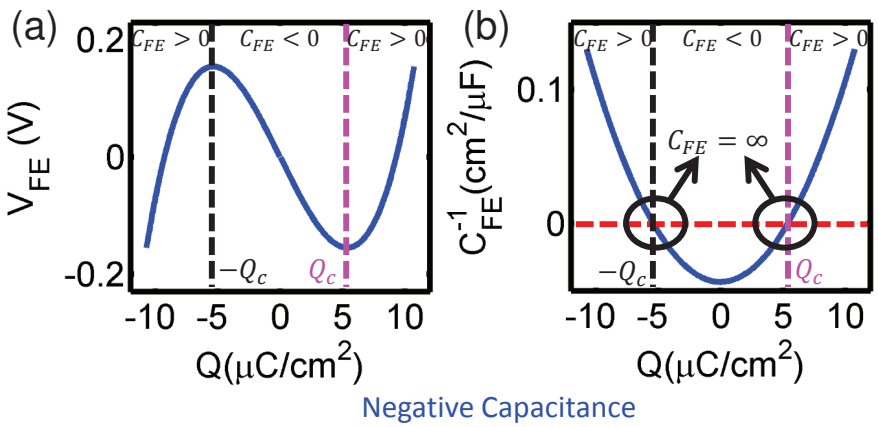

Fig. 2.10. (a) Voltage drop across ferroelectric and (b) its capacitance as a function of charge Q. In the unstable regime, C_{FE} is negative.

voltages, V_{sp} & V_{sn}, respectively. Therefore, there is an intrinsic hysteresis, whose value (for $\gamma_0 = 0$) is given by-

$$H_V = V_{sp} - V_{sn} = -\frac{4Q_c\alpha_0 y_{FE}}{3}. \tag{2.30}$$

Equation 2.30 suggests that H_V and jump in $Q - V_G$ characteristics are directly related. If one disappears, other also disappears. Therefore, whether hysteresis-free abrupt transition is possible or not, is an important question. We will address this question in chapter 5.

Dynamic Response

Like static response, dynamic behavior of ferroelectric materials is also qualitatively similar to MEMS capacitive actuators. Below, we briefly point out the corresponding similarities.

(i) Switching below Switching Voltage: Ferroelectric material can also switch from one stable regime to another stable regime even when $V_G < V_{sp}$ or $V_G > V_{sn}$. This switching can occur because of two reasons. Similar to dynamic pull-in, if initial

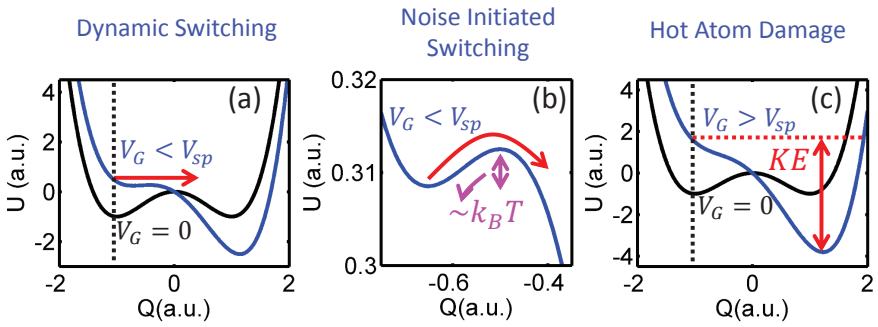

Fig. 2.11. Qualitative dynamic response of ferroelectric materials. (a) Dynamic switching when V_G is changed abruptly from zero to $V_G < V_{sp}$ and (b) noise initiated switching if the energy barrier is couple of k_BT. (c) Hot atom damage due to huge acceleration of atoms while crossing the unstable regime. KE is the amount of energy gained.

energy of the ferroelectric is larger than the energy at the top of energy barrier (unstable equilibrium), ferroelectric may switch (Fig. 2.11 a). Similar to noise initiated pull-in, if the energy barrier for ferroelectric is couple of k_BT at some V_G, it may get energy from the surroundings and surmount the energy barrier (Fig. 2.11 b).

(ii) Hot Atom Damage During Switching: Similar to the phenomenon of hard-landing in MEMS capacitive actuators, there is corresponding hot atom damage in ferroelectrics [43]. When a voltage $V_G > V_{sp}$ is applied, atoms (responsible for ferroelectricity) inside the ferroelectric material travels from one stable state to another stable state. During this travel, they go through the unstable regime and undergo a huge acceleration. As a result, their velocity increases rapidly during switching (that's why the name hot atom). They come to rest and stabilize at the stable equilibrium position by dissipating all the gained kinetic energy (Fig. 2.11 c). This dissipated energy may damage internal atomic structure of the ferroelectric and therefore is one of the reliability concerns for ferroelectrics.

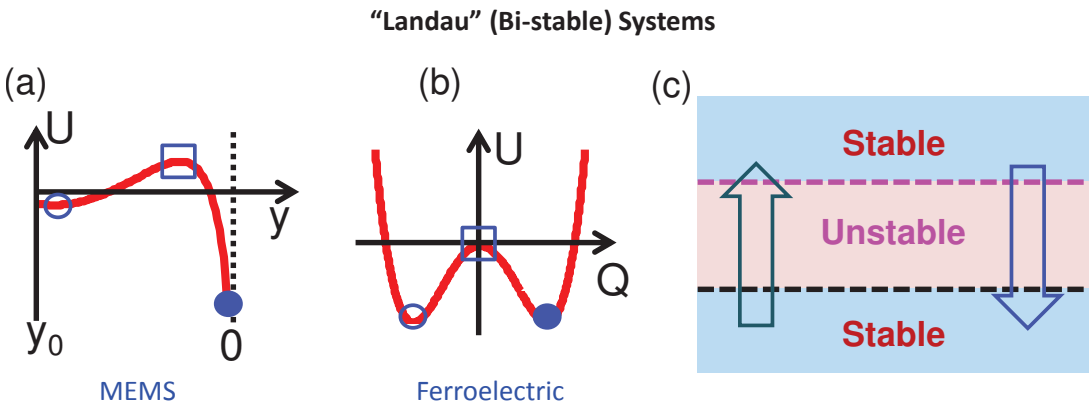

Fig. 2.12. (a) MEMS capacitive actuators and (b) ferroelectric materials are example of a generic class of Landau systems characterized by two well energy landscapes. (c) Each Landau system is associated with two stable regimes separated by an unstable regime.

2.3 Landau Systems

In this chapter, we have looked at the operation of MEMS capacitive actuators and ferroelectric dielectric based capacitors. Although, the underlying physics is very different, their qualitative behavior is very similar. The hysteretic behavior with instability characteristics arise because of the two well energy landscapes (Figs. 2.2 & 2.8). We classify such systems as Landau systems due to the similarity with Landau energy landscape of phase transition. Other examples of Landau systems include a buckled beam [44]. The qualitative consequences that we have discussed for MEMS capacitive actuators and ferroelectrics should be applicable to any another Landau systems.

2.4 Conclusions

In this chapter:

- We explained the origin of instability in MEMS capacitive actuators and ferroelectric materials using the evolution of respective energy landscapes as a function of the applied voltage.
- We highlighted the consequences of this instability on the static and dynamic response. Two stable regimes separated by an unstable regime, negative capacitance in the unstable regime, spring-softening effect, abrupt transition, and hysteresis are the key consequences related to the static response. Dynamic pull-in, noise initiated pull-in, and hard-landing are the corresponding consequences related to the dynamic response.
- We also pointed out the relevance of various instability features in different applications. For example, we will see the significance of negative capacitance in novel Landau switches in chapter 5 and spring-softening effect in novel Flexure biosensors in chapter 6.
- We finally proposed a new class of system which we call Landau system-switches, sensors, and actuators. We believe that the general features of any Landau system should be similar. Therefore, once you have understood one, other should easily follow.

In the next chapter, we will explore the features and consequences of instability in MEMS capacitive actuators in more detail. In this chapter, we illustrated the pull-in instability for planar electrodes and linear spring only. In next, we will discuss the effect of nonlinear spring, electrode geometry, and actuation mechanism on the pull-in instability and related characteristics and capture all the details in very simple analytical formulas.

3. UNIVERSAL SCALING RELATIONSHIPS FOR INSTABILITY IN MEMS CAPACITIVE ACTUATORS

In chapter 2, we discussed the physics of instability and its consequences in MEMS capacitive actuators and ferroelectric materials. We highlighted that these two examples belong to a broader class of systems which we call Landau systems. While discussing the operation of MEMS capacitive actuators, we made three major assumptions: (i) the spring force is linear, (ii) the electrodes are planar, and (iii) the actuation mechanism is voltage controlled. In general, however, capacitive actuators can have nonlinear springs, non-planar electrodes, and can be actuated by other mechanisms such as charge actuation. Understanding how does these variations affect the instability and actuation characteristics, is the goal of this chapter[1]. We plan to achieve the following:

- We will develop scaling relationships for pull-in instability, pull-in voltage/charge, and resonance frequency in terms of only two scaling parameters, n and p. The parameter n is fundamentally related to the electrode geometry and actuation mechanism; whereas p is related to the nature of spring.
- We will not only use the developed scaling theory to explain a broad range of experimental data within a single theoretical framework, but also use it to characterize electrode geometry and nature of spring for any new actuator.
- We believe that these scaling relationships should enable the design of electrode geometry, actuation mechanism, and/or spring for desired actuation characteristics.

[1]The content (text and figures) in this chapter have been adapted from [45]

Rest of the chapter is organized as follows. In section 3.1, we discuss why there is a need of universal scaling relationships for instability. We derive the analytical formulas of pull-in voltage/charge and resonance frequency in section 3.2. We then use these scaling relationships to explain a broad range of experimental data in a single theoretical framework in section 3.3. We show the power of scaling relationships for characterization of novel actuators in section 3.4 and conclude in section 3.5.

3.1 Background

As discussed in chapters 1 & 2, tunable-gap electromechanical actuators have found wide range of applications in diverse fields as RF-MEMS varactors [30], resonators [1], deformable mirrors [25], and photonic laser cavity [49]. And, electrode geometry, actuation mechanism and/or the nature of spring in electromechanical actuators have broadened over the years. First, advances in nano-fabrication and discovery of new materials have allowed electrode geometry to evolve from being planar (e.g., graphene [50]) to cylindrical (e.g., single carbon nanotubes (CNTs) [46] or nanowires [47]) to array of cylinders (e.g., array of aligned carbon nanotubes [48]) (Figs. 3.1 a-c). And yet, the actuation characteristics have been treated independently for the respective electrode geometries [51–54]. Moreover, the effect of nonlinear restoring spring force arising from mid-plane stretching [55] for planar electrodes, and tension developed due to stretching in cylindrical electrodes [56, 57], resulting in spring-hardening (Fig. 3.1 e), have only been considered for few isolated electrode geometries. Finally, although V-actuation is widely used, Q-actuation [58, 59] has also been suggested to overcome the problem of pull-in instability. Note that, in V-actuation a constant voltage (V) is applied between M_1 & M_2; whereas in Q-actuation a fixed amount of charge(Q) is deposited on M_1 using current sources [58, 59]. However, the effects of Q-actuation on the actuation characteristics have not been considered in detail.

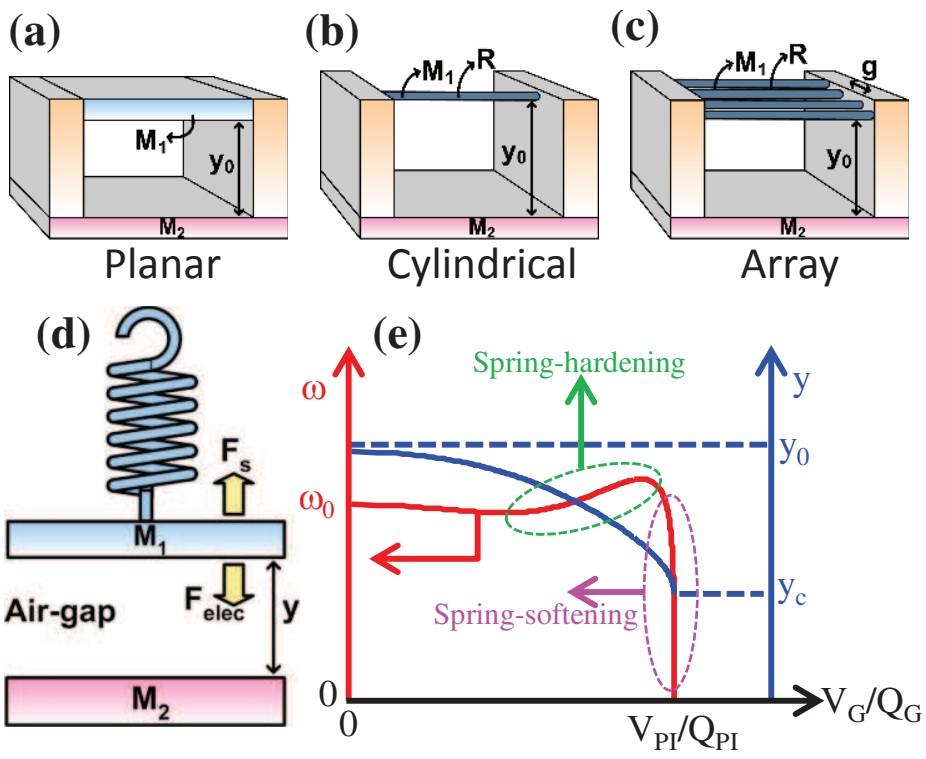

Fig. 3.1. Electromechanical actuators with varying electrode geometries e.g., (a) classical parallel-plate actuator with M_1 and M_2 as planar electrodes, (b) M_1 as carbon nanotube (CNT) [46] or nanowire [47] (example case of cylindrical electrode), and (c) aligned array of CNTs [48] as M_1 (example of aligned array of cylinders). (d) Equivalent spring-mass model of the actuator. (e) Typical actuation characteristics showing the position (y) of M_1 and resonance frequency (ω) as a function of voltage/charge (V_G/Q_G).

In general, the actuation characteristics, such as the capacitance ($C(y)$) in RF-MEMS varactors [30], travel range ($y_0 - y_c$) in analog-tuned actuators [60] (Fig. 3.1 e), or resonance frequency (ω) in resonators [1], are governed by a geometry-dependent, complex interplay between F_{elec} and F_s (Fig. 3.1 d-e), and are accessible only to the problem-specific detailed numerical simulations.

This case-by-case analysis of actuators reflects the fact that there is no general theory or guideline, which can be used to analyze an actuator with arbitrary electrode geometry, actuation or spring mechanism. Therefore, a general theoretical framework

is needed that (i) applies equally well to V and Q actuation for arbitrary electrode geometry, (ii) correlates the response of different electrode geometries and actuation mechanisms, (iii) works both for linear and nonlinear springs, (iv) is consistent with the available experimental data, (v) can be used to characterize novel actuator with arbitrary electrode geometry, and (vi) enables design of electrode geometry for desired performance.

In next section, we develop a set of universal scaling relationships for pull-in instability, pull-in voltage/charge and resonance frequency, that depend only on two scaling parameters, n and p. Here, n is related to the electrode geometry and actuation mechanism; whereas p is related to the nature of spring.

3.2 Theory of Electromechanical Actuators

As discussed in chapter 2, the response of the actuator is dictated by the balance of F_s and F_{elec}, i.e., $F_s = F_{elec}$. While F_{elec} depends on the voltage/charge (V/Q) actuation and the geometry of electrodes, F_s is determined by the geometrical dimensions (e.g., length and thickness), material properties (e.g., Youngs modulus), and mechanical support (e.g., fixed-fixed vs. fixed-free) of M_1. In general, for a nonlinear spring with $F_s = \sum_{p=1}^{p=\infty} k_p (y_0 - y)^p$ and general electrode geometry and actuation mechanism with $F_{elec} = -\frac{1}{2}\frac{dC}{dy}V_G^2 = -\frac{1}{2}\frac{dC^{-1}}{dy}Q_G^2 \approx \frac{\gamma}{2y^n}\phi_G^2$, the condition of force balance implies-

$$\sum_{p=1}^{p=\infty} k_p (y_0 - y)^p = \frac{\gamma}{2y^n}\phi_G^2, \tag{3.1}$$

where k_p are spring constants associated with the nonlinearity of order p, C is the capacitance of the actuator, γ is a geometrical constant, and n is related to the electrode geometry and actuation mechanism. ϕ_G is the forcing function i.e., $\phi_G = V_G$ for V-actuation and $\phi_G = Q_G$ for Q-actuation. Note that, restoring spring force typically consists of linear and cubic terms i.e., $F_s = k_1 (y_0 - y) + k_3 (y_0 - y)^3$ (considered in

this chapter), where the cubic nonlinearity arises due to the tension developed in M_1 because of stretching [38,55]. For parallel-plate actuator (Fig. 3.1 a), $C = \frac{\epsilon_0 A_e}{y}$ implies $\gamma = \epsilon_0 A_e$ and $n = 2$ for V-actuation, while $\gamma = \frac{1}{\epsilon_0 A_e}$ and $n = 0$ for Q-actuation. Here, A_e is the area of M_1 and ϵ_0 is the permittivity of free space. Although, $F_{elec} \approx \frac{\gamma}{2y^n}\phi_G^2$ should be viewed as an approximation, which may not hold for arbitrary electrode geometry, we find that it provides a good approximation to broad range of regular electrode geometries considered in this chapter (see below) and fractal electrode geometries discussed in ref. [61]. And, when the approximations are numerically justified (as we do in this chapter), the empirical parameter n allows us to relate the actuation characteristics with the electrode geometry.

The application of ϕ_G (V_G or Q_G) not only changes the position (y) of M_1, but also modifies the effective stiffness $k_{eff} \equiv -\frac{d(F_s - F_{elec})}{dy}$ as discussed in chapter 2. This allows tuning of the resonance frequency $\omega \propto \sqrt{k_{eff}}$, which is given by-

$$\frac{\omega}{\omega_0} = \sqrt{\sum_{p=1}^{p=\infty} \frac{k_p}{k_1} (y_0 - y)^{p-1} \left(n + p - n\frac{y_0}{y}\right)}, \tag{3.2}$$

where $\omega_0 \propto \sqrt{k_1}$ is the resonance frequency at $\phi_G = 0$, or, equivalently, $y = y_0$. Note that, Eq. 3.2 expresses ω/ω_0 as an explicit function of y. Since the corresponding $\phi_G(y)$ is analytically known from Eq. 3.1, ω/ω_0 vs. ϕ_G characteristics can be obtained using Eqs. 3.1 - 3.2. Interestingly, Eq. 3.2 reduces to $\frac{\omega}{\omega_0} = \sqrt{3 - 2\frac{y_0}{y}}$ for a parallel-plate actuator with linear spring ($n = 2$ and $k_p \approx 0$, for $p > 1$) (see Eq. 2.24 in chapter 2), a well-known result for resonant gate transistor [1].

Note that, both ω and k_{eff} vanish at pull-in (i.e., $\frac{dF_s}{dy} = \frac{dF_{elec}}{dy}$ and $F_s = F_{elec}$) and beyond which M_1 can no longer be stabilized in air. The critical-gap y_c at pull-in can be determined from Eq. 3.2 by requiring that $\omega = 0$. A simple analytical solution is possible, if the infinite series associated with the restoring spring force F_s is dominated by a single term, such that $F_s \approx k_p (y_0 - y)^p$. For example, a linear spring is characterized by $p = 1$ such that $F_s = k_1 (y_0 - y)$, while a spring with

dominant cubic nonlinearity is characterized by $p = 3$ such that $F_s \approx k_3 (y_0 - y)^3$. The analytical solution is thus given by-

$$\frac{y_c}{y_0} = \frac{n}{n+p}. \tag{3.3}$$

Surprisingly, y_c depends neither on the absolute value of k_p, nor on the magnitude of applied ϕ_G. It only depends on the electrostatic dimension n and the order of spring nonlinearity p. Equation 3.3 anticipates the well-known results for parallel plate actuators with linear spring (i.e., $p = 1$), namely, $y_c = 2/3y_0$ for V-actuation (see Eq. 2.15 in chapter 2) and $y_c = 0$ for Q-actuation [62]. The corresponding value of pull-in voltage (V_{PI}) or charge (Q_{PI}) is given by (obtained using Eqs. 3.1 & 3.3 with $F_s \approx k_p (y_0 - y)^p$)-

$$\phi_{PI}^2 = \frac{2k_p}{\gamma} \left(\frac{n}{n+p}\right)^n \left(\frac{p}{n+p}\right)^p y_0^{n+p}. \tag{3.4}$$

Here, Eq. 3.4 reduces to the well-known result of pull-in voltage $V_{PI}^2 = \frac{8k_1 y_0^3}{27\epsilon_0 A_e}$ [1] (Eq. 2.16 in chapter 2 with $y_d = 0$) and pull-in charge $Q_{PI}^2 = 2k_1\epsilon_0 A_e y_0$ [62] for parallel-plate actuator with linear spring ($k_p = k_1$; $p = 1$ in Eq. 3.4 with $\gamma = \epsilon_0 A_e$, $n = 2$ for V-actuation and $\gamma = \frac{1}{\epsilon_0 A_e}$, $n = 0$ for Q-actuation). The scaling relationships (Eqs. 3.2 - 3.4) are the main results of this chapter, and suggest that the actuation characteristics (Fig. 3.1 e) are dictated essentially by n & p. We emphasize that in spite of the simplicity of the model; it captures the essential physics of the electrostatic actuation very well and explains broad range of the experimental data. Therefore, when working with a novel device, starting with such a simple model will be very useful and details of the support or fringing fields can be added later using other existing modeling framework [61].

Electrode	Capacitance (C)	F_{elec} for V-actuation	F_{elec} for Q-actuation
Planar	$\frac{\epsilon_0 A_e}{y}$	$\frac{\epsilon_0 A_e}{2y^2}V_G^2$ ($n=2$, $\gamma=\epsilon_0 A_e$)	$\frac{1}{2\epsilon_0 A_e}Q_G^2$ ($n=0$, $\gamma=\frac{1}{\epsilon_0 A_e}$)
Cylinder	$\frac{2\pi\epsilon_0 L}{\ln\left(2\left(1+\frac{y}{R}\right)\right)}$	$\frac{\pi\epsilon_0 L}{(y+R)\left[\ln\left(2\left(1+\frac{y}{R}\right)\right)\right]^2}V_G^2$ ($n\approx 1.4$, $\gamma=2\pi\epsilon_0 L$)	$\frac{1}{4\pi\epsilon_0 R(y+R)}Q_G^2$ ($n\approx 1$, $\gamma=\frac{1}{2\pi\epsilon_0 L}$)
Array	$\frac{2\pi\epsilon_0 L}{\ln\left(\frac{\sinh\left(\frac{2\pi(y+R)}{g}\right)}{\frac{\pi R}{g}}\right)}$	$\frac{2\pi^2\epsilon_0 L\coth\left(\frac{2\pi(y+R)}{g}\right)}{g\left[\ln\left(\frac{\sinh\left(\frac{2\pi(y+R)}{g}\right)}{\frac{\pi R}{g}}\right)\right]^2}V_G^2$ (n & γ depend on g)	$\frac{\coth\left(\frac{2\pi(y+R)}{g}\right)}{2g\epsilon_0 L}Q_G^2$ (n & γ depend on g)

Table 3.1
Analytical expression of electrostatic force with values of n & γ for all the actuators considered in this chapter. n & γ have been obtained from the analytical formula of F_{elec}. A_e is the area of M_1 for planar electrode, R is the radius of cylinder, L is the length of cylinder, and g is the spacing between individual cylinder for array electrodes.

3.3 Numerical/Experimental Validation

The power of the scaling relationships (Eqs. 3.2 - 3.4) can be best appreciated by interpreting numerical simulation results and experimental data for different actuators as shown in Figs. 3.1 a - c. The actuation characteristics are obtained by numerically solving the equations of motion of spring-mass system (Fig. 3.1 d) (details in appendix D about numerical simulations). Electrostatic force for each of the actuator has been obtained using the analytical formula of capacitance (Table 3.1) .

3.3.1 Fixed Regular Electrode Geometry

Figures 3.2 a - h summarize the displacement (y) vs. ϕ_G characteristics for planar and cylindrical electrodes for two values of p and four values of n. As mentioned previously, p corresponds to the order of spring nonlinearity with $p=1$ corresponding

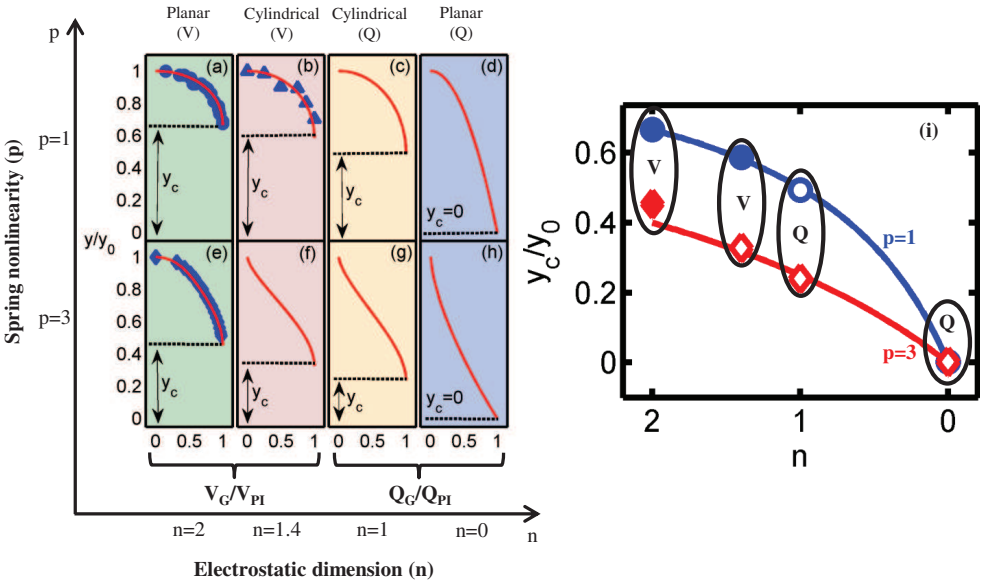

Fig. 3.2. Pull-in instability of electromechanical actuators. (a)-(h) y vs. V_G/V_{PI} or Q_G/Q_{PI} characteristics in $p-n$ space. Symbols denote the experimental data taken from literature (planar electrode with linear spring [63] (a), cylindrical electrode with linear spring [64] (b) and planar electrode with nonlinear spring [65] (e)) and solid line numerical simulations. (i) y_c as a function of n for linear ($p=1$) and nonlinear springs ($p=3$). Filled symbols denote the experimental data, open symbols denote numerical simulations, and solid line denotes the analytical formula given by Eq. 3.3. Symbols have been grouped in voltage (V) and charge (Q) actuation.

to linear spring (with $k_3 \approx 0$), and $p=3$ corresponding to cubic nonlinearity (i.e., $k_3\left(y_0-y\right)^3 \gg k_1\left(y_0-y\right)$). On the other hand, n corresponds to different electrode geometry and V/Q actuation mechanisms. For example, n for cylindrical electrode can be determined from analytical formula of C (Table 3.1), as follows. For V-actuation, we have $\frac{dC}{dy} \propto \frac{1}{(y+R)\left[\ln\left(2\left(1+\frac{y}{R}\right)\right)\right]^2} \sim \frac{1}{y^{1.4}}$; whereas for Q-actuation $\frac{dC}{dy} \propto \frac{1}{(y+R)} \sim \frac{1}{y^1}$. Therefore, for cylindrical electrode, $n \approx 1.4$ for V-actuation and $n \approx 1$ under Q-actuation (see Table 3.1 n & γ for different electrode geometries).

In Figures 3.2 a - h, solid lines denote the numerical simulations and filled symbols denote the experimental data reproduced from Refs. [63–65]. The available

experimental data both for planar and cylindrical electrodes agree very well with the numerical simulations, as shown in Figs. 3.2 a - b & e. Note that, y_c as determined from the numerical simulations or experimental data for different electrode geometries, actuation and spring mechanism is summarized in Fig. 3.2 i. The experimental data is exactly predicted by the scaling relationship of Eq. 3.3. Typically, y_c under V-actuation is larger than that of Q-actuation both for planar as well as cylindrical electrodes, which is consistent with the conclusions of Bochobza-Degani, et al. [66].

To validate the scaling relationship suggested in Eq. 3.2, we plot (see Figs. 3.3 a - h) ω vs. V_G/Q_G characteristics for variety of actuators. Experimental data (Filled symbols) for planar and cylindrical electrode with linear/nonlinear spring under V/Q actuation is exactly matched by the numerical simulations (open symbols) and scaling formula (Eq. 3.2 solid line). Note that, each open symbol in Fig. 3.3 corresponds to one dynamic numerical simulation (see appendix D for details). Hundreds of numerical simulations were performed to generate one of ω vs. V_G/Q_G characteristics. (e.g., Fig. 3.3 a), and that is very well reproduced by the scaling relationship of Eq. 3.2.

3.3.2 Array Electrode Geometry

We now show the generality of Eqs. 3.2 - 3.3 by using them to explore the actuation characteristics of actuators based on aligned array of cylinders (Fig. 3.1 c). It should be appreciated that actuation characteristics change as g changes due to change in the capacitance and therefore F_{elec}. Based on the numerical simulations for the case of a linear spring, Fig. 3.4 a plots y_c as a function of g, suggesting possibility of tuning y_c by tuning of g. When g is small and the electrodes are closely spaced, the array of cylinders behaves like a planar electrode, and y_c is identical to that of a parallel-plate actuator both for V and Q actuation, as expected. For larger g, the electrodes are spaced further apart, and the elements of the array interact with M_2 as isolated cylinders, and y_c matches with that of a single cylinder. Interestingly,

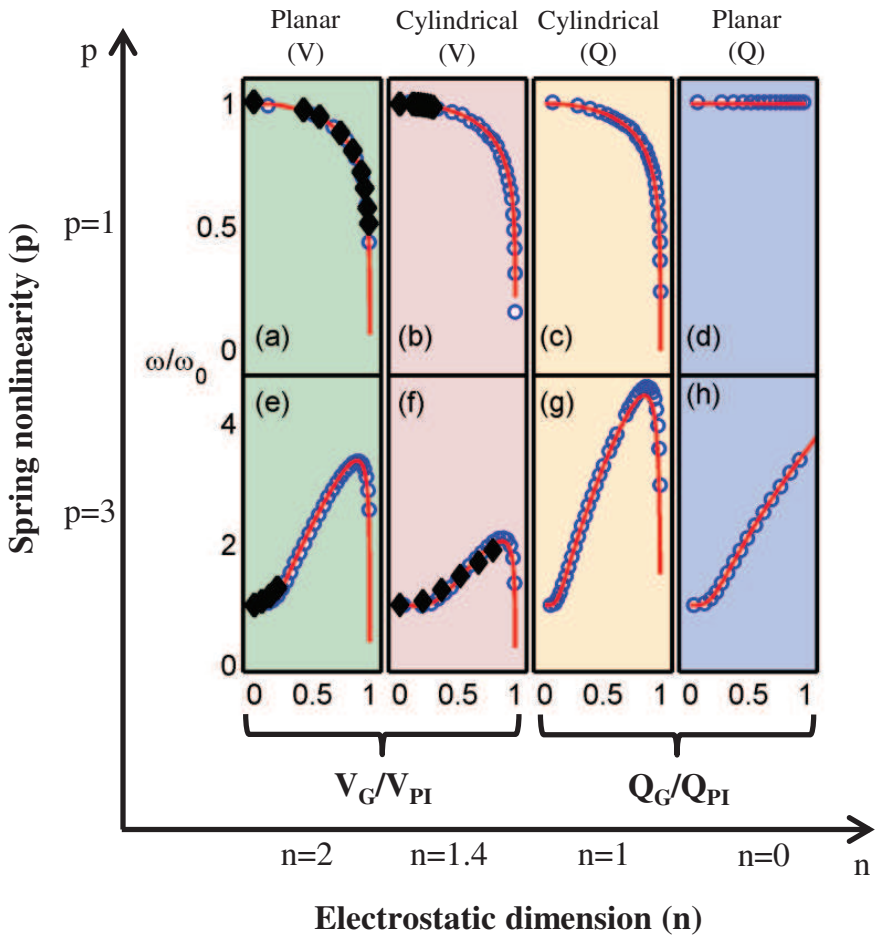

Fig. 3.3. (a)-(h) ω vs. V_G/Q_G characteristics in $p-n$ space showing the spring-softening and spring-hardening behavior of electromechanical resonators. Filled symbols denote the experimental data taken from literature (planar electrode with linear spring [67] (a), cylindrical electrode with linear spring [68] (b), planar electrode with nonlinear spring [69] (e) and cylindrical electrode with nonlinear spring [56] (f)), open symbols denote the numerical simulations, and solid line denotes the analytical formula given by Eq. 3.2.

y_c under V-actuation is larger than that of Q-actuation for all values of g, again confirming the conclusions of Bochobza-Degani, et al. [71].

The corresponding ω vs. V_G/Q_G characteristics are shown in Figs. 3.4 b - g for three different values of g. Open symbols denote numerical simulations and filled

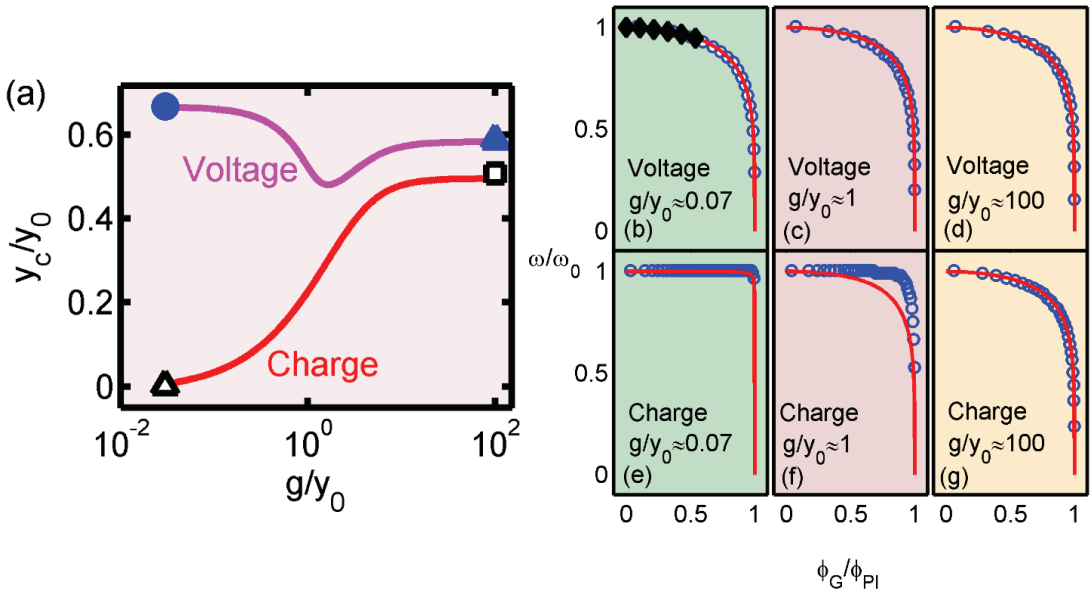

Fig. 3.4. Application of scaling relationships to interpret the actuation characteristics of an array of cylinders based electrode with linear spring. (a) y_c as a function of the spacing (g) between individual cylinders. Solid line denotes numerical simulations, • denotes y_c for vertically aligned array of CNTs [70] and ▲ denotes y_c for an individual CNT [64] under V-actuation. △ denotes y_c for an isolated parallel-plate actuator and □ for cylindrical electrode under Q-actuation. (b)-(g) ω for different g. Filled symbols denote the experimental data (aligned array of CNTs for very small spacing [48] (a)), open symbols denote numerical simulations and solid line scaling relationship given by Eq. 3.2.

symbols experimental data, which are in excellent agreement with each other. Note that, here Eq. 3.2 cannot be directly used to interpret numerical simulations, because n is not analytically known via Eq. 3.1 due to complex dependence of C on y (Table 3.1). However, once y_c is known from static numerical simulations as shown in Fig. 3.4 a, n can be estimated using Eq. 3.3, and Eq. 3.2 can then be applied. Considering this, the results of the numerical simulations are very well reproduced by scaling relationship of Eq. 3.2 with $n = \frac{y_c}{1-y_c}$ obtained from Fig. 3.4 a, see solid lines in Figs. 3.4 b-g.

3.4 Characterization of Novel Actuators

In general, it is possible that values of n & p are not known a-priori for a newly fabricated actuator. In that case, following simplified scaling relationships (obtained from Eqs. 3.1 - 3.2) can be used to extract parameters n & p to characterize the essential response of the new actuator. If F_s consists of only two terms (one linear and other higher order term such as cubic) i.e., $F_s = k_1 (y_0 - y) + k_r (y_0 - y)^r$, with $r > 1$, equation 3.1 can be re-written as follows-

$$\left(\frac{y}{y_0}\right)^n \left[\frac{1}{\beta}\left(1 - \frac{y}{y_0}\right) + \left(1 - \frac{y}{y_0}\right)^r\right] = \left(\frac{\phi_G}{\phi_0}\right)^2, \tag{3.5}$$

where $\beta = k_r y_0^{r-1}/k_1$ is a constant and depends on the nature of the spring; whereas $\phi_0 = 2k_r y_0^{r+n}/\gamma$. Equation 3.5 suggests that y/y_0 is only a function of ϕ_G/ϕ_0. Scaling relationship of ω (Eq. 3.2) can also be simplified to-

$$\frac{\omega}{\omega_0} = \sqrt{\left(n + 1 - n\frac{y_0}{y}\right) + \beta\left(1 - \frac{y}{y_0}\right)^{r-1}\left(n + r - n\frac{y_0}{y}\right)}. \tag{3.6}$$

Equation 3.6 suggests that ω/ω_0 is only a function of y/y_0 and (therefore of ϕ_G/ϕ_0) for given values of n, r, and β. Analytical expression of ϕ_{PI} is now given by-

$$\phi_{PI}^2 = \phi_0^2 \left(\frac{n}{n+p}\right)^n \left(\frac{p}{n+p}\right)^p, \tag{3.7}$$

that implies that ϕ_{PI}/ϕ_0 is just a constant for given values of n and p. Here, $p = 1$ when $k_{(r(>1))} \approx 0$ (linear spring) or $p = r$ when nonlinear term dominates i.e., $k_r (y_0 - y)^r \gg k_1 (y_0 - y)$.

One can now use Eqs. 3.5 - 3.6 or Eq. 3.3 to extract parameters n, p, β, and ϕ_0 for novel actuators. For example, if value of y_c is precisely known from experiments, n can be obtained using Eq. 3.3, provided value of p is known. On the other hand, if y/y_0 vs. ϕ_G is known from experiments, the force balance equation (Eq. 3.5) can be

used to fit the data for the extraction of n & p. Finally, ω/ω_0 vs. ϕ_G experimental data can be fitted using Eqs. 3.5 - 3.6, and various parameters can be extracted. Note that, these extracted values of n & p can then be used to infer about the electrode geometry (through n) and the nature of spring (through p & β). Note that, a large value of $1/\beta$ implies a linear spring (i.e., $k_{(r(>1))} \approx 0$); whereas a small value of $1/\beta$ indicates dominance of nonlinear spring force (i.e., large value of $k_{(r(>1))}$).

3.4.1 Parameters Extraction from Data of Critical-Gap (y_c)

If y_c is known for a novel actuator, n can be extracted using Eq. 3.3, provided p is known. We use numerical simulation results of array of cylinders based actuator to show how we can extract different parameters. Figure 3.5 a shows y_c as a function of g for V-actuation. Assuming that the spring is linear (i.e., $p = 1$), we can use Eq. 3.3, and extract n, see Fig. 3.5 b. To assess the presumption that the contribution from cubic nonlinear spring (i.e., $r = 3$) is negligible, we use the just extracted value of n in Eqs. 3.5 - 3.6 with $r = 3$ to reproduce ω/ω_0 vs. V_G characteristics, as shown in Figs. 3.6 c - e. The fitting parameter $1/\beta \gg 1$, implies that the linear spring dominates, and confirms the presumption of $p = 1$.

3.4.2 Parameters Extraction from Gap (y) vs. Voltage (V_G) Characteristics

We use the available experimental y/y_0 vs. V_G characteristics of planar and cylindrical electrodes to extract parameters n & $1/\beta$ using Eq. 3.5 with $r = 3$. Figures 3.6 a - b show two set of experimental data (symbols), corresponding fit (solid line), and extracted parameters for planar electrode. The extracted value of $n \approx 1.88$ (Fig. 3.6 a) and $n \approx 1.86$ (Fig. 3.6 b) is close to 2, which is expected for actuators based on planar electrodes with voltage actuation. A slight difference in the value of n from 2 could be attributed to fringing fields, because $n = 2$ does not account for the fringing fields.

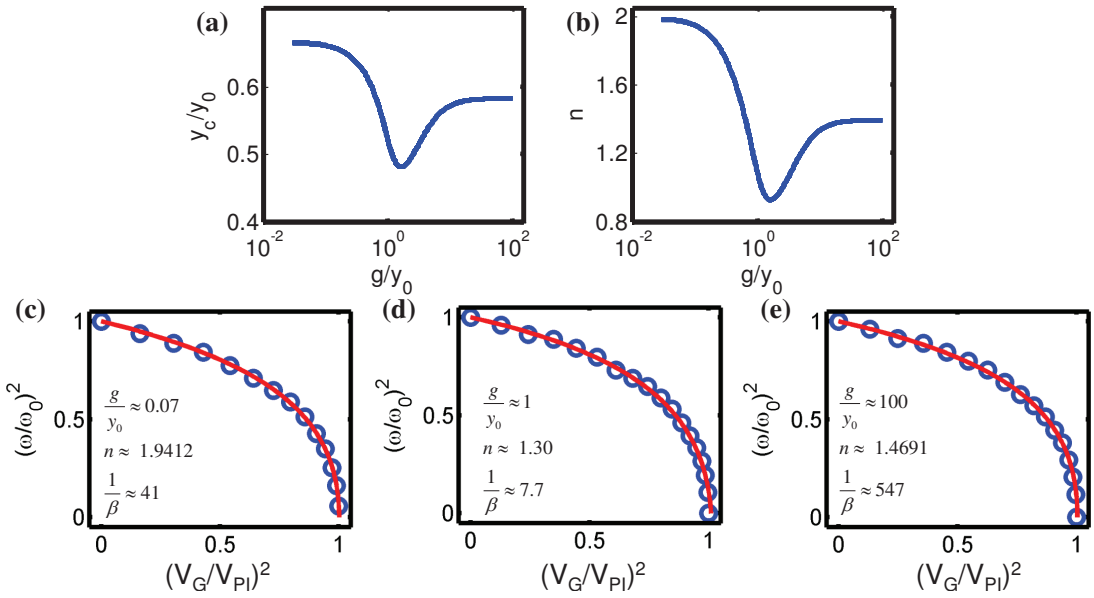

Fig. 3.5. Parameters extraction using the critical-gap y_c of actuators based on an array of cylinders. (a) y_c as a function of the separation g, (b) corresponding effective n obtained using Eq. 3.3 with $p = 1$. (c)-(e) Resonance frequency vs. voltage characteristics for three different values of g. Symbols denote numerical simulations and solid line is the fit based on Eq. 3.5 - 3.6 using the value of n from Fig. 3.5 b.

The corresponding extracted value of $1/\beta$ suggests that linear spring dominates (large value of $1/\beta$) for the actuator in Fig. 3.6 a, whereas nonlinear spring dominates (small value of $1/\beta$) in Fig. 3.6 b. Similarly, Figure 3.6 c shows experimental data and corresponding fit for an actuator based on cylindrical electrode. The extracted value of $n \approx 1.4$ is consistent with the analytical formula of capacitance of a cylinder (Table 3.1). The small value of $1/\beta$ indicates that nonlinear spring behavior is dominant for this actuator. Therefore, extracted values of n & $1/\beta$ can be used to infer about electrode geometry and the nature of spring.

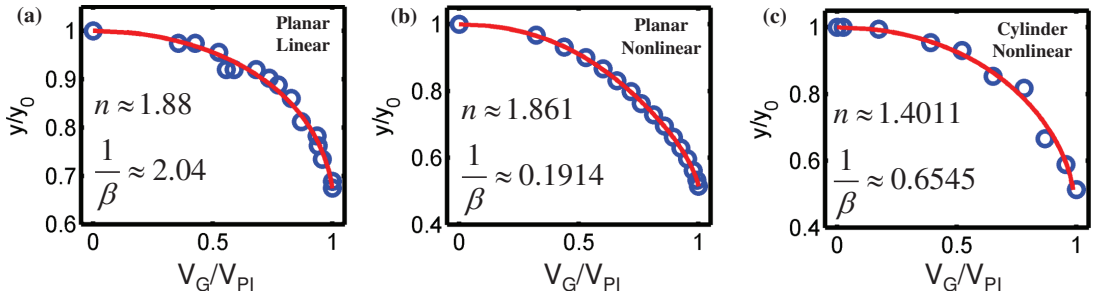

Fig. 3.6. Parameters extraction using the experimental y/y_0 vs. V_G characteristics of planar electrode for (a) linear [63] spring, (b) nonlinear [65] spring and (c) cylindrical [72] electrode for nonlinear spring. Symbols denote the experimental data and solid line is the fit.

3.4.3 Parameters Extraction from Resonance Characteristics

Finally, we show the method of extracting parameters using experimental ω/ω_0 vs. V_G characteristics. Figure 3.7 shows the experimental data (blue open circles) for three different actuators. In order to extract parameters, one should use only a part of ω/ω_0 vs. V_G characteristics (black open squares in Fig. 3.7) due to the following reasons. First note that, Eq. 3.6 can also be written as follows:

$$\left(\frac{\omega}{\omega_0}\right)^2 = 1 + r\frac{k_r}{k_1}(y_0 - y)^{r-1} - \frac{\gamma}{2k_1 y^n}V_G^2,$$

which suggests that $\left(\frac{\omega}{\omega_0}\right)^2 \approx a - bV_G^2$ for lower voltages when $y \approx y_0$, where $a \approx 1$ & $b = \frac{\gamma}{2k_1 y_0^n}$. Therefore, $\left(\frac{\omega}{\omega_0}\right)^2$ vs. V_G^2 profile is linear for smaller voltages, as confirmed by black dotted line in Fig. 3.7. This linear dependence of $\left(\frac{\omega}{\omega_0}\right)^2$ on V_G^2 suggests that the characteristic is not very sensitive to the value of n at low voltages. Instead, the best results are obtained by using the segment of the characteristics that deviate from linear behavior. In Fig. 3.7, we use experimental data such that $\left(\frac{\omega}{\omega_0}\right)^2 < 0.8$ (data below horizontal dotted green line) to extract parameters (using Eqs. 3.5 - 3.6 with $r = 3$). Extracted value of $n \approx 1.81$ (Fig. 3.7 a), $n \approx 2.08$ (Fig. 3.7 b), and $n \approx 2.03$ (Fig. 3.7 c) is close to 2, as expected for actuators with planar electrodes under voltage actuation. Slight difference in the value of n from 2 in Fig. 3.7 a could

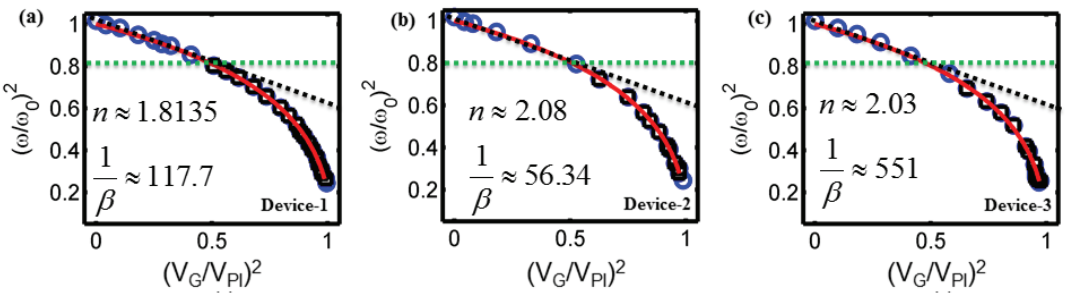

Fig. 3.7. Parameters extraction using the experimental resonance frequency vs. voltage characteristics of planar electrode with linear spring [67]. Blue open circles denote the experimental data and black open squares denote the experimental data used to extract various parameters. Solid line is the fit, black dotted line suggests that the characteristic is linear at low voltages. Green dotted line defines the boundary when characteristic starts to deviate from linear behavior.

be due to fringing fields. Extracted values of $1/\beta$ (large values) for all the actuators suggest that linear spring dominates.

3.5 Conclusions

In this chapter:

- We saw that planar electrodes, linear spring, and voltage actuation are a special case of tunable-gap electromechanical actuators. In general, electrodes may be nanostructured, spring may be nonlinear, and actuation can also be done using charge or a current source (as opposed to a voltage source).

- We found that instability related actuation characteristics are fundamentally related to the electrode geometry, nature of spring, and actuation mechanisms.

- We provided scaling relationships for the resonance frequency ω, pull-in instability (y_c), and pull-in voltage/charge (V_{PI}/Q_{PI}), which capture all the essential physics in only two scaling parameters, n & p. n is related to the electrode geometry and actuation mechanism; whereas p is related to the nature of spring.

- We used the universal scaling relationships to explain a wide range of existing experimental data from literature in a single theoretical framework. Previously, all the analysis was done on case-by-case basis.

- We illustrated how the scaling relationships can be used to characterize and extract values of n & p for any novel actuator.

The key message from this chapter is that the actuation characteristics can be tuned by tuning the electrode geometry. In the next chapter, we will use this understanding to address two problems associated with classical planar electrodes based tunable actuators and switches. We will show how modifying the electrode geometry can address the problem of travel (or tuning) range in tunable actuators and problem of hard-landing in MEMS switches.

4. SOLUTIONS TO THE PROBLEMS ARISING DUE TO INSTABILITY : TRAVEL RANGE AND HARD LANDING

In chapter 2, we looked at the origin and the consequences of instability in Landau systems. In context of MEMS capacitive actuators, we identified the following two problems because of this intrinsic instability:

- First problem was related to the travel range of tunable-gap electromechanical actuators because instability limits the travel (or tuning) range to $y_0 - y_c$, which is only one third of the air-gap for planar electrodes.
- Second problem was of hard-landing in MEMS based switches. We saw that when movable electrode M_1 transitions from one stable regime to another stable regime during switching, it experiences a huge acceleration while crossing the unstable regime. As a result, its velocity increases rapidly and it lands on the dielectric with very high impact velocity, leading to the damage of dielectric surface.

In this chapter[1], we address these two problems. Based on our understanding from previous chapter that electrode geometry can help tune the instability, we propose novel device structures that can extend the travel range. We also provide novel strategies that can reduce the impact velocity during switching.

Rest of the chapter is organized as follows. In section 4.1.1, we discuss the background of the problem of travel range and provide theory of travel range in section 4.1.2. Our proposal of reconfigurable nano-structured electrodes is discussed in section 4.1.3. We summarize our key findings for travel range in section 4.1.6. We

[1]The content (text and figures) in this chapter have been adapted from [73] ©AIP 2011 and [74] ©IEEE 2013.

discuss the background of the problem of hard-landing in section 4.2.1, propose various strategies of soft-landing in section 4.2.2, summarize our findings in section 4.2.5. We finally conclude this chapter in section 4.3.

4.1 Problem of Limited Travel Range

4.1.1 Travel Range Background

Tunable microelectromechanical actuators have found wide range of applications in various fields. Examples include tunable vertical cavity lasers [75], reflective diffraction grating (polychromator) [60], photonic crystal cavity [49], interferometric Mirasol displays [26], deformable mirrors for adaptive optics [25], and micro membrane pumps for drug delivery [76]. The functions of these devices rely on the analog position control of a movable electrode. Figure 4.1(a) shows the schematic of a classical parallel-plate actuator (having planar electrodes) with movable electrode M_1 and fixed electrode M_2. As discussed in chapters 2 & 3, voltage controlled tunable micoactuators suffer from well-known pull-in instability that snaps M_1 and M_2, when the gap (y) between the two is reduced below 2/3 of the initial air-gap (y_0) (Fig. 4.1(d) for planar electrodes). This pull-in instability limits the travel range (t_r^V) of M_1 to just 1/3 of the initial air-gap and poses a fundamental challenge for applications requiring large travel range.

In literature, various techniques have been proposed to extend the travel range. For example, closed-loop control techniques [77] dynamically modify the voltage across the actuator based on the position of M_1 as feedback to achieve desired travel range. Estimating position of M_1, however, requires complex circuits; moreover a control circuit optimized for one actuator is unlikely to work for another due to process variations requiring adaptive control [78] for an ensemble of actuators. Likewise, while techniques such as charge actuation [62] do not have the problem of pull-in instability, it requires extra circuitry for precise control of charge [58]. In practice, parasitic capacitances in charge-based actuators lead to uncontrolled pull-in [59], di-

minishing advantages of charge actuation. In another approach, one increases the effective air-gap to $3y_0$ by adding a series capacitor [79] so that desired travel range (y_0) is achieved [63]. In this case as well, uncontrolled parasitic capacitance in parallel to the actuator degrades the travel range [63]. Finally, travel range can also be tailored by a geometric redesign of electrode, (Figs. 4.1 b-c), however, these fixed-electrode geometries do not allow tailoring of travel range, once the devices have been fabricated.

Therefore, techniques which (i) do not use any external feedback circuit, (ii) do not suffer from any parasitic capacitance, (iii) do not rely on the increase of an effective air-gap, and (iv) can enable post-fabrication tuning of the travel range, are desirable. To address these issues, we propose to replace the planar electrodes by electrically re-configurable nano-structured electrodes to not only extend the travel range beyond 1/3 of the initial air-gap, but also electrically tune the travel range after the fabrication of microactuator.

4.1.2 Theory of Travel Range

We have discussed the basic operation of the tunable microactuator in chapters 2 & 3. In chapter 3, we also provided a very general analytical formula for the critical-gap y_c. Using Eq. 3.3 from chapter 3, we found that travel range (t_r^V) is given by-

$$t_r^V = 1 - \frac{y_c}{y_0} = \frac{p}{p+n}, \tag{4.1}$$

where p is the order of nonlinearity of spring and n is the elctrostatic dimension of the electrodes. Equation 4.1, therefore, suggests ways to extend and tune t_r^V by manipulating the electrode geometry factor n and changing the nonlinearity of the spring p. Remarkably, $n = 0$ ensures that the M_1 can travel across the entire gap without being pulled-in.

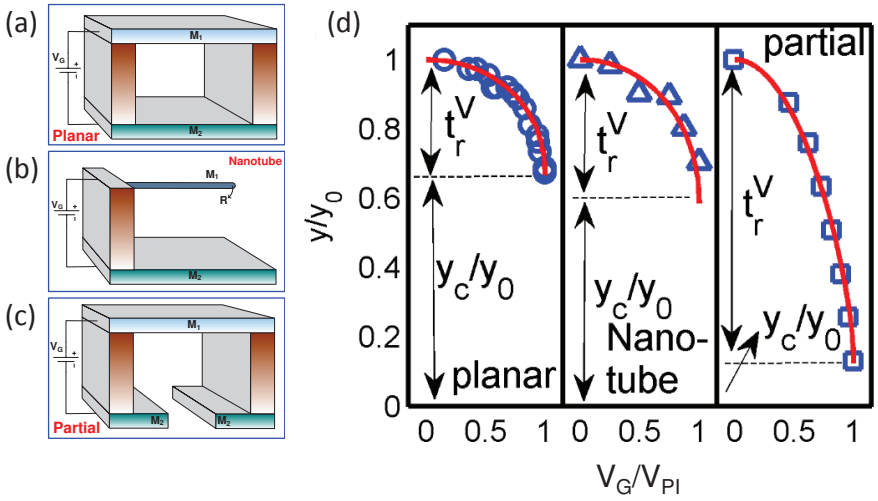

Fig. 4.1. Fixed-geometry classical microelectromechanical actuators: (a) planar electrodes [63] (b)Nanotube (example of cylinder) electrodes [52], and (c) partial electrode [60]. (d) Corresponding displacement vs. voltage characteristics showing the travel range t_r^V for all the structures; symbols denote the experimental data and solid line is the numerical simulation.

Equation 4.1 can be experimentally validated by interpreting the corresponding displacement vs. voltage characteristics for all the structures ($0 < n < 2$), as shown in Fig. 4.1 d. The experimental data are indicated by symbols, whereas solid line is the numerical simulation of Eqs. 2.5 - 2.7 discussed in chapter 2. For planar electrode ($n = 2$) travel range of $1/3$ is consistent with the experimental data. The travel range of nanotube electrode suggests that $n \approx 1.4$ which is consistent with the capacitance of a cylindrical electrode (Table 3.1). Similarly, the travel range for partial electrode can be matched by $n \approx 0.14$, see last panel in Fig. 4.1 d. Using this value of n, experimental data is correctly reproduced by the numerical simulations in Fig. 4.1 d. Solid line in Fig. 4.2 is the plot of Eq. 4.1 with $p = 1$ (i.e., for linear spring), whereas empty symbols denote experimental data for structures such as planar, nanotube (example of a cylindrical electrode) and partial electrodes (Fig. 4.1). Therefore, Eq. 4.1 captures the essence of travel range for different fixed-geometry electrode structures.

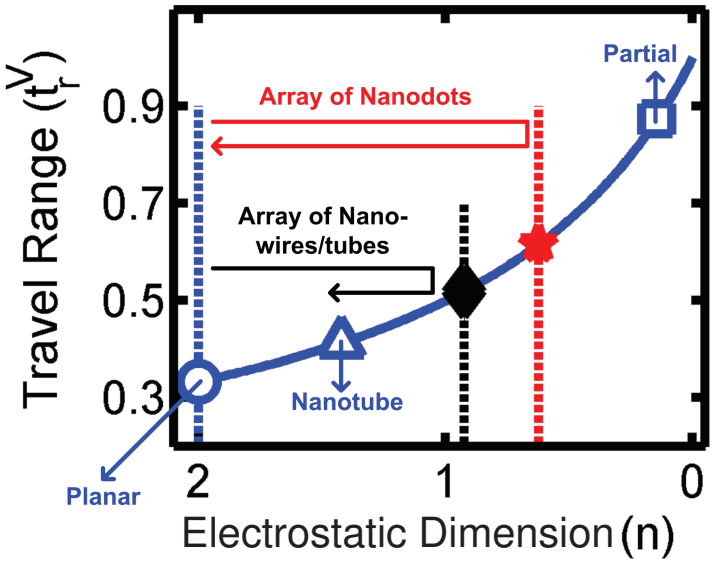

Fig. 4.2. Travel range as a function of electrode geometry parameter n. Solid line denotes the analytical formula of travel range (Eq. 4.1); whereas open symbols denote experimental data for fixed-geometry electrodes-planar [63] (open circle), nanotube [52] (open triangle), and partial electrode [60] (open square). Filled symbols denote the maximum achievable travel range using reconfigurable nano-structured array of cylinders (diamond) and spheres (pentagon) (see Figs 4.3-4.4 for details). For reconfigurable electrodes n and therefore travel range can be tuned in the range shown by arrows.

4.1.3 Reconfigurable Nanostructured Electrodes

4.1.4 Actuation with Linear Spring ($p = 1$)

Equation 4.1 and Fig. 4.2 suggest that travel range can be tuned through tuning of n dynamically. We propose to use reconfigurable nano-structured electrodes M_2 such as a regular array electrode e.g., array of electrically connected nano- wires/tubes (example case of cylinders) (Fig. 4.3 a) and nanodots (example case of spheres) (Fig. 4.3 b) that can modify the value of n dynamically. In general, M_2 can be a fractal or any other complex geometry electrode, but we restrict ourselves to simple, regular structures as they can easily be fabricated using nanofabrication techniques

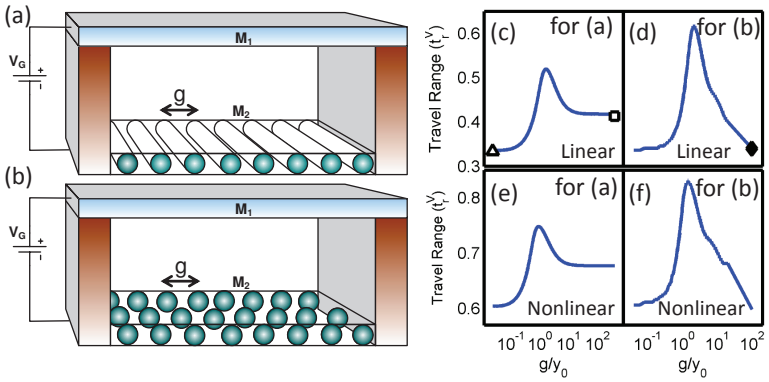

Fig. 4.3. Extension and tuning of travel range by reconfigurable nano-structured regular electrodes e.g., array of electrically connected (a) nano- wires/tubes (example of cylinders) and (b) nanodots (example of spheres). (c)-(f) Corresponding travel range as a function of tuning parameter g the separation between individual elements both for linear (c-d) and non-linear spring (e-f) of cubic nonlinearity. Solid line denotes numerical simulations, open symbol experimental data and filed symbol analytical result.

like transfer printing [80], bottom-up assembly [81] or/and liquid-filled microchannels [82].

The array electrodes are characterized by the separation g between the individual elements that dictate the electrostatic field and therefore the static behavior of microactuators. Equations 2.5 - 2.7 have been numerically solved for the static behavior of the actuator. The capacitance $C(y)$ of the nano-structured electrode system has been obtained from the solution of Poisson's equation, i.e., $\nabla^2\phi(x,y,z) = 0$ (ϕ being the electrostatic potential at (x,y,z) and x,z are parallel to the M_1/M_2 surface) for each y and then used in Eq. 2.7. The results are summarized in Figs. 4.3-4.4. We find that (i) *travel range for both the structures is larger than* $1/3$ *and* (ii) *travel range can be tuned by changing the separation* g. This separation g can be tuned electrically by selectively applying the voltage to different elements, and thus enabling post fabrication control of travel range. For example, if voltage is applied to alternate elements, it behaves as if g is doubled compared to the case when voltage is applied to all the

elements. Figure 4.2 also highlights this fact and the arrows show the limit in which travel range can be tuned by manipulating n through the tuning of g.

Interestingly, Figs. 4.3 c - d show that the dependence of travel range on g is non monotonic, with a peak at $g \sim 1.6y_0$. To interpret this peak for an array of nanowires/tubes, Figure 4.4 a shows the potential profile for five different values of g at the same applied voltage. The corresponding dC/dy as a function of y is shown in Fig. 4.4 b. For small values of $g \approx 2R$, field lines emanating from individual wire/tube merge and potential profile resembles that of regular planar electrodes (Fig. 4.4 a, A). Indeed, we find that the negative of the slope of $log(dC/dy) - log(y)$ is $n \approx 2$ and travel range is 1/3 (Fig. 4.4 b - c, A), as expected for planar electrodes. Indeed, the results at this limit has been validated by recent experiments in vertically aligned carbon nanotube arrays [70] (open triangle in Fig. 4.3 a). In contrast, for large separation of $g \gg y_0$, the field lines emanating from individual wire/tube do not interact, and the structure behaves like an isolated wire/tube (Fig. 4.4, E). Therefore, travel range for large values of g is same as that of an individual wire/tube and is consistent with the experimental data of an individual carbon nanotube [52] (open square in Fig. 4.3 a). At intermediate values of ($g \approx y_0$), structure behaves like a series combination of planar and cylindrical electrode, that minimizes n and maximizes travel range (Fig. 4.4, C).

One can analytically interpret the maxima in travel range for array of nanowires/tubes. To the left of C in Fig. 4.4, when the structure resembles planar electrodes, we find that (see appendix F for derivation)-

$$\frac{g}{y_0} \approx \frac{2\pi(3t_r - 1)}{W\left(\frac{y_0}{R}(3t_r - 1)\right)}; \quad \text{left of the C} \tag{4.2}$$

To the right of C, the capacitance behavior is similar to that of an individual nanowire/tube, which leads to -

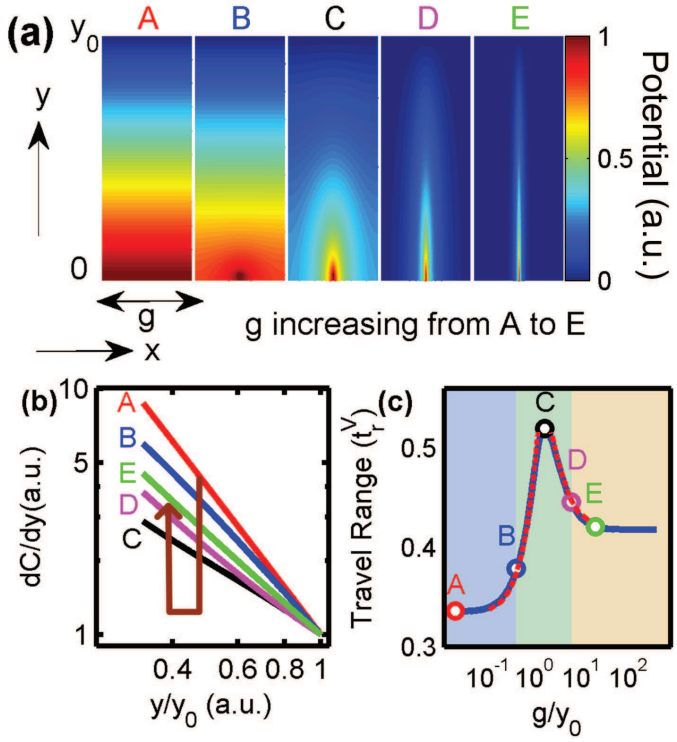

Fig. 4.4. Physics of tuning behavior and maximum achievable travel range for nano-structured array electrodes e.g., array of nanowires/tubes. (a) Two dimensional potential profile for various separation g, (b) corresponding dC/dy as a function of y, and (c) travel range as a function of g. Solid line denotes the numerical simulation and dotted line is the analytical formula given by Eqs. 4.2-4.3.

$$\frac{g}{y_0} \approx \pi(1-t_r)\sqrt{\left(\frac{(\lambda+3)t_r-\lambda}{\lambda-2(\lambda+1)t_r}\right)}; \quad \text{right of C} \tag{4.3}$$

where $\lambda \approx \log\left(2(1+y_0/R)\right)$ and W is the Lambert function. Equations 4.2-4.3 correctly anticipates the numerical simulation, as shown in Fig. 4.4(c).

Similar characteristics are also expected for electrodes composed of array of nanodots, see Fig. 4.3 d. The array of nanodots transitions from a planar like behavior to a single nanodot (single sphere) like behavior when separation g is increased. Note that, for large g, the isolated nanodot has approximately the same travel range as

that of electrodes with small g. This is expected from the characteristic dependence of capacitance between a single sphere and a plane as a function of y given by Maxwell formula, $C \approx 4\pi\epsilon_0 R\left(1+\frac{R}{2(y+R)}+\frac{R^2}{4(y+R)^2}+\cdots+\infty\right)$ (see the filled diamond in Fig. 4.3 d). Moreover, array of nanodots achieves travel range which is more than 0.6 of the initial air-gap.

4.1.5 Actuation with Non-Linear Spring ($p = 3$)

The travel range of microactuator can be further extended by the use of a nonlinear spring [83], as is evident from Eq. 4.1. For example, mid-plane stretching [55] gives rise to cubic non-linearity i.e.,$F_s = k(y_0 - y) + k'(y_0 - y)^3$ where k' is spring-constant associated with cubic nonlinearity. If the cubic nonlinear term dominates the linear term (i.e., $F_s \approx k'(y_0 - y)^3$), $t_r^V = 3/(n+3)$ (From Eq. 4.1 with $p = 3$). Therefore, nonlinear spring extends the travel range to 3/5 for planar electrodes. Figures 4.3 e - f show the travel range for the array electrodes with a nonlinear spring of cubic nonlinearity. In this case, the electrode with array of nanodots can achieve travel range of close to 0.8, and electrode with array of nano- wires/tubes achieves a travel range of 0.7, significantly higher than those obtained from linear springs. Therefore, the combination of nonlinear spring and nano-structured electrode extends the travel range well beyond the 1/3 limit of classical planar electrodes.

4.1.6 Travel Range Summary

We showed that reconfigurable nano-structured electrode extends the travel range beyond the perceived fundamental limit of 1/3 without using any external circuit, a series capacitor and/or modifying the actuation mechanism. Moreover, electrical tuning of the separation between the individual elements of array electrodes will enable post fabrication tuning of the travel range. The use of nonlinear spring coupled with the nano-structured electrode provides additional flexibility in further extending the travel range.

4.2 Problem of Hard Landing

4.2.1 Hard Landing Background

Hard-landing is one of the major reliability concerns for electromechanical switches e.g., RF-MEMS capacitive switches (Fig. 4.5 a), RF-MEMS ohmic switches or nanoelectromechanical relays (Fig. 4.5 b) [84]. It is the degradation of the dielectric or drain surface (Figs. 4.5 a - b) caused by the impact velocity v_{impact}, the velocity with which the movable electrode M_1 impacts the dielectric or drain, and dissipates $E_d = 1/2mv_{impact}^2$ on the dielectric surface or drain (m is the mass of M_1). This impact damages the dielectric or drain and increases the adhesion forces [85], which may eventually lead to the malfunction of the switch due to stiction [86]. Reliability and performance concerns therefore dictate that electrode M_1 should land softly in an ideal electromechanical switch (i.e., with lower v_{impact}) without compromising other critical parameters like pull-in time (t_{PI}) and pull-in voltage (V_{PI}).

Various open and closed loop control [87] techniques have been employed to reduce v_{impact} for individual [88] and ensemble [89] of switches. These techniques modify the input waveform so that $V_G(t)$ is reduced below V_{PI} as M_1 approaches the dielectric, thereby ensuring softer landing. An innovative self learning control algorithm has also been proposed to minimize the impact velocity and contact bounce by correcting the $V_G(t)$ waveform iteratively [90]. These external circuits add to the cost and the waveform developed for a nominal switch is often not optimal for an ensemble of switches (due to process variations) and the worst-case design inevitably compromise global performance.

Towards the goal of developing a self corrective, cost effective, and process variation tolerant soft-landing scheme, we propose following two techniques to reduce v_{impact} during pull-in the switch without compromising V_{PI} and t_{PI} significantly-

- The first method involves resistive feedback/braking so that part of E_d is remotely dissipated in a resistor away from the dielectric or drain surface.

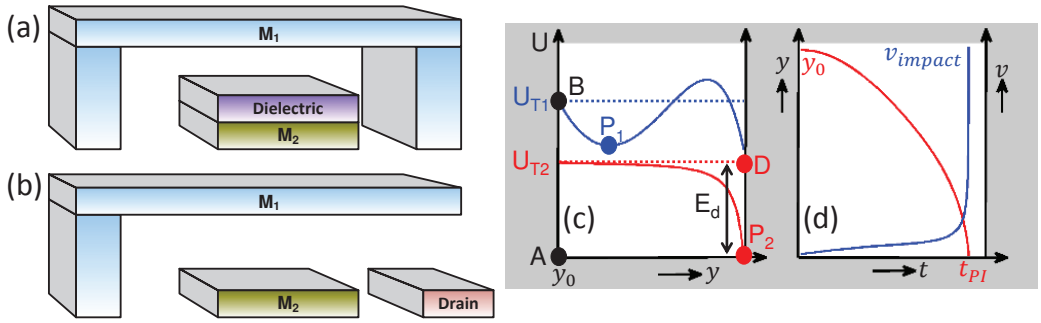

Fig. 4.5. Problem of Hard-landing during pull-in. Schematic of (a) RF-MEMS capacitive switch and (b) ohmic switch or NEMS relay. (b) Energy (U) vs. displacement (y) profile for $V_G < V_{PI}$ (blue curve) and $V_G > V_{PI}$ (red curve). V_G is the applied voltage between M_1 and M_2. E_d is the energy dissipation at M_1/dielectric or drain interface during pull-in. (c) Displacement (y) and velocity (v) as a function of time (t) during pull-in showing pull-in time (t_{PI}) and impact velocity (v_{impact}).

- The second method relies on the patterning of either of M_1, M_2 or the dielectric in such a way that the effective capacitor area decreases dynamically as M_1 approaches the dielectric or drain to reduce v_{impact}.

4.2.2 Strategies of Soft-Landing

The pull-in of an electromechanical switch is achieved by applying a step potential V_G between the electrodes M_1 and M_2 (Figs. 4.5 a - b). Assuming M_1 at rest at y_0 (Fig. 4.5 c, point A), a step voltage $V_G < V_{PI}$ imparts an energy $U_{T1} = -1/2C(y_0)V_G^2$ to the membrane (Fig. 4.5 c, point B). Electrode M_1 eventually comes to rest at the minima (point P_1) of the total potential energy (U) landscape defined by the sum of electrostatic ($-1/2C(y)V_c^2$, V_c being the voltage across the capacitor) and spring ($1/2k(y_0-y)^2$) potential energies (blue solid line in Fig. 4.5 c). The energy difference between U_{T1} and P_1 is lost due to air-damping. For step voltage $V_G > V_{PI}$, however, the energy of M_1 jumps to U_{T2} and since the energy landscape this time (red solid line in Fig. 4.5 c) does not have any minima, the "pull-in instability" results in

uninhibited acceleration of M_1 that is eventually brought to hard-stop at $y = 0$ (point P_2 in Fig. 4.5c) by slamming against the dielectric or drain. It is this kinetic energy ($E_d = 1/2mv_{impact}^2$, Fig. 4.5 b) at the M_1/dielectric or drain interface that damages the dielectric or drain. Figure 4.5 d shows the displacement (y) and velocity (v) of the electrode M_1 as a function of time (t) during pull-in.

The dynamics of the switch that is governed by Eq. 2.9 in chapter 2, indicates that the acceleration of M_1 is directly proportional to the electrostatic force which is given by-

$$F_{elec} = \frac{1}{2}\frac{d(CV_c^2)}{dy} = \frac{1}{2}V_c^2\frac{dC}{dy} + \frac{1}{2}C\frac{dV_c^2}{dy}. \tag{4.4}$$

where V_c is the voltage between M_1 and M_2 such that $V_G = IR+V_c$ and $I = d(CV_c)/dt$ with V_G being the applied voltage and R being the series resistance. As M_1 approaches the dielectric or drain, v_{impact} can be dynamically reduced by modulating V_c or C such that either the point D or P_2 in Fig. 4.5 c move in a way to reduce E_d and v_{impact}. Traditional schemes like waveform shaping [91] attempt to reduce v_{impact} by modulating V_G - the applied bias (with $R = 0$, $V_c = V_G$). Here we propose two new and simpler schemes for soft-landing that are as follows:

4.2.3 Resistive Braking

One can reduce v_{impact} by inserting a resistance R in series with the voltage source. Initially, there will be large $t = 0^+$ transient (few ns) to charge the capacitor during which the charging current I can be significant. Once this $t = 0^+$ transient is over and the upper electrode begins to move, I is relatively small at the early stages of pull-in such that $V_c \sim V_G$ and M_1 pulls in classically. For t close to t_{PI}, I increases rapidly, causing significant remote resistive dissipation across R. As a result, the point D moves down closer to P_2 in Fig. 4.5(b), with corresponding reduction in E_d and v_{impact}. This self retardation does not require any complex external circuitry

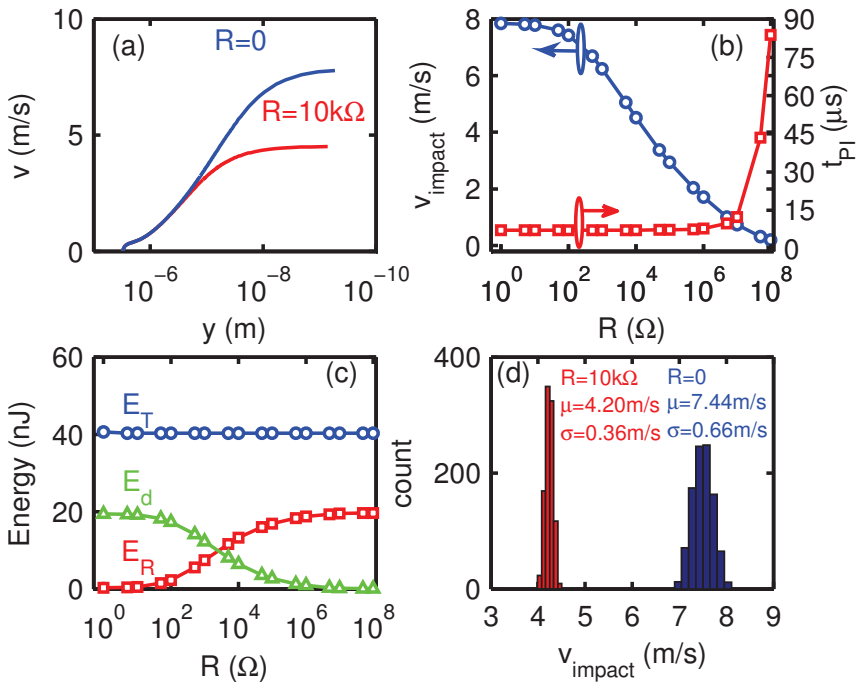

Fig. 4.6. Soft-landing by resistive braking. (a) Velocity (v) as a function of displacement (y) during pull-in for $R = 0$ and $R = 10k\Omega$ (b) v_{impact} and t_{PI} as a function of R. Below $R = 1M\Omega$, v_{impact} changes but t_{PI} remains almost the same. (c) Different components of energy as a function of R. E_T is the total energy supplied by the voltage source, $E_d = \frac{1}{2}mv_{impact}^2$ is energy dissipation at the dielectric surface, and E_R is the total energy dissipated through R during pull-in process. (d) Distribution of v_{impact} due to process variation for $R = 0$ and $R = 10k\Omega$. Both, the mean (μ) and standard deviation (σ) decreases for $R = 10k\Omega$.

to shape V_c, but achieves the same effect dynamically through the negative feedback introduced by R in the scheme.

Figure 4.6 a shows v as a function of y during pull-in with (i) $R = 0$ and (ii) $R = 10k\Omega$. In both the cases, electrode M_1 lands on the dielectric in almost same t_{PI} (Fig. 4.6 b), but with $R = 10k\Omega$, v_{impact} is reduced by almost 50%, so that only 25% of the kinetic energy is dissipated on the M_1/dielectric interface, while the rest 75% is dissipated in the remote resistance. Since resistive braking is only

operative for a short duration close to $t \sim t_{PI}$ when $v(t)$ is high (Fig. 4.5 c), therefore resistive braking changes v_{impact} without affecting t_{PI} significantly. The upper limit of R is determined by the fact that if R is too high, the increase in t_{PI} may be unacceptable, as I becomes large enough to reduce V_c and retard the motion of M_1 throughout the pull-in process. For the illustrative problem, $R < 1M\Omega$ provides large reduction in v_{impact}, without changing t_{PI} significantly (Fig. 4.6 b). Figure 4.6 c shows various components of energy dissipation as a function of R. Total energy ($E_T = C(0)V_G^2 = (\epsilon_0\epsilon_d WL/y_d)V_G^2$) is independent of R whereas energy dissipation at the dielectric surface ($E_d = 1/2mv_{impact}^2$) decreases with R and energy dissipated through R ($E_R = \int_0^\infty I^2 R dt$) increases with R. Interestingly, note that $E_R + E_d = E_T - 1/2C(0)V_G^2 - 1/2ky_0^2$ (by energy conservation) is independent of R. This means that the energy dissipation at the dielectric surface decreases because of increase in the (remote) resistive dissipation through R, while keeping the energy supplied by the voltage source unchanged. One major advantage of resistive braking is that it works well for an ensemble of switches in presence of process variation. Fig. 4.6 d shows the distribution of impact velocity with 10% variation in the input parameters (L, W, y_0, y_d, etc.). Both, the mean (μ) and the standard deviation (σ) of the impact velocity are reduced significantly for $R = 10k\Omega$.

4.2.4 Capacitive Braking

An alternate scheme for reducing v_{impact} is to pattern M_1 or M_2 or dielectric as shown in Fig. 4.7 p1 - p5. For example, electrode M_1 or M_2 can be an array of electrically connected nano- wires/tubes (example case of cylinders) or nanodots (example case of spheres) (Fig. 4.7 p2 & p3) and/or the dielectric can be patterned to have an array/fractal of linear slots (Fig. 4.7 p4 & p5). Note that, this idea of patterning of the bottom electrode M_2 is similar to our proposal of reconfigurable nano-structured electrodes for the problem of travel range.

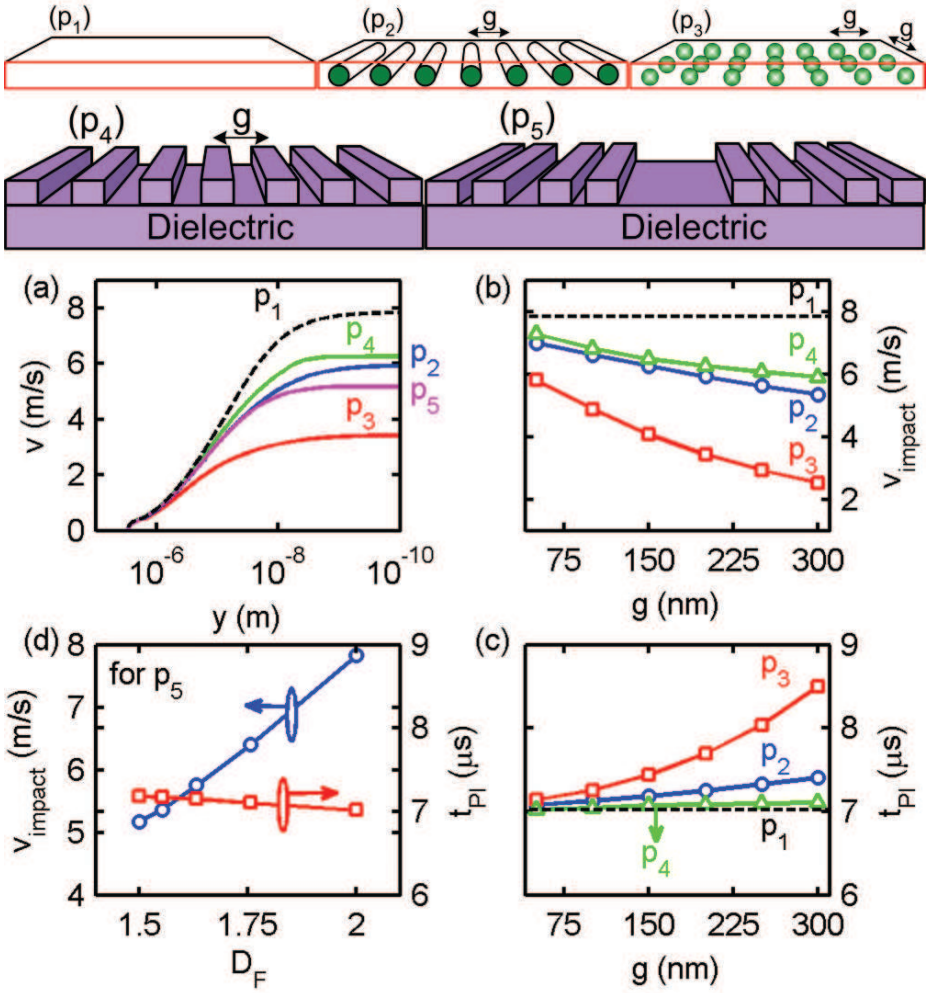

Fig. 4.7. Soft-landing by patterning the electrode M_1/M_2 or the dielectric. Electrode M_1/M_2 can be - (p1) rectangular plate, (p2) array of nano- wires/tubes, (p3) array of nanodots, and dielectric can be - (p4) an array of linear slots, or (p5) a fractal of linear slots. (a) v as a function of y for patterned electrode or dielectric. Velocity reduction is maximum for an array of nanodots. (b) v_{impact} (c) t_{PI} as a function of separation (g) between individual elements. As g increases v_{impact} reduces at the cost of increased t_{PI}. (d) v_{impact} and t_{PI} for fractal dielectric as a function of D_F. As D_F increases v_{impact} increases and t_{PI} decreases.

Now, regardless the patterning, in the up-state of M_1, the fringing fields between the plates ensure that these patterned capacitors are indistinguishable from unpatterned parallel plate capacitor and therefore $C = Ay^{-1}$ before pull-in; V_{PI} is therefore unaffected by patterning. As M_1 approaches the dielectric during pull-in, however, the individual field lines associated with the patterned array begins to separate rapidly from each other and elements of the array begins to behave as an isolated cylinders or spheres, with dramatic reduction in the effective area of the capacitor and hence the capacitance ($C = A(y)y^{-1}$). This dramatic reduction in the capacitance of a patterned capacitor causes electrostatic potential energy to reduce in magnitude, pushing point P_2 up closer to D (Fig. 4.5 c) resulting in reduced E_d and v_{impact}.

The capacitance $C(y)$ for the patterned structures shown in Fig. 4.7 p1 - p5 has been obtained in the same way as discussed in section 4.1.3 and then used in Eq. 4.4. The results for the pull-in dynamics are summarized in Fig. 4.7 a - d. Figure 4.7 a shows v as a function of y for patterned electrodes or dielectric. Reduction in v_{impact} is maximum for an array of nanodots. Figures 4.7 b - c shows v_{impact} and t_{PI} as a function of separation (g) between individual elements of the patterned electrode or dielectric. As g increases, v_{impact} decreases at the cost of increased t_{PI}. Figure 4.7 d shows v_{impact} and t_{PI} as a function of fractal dimension (D_F) of patterned dielectric of Fig. 4.7 p5. As D_F of the patterned dielectric increases, the dielectric begins to resemble a classical parallel plate MEMS switch and the advantages of patterning are rapidly diminished.

4.2.5 Hard Landing Summary

To summarize this section, we proposed two novel schemes of resistive and capacitive braking (rather than the pulse shaping) for dynamic soft landing in electromechanical switches. The proposed resistive braking scheme also provides an optimum solution for the design of an ensemble of switches in presence of process variations. Note that, one disadvantage of the patterned electrode/dielectric is the

loss of ON-state capacitance (C_{ON}), therefore a combination of resistive braking as well as electrode/dielectric patterning may offer the best compromise between reliability vs. performance (t_{PI},and C_{ON}).

4.3 Conclusions

In this chapter:

- We saw that intrinsic pull-instability poses problem of limited travel range for tunable-gap electromechanical actuators such as deformable mirrors and hard-landing for MEMS switches.
- To address the respective problems, we provided novel device level solutions, which do not require any extra circuits or feedback mechanism.
- The proposed solutions utilize electrode geometry as a new design variable in electromechanical actuators and switches to address the problems arising due to pull-in instability.
- The proposed solutions for hard-landing are very general and can inspire solutions to minimize damage in other Landau systems such as ferroelectric materials also [43].

In this chapter, we focused on addressing the problems due to instability. It may therefore appear that instability is a bad thing. In the next two chapters, we will try to convince that instability can be very useful, if used properly. In the next chapter, we will discuss the strategies to harness instability, mainly its negative capacitance behavior for voltage amplification in field effect transistors.

5. HARNESSING NEGATIVE CAPACITANCE : HYSTERESIS-FREE SUB-60mV/DECADE FIELD EFFECT TRANSISTORS

In the last chapter, we addressed the problems that arise due to instability. Specifically, we proposed novel device structures to address the problems of travel range and hard-landing. In contrast to the existing solutions for the respective problems, the proposed solutions do not require any external circuit or feedback mechanisms.

The goal of this as well as next chapter is very different from the last chapter. Here (as well as in the next chapter), instead of treating instability as a source of problems, we harness instability for performance enhancement. In this chapter, we focus on field effect transistors (FETs), namely a suspended-gate FET and ferrooelectric FET, that use air-gap of MEMS and ferroelectrics as the gate insulator, respectively. We utilize the negative capacitance behavior of these novel gate insulators as discussed in chapter 2, to beat the fundamental thermodynamic limit of sub-threshold swing of $60mV/decade$ in classical FETs. The specific goals of this chapter[1] are as follows:

- Illustrate how the negative capacitance behavior of air-gap in MEMS and ferroelectrics (seen in chapter 2) can lead to hysteresis-free sub-$60mV/decade$ switching characteristics.
- Once we understand that negative capacitance of the gate insulator can lower sub-threshold swing below $60mV/decade$, we answer the question: "How low can the sub-threshold swing be in a negative capacitance FET (NC-FET)?".
- We end the search of an ideal switch and propose a novel device concept that achieve hysteresis-free $0mV/decade$ switching characteristics.

[1]The content (text and figures) in this chapter have been adapted from [92] ©IEEE 2013 and [93] ©IEEE 2014.

Rest of the chapter is organized as follows. In section 5.1, we start with the background and motivation of the need of sub-$60mV/decade$ switch. We discuss both the hysteretic and hysteresis-free switching characteristics of novel Landau switches in section 5.2. In section 5.3, we discuss the conditions of hysteresis-free sub-$60mV/decade$ switching in Landau switches and establish the fundamental lower limits of sub-threshold swing in negative capacitance field effect transistors. We discuss our proposal of hysteresis-free ideal switching characteristics in section 5.4 and conclude in section 5.5.

5.1 Background

Reducing power supply voltage (V_{DD}) to lower power dissipation ($P_{dyn} \propto V_{DD}^2$) in an integrated circuit (IC) is one of the fundamental challenge for the scaling of modern ICs. The reduction of V_{DD} requires reducing threshold voltage (V_T) to meet the ON current ($I_{ON} \propto (V_{DD} - V_T)^{\alpha}$, here $\alpha \sim 1 - 2$) requirement. However, lowering of V_T comes at the expense of increased OFF state power dissipation ($P_{OFF} \propto I_{OFF}$) due to increased OFF current ($I_{OFF} \propto 10^{\left(-\frac{V_T}{S}\right)}$ [94]. Here, S is the sub-threshold swing of the underlying switch. These conflicting requirements suggest that the advantages obtained by reducing V_{DD} can be offset by either reduced performance (lower I_{ON}) or increased P_{OFF} [95]. The situation therefore demands for reducing S so that V_{DD} and V_T can be reduced simultaneously without sacrificing the performance or power (Figs. 5.1). An ideal switch with $S_{ideal} = 0mV/decade$ is thus needed to realize the ultimate scaling of ICs [96]. However, thermodynamics dictate that S for classical field effect transistors (FETs) (Fig. 5.1 a) cannot be lower than the Boltzmann limit of $S_{BZ} = 60mV/decade$ [94].

The sub-threshold swing is the change in gate voltage (V_G) required to change the drain current (I_{DS}) by one order of magnitude. When an FET is operated between gate voltage $V_{G1} < V_G < V_{G2}$, writing sub-threshold swing (S) as-

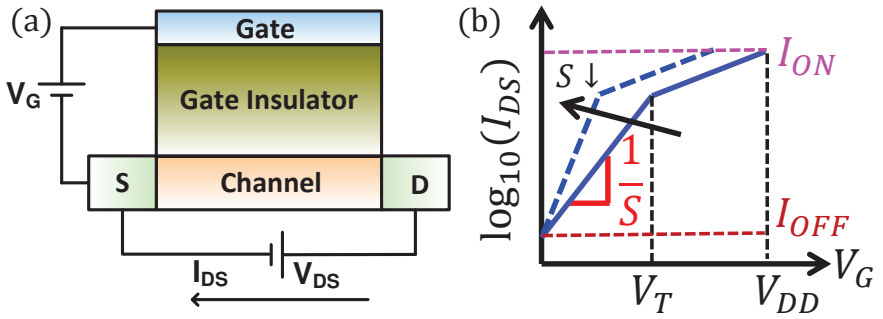

Fig. 5.1. (a) Schematic of a field effect transistor (FET).(b) Corresponding $I_{DS} - V_G$ characteristics for two devices with different subthreshold swings (S). As S reduces, power supply voltage (V_{DD}) and threshold voltage (V_T) can be reduced keeping the same on (I_{ON}) and off (I_{OFF}) current.

$$S \equiv \frac{\Delta V_G}{\Delta \psi_s} = \frac{\Delta V_G}{\log_{10}\left(\frac{I_{DS2}}{I_{DS1}}\right)} = \frac{\Delta \psi_s}{\log_{10}\left(\frac{I_{DS2}}{I_{DS1}}\right)} \frac{\Delta V_G}{\Delta \psi_s} = n \times m, \tag{5.1}$$

shows that S is the product of two factors. Here I_{DS1}, I_{DS2} are drain currents at V_{G1}, V_{G2} respectively, $\Delta\psi_s$ is the change in surface potential and $\Delta V_G = V_{G2} - V_{G1}$. The transport factor, $n \equiv \frac{\Delta \psi_s}{\log_{10}\left(\frac{I_{DS2}}{I_{DS1}}\right)} = 2.3 k_B T/q$ (k_B = Boltzmann constant, T= absolute temperature, and q=electron charge) is $60mV/decade$ at room temperature for above the barrier current transport. Using the capacitor divider model of a FET (Fig. 5.2 a), the parameter m (also known as the body factor) can be written as-

$$m \equiv \frac{\Delta V_G}{\Delta \psi_s} = \frac{\int_{Q_1}^{Q_2} \left(C_s(Q)^{-1} + C_{ins}(Q)^{-1}\right) dQ}{\int_{Q_1}^{Q_2} \left(C_s(Q)^{-1}\right) dQ}. \tag{5.2}$$

Here, $C_s(Q)$ is the channel depletion capacitance, $C_{ins}(Q)$ is the capacitance of the gate insulator, Q is charge on the gate, and Q_1, Q_2 correspond to V_{G1}, V_{G2} respectively. For an FET with constant C_s and C_{ins}, Eq. 5.2 reduces to the well-known formula of m i.e.,

$$m = 1 + \frac{C_s}{C_{ins}}. \tag{5.3}$$

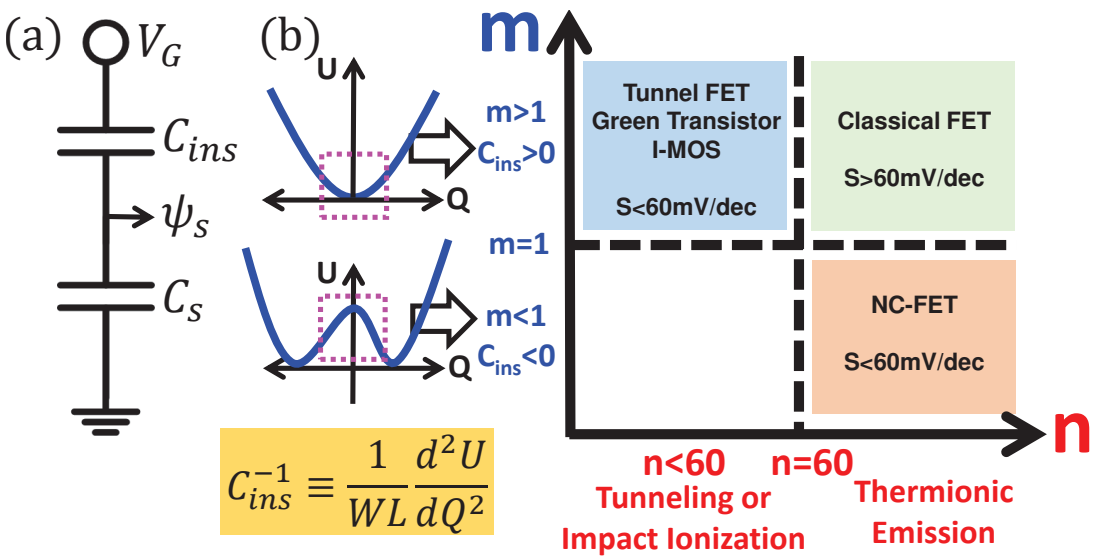

Fig. 5.2. Phase space of FETs based on their sub-threshold swing. (a) Equivalent capacitor divider model of an FET. (b) Classification of various proposals of novel FETs based on the values of body factor (m) and transport factor (n). FETs with gate insulators having $C_{ins} > 0$, exhibits $m > 1$; whereas FETs with gate insulators having $C_{ins} < 0$, exhibits $m < 1$. U is the total energy and Q is the charge on C_{ins}.

In a classical FET, gate insulator such as SiO_2 (Fig. 5.1 a) exhibits positive capacitance i.e., $C_{ins} > 0$, which results in body factor $m \geq 1$ (Eq. 5.3). As a result, S cannot be lower than $S_{BZ} = 60mV/decade$ (Fig. 5.2 b).

In literature, there have been two major approaches to reduce S below S_{BZ} (Fig. 5.2 b). The first scheme involves reducing $n < 60mV/decade$ (while keeping m fixed) by modifying the transport within the channel. For example, instead of relying on the thermionic emission based transport ($n = 60mV/decade$), Tunnel-FETs [18] and green transistors [97] utilize band-to-band tunneling; whereas Impact Ionization FETs [98] utilize impact ionization to reduce $S < S_{BZ}$. In the second approach, m is reduced below one by changing the gate insulator. In this scheme, the classical gate insulator (C_{ins}) characterized by a single well energy landscape as shown in Fig. 5.2 b, is replaced by an inherently unstable gate insulator that exhibits a two-well energy

landscape, Fig. 5.2 b. As illustrated in chapter 2, the capacitance (C_{ins}) in the unstable regime (dotted square for two well energy landscape in Fig. 5.2 b), is negative. Therefore, this negative capacitance behavior has the potential to reduce body factor m below one and $S < S_{BZ}$ (Fig. 5.2 b). We call these new class of switches Landau switches (as opposed to Boltzmann switches), because the operation of these devices rely on an energy landscape defined by a pair of energy wells. This characteristic two-well energy landscape is associated with phase transition processes [99] and is elegantly interpreted by the Landau theory. Landau switches are also called negative capacitance field effect transistors (NC-FETs) due to their negative capacitance behavior in the unstable regime. In this chapter, we focus on two illustrative examples of Landau switches, namely, Ferroelectric-FET (FE-FET) [100] and suspended gate FET (SG-FET) [21, 101].

5.2 Switching Characteristics of NC-FETs

In this section, we show that in a properly designed SG-FET and FE-FET, negative capacitance of the air-gap and ferroelectric material, respectively, provide the necessary voltage amplification to exhibit hysteresis-free sub-$60mV/decade$ behavior. Before that, let us extend our understanding of instability in MEMS capacitive actuators and ferroelectric materials to explain the basic operation of an SG-FET and FE-FET.

5.2.1 Abrupt Switching Characteristics of SG-FET and FE-FET with Hysteresis

Figure 5.3 a shows the schematic of an SG-FET in which gate is suspended from a spring and air-gap creates the gate insulator. The structure is similar to a MEMS capacitive actuator discussed in chapter 2, except that the thin dielectric in Fig. 2.1 has been replaced by a semiconductor channel to create a FET with movable gate. In the equivalent capacitor divider model of an FET as shown in Fig. 5.2 a, C_s for

SG-FET is same as that of a regular classical FET. However, air-gap capacitance C_{air} replaces C_{ins}. Note that, the physics of C_{air} in SG-FET is exactly same as in a MEMS capacitive actuator and was discussed in chapter 2. Figure 5.3 b shows C_{air} as a function of the charge (Q) on the gate. C_{air} (Eq. 2.21) is positive for $0 < Q < Q_{c1}$ and negative for $Q_{c1} < Q < Q_{c2}$. The charge Q_{c1} corresponds to the instability point $y = 2y_0/3$; whereas Q_{c2} corresponds to the physical boundary $y = 0$ between the gate and channel (Eq. 2.22 and Fig. 2.4). As explained in chapter 2, movable gate is unstable in the negative capacitance regime and therefore exhibits a hysteretic $y - V_G$ characteristics (Fig. 2.2 c). As a result, SG-FET also exhibits hysteretic $I_{DS} - V_G$ switching characteristics as shown in Fig. 5.3 c. Abrupt transition of the gate from top to down position at pull-in voltage and from down to the top position at pull-out voltage, results in vertical jump in $I_{DS} - V_G$ characteristics which is equivalent to sub-threshold swing of $0mV/decade$. Note that, this abrupt switching behavior of SG-FET is associated with an intrinsic hysteresis (Fig. 5.3 c).

We saw in chapter 2, the qualitative physics of a ferroelectric is similar to the physics of MEMS capacitive actuator. Similarly, the behavior of an FE-FET (Fig. 5.3 d) is qualitatively very similar to the behavior of an SG-FET. Recall that an FE-FET is similar to a regular FET, except with a ferroelectric material as the gate insulator (Fig. 5.3 d). Like SG-FET, C_s in Fig. 5.2 a is same as that of a classical FET; whereas C_{ins} is replaced by ferroelectric capacitance C_{FE}. Figure 5.3 e shows C_{FE} as a function of the gate charge (Q). We consider only positive values of Q for an n-channel FET. C_{FE} is positive for $Q > Q'_{c1}$ and negative for $Q'_{c2} < Q < Q'_{c1}$. The charge Q'_{c1} corresponds to the boundary between stable and unstable regime and is same as Q_c discussed in chapter 2 (Fig. 2.9); whereas $Q'_{c2} = 0$ for an n-channel FE-FET. As explained in chapter 2, ferroelectric is unstable in the negative capacitance regime and exhibits hysteretic $Q - V_G$ characteristics (Fig. 2.8 d). As a result, FE-FET also exhibits hysteretic $I_{DS} - V_G$ characteristics (Fig. 5.3 f).

As evident from the responses of SG-FET and FE-FET, a typical Landau switch exhibits hysteretic $I_{DS} - V_G$ characteristics with abrupt transition equivalent to

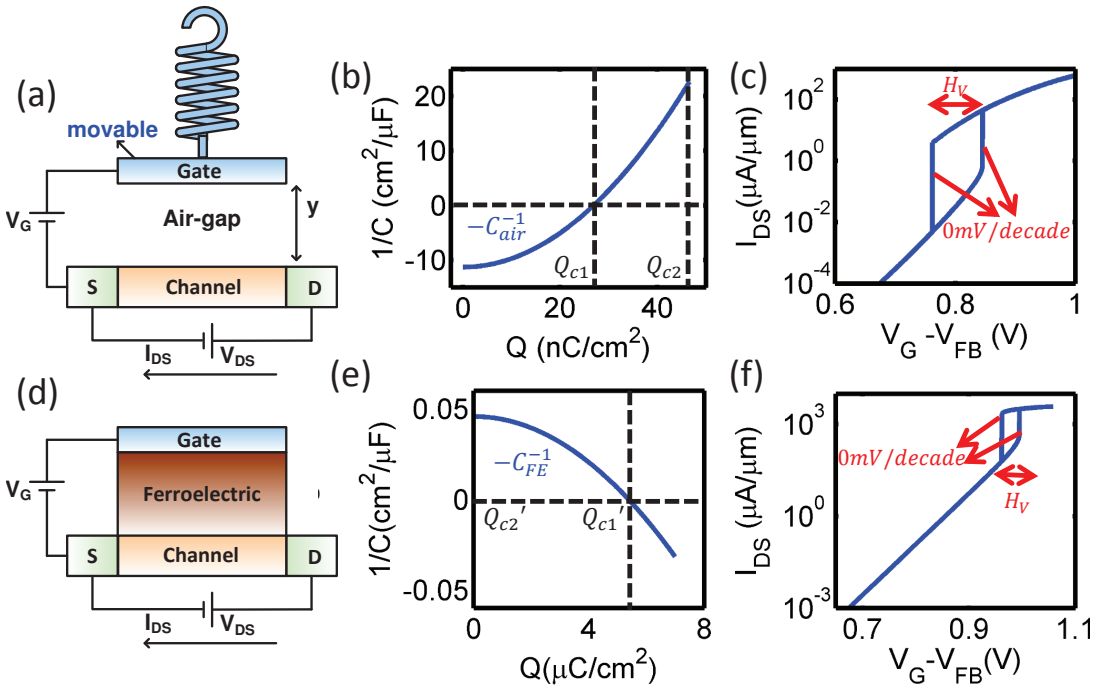

Fig. 5.3. (a) Schematic of a suspended-gate FET in which an air-gap serves as the gate insulator.(b) Capacitance of the air-gap as a function of the gate charge (Q) and (c) typical hysteretic $I_{DS} - V_G$ characteristics of SG-FET. The parameters used in the simulations are $y_0 = 10nm$, $\epsilon_s = 11.7$, $L = 100nm$, $W = 4\mu m$, $H = 33.9nm$, $E = 200GPa$, $N_A = 6.22 \times 10^{15} cm^{-3}$, and $V_{DS} = 0.5V$. (e) Schematic of a ferroelectric FET in which a ferroelectric material serves as the gate insulator.(f) Capacitance of ferroelectric as a function of the gate charge (Q) and (c) typical hysteretic $I_{DS} - V_G$ characteristics of FE-FET. The parameters used in the simulations are $y_0 = 35.2nm$, $\epsilon_s = 11.7$, $L = 100nm$, $W = 4\mu m$, $N_A = 5 \times 10^{18} cm^{-3}$, $V_{DS} = 0.5V$, $\alpha_0 = -6.5 \times 10^7 m/F$, $\beta_0 = 3.75 \times 10^9 m^5 F/C^2$, and $\gamma_0 = 0$. Note that, numerical simulation framework for SG-FET and FE-FET have been discussed in appendix B and C, respectively.

$0mV/decade$ (Fig. 5.4 a). In principle, abrupt switching ($S = 0mV/decade$) of Landau switches could potentially reduce the energy dissipation to $E_d = Q_V \Delta V_G$, when operated between points O_1 and O_2 in Fig. 5.4 a. Here Q_V is the difference in the charge between the two states (O_1 and O_2) and ΔV_G is fundamentally dictated by thermal noise [102]. Unfortunately, as we saw, abrupt switching always comes at the

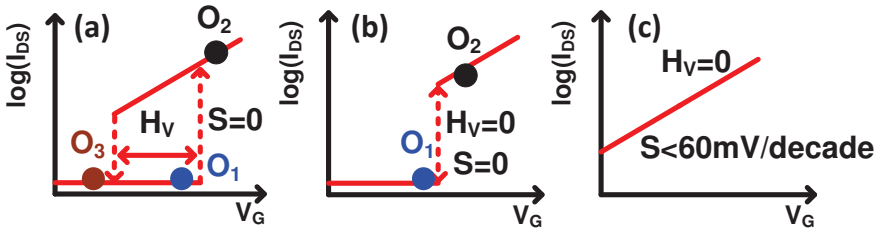

Fig. 5.4. Summary of the response of Landau switches, namely SG-FET and FE-FET. (a) Typical hysteretic $I_{DS} - V_G$ characteristics with abrupt transition, (b) ideal switching characteristics which we are after in this chapter, and (c) hysteresis-free sub-$60mV/decade$ switching characteristics of properly designed Landau switches.

cost of an intrinsic hysteresis, because once switched from one stable regime to another stable regime (or vice versa), switching back does not occur at the same applied voltage. Therefore, hysteresis in Landau switches (Fig. 5.4 a) dictates the energy dissipation ($E_d = Q_V H_V$ with H_V being the width of the hysteresis), because the switch must operate between points O_3 and O_2 (Fig. 5.4 a). The fundamental question is: under what condition hysteresis-free abrupt switching ($H_V = 0, S = 0mV/decade$) can be realized in a Landau switch? (Fig. 5.4 b). We will answer this question below in section 5.4. Before that, we discuss how can we get a hysteresis-free response (even with $S \neq 0$) in a Landau switch. We will show below, hysteresis-free response in a Landau switch requires stabilization in the unstable regime and consequently lead to sub-$60mV/decade$ switching (Fig. 5.4 c).

5.2.2 Hysteresis-Free sub-60mV/decade Switching Characteristics of SG-FET and FE-FET

In the previous section, we saw that intrinsic instability of SG-FETs and FE-FETs is responsible for the hysteresis of $I_{DS} - V_G$ characteristics (Fig. 5.4 a). Therefore, if the movable gate in SG-FET and ferroelectric in FE-FET, respectively, can be stabilized in the unstable regime, hysteresis will go away. Although, C_{ins} is negative in the unstable regime, if C_s is properly chosen such that $C_G^{-1} = C_{ins}^{-1} + C_s^{-1} > 0$,

movable gate and ferroelectric will be stabilized in the unstable regime. We show below that this stabilization in the unstable regime provides the necessary voltage amplification to reduce $S < S_{BZ}$.

Hysteresis-free smooth switching ($H_V = 0$ & $S > 0mV/decade$, Fig. 5.4 c) in SG-FET requires a benign $y - V_G$ characteristics that displays no hysteresis, but then have no pull-in instability either, i.e., $H_V = 0$ & $y_c = 0$. Since $H_V \propto y_c^2$ (Eq. 2.23 in chapter 2) and y_c is given by Eq. 2.15. $y_d = 2y_0$ makes both H_V and y_c zero. As there is no dielectric in SG-FET as opposed to MEMS capacitive actuators, y_d is just the equivalent thickness corresponding to the channel capacitance C_s. It means that a constant series capacitor $C_s = \epsilon_0/2y_0$ makes the overall capacitance $C_G^{-1} = C_{air}^{-1} + C_s^{-1}$ positive and enables hysteresis-free smooth switching. Figures 5.5 a-b show the energy landscape (Eq. 2.4 with $y_d = 2y_0$) when V_G is increasing and decreasing respectively. Interestingly, $U - y$ profile at different voltages exhibits only one minima which is the characteristic of a single well energy landscape. Open circles and open triangles in Figs. 5.5 a-b denote the position where gate is stabilized. Figure 5.5 c shows the corresponding $y - V_G$ characteristics which does not exhibit any hysteresis as expected from single well energy landscape.

Note that, this switching behavior has fundamentally been made possible by stabilizing the gate in its inherently unstable regime. This stabilization comes from an inherent negative feedback provided by the series capacitor (C_s) (channel depletion capacitance), so that the voltage-drop across air-gap capacitor (V_{air}) decreases when the gate enters in the unstable regime (Fig. 5.5 d). This decrease in V_{air} amplifies the voltage-drop across C_s(surface potential (ψ_s)) (Fig. 5.5 d). This amplification in ψ_s is directly reflected in the body factor $m < 1$, symbols in Fig. 5.5 e . If one accounts for the charge build up inside the semiconductor (i.e., voltage dependence of C_s), it can be shown that -

$$m \equiv \frac{dV_G}{d\psi_s} = 1 + \frac{C_s}{C_{air}}, C_s = \sqrt{\frac{q\epsilon_0\epsilon_s N_A}{2\psi_s}} \tag{5.4}$$

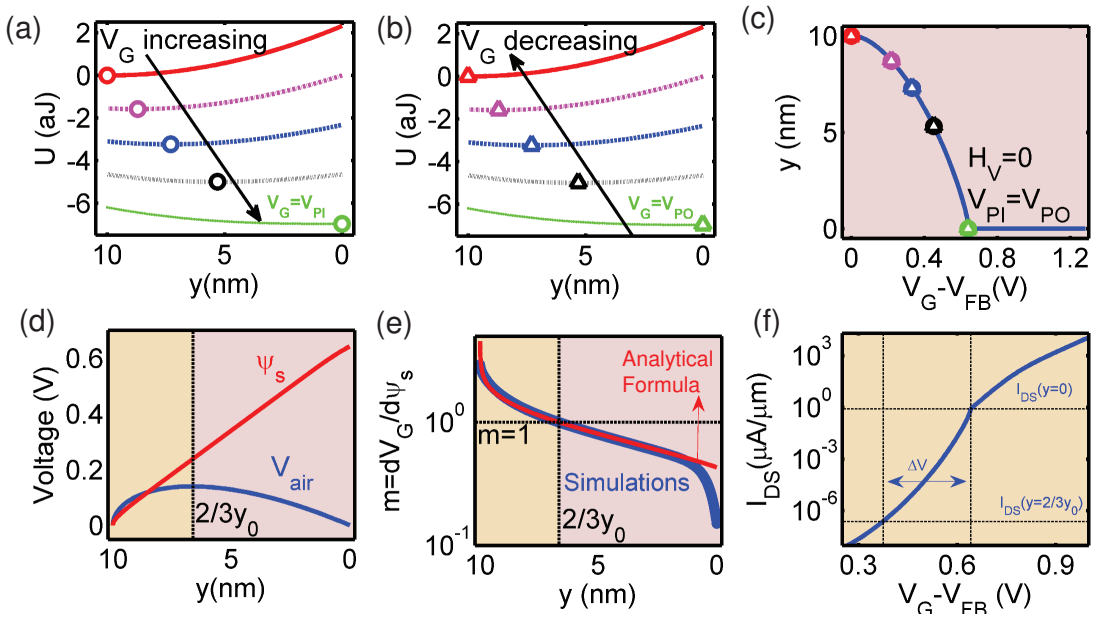

Fig. 5.5. Hysteresis-free sub-$60mV/decade$ switching in SG-FET. Single well energy landscape for hysteresis-free smooth switching when (a) V_G is increasing and (b) V_G is decreasing. Open circles denote the position where gate is stabilized. Corresponding (c) $y - V_G$ characteristics for hysteresis-free smooth switching. (d) Voltage-drop across air-gap capacitor (V_{air}) and series capacitor (ψ_s) showing the voltage amplification in ψ_s in the unstable regime. (e) Body factor m which is less than one in the unstable regime of SG-FET. Symbols denote the numerical simulations and solid line Eq. 5.4. (f) Corresponding $I_{DS} - V_G$ characteristics with an effective subthreshold swing of $39.3mV/decade$ reflecting the voltage amplification provided by the negative capacitor. The parameters used for simulations are same as the one used in Fig. 5.3 except $H = 26.4nm$ and $N_A = 4.95 \times 10^{15} cm^{-3}$.

where q is the charge on an electron, ϵ_s is dielectric constant of channel material, and N_A is the channel doping. C_{air} is the effective air-gap capacitance (Eq. 2.21 and Fig. 5.3 b). Note that, in contrast to Eq. 5.2 which gives an effective value of m between $V_{G1} < V_G < V_{G2}$, Eq. 5.4 gives value of m at single V_G. As expected, air-gap capacitor effectively acts like a negative capacitor when gate enters in the unstable regime (i.e.,

$C_{air} < 0$ when $y < 2/3y_0$) and thus, provides necessary voltage amplification to reduce m below one. Equation 5.4 correctly reproduces the numerical simulations results in Fig. 5.5 e. The corresponding $I_{DS} - V_G$ for the same SG-FET obtained from the self-consistent numerical simulations is shown in Fig. 5.5 f and confirms the hysteresis-free smooth switching of SG-FET. In sub-threshold regime, $I_{DS} - V_G$ characteristics is highly nonlinear and does not exhibit a constant sub-threshold swing. Therefore, we define an effective sub-threshold swing (same as Eq. 5.1) for $I_{DS}(y = 2/3y_0) < I_{DS} < I_{DS}(y = 0)$ when SG-FET is biased in negative capacitance regime. Considering this, S is given by $\Delta V / \log_{10}(I_{DS}(y = 0)/I_{DS}(y = 2/3y_0))$, where ΔV is defined in Fig. 5.5 f. The value of S for the chosen parameters is $39.3mV/decade$ and is less than the fundamental thermodynamic limit of $60mV/decade$. Reduction in S confirms the voltage amplification provided by the air-gap capacitor in its negative capacitance regime.

Similar to an SG-FET, hysteresis-free smooth switching in FE-FET, requires a benign $Q - V_G$ characteristics such that it does not exhibit any hysteresis with no instability in Qs. It has previously been shown that a series capacitor $C_s \leq \frac{-1}{\alpha_0 y_{FE}}$ stabilizes the ferroelectric for all values of Q as shown in Fig. 5.6 a [19] (α_0 is the material constant of the ferroelectric and y_{FE} is the thickness, see chapter 2 also). Fundamentally, stabilization of the ferroelectric in inherently unstable regime ($Q'_{c2} \leq Q \leq Q'_{c1}$) comes from an inherent negative feedback provided by the series capacitor. Similar to an SG-FET, in the unstable regime, the voltage drop across the ferroelectric (V_{FE}) decreases (Fig. 5.6 b). This decrease in V_{FE} amplifies the change in surface potential (Fig. 5.6 b). Like SG-FET, the value m in FE-FET can be analytically given by-

$$m \equiv \frac{dV_G}{d\psi_s} = 1 + \frac{C_s}{C_{FE}}, \tag{5.5}$$

where C_{FE} is the capacitance of the ferroelectric (Eq. 2.29 and Fig. 5.6 e). As expected, ferroelectric effectively acts like a negative capacitor ($C_{FE} < 0$, when $Q'_{c2} \leq$

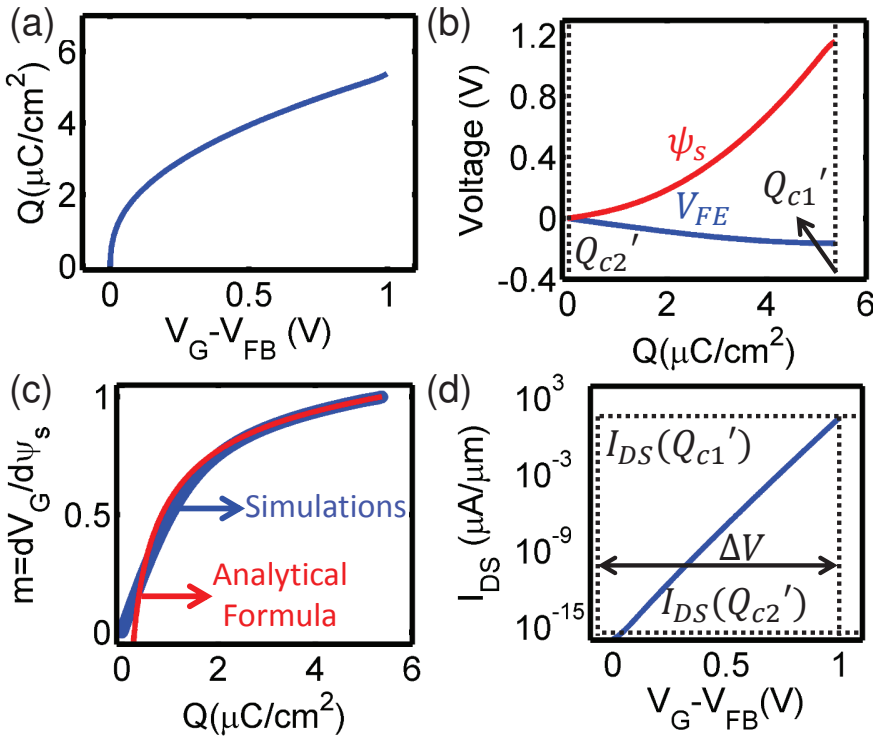

Fig. 5.6. Hysteresis-free sub-$60mV/dec$ switching in an n-channel FE-FET. (a) $Q - V_G$ characteristics for hysteresis-free smooth switching. (b) Voltage-drop across ferroelectric (V_{FE}) and series capacitor (ψ_s) showing the voltage amplification in ψ_s in the unstable regime($Q'_{c1} \leq Q \leq Q'_{c2}$). (c) Body factor m which is less than one in the unstable regime of FE-FET. Symbols denote the numerical simulations and solid line Eq. 5.5. (d) Corresponding $I_{DS} - V_G$ characteristics with an effective sub-threshold swing of $52mV/decade$ reflecting the voltage amplification provided by the negative capacitor. The parameters used in the simulations are simulations are same as the one used in Fig. 5.3 except $N_A = 7.5 \times 10^{19} cm^{-3}$.

$Q \leq Q'_{c1}$) in the unstable regime and provides the necessary voltage amplification to lower m below one (Fig. 5.6 c). Equation 5.5 matches the numerical simulations result very well. The corresponding $I_{DS} - V_G$ characteristics is shown in Fig. 5.6 d, which confirms the hysteresis-free smooth switching. The effective sub-threshold swing in the unstable regime is $S = \Delta V / \log_{10}(I_{DS}(Q = Q'_{c1})/I_{DS}(Q = Q'_{c2}))$ is $52mV/decade$ confirming the voltage amplification provided by the negative capacitor.

To summarize, we saw that Landau switches (SG-FET or FE-FET) typically exhibit hysteretic $I_{DS} - V_G$ characteristics. However, if C_s is properly chosen so that negative capacitance gate insulator is stabilized throughout the negative capacitance regime, Landau switches exhibit hysteresis-free sub-$60mV/decade$ switching characteristics. The question: "Can the sub-threshold swing be lowered all the way to $0mV/decade$ by any combination of C_s or C_{ins}?" is explored in the next section.

5.3 Minimum Sub-threshold Swing in Negative Capacitance FETs

In the last section, we showed that stabilization of the gate insulator in the unstable regime gives rise to hysteresis-free sub-$60mV/decade$ switching characteristics in NC-FET. And, it is now well accepted in the literature that NC-FETs can lower S [103–105] , but given a specific device architecture, the question whether there is a lower limit of S (and if so, the conditions that define the limit) have not been answered. Without this limit, one cannot ascertain the technological relevance of NC-FETs. Therefore, in this section, we:

- demonstrate that the fundamental constraints related to the stability and hysteresis-free operation dictate that there is a lower limit of S associated with each NC-FET technology,
- provide a general algorithm to calculate the minimum sub-threshold swing (S_{min}), and
- illustrate the concept using SG-FET and FE-FET for two channel configurations namely a partially depleted bulk FET and a FET with constant channel capacitance.

The lower limit reflects the fact that the choice of C_s is fundamentally dictated by the need to stabilize the gate insulator in the negative capacitance regime.

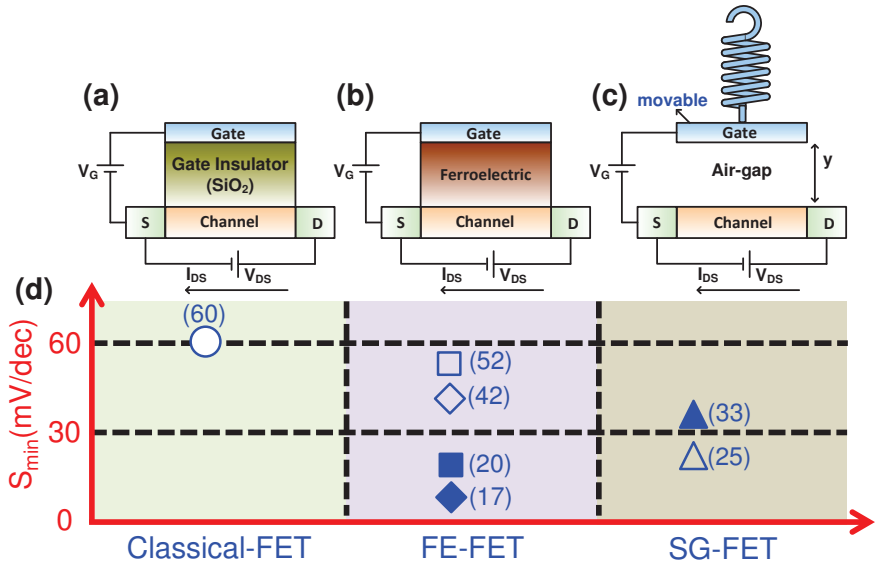

Fig. 5.7. Summary of various field effect transistors, namely (a) classical FET with traditional gate insulator such as SiO_2, (b) FE-FET with a ferroelectric material as the gate insulator, (c) SG-FET which has an air-gap as the gate insulator, and (d) corresponding minimum achievable sub-threshold swing: classical-FET ($\circ$), FE-FET with $BaTiO_3$ ($\diamond$), PZT ($PbZr_{1-x}Ti_xO_3$) with $x = 0$ and SBT ($Sr_{0.8}Bi_{2.2}Ta_2O_9$) ($\square$) as ferroelectric material, and SG-FET ($\triangle$). Open symbols denote bulk FETs with constant channel doping and solid symbols denote FETs with constant channel capacitance. For classical FETs, the value is same for both cases. For FE-FET, S_{min} depends on the material property of ferroelectric; whereas for SG-FET, it is material independent.

5.3.1 Stability Constraints Dictate Minimum S

We have seen that gate insulators in both FE-FET and SG-FET exhibit negative $C_{ins}(Q)$ (with $C_{ins} = C_{FE}$ in FE-FET and $C_{ins} = C_{air}$ in SG-FET) in the unstable regime. Hysteresis-free smooth switching requires stabilization of C_{ins} in the negative capacitance regime by proper choice of C_s. It means that the overall gate capacitance, $C_G(Q)^{-1} = C_s(Q)^{-1} + C_{ins}(Q)^{-1}$ (Fig. 5.8 a) must still be positive at all charges for hysteresis-free stable operation [19, 106, 107]. This stability requirement places a fundamental constraint on $C_s(Q)$ i.e.,

$$C_s(Q)^{-1} \geq -C_{ins}(Q)^{-1}, \tag{5.6}$$

which should hold throughout the negative capacitance regime. Equation 5.6 is the key equation that distinguishes a classical FET from an NC-FET and has been discussed by many researchers in context of FE-FETs [105, 108]. Equations 5.1-5.2 & 5.6 suggest that an obvious choice of $C_s(Q) = -C_{ins}(Q)$ will make $S = 0$. However, as we will see, in FE-FET or SG-FET, $C_s(Q)$ cannot be made equal to $C_{ins}(Q)$ at all charges due to their different functional dependencies on Q, which in turn places a lower limit on S.

For a given dependence of $C_{ins}(Q)$ and $C_s(Q)$ on Q, sub-threshold swing is minimized when $C_s(Q)$ and $-C_{ins}(Q)$ are matched as closely as possible (Eqs. 5.1-5.2 & 5.6). The exact value of the minimum sub-threshold swing depends on the choice of $C_s(Q)$ and $C_{ins}(Q)$. For example, $C_s(Q)$ is defined by the specific FET technology, e.g., single gate vs. multi-gate FET or partially depleted vs. fully depleted. Similarly, $C_{ins}(Q)$ depends on the particular design (or details) of negative capacitance gate insulators e.g., ferroelectric in FE-FET vs. air-gap in SG-FET or single crystalline ferroelectric vs. polycrystalline ferroelectric. However, the critical point is, for a given choice of $C_s(Q)$ and $C_{ins}(Q)$, there is always a minimum sub-threshold swing that characterizes the NC-FET. Below, as an illustrative example, we calculate the minimum sub-threshold swing for SG-FET and FE-FET with a partially depleted channel with constant doping and FETs with constant channel capacitance.

To understand the specific lower limit of S for an NC-FET, it is essential to understand $C_{ins}(Q) - Q$ and $C_s(Q) - Q$ characteristics. As discussed in chapter 2 and in previous secion, for any NC gate insulator, there are two regimes of operation defined by its: (i) positive ($C_{ins}(Q) > 0$) and (ii) negative ($C_{ins}(Q) < 0$) capacitance (solid line in Fig. 5.8 b). These regimes are separated by a boundary which occurs at $Q = Q_{c1}$ such that $C_{ins}(Q_{c1}) = \infty$ (infinite insulator capacitance, see Figs. 2.4 & 2.9). Note that, NC regime thus extends from $Q = Q_{c1}$ to $Q = Q_{c2}$ where Q_{c2} is

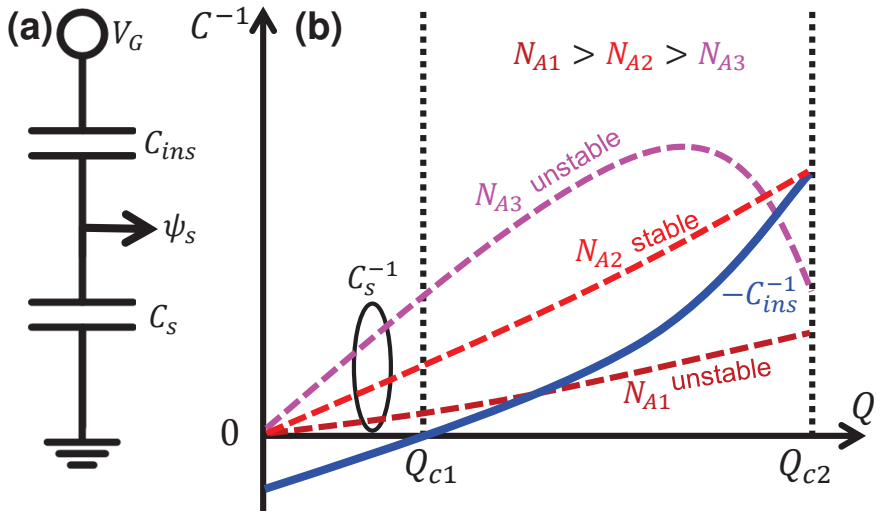

Fig. 5.8. Physics of minimum sub-threshold swing in NC-FETs. (a) Equivalent capacitor divider model of a FET. Value of C_s must be chosen such that Eq. 5.6 is satisfied at all charges. (b) Illustrating generic $C_{ins}(Q) - Q$ (solid line) and $C_s(Q) - Q$ (dotted lines for three channel doping) characteristics in an NC-FET. Value of N_A (N_{A2} in this illustrative example) for which $C_s(Q)$ and $-C_{ins}(Q)$ match closely, S is minimized.

defined by a physical constraint associated with a specific system. Regarding $C_s(Q)$, note that: (i) $C_s(Q)$ depends on the channel doping N_A, (ii) $C_s(Q)$ depends whether channel is in sub-threshold ($C_s(Q) \propto N_A/Q$) or in inversion ($C_s(Q) \propto Q$) and (iii) value of $C_s(Q)$ is large in inversion than in sub-threshold [94].

To illustrate the point that sub-threshold swing is minimized for close matching between $C_s(Q)$ and $-C_{ins}(Q)$, let us plot $C_s(Q)$ in Fig. 5.7 b for three different values of N_A such that: (i) for N_{A1}, $C_s(Q)$ exceeds $-C_{ins}(Q)$ even in sub-threshold regime and therefore the gate insulator becomes unstable, (ii) for N_{A3}, channel gets inverted (reflected in the downward transition of magenta curve) so that $C_s(Q)$ exceeds $-C_{ins}(Q)$ and gate insulator becomes unstable once again, (iii) for N_{A2}, channel remains in sub-threshold throughout the NC regime, and $C_s(Q)$ and $-C_{ins}(Q)$ are matched as close as possible for the given dependencies of $C_s(Q)$ and $C_{ins}(Q)$; which

results in minimum S. Therefore, for monotonic $C_s(Q)^{-1}$ and $-C_{ins}(Q)^{-1}$, the necessary condition for minimum sub-threshold swing is that: (i)

$$C_s(Q = Q_{c2}) = -C_{ins}(Q = Q_{c2}), \tag{5.7}$$

and (ii) channel should be in sub-threshold throughout the NC regime. The condition of channel being in sub-threshold is mathematically equivalent to $\psi_s < 2\psi_B = 2k_BT/q \log(N_A/n_i)$ (n_i = intrinsic carrier concentration) throughout NC regime, which simplifies to $\psi_s(max(|Q_{c1}|, |Q_{c2}|)) = l\psi_B$ with $l < 2$. For a partially depleted FET with constant channel doping, ψ_s is related to Q by depletion charge i.e., $\psi_s = Q^2/(2q\epsilon_0\epsilon_s N_A)$ [94], the condition thus translates to-

$$l\psi_B = \frac{(max(|Q_{c1}|, |Q_{c2}|))^2}{2q\epsilon_0\epsilon_s N_A}, \tag{5.8}$$

where ϵ_0 is the permittivity of free space and ϵ_s is the dielectric constant of the channel material. In Figure 5.8 b, N_{A2} satisfies both the conditions (Eqs. 5.7 - 5.9) and exhibits minimum sub-threshold swing. The corresponding value of minimum sub-threshold swing (S_{min}) can be obtained from Eqs. 5.1 - 5.2 with $Q_1 = Q_{C1}$ & $Q_2 = Q_{c2}$, and is given by-

$$S_{min} = \frac{2.3k_BT}{q}\left(1 + \frac{V_{ins}(Q_{c2}) - V_{ins}(Q_{c1})}{\psi_s(Q_{c2}) - \psi_s(Q_{c1})}\right) \tag{5.9}$$

Here, $V_{ins}(Q)$ is the voltage drop across gate insulator such that $V_G = V_{ins}(Q) + \psi_s(Q)$ and $C_{ins}(Q) = dQ/dV_{ins}$. Note that, S_{min} defined by Eq. 5.9 corresponds to the maximum current modulation in NC regime. We emphasize that the approach to determine S_{min} (Eq. 5.9) and stability condition (Eq. 5.8) are very general and will work irrespective of the choice of C_s and C_{ins}. However, Eq. 5.8 is valid only for a partially depleted FET with constant channel doping. Equation 5.8 (and therefore

Quantity	SG-FET	FE-FET
Q_{c1}	$\sqrt{\frac{2\epsilon_0 k y_0}{3WL}}$	$5\gamma_0 Q_{c1}^4 + 3\beta_0 Q_{c1}^2 + \alpha_0 = 0$
Q_{c2}	$\sqrt{\frac{2\epsilon_0 k y_0}{WL}}$	0
$V_{ins}(Q_{c1})$	$\sqrt{\frac{8k y_0^3}{27\epsilon_0 WL}}$	$y_{FE}\left(\alpha_0 Q_{c1} + \beta_0 Q_{c1}^3 + \gamma_0 Q_{c1}^5\right)$
$V_{ins}(Q_{c2})$	0	0
$\psi_s(Q_{c1})$	$l\psi_B/3$	$l\psi_B$
$\psi_s(Q_{c2})$	$l\psi_B$	0

Table 5.1
Various quantities that determine the value of S_{min} in SG-FET and FE-FET. Note that, Q_{c1} & Q_{c2} for FE-FET are same as Q'_{c1} & Q'_{c2}. Values of V_{ins} are relevant both for partially depleted FET and FET with constant channel capacitance; whereas values of ψ_s are relevant only for partially depleted FETs.

minimum S) will change as we change the FET structure (e.g., single gate vs. multi gate [109] [17] or bulk FET vs. fully depleted FET). Below, we will discuss two specific examples to illustrate how the charges Q_{c1} and Q_{c2} are obtained for FE-FET and SG-FET, respectively, and explain how these charges dictate S_{min} (see Table 5.1).

5.3.2 Minimum S in Partially Depleted SG-FET

In order to evaluate the minimum sub-threshold swing in SG-FET, we recall that V_{air} and C_{air} that are obtained from Eq. 2.20, are given by-

$$V_{air} = \alpha_0^{'} Q + \beta_0^{'} Q^3, C_{air}^{-1} \equiv \frac{dV_{air}}{dQ} = \alpha_0^{'} + 3\beta_0^{'} Q^2, \tag{5.10}$$

where $\alpha_0^{'} = y_0/\epsilon_0$ and $\beta_0^{'} = -WL/(2\epsilon_0^2 k)$ are material and geometrical constants (Eq. 2.21). To recall, $V_{air} - Q$ and $C_{air}(Q) - Q$ characteristics consist of positive ($C_{air}(Q) > 0$) and negative ($C_{air}(Q) < 0$) capacitance regimes (Figs. 5.9 a-b). This negative capacitance behavior has been previously verified experimentally in electrostatic actuators using charge-based actuation [59]. The two regimes are separated by a boundary which occurs at $Q = Q_{c1}$ or (physically at $y = 2y_0/3$) such that $dV_{air}/dQ = 0$ i.e., $Q_{c1} = \pm\sqrt{\frac{2\epsilon_0 k y_0}{3WL}}$ (Eq. 2.22). $Q_{c2} = \pm\sqrt{\frac{2\epsilon_0 k y_0}{WL}}$ corresponds to the physical boundary at $y = 0$ (Eq. 2.22). As discussed in chapter 2, the NC region in SG-FET is limited to $0 < y < 2y_0/3$ which corresponds to $Q_{c1} < Q < Q_{c2}$ for an n-channel SG-FET.

Using the value of C_{air} and Q_{c2}, Eq. 5.7 for SG-FET reduces to $C_s(Q_{c2}) = -C_{air}(Q_{c2}) = \epsilon_0/2y_0$. Realizing that $C_s = \sqrt{\frac{q\epsilon_0\epsilon_s N_A}{2\psi_s}}$ is the depletion capacitance and $\psi_s(Q_{c2}) = l\psi_B$ as $Q_{c2} = max(|Q_{c1}|, |Q_{c2}|)$ (from the derivation of Eq. 5.8), Eq. 5.7 is further simplified to-

$$\frac{y_0^2 N_A}{\psi_B} = \frac{l\epsilon_0}{2q\epsilon_s} \tag{5.11}$$

Similarly, Eq. 5.8 of channel being in sub-threshold reduces to

$$\frac{y_0}{N_A \psi_B} = \frac{lq\epsilon_s WL}{k}. \tag{5.12}$$

Equations 5.11-5.12 relate N_A and y_0 (corresponding to minimum S) for a given value of k and their explicit values are given by-

$$N_A = \left(\frac{\epsilon_0 k^2}{2lq^3\epsilon_s^3 W^2 L^2 \psi_B}\right)^{\frac{1}{3}}, y_0 = \left(\frac{l^2\epsilon_0 WL\psi_B^2}{2k}\right)^{\frac{1}{3}}, \tag{5.13}$$

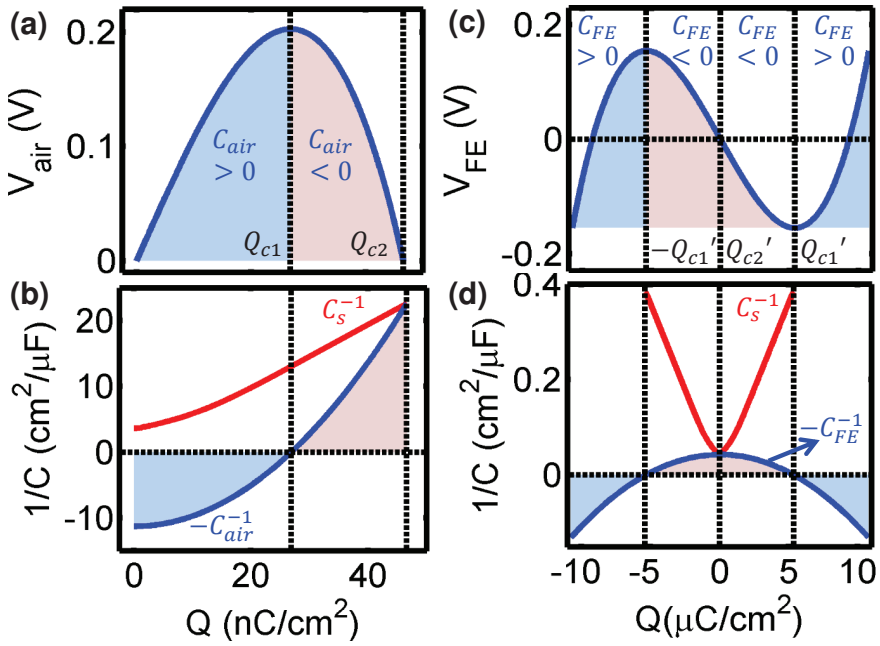

Fig. 5.9. Voltage drop and capacitance characteristics of gate insulators in SG-FET and FE-FET. (a) voltage drop across air-gap (V_{air}), (b) air-gap capacitance (C_{air}), and channel depletion capacitance (C_s) as a function of the gate charge (Q) in SG-FET. (c) Similarly, voltage drop across the ferroelectric (V_{FE}), (d) ferroelectric capacitance (C_{FE}), and channel depletion capacitance (C_s) as a function of the gate charge (Q) in FE-FET. $Q > 0$ behavior corresponds to an n-channel whereas $Q < 0$ corresponds to a p-channel FE-FET. Here, value of N_A is such that $C_s(Q)$ and $-C_{ins}(Q)$ match closely in NC regime giving rise to minimum sub-threshold swing.

The corresponding value of minimum sub-threshold swing can thus be obtained from Eq. 5.9 with other parameters in Table 5.1-

$$S_{min}^{SGFET} = \frac{2.3k_BT}{q}\left(1 - \frac{1}{\sqrt{3}}\right) \tag{5.14}$$

which is independent of any material or geometrical parameters of SG-FET and is $25mV/decade$ at room temperature (Fig. 5.7 d). Note that, while deriving Eq. 5.14, we have neglected various non-ideal effects such as strain gradients in the suspended

beam [110,111], stiction of the gate to the substrate [112,113], which may be present in a realistic SG-FET. These non-ideal effects would make the sub-threshold swing material dependent. For an idealized switch, however, the sub-threshold swing is material independent and is given by Eq. 5.14. Moreover, the value of minimum sub-threshold swing ($25mV/decade$) should not be confused or compared with the ultra-low values of sub-threshold swing (close to $0mV/decade$) achieved during pull-in and pull-out phase of a SG-FET (Fig. 5.3 c) [21,114] due to the following reasons: these low sub-threshold swings arise due to the inherent instability when C_s is not sufficient to stabilize the gate throughout the negative capacitance regime and therefore, such abrupt transitions are always associated with an intrinsic hysteresis (Fig. 5.3 c). In contrast, $S_{min} = 25mV/decade$ corresponds to the effective sub-threshold swing which arises when C_s is sufficient to stabilize the gate throughout the negative capacitance regime resulting in hysteresis-free sub-$60mV/decade$ switching characteristics. Our analysis should also not be confused with the sharp switching characteristics of NEMS relays [20] which have structure similar to an SG-FET, but involves metal-to-metal contact for current conduction.

Based on the values of N_A and y_0 obtained for an SG-FET with parameters shown in the caption of Fig. 5.10, C_s is shown in Fig. 5.9 b suggesting $C_s(Q)^{-1} \geq -C_{air}(Q)^{-1}$ at each Q. The corresponding V_{air} and ψ_s obtained from numerical simulations are shown in Fig. 5.10 a. As expected, V_{air} decreases with the increase in Q and amplifies ψ_s making $m < 1$ and $S < 60mV/decacde$. Figures 5.9 b & 5.10 a confirm the design rules used for deriving the Eqs. 5.12 - 5.13 i.e., (i) $C_s(Q_{c2}) = -C_{air}(Q_{c2})$ and (ii) $\psi_s(Q_{c2}) = 0.5523V < 2\psi_B = 0.7310V$. The value of S_{min}^{SGFET} is $25mV/decade$ and is consistent with the analytical formula of Eq. 5.14.

5.3.3 Minimum S in Partially Depleted FE-FET

To determine the critical charges $Q_{c1}^{'}$, $Q_{c2}^{'}$ and thus S_{min} for FE-FET, recall from chapter 2 and Eqs. 2.27 & 2.29 that V_{FE} and C_{FE} are given by-

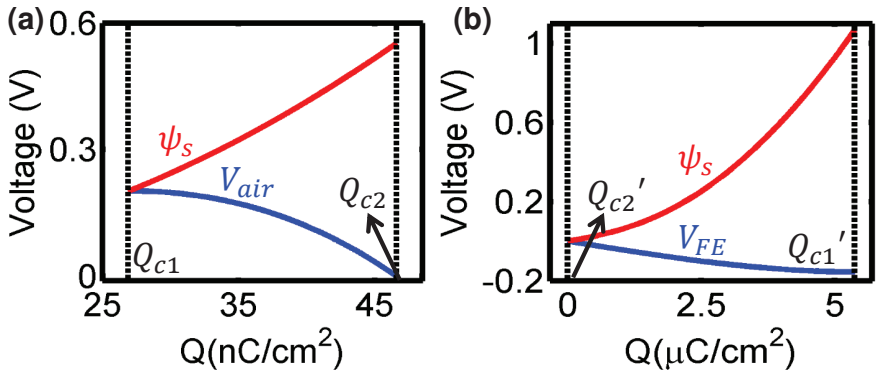

Fig. 5.10. Minimum achievable sub-threshold swing in NC-FETs. (a) V_{air} and ψ_s as a function of gate charge Q for the values of $N_A = 1.2\times 10^{16}cm^{-3}$ and $y_0 = 10nm$ obtained from Eq. 5.13 for $k = 0.45N/m$ and $A = 4\mu m\times 0.1\mu m$. (b) V_{FE} and ψ_s as a function of the gate charge Q for the values of $N_A = 7.5\times 10^{19}cm^{-3}$ and $y_{FE} = 35.2nm$ obtained from Eq. 5.18 for SBT ($Sr_{0.8}Bi_{2.2}Ta_2O_9$) used as the ferroelectric material (taken from ref. [42]).

$$\frac{V_{FE}}{y_{FE}} = \alpha_0 Q + \beta_0 Q^3 + \gamma_0 Q^5, C_{FE}^{-1} \equiv \frac{dV_{FE}}{dQ} = y_{FE}\left(\alpha_0 + 3\beta_0 Q^2 + 5\gamma_0 Q^4\right), \quad (5.15)$$

where α_0, β_0, γ_0 are the material constants and y_{FE} is the thickness of the ferroelectric gate insulator. Figures 5.9 c-d show again V_{FE} and C_{FE}, respectively as a function of Q for typical parameters of a ferroelectric with $\alpha_0 < 0$, $\beta_0 > 0$, & $\gamma_0 = 0$. As discussed previously, $C_{FE}(Q)-Q$ characteristics consist of two regimes corresponding to positive ($C_{FE}(Q) > 0$) and negative ($C_{FE}(Q) < 0$) capacitance (Figs. 5.9 c-d). The boundary between the two occurs at $Q = Q_{c1}^{'}$ such that $C_{FE}^{-1} = 0$ i.e., $\alpha_0 + 3\beta_0 Q_{c1}'^2 + 5\gamma_0 Q_{c1}'^4 = 0$. Thus, V_{FE} decreases and C_{FE} is negative for $-Q_{c1}' < Q < Q_{c1}'$ (Fig. 2.9). However, an n-channel FE-FET must be operated in the $Q > 0$ branch of the NC regime, so that it can be balanced by the negative charges of the channel. Operation of an n-channel FE-FET for $Q > 0$ thus defines $Q_{c2}' = 0$ (other boundary of the NC regime).

Based on the value of C_{FE} and $Q_{c2} = 0$, Eq. 5.7 reduces to $C_s(Q = Q_{c2}' = 0) = -1/\alpha_0 y_{FE}$. As $C_s(Q)$ is a variable capacitance with $C_s(Q = 0) = \sqrt{q\epsilon_0\epsilon_s N_A/\phi_t}$ (flat

band capacitance of a FET [94]) with $\phi_t = k_B T/q$, the condition (Eq. 5.7 further simplifies to

$$y_{FE}^2 N_A = \frac{\phi_t}{q\epsilon_0\epsilon_s\alpha_0^2}, \tag{5.16}$$

which relates N_A, y_{FE}, and α_0. Similarly, knowing that $Q'_{c1} = (max(|Q'_{c1}|, |Q'_{c2}|)$, Eq. 5.9 of channel being in sub-threshold reduces to-

$$l\psi_B = \frac{Q'^2_{c1}}{2q\epsilon_0\epsilon_s N_A}. \tag{5.17}$$

Equations 5.16-5.17 are similar to Eqs. 5.11 - 5.12 for SG-FET and relate N_A and y_{FE} with the material constants α_0, β_0, and γ_0 of a ferroelectric material. Using Equations 5.16-5.17, values of N_A and y_{FE} can be simply expressed as-

$$N_A = \frac{Q'^2_{c1}}{2lq\epsilon_0\epsilon_s\psi_B}, y_{FE} = \sqrt{\frac{2l\psi_B\phi_t}{Q'^2_{c1}\alpha_0^2}}. \tag{5.18}$$

The value of sub-threshold swing is minimized for N_A and y_{FE} given by Eq. 5.18. The corresponding value of minimum sub-threshold swing obtained from Eq. 5.9 and other parameters in Table 5.1 is given by -

$$S_{min}^{FEFET} \approx \frac{2.3k_BT}{q}\left(1 + \frac{M}{y_{FE}}\right), \tag{5.19}$$

where $M = 2\phi_t\left(\alpha_0 Q'_{c1} + \beta_0 Q'^3_{c1} + \gamma_0 Q'^5_{c1}\right)/\left(\alpha_0^2 Q'^2_{c1}\right)$ is a material dependent constant. The y_{FE} in Eq. 5.19 is not arbitrary, but can be related to other constants described by Eq. 5.18. S_{min}^{FEFET} is $42mV/decade$ for $BaTiO_3$ and $S_{min}^{FEFET} \approx 52mV/decade$ for PZT ($PbZr_{1-x}Ti_xO_3$, $x = 0$) (see Table 5.2 for various parameters of ferroelectric material) (Fig. 5.8 d).

Based on the values of N_A and y_{FE} obtained for SBT ($Sr_{0.8}Bi_{2.2}Ta_2O_9$), C_s is shown in Fig. 5.9 d suggesting $C_s(Q)^{-1} \geq -C_{FE}(Q)^{-1}$ at each Q. The corresponding V_{FE} and ψ_s obtained from numerical simulations of an ideal MOS capacitor type structure are shown in Fig. 5.10 b. With the increase in Q, V_{FE} decreases and that in turn amplifies ψ_s making $m < 1$ and $S < 60mV/decade$. Figures 5.9 d & 5.10 b confirm the design rules used for deriving the Eqs. 5.18 - 5.19 i.e., (i) $C_s(0) = -C_{FE}(0)$ and (ii) $\psi_s(Q'_{c1}) = 1.0664V < 2\psi_B = 1.1893V$. The value of S_{min}^{FEFET} is $52mV/decade$ and is consistent with the analytical formula of Eq. 5.19 (Fig. 5.7 d).

Note that, while deriving Eq. 5.19, we have considered a one dimensional single crystalline model of the ferroelectric which is the most common model used in the literature [19,105,109,115] for negative capacitance FE-FET. As the non-ideal effects of a realistic ferroelectric such as domain nucleation, domain propagation, grains, and grain boundaries degrade the sub-threshold swing of a realistic device [116], the minimum sub-threshold swing for a given ferroelectric material is achieved when these non-idealities are absent and is estimated using Eq. 5.19.

Discussion on S_{min}

It is important to emphasize that while the physics of minimum sub-threshold swing discussed in previous sections is completely general, the value of S_{min} is fundamentally governed by the particular choice of $C_{ins}(Q)$ and $C_s(Q)$. Unlike $S_{min} = 60mV/decade$ for classical-FETs, a single S_{min} does not define the performance of all NC-FETs; instead, the stability-constrained S_{min} depends on the choice of material system and channel type. To illustrate how the value of S_{min} can change with a different channel configuration, we consider FET architectures with constant $C_S(Q)$ below. This example will be directly relevant for fully depleted FETs.

Parameters	$BaTiO_3$ [19]	PZT [42]	SBT [42]
$\alpha_0(m/F)$	-10^7	-4.5×10^7	-6.5×10^7
$\beta_0(m^5F/C^2)$	-8.9×10^8	5.2×10^8	3.75×10^9
$\gamma_0(m^9F/C^4)$	4.5×10^{10}	5.9×10^8	0
$N_A(cm^{-3})$	2.3×10^{20}	3.3×10^{20}	7.5×10^{19}
$y_{FE}(nm)$	129	23.7	35.2

Table 5.2
Various parameters of ferroelectric material used for the simulations.

5.3.4 Minimum S in Fully Depleted SG-FET

For an SG-FET with constant channel capacitance C_S, Eq. 5.7 dictates that the value of constant C_s should be-

$$C_s = -C_{air}(Q_{c2}) = \frac{\epsilon_0}{2y_0} \tag{5.20}$$

Now, using Eq. 5.9 and $\psi_s = Q/C_s$ for a constant C_s, one can show that (See Table 1 for other values)-

$$S_{min}^{SGFET} = \frac{2.3k_BT}{q}\frac{3\sqrt{3}-4}{3\sqrt{3}-3}, \tag{5.21}$$

which suggests that the value of S_{min} for constant C_s is $33mV/decade$ (Fig. 5.7 d).

Interestingly, value of S_{min} for partially depleted FET is lower than that of FET with constant C_s due to better matching between $C_s(Q)$ and $-C_{air}(Q)$.

5.3.5 Minimum S in Fully Depleted FE-FET

For FE-FET with constant C_s, Eq. 5.7 suggests that the constant value of the capacitance C_s should be-

$$C_s = -C_{FE}(Q'_{c2} = 0) = -\frac{1}{\alpha_0 y_{FE}}. \tag{5.22}$$

Now, using Eq. 5.9 and $\psi_s = Q/C_s$ for a constant C_s, one can show that(See Table 1 for other values)-

$$S_{min}^{FEFET} = \frac{2.3k_BT}{q}\left(-\frac{\beta_0 Q'^2_{c1} + \gamma_0 Q'^4_{c1}}{\alpha_0}\right). \tag{5.23}$$

As shown in Fig. 5.7 d, S_{min} for constant C_s is lower than partially depleted FE-FET due to improved matching between $C_s(Q)$ and $C_{FE}(Q)$. Note that, Eq. 5.22 is only valid for ferroelectrics with $\alpha_0 < 0$ and $\beta_0, \gamma_0 > 0$. For ferroelectrics with $\alpha_0, \beta_0 < 0$ & $\gamma_0 > 0$, Eq. 5.7 will not apply as $C_{FE}(Q)^{-1}$ will not be monotonic. In such case, the value of the constant series capacitance for hysteresis-free operation should be equal to-

$$C_s = \frac{1}{\left(-\alpha_0 + \frac{9\beta_0^2}{20\gamma_0}\right) y_{FE}} \tag{5.24}$$

where C_s^{-1} in Eq. 5.24 is equal to the maximum value of $-C_{FE}(Q)^{-1}$. Now, the value of the minimum sub-threshold swing is given by-

$$S_{min}^{FEFET} = \frac{2.3k_BT}{q}\left(1 + \frac{\alpha_0 + \beta_0 Q'^2_{c1} + \gamma_0 Q'^4_{c1}}{-\alpha_0 + \frac{9\beta_0^2}{20\gamma_0}}\right). \tag{5.25}$$

The value of S_{min} for $BaTiO_3$ for constant C_s is $17mV/decade$ (Fig. 5.7 d) which is lowest of all the ferroelectric materials considered. Interestingly, in case of partially depleted FE-FETs, due to the opposite voltage dependence of $C_s(Q)^{-1}$ and $-C_{FE}(Q)^{-1}$, Eq. 5.19 describes the S_{min} for both the above mentioned cases for ferroelectrics.

Summary of S_{min}

We have established that the sub-threshold swing cannot be arbitrarily lowered in negative capacitance field effect transistors. There is a fundamental lower limit of S associated with each NC-FET. The analysis also highlights that the value of S_{min} for FE-FET or SG-FET can further be reduced by properly optimizing $C_s(Q)$ and $-C_{ins}(Q)$ so that the matching between the two improves. In the next section, we will address the question: "can we achieve sub-threshold swing of $0mV/decade$ using any combination of C_S and C_{ins}?"

5.4 Proposal of a Hysteresis-free Zero Sub-threshold Swing FET (ZSub-FET)

Before we begin, let us remind that our ultimate goal is to find the ideal switch with $S_{ideal} = 0mV/decade$ switching characteristics. We have seen that the classical Boltzmann switch is far from ideal due to thermodynamically limited sub-threshold swing $S \geq S_{BZ} = 60mV/decade$ (Figs. 5.11 a-b). We also saw that sub-threshold swing in NC-FETs with a single NC gate insulator S cannot be reduced arbitrarily (Figs. 5.11 c-d). In this section, we focus on FETs in which gate insulator is a series combination of two different types of NC gate insulators (Fig. 5.11 e). The two NC gate insulators (NC1 & NC2 in Fig. 5.11 e) are chosen such that the capacitance of the series combination is negative and constant (i.e., voltage independent). This constant negative capacitance of the gate insulator is matched by a constant channel

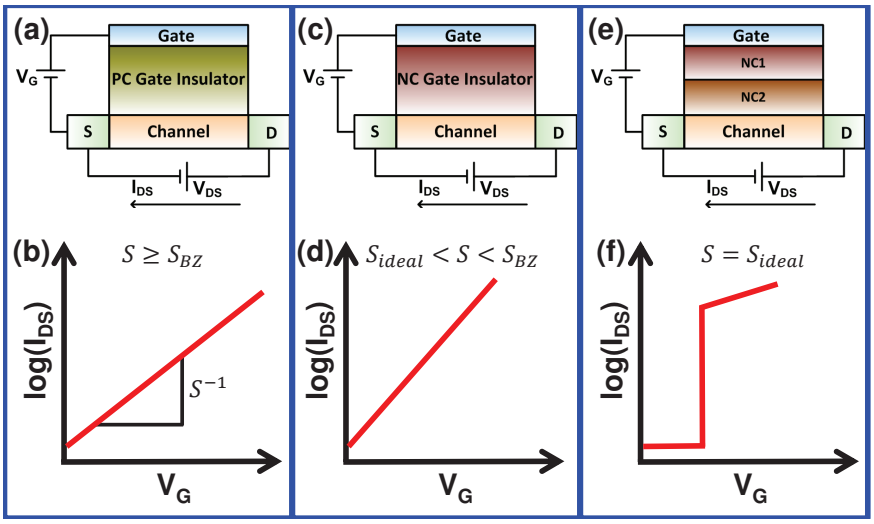

Fig. 5.11. In search of an ideal switch with hysteresis-free $S_{ideal} = 0mV/decade$ switching characteristics. (a)-(b) Classical FET with a positive capacitance (PC) gate insulator exhibits $S \geq S_{BZ}$. (c)-(d) A FET with negative capacitance (NC) gate insulator e.g., FE-FET and SG-FET can exhibit $S < S_{BZ}$. (e)-(f) Proposed ZSubFET architecture with gate insulator as a series combination of two different types of NC gate insulators, namely, NC1 & NC2, can achieve ideal switching characteristics.

capacitance to achieve ideal switching (Fig. 5.11 f). We will show the following in this section:

- The sub-threshold swing in an NC-FET with a single NC gate insulator cannot be reduced all the way to $0mV/decade$.
- We propose a novel device concept namely a ZSubFET that achieves hysteresis-free $0mV/decade$ switching. We illustrate the concept by a suspended-gate ferroelectric FET in which ferroelectric behaves as one NC and air-gap as the another.

5.4.1 Series Combination of Negative Capacitance Gate Insulators

We recall that sub-threshold swing in an NC-FET is governed by Eqs. 5.1 - 5.2 & 5.6, which suggest that the value of S depends on the matching between $C_s(Q)^{-1}$ and $-C_{ins}(Q)^{-1}$ (Fig. 5.12 a). As shown in Fig. 5.12 b, closer matching between the two, decreases S. One can therefore expect that an obvious choice of $C_s(Q) = -C_{ins}(Q)$ should make $S = S_{ideal} = 0mV/decade$.

However, S cannot be lowered all the way to S_{ideal}, because none of the known negative capacitors allows point-by-point matching of $C_s(Q)$ with $-C_{ins}(Q)$. Even if $C_s(Q)$ and $-C_{ins}(Q)$ are matched at almost all values of Q, they cant be matched at $Q = Q_{c1}$ due to the fact that $C_{ins}(Q_{c1}) = \infty$ (open circle in Fig. 5.12 b at $Q = Q_{c1}$). Therefore, a single NC gate insulator can never exhibit ideal switching [107, 117]. Moreover, we just saw that this matching argument is responsible for fundamental lower limit of subthreshold swing ($0 < S_{min} < 60$) for a given $C_{ins}(Q)$ (determined by the type of NC gate insulator) and $C_s(Q)$ (determined by the type of channel configuration) [117]. For example, S_{min} is $25mV/decade$ for a bulk SG-FET and $33mV/decade$ for a SG-FET with constant channel capacitance (relevant for modern fully depleted FET architectures). On the other hand, the corresponding limits for FE-FET with SBT ($Sr_{0.8}Bi_{2.2}Ta_2O_9$) as the ferroelectric material are $52mV/decade$ and $20mV/decade$, respectively (Fig. 5.7 d). Therefore, unless the point of infinite capacitance of NC is removed, ideal switching cannot be achieved.

We show below that a series combination of NCs, in which (i) infinite capacitance of individuals NCs occurs at different values of charge and (ii) they have opposite capacitance-charge characteristics (one increasing and other decreasing), can lead to an ideal switching characteristics (Figs. 5.12 c-d). In a series combination of two capacitors (say NC1 and NC2 in Figs. 5.11 e & 5.12 c), if one of the capacitance is infinite, the total capacitance will be equal to the other finite capacitance i.e., $C_{ins}^{-1} = C_{NC1}^{-1} + C_{NC2}^{-1} = C_{NC1}^{-1}$, provided $C_{NC2} = \infty$. Therefore, NC gate insulators such that (i) $C_{NC1} = \infty$ with $C_{NC2} < 0$ or vice versa (see open circles, squares, arrows

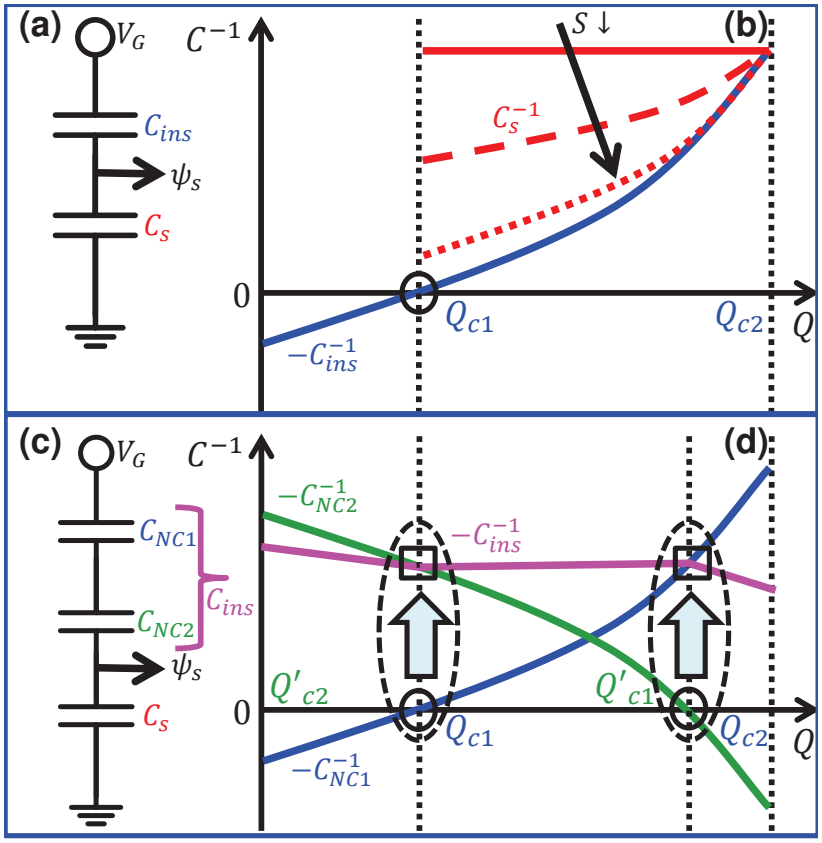

Fig. 5.12. (a) Equivalent capacitive divider model of a FET and (b) capacitance-charge characteristics for an NC-FET. Insulator capacitance being infinity at $Q = Q_{c1}$ makes perfect matching of $C_s(Q)$ and $-C_{ins}(Q)$ impossible. (c) Capacitive divider model of a FET with the gate insulator as a series combination of two different types of gate insulators (NC1 & NC2 in Fig. 5.11 e) and (d) capacitance-charge characteristics for the same NC-FET. NC1 and NC2 are chosen such that overall gate capacitance $C_{ins}^{-1} = C_{NC1}^{-1} + C_{NC2}^{-1}$ is not infinity at any point in the NC regime.

and oval in Fig. 5.12 d at $Q = Q_{c1}$ and $Q = Q'_{c1}$) and (ii) total capacitance remains negative in the regime where one of the capacitance is positive and other negative i.e., $C_{ins} < 0$ with $C_{NC1} < 0$ and $C_{NC2} > 0$ or vice versa (see region with $Q < Q_{c1}$ and $Q > Q'_{c1}$ in Fig. 5.12 d), can make $C_{ins}(Q)$ negative by bypassing the point of infinite

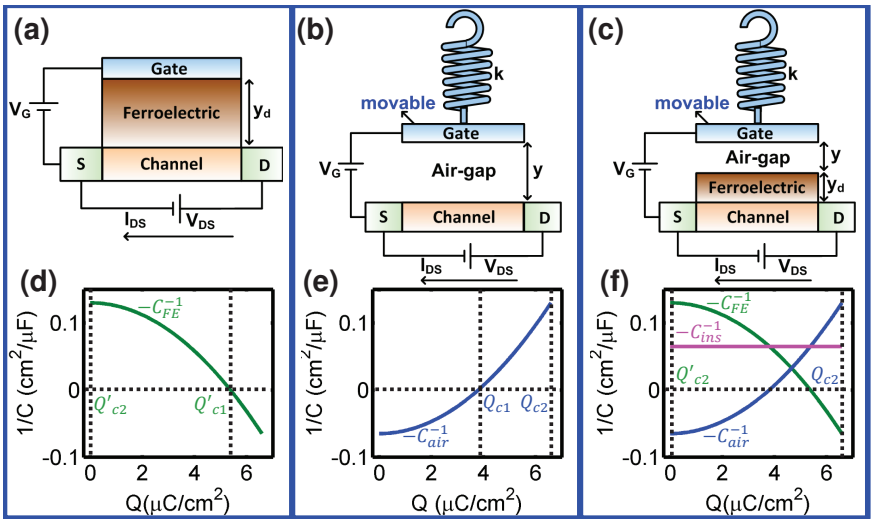

Fig. 5.13. Series combination of an air-gap capacitor and ferroelectric in ZSubFET can lead to a constant negative capacitance behavior and that is the key to $0mV/decade$ switching. (a)-(c) Schematic of FE-FET, SG-FET, and ZSubFET. Corresponding negative capacitance behavior of (d) ferroelectric in FE-FET, (e) air-gap in SG-FET, and (f) their series combination in ZSubFET.

capacitance of individual NCs. This negative $C_{ins}(Q)$ can then be matched by $C_s(Q)$ through a proper design of the channel leading to ideal switching characteristics.

5.4.2 Zero Sub-threshold Swing FET (ZSubFET)

We illustrate the concept of ZSubFET using the series combination of ferroelectric of FE-FET (Fig. 5.13 a) and air-gap capacitor of SG-FET (Fig. 5.13 b) in a suspended-gate ferroelectric FET (Fig. 5.13 c). Figure 5.13 d shows C_{FE}^{-1} as a function of Q for a ferroelectric material with $\alpha_0 < 0$, $\beta_0 > 0$, & $\gamma_0 = 0$ (Eq. 5.15). Equation 5.15 implies that $Q'_{c1} = \sqrt{-\alpha_0/3\beta_0}$ and $Q'_{c2} = 0$ for an n-type FE-FET. The air-gap capacitance ($C_{air}(Q)$) is given by Eq. 5.10. As shown in Fig. 5.13 e, the dependence of C_{air}^{-1} and C_{FE}^{-1} are opposite to each other. Now, the capacitance of the series combination can be obtained from Eqs. 5.10 & 5.15 as follows-

$$C_{ins}^{-1} \equiv C_{FE}^{-1} + C_{air}^{-1} = (\alpha_0 y_{FE} + \alpha_0') + 3\,(\beta_0 y_{FE} + \beta_0')\,Q^2. \tag{5.26}$$

Equation 5.26 suggests that the capacitance of the series combination (C_{ins}) can be tuned by tuning the parameters of the ferroelectric or suspended-gate. Note that, if the parameters are chosen such that $\alpha_0 y_{FE} + \alpha_0' < 0$ and $\beta_0 y_{FE} + \beta_0' < 0$, C_{ins} will be strictly negative from $Q = Q_{c2}' = 0$ to $Q = Q_{c2} = \sqrt{2\epsilon_0 k y_0 / WL}$. In such case, a variable channel capacitance such that $C_s = -C_{ins}$ will make the sub-threshold swing identically zero. Since the design of a channel with specific charge dependence may not be easy, we propose a simpler design in which parameters are chosen such that $\beta_0 y_{FE} + \beta_0' = 0$ and $\alpha_0 y_{FE} + \alpha_0' < 0$ leading to a constant negative insulator capacitance $C_{ins}^{-1} = \alpha_0 y_{FE} + \alpha_0' < 0$ (Fig. 5.13 f). These two conditions are equivalent to designing suspended-gate stiffness (k) and air-gap (y_0) as follows-

$$k = \frac{WL}{2\epsilon_0^2 \beta_0 y_{FE}}, y_0 < -\epsilon_0 \alpha_0 y_{FE}. \tag{5.27}$$

Now, the choice of the channel capacitance

$$C_s^{-1} = -\left(\alpha_0 y_{FE} + \alpha_0'\right) \tag{5.28}$$

will make the overall gate capacitance ($C_G^{-1} = C_{ins}^{-1} + C_s^{-1} = 0$) infinity and S to be $0mV/decade$. In equation 5.27, α_0 and y_{FE} are related to the ferroelectric; whereas α_0' is related to suspended-gate and air-gap. It should be noted that the parameters used in Fig. 5.13 are only for illustration purposes, in general one should follow conceptual framework of Eqs. 5.27 - 5.28 to design an ideal switch.

5.4.3 Switching Behavior

In the previous section, we showed that the gate insulator capacitance of a ZSub-FET can be constant and negative, thus giving rise to ideal switching behavior. To

gain insights into the mechanics of the extraordinary switching, we now discuss both the steady state and dynamic response using the two dimensional energy landscape of ZSubFET, as follows-

Static Response

The static response of a ZSubFET can be understood by looking at the evolution of energy landscapes as a function of the applied gate voltage (V_G). The total energy (U) has four main components: (i) ferroelectric energy given by two-well Landau energy landscape of the ferroelectric (Eq. 2.25 with $\gamma_0 = 0$) i.e.,

$$U_{FE} = \left(\tfrac{1}{2}\alpha_0 Q^2 + \tfrac{1}{4}\beta_0 Q^4\right) WLy_{FE},$$

(ii) air-gap energy comprising of spring and electrostatic energy i.e.,

$$U_{air} = \tfrac{1}{2}k\left(y_0 - y\right)^2 + \tfrac{Q^2 WLy}{2\epsilon_0}.$$

(iii) series capacitor energy i.e.,

$$U_s = \tfrac{Q^2 WL}{2C_s},$$

(iv) energy due to the applied bias i.e.,

$$U_{V_G} = -QWLV_G.$$

The total energy ($U \equiv U_{FE} + U_{air} + U_s + U_{V_G}$) is therefore given by-

$$U = \left(\frac{1}{2}\alpha_0 Q^2 + \frac{1}{4}\beta_0 Q^4\right) WLy_{FE} + \frac{1}{2}k\left(y_0 - y\right)^2 + \frac{Q^2 WLy}{2\epsilon_0} + \frac{Q^2 WL}{2C_s} - QWLV_G \quad (5.29)$$

Note that, ZSubFET is stabilized at the minimum of total system energy (U) for a given V_G. On the energy landscape, points with $\partial U/\partial y = 0$ and $\partial U/\partial Q = 0$ correspond to equilibrium and are given by the solutions of following equations-

$$k\left(y_0 - y\right) = \frac{Q^2 WL}{2\epsilon_0}, \quad (5.30)$$

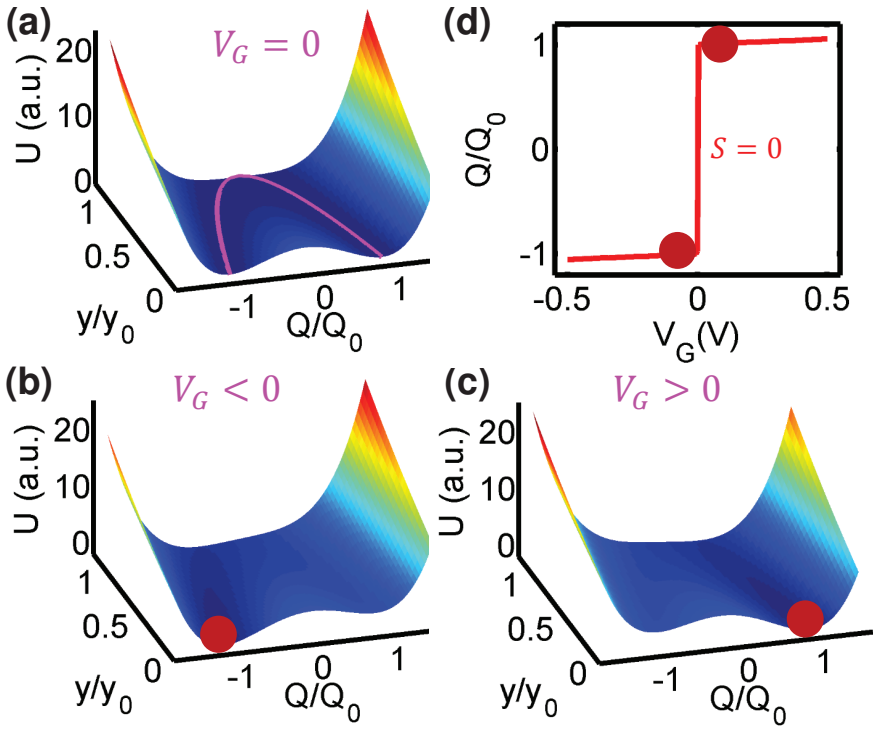

Fig. 5.14. Two dimensional energy landscapes of ZSubFET at (a) $V_G = 0$, (b) $V_G < 0$, and (c) $V_G > 0$. Along magenta curve in (a) all points correspond to equilibrium with same energy. In (b)-(c) solid circles denote the point where ZSubFET is stabilized at the respective voltages. (d) Corresponding gate charge vs. gate voltage characteristics.

$$WLV_G = \left(\alpha_0 y_{FE} + y\epsilon_0^{-1} + C_s^{-1}\right) WLQ + \beta_0 WLy_{FE}Q^3. \tag{5.31}$$

Equation 5.30 describes the balance of spring and electrostatic forces acting on the suspended-gate; whereas Eq. 5.31 is Kirchhoffs voltage law applied to the series combination of three capacitors namely air-gap, ferroelectric and the channel. Figure 5.14 a shows the energy landscape as a function of y and Q at $V_G = 0$ for parameters following Eq. 5.27. Magenta curve in Fig. 5.14 a shows the points at which U is minimized. All the points on the magenta curve have the same energy. Note that, instead of discrete distinct points of stabilization, there is a connected path

on the energy landscape and ZSubFET can be stabilized at any point on that path. This connected path is equivalent to the flat energy landscape for hysteresis-free $0mV/decade$ switching as discussed in reference [107]. Also, equation of path is given by Eq. 5.30. Note that, Eqs. 5.30 and 5.31 become identical for parameters following Eq. 5.27. If V_G is increased or decreased, energy landscapes tilts resulting in only one point of stable equilibria shown by a solid circle in Figs. 5.14 b-c. Therefore, slight change of gate voltage from negative to positive, switches ZSubFET abruptly from a negative charge state ($Q \approx -Q_0$) to a positive charge state ($Q \approx Q_0$) (Fig. 5.14 d). Here, $Q_0 = Q_{c2}$ is the value of gate charge at $V_G = 0$. This abrupt switching of the gate charge is equivalent to $0mV/decade$ switching. Note that, although the charge switches from $Q \approx -Q_0$ to $Q \approx Q_0$, the initial and final position of the suspended gate are both located at $y = 0$. In order to understand the role of the gate in $0mV/decade$ switching, one needs to look at the switching dynamics, which we discuss next.

Dynamic Response

When gate voltage is switched from negative to positive, state changes from $y = 0, Q \approx -Q_0$ (Fig. 5.14 b) to $y = 0, Q \approx Q_0$ (Fig. 5.14 c). The dynamics of this abrupt switching can be modeled by coupling gate dynamics with ferroelectric dynamics. The coupled equations are given as follows-

$$m\frac{dv}{dt} + bv = k\left(y_0 - y\right) - \frac{Q^2WL}{2\epsilon_0} \tag{5.32}$$

$$\rho_0\frac{dQ}{dt} = V_G - V_{air} - \psi_s - \left(\alpha_0 Q + \beta_0 Q^3\right) y_{FE} \tag{5.33}$$

$$\psi_s = \frac{Q}{C_s} \tag{5.34}$$

Equation 5.32 is Newtons law applied to the movable gate. Here, m is the mass of the gate, $v = dy/dt$ is velocity, t is time, b is the damping coefficient, $k\left(y_0 - y\right)$

is the restoring spring force and $Q^2WL/2\epsilon_0$ the electrostatic force. Equation 5.33 is Landau-Khalatnikov (LK) equation and describes the dynamics of ferroelectric switching [19]. Here, ρ_0 is material dependent constant. $V_{air} = Qy/\epsilon_0$ is the voltage drop across air-gap and ψ_s (Eq. 5.34) is the surface potential or voltage drop in the channel. Equations 5.32 - 5.34 are solved self-consistently to simulate the switching dynamics when V_G changes from negative to positive. Before switching (i.e., $V_G < 0$), ZSubFET is in the state $y = 0, Q \approx -Q_0$ (at $t = 0$) (open circle in Fig. 5.15). Switching occurs along the magenta curve shown in Fig. 5.15 a. Solid circles denotes the final state at $V_G > 0$. With the change in V_G, first Q starts to change following Eq. 5.33 (Fig. 5.15 c). Change in Q modifies the electrostatic force on the movable gate and causes it to move upward (Fig. 5.15 b). During switching, gate moves up and then comes down to stabilize at $y = 0$. Note that, movement of the gate plays an intriguing role to facilitate ferroelectric switching. If the gate was fixed at $y = 0$, ferroelectric and thus ZSubFET cannot switch due to the presence of an energy barrier (Fig. 5.15 a). Coupling of the ferroelectric with movable gate creates a path in two dimensional energy landscape for hysteresis-free abrupt switching. Similar switching dynamics take place when gate voltage is switched from positive to negative voltage. Note that, the exact path followed on the energy landscape during switching depends on the exact values of m, b and ρ_0. Again, the parameters used in Fig. 5.15 are only for illustration purposes to highlight the intriguing role of gate in $0mV/decade$ switching.

Summary of 0mV/decade Switching

To summarize this section, we have proposed the novel idea of hysteresis-free $0mV/decade$ switching based on a series combination of two different types of negative capacitance gate insulators. This series combination helps bypass the point of infinite capacitance of individual NCs and makes the overall capacitance negative in a certain regime. We illustrated the concept using ferroelectric and air gap insulators

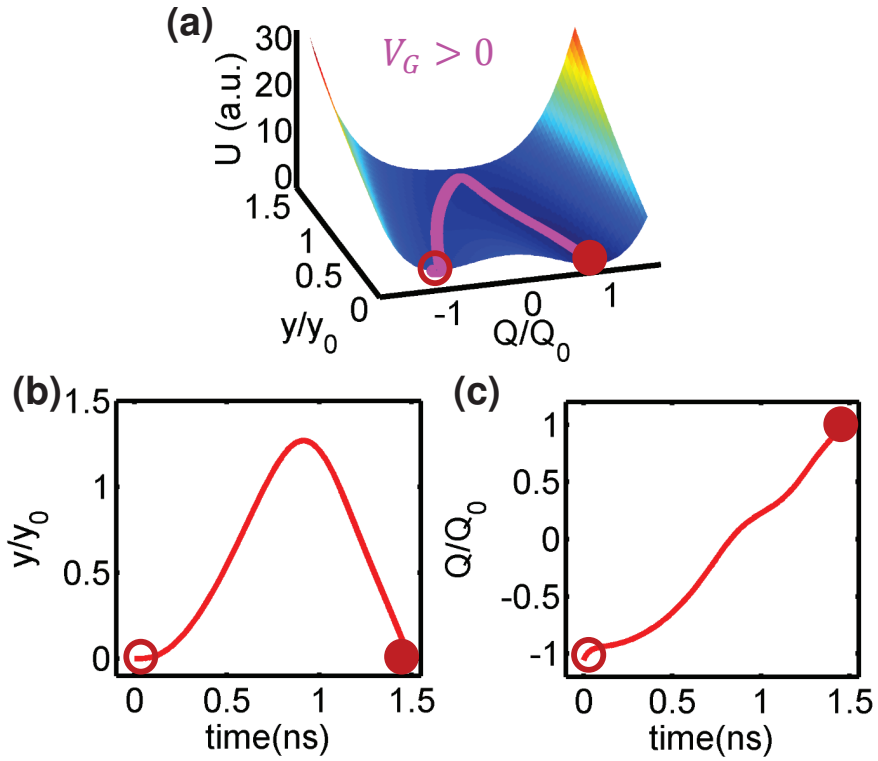

Fig. 5.15. Switching dynamics in a ZSubFET when gate voltage is switched from negative to positive. (a) Total energy landscape at $V_G > 0$. Open circle denotes the state before switching and solid circle after the switching. Switching occurs along the magenta line. Corresponding (b) position of the movable gate and (c) gate charge as a function of time.

in a ZSubFET. We believe that the proposed device should reduce the power supply voltage and corresponding power dissipation of integrated circuits to the lowest possible which is to be determined by noise considerations only [102].

5.5 Conclusions

In this chapter:

- We showed that instability need not to lead to problems always. Instability can be harnessed for performance enhancement also. In other words, we highlighted operation regime as a new design variable. It means that performance can be improved through operating in the unstable regime.

- We showed that negative capacitance behavior of Landau systems, namely, MEMS capacitive actuators and ferroelectrics, can be used for voltage amplification in SG-FET and FE-FET, respectively, to lower sub-threshold swing below $60mV/decade$.

- We established the fundamental lower limits of sub-threshold swing of negative capacitance field effect transistors. We find that sub-threshold swing cannot be reduced all the way to $0mV/decade$ in an NC-FET with single NC gate insulator.

- To overcome the limitations of single NC gate insulators based FET, we proposed to use a series combination of two different types of NC gate insulators for realizing ideal switching characteristics. Specifically, we showed that hysteresis-free zero sub-threshold swing can be achieved in a suspended-gate ferroelectric FET.

- Basically, we have addressed two very fundamental questions such as (i)"How low can the sub-threshold swing be in an NC-FET?" and (ii) "Is it at all possible to achieve hysteresis-free $0mV/decade$ switching characteristics in a FET?" We believe that the results of this chapter will serve as the guidelines for the design of novel field effect transistors.

In the next chapter, we will continue with the philosophy of harnessing instability or using operation regime as a design variable for performance enhancement. We will

show how spring-softening effect of MEMS can be used to enhance signal-to-noise ratio in Flexure sensors.

6. HARNESSING SPRING-SOFTENING : IMPROVED SENSITIVITY AND SIGNAL-TO-NOISE RATIO IN FLEXURE BIOSENSORS

In the last chapter, we illustrated how instability can be used for performance enhancement. Specifically, we showed that negative capacitance behavior of Landau switches can lead to (i) hysteresis-free sub-$60mV/decade$ switching characteristics in FETs with single NC gate insulator and (ii) hysteresis-free $0mV/decade$ characteristics in properly designed FETs with series combination of two NC gate insulators.

In this chapter, we show one more example where harnessing instability can lead to improved performance. We propose a novel Flexure biosensor targeted to detect specific biomolecules. We show that biasing the proposed sensor at the boundary of stable and unstable regimes not only enhances the sensitivity, but also improves signal-to-noise ratio. This chapter is divided in two parts:

- In the first part[1], we introduce the novel Flexure-FET biosensor and show how it is better than existing state-of-the-art other electronic or mechanical biosensors.
- In the second part, we show how internal low pass filtering of MEMS (decrease in the resonance frequency with applied bias as seen in chapter 2) helps amplify the signal-to-noise ratio in Flexure sensors.

Rest of the chapter is organized as follows. For the sensitivity analysis, we discuss the motivation behind the need of a new biosensor in section 6.1.1. The operation of novel Flexure-FET biosensor is discussed in section 6.1.2. We compare the proposed sensor with the existing electronic/mechanical sensors in section 6.1.3 and provide a brief summary of findings in section 6.1.4. For the noise analysis, we identify

[1]The content (text and figures) in this part have been adapted from [118].

Flexure sensors as a positive feedback system in section 6.2.1. We evaluate signal-to-noise ratio and limit-of-detection for various noise sources in section 6.2.2. The safe operating voltage of Flexure sensors has been discussed in section 6.2.3. We discuss the assumptions of our analysis in section 6.2.4 and summarize the findings of signal-to-noise ratio in section 6.2.5. We finally conclude in section 6.3

6.1 Proposal of Flexure-FET Biosensor

6.1.1 Background and Motivation

Detection of biological molecules e.g., viruses, proteins, and DNA is essential for food safety, early warning of biological attack, early stage diagnosis of cancer, and genome sequencing. Nanoscale devices are widely regarded as a potential candidate for ultra-sensitive, low-cost, label-free detection of biomolecules. They are considered as a technology alternative to the existing chemical or optical detection schemes. Label-free schemes detect biomolecules using their intrinsic properties, e.g., size, mass or charge of a molecule, instead of using extrinsic optical or magnetic labels attached to the target molecule. Among the various label-free technologies, significant research have focused on developing ultrasensitive nanoscale electrical [119] and mechanical [24] biosensors. Despite remarkable progress over the last decade, these technologies have fundamental challenges that limit opportunities for further improvement in their sensitivity, see Fig. 6.1 a [120–123]. For example, the sensitivity of electrical nanobiosensors such as Si-Nanowire (NW) FET (Fig. 6.1 b) is severely hindered by the electrostatic screening due to the presence of other charged ions/molecules in the solution [124], which limits its sensitivity to vary linearly (in subthreshold regime [120]) or logarithmically (in accumulation regime [121,125,126]) with respect to the captured molecule density N_s. Moreover, the miniaturization and stability of the reference electrode have been a persistent problem, especially for lab-on-chip applications [119]. Finally, it is difficult to detect neutral biological entities such as viruses or proteins using charge-based electrical nanobiosensors.

In contrast, nanomechanical biosensors like nanocantilevers [127, 128] (Fig. 6.1 c) can detect neutral molecules also. Here, the capture of target molecules on the cantilever surface modulates its mass, stiffness, and/or surface stress [122, 128, 129]. This change in the mechanical properties of the cantilever can then be observed as a change in its resonance frequency (dynamic mode), mechanical deflection, or change in the resistance of a piezoresistive material (static mode) attached to the cantilever [123, 130]. Unfortunately, the response of the nanomechanical biosensors varies only linearly [122] or logarithmically [123, 131, 132] with the change in the mass or surface stress of the cantilever, and therefore, these sensors may not be sufficiently sensitive to detect target molecules at very low analyte concentrations, unless sophisticated, low-noise setup is used.

To overcome the respective limitations of classical electrical and mechanical biosensors, we propose the concept of a Flexure-FET biosensor that integrates the key advantages of both technologies, but does not suffer from the limitations of either approach. The Flexure-FET consists of a nanoplate channel biased through a thin-film suspended gate (Fig. 6.1 d). While the structure is similar to that of a suspended-gate FET (discussed in the previous chapter) [21,101] or a resonant gate transistor [1], we call the device Flexure-FET to emphasize its distinctive nonlinear operation specifically optimized for ultrasensitive detection of biomolecules. As shown in Fig. 6.1 e, the ultra high sensitivity arises from the coupling of two electro-mechanical nonlinear responses, namely (i) spring-softening [133] in which stiffness decreases nonlinearly with the applied gate bias V_G and vanishes at the pull-in point (Chapter 2) and (ii) subthreshold electrical conduction [94] in which current depends exponentially on the surface potential. Such non-linear electro-mechanical coupling enables exponentially high sensitivity for Flexure-FET sensors (Fig. 6.1 a), which is fundamentally unachievable by exclusive use of existing nanoscale electronic or mechanical biosensors. Moreover, the reliance of change in stiffness [134, 135] ensures screening-free detection of charged/neutral molecules, with no need for a reference electrode, and the measurement of drain current for detection requires no complex instrumentation.

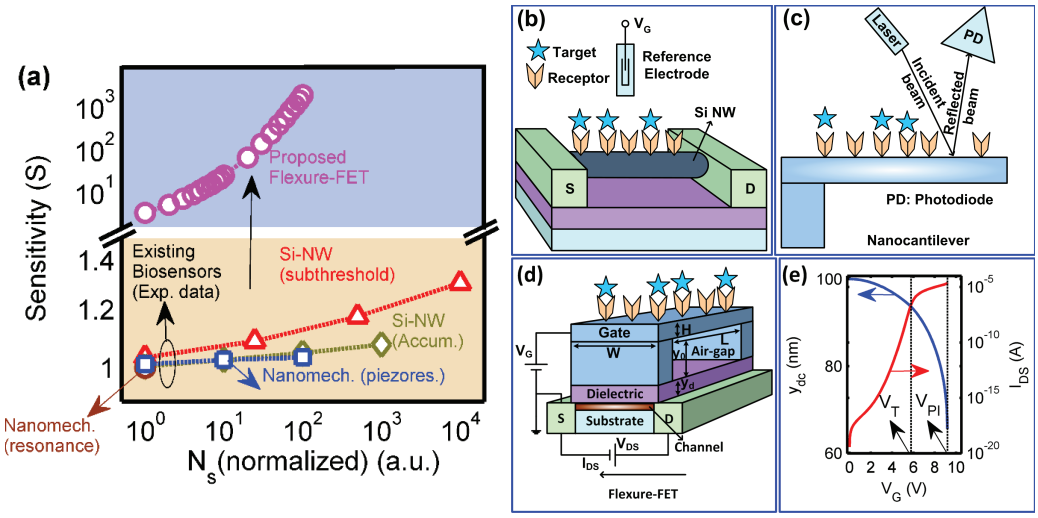

Fig. 6.1. (a) Sensitivity (S) of different types of biosensors, e.g., (b) Electrical sensor (Si-NW FET) in which transduction is achieved by modulation of channel conductivity (G) when charged biomolecules are captured by the gate. (c) Transduction in cantilever-based nanomechanical biosensors is achieved by change in its mass, stiffness, or surface stress. Nanocantilever can be operated in dynamic mode (mass change based detection using shift in resonance frequency) or in static mode (surface stress change based detection using piezoresistive material). (d) Proposed Flexure-FET biosensor in which transduction is achieved due to change in the stiffness of the suspended gate, (e) Operation of Flexure-FET below pull-in. Displacement of the suspended gate (y_{dc}) and drain current (I_{DS}) as a function of applied gate bias V_G. y_{dc} changes rapidly near pull-in ($V_G \approx V_{PI}$) and I_{DS} increases exponentially with V_G in the subthreshold regime ($V_G < V_T$).

It should be noted that from a mechanical perspective, the Flexure-FET operates close to pull-in instability (a critical point) and operates in static mode. Similar critical point sensing has also been reported for sensors operating in dynamic mode [136–140]. These sensors detect the stimuli by observing: (i) change in the resonance frequency [137, 139], (ii) change in the amplitude at a given frequency [136–138, 140], or (iii) switching triggered by a detection event [138]. In terms of instability, Flexure-FET utilize the pull-in instability; whereas these sensors utilize parametric resonance [136, 137], buckling instability [139], bifurcations [138, 140], and

escape phenomenon [138]. However, beyond the critical point sensing, the integrated transistor-action in the sub-threshold regime provides the Flexure-FET an additional exponential sensitivity (and simpler DC read-out) that could not be achieved by the classical nonlinear sensor schemes.

6.1.2 Operation of Flexure-FET

Flexure-FET Response to Target Capture

For transduction, the proposed Flexure-FET biosensor utilizes the change in suspended-gate stiffness from k to $k + \Delta k$, [129, 135, 141–143] due to the capture of biomolecules. The change in stiffness due to the capture of biomolecules has been demonstrated by several recent experiments of mass sensing using nanocantilever based resonators [129, 141, 142]. This well-known observation of stiffness change has been attributed to the change in the membrane thickness, Young's modulus, and/or surface stress of the beam [129, 134, 135, 144]. In the following analysis, we model the change in k by the change in the effective thickness H of the gate (ΔH), although it should be stressed that the conclusions do not depend on the particular hypothesis regarding Δk. For now, we ignore the details of the spatial distribution of molecules associated with random sequential adsorption [145], and assume a uniform distribution of adsorbed molecules on the sensor surface. Therefore, the conservation of volume suggests $\Delta H = N_s A_t H_t$, where N_s is the areal density, A_t is the effective cross-sectional area, and H_t is the effective thickness of the target molecule. Using the fact that $k = \frac{\alpha E W H^3}{12 L^3}$, the change in stiffness Δk due to $\Delta H (\ll H)$ can be related to adsorbed molecule density N_s as follows-

$$\frac{\Delta k}{k} \approx \frac{3 N_S A_t H_t}{H}. \tag{6.1}$$

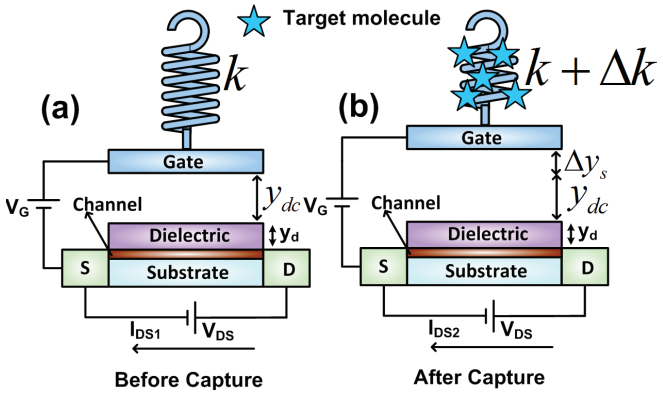

Fig. 6.2. (a)-(b) Equivalent spring-mass model of Flexure-FET. Stiffness changes from k to $k + \Delta k$ after the capture of biomolecules, and therefore, position of gate changes from y_{dc} to $y_{dc} + \Delta y_s$ which results in the modulation of drain current from I_{DS1} to I_{DS2}.

For simplicity, we have taken the Young's modulus of captured molecules to be same as that of the membrane, but this is obviously not necessary, and the theory can be generalized by the methods developed in reference [134]. Combining Eqs. B.1-B.3 from appendix B, we get $k(y_0 - y_{dc})y_{dc}^2 \approx \epsilon_0 A(V_G - \psi_s)^2/2$. y_{dc} is the position of the gate before capture and $y_{dc} + \Delta y_s$ after capture. y_0 is the initial air-gap. The change in gate position Δy_s for small change in stiffness Δk due to capture of biomolecules is given as -

$$(3y_{dc} - y_0)\Delta y_s^2 + y(3y_{dc} - 2y_0)\Delta y_s \approx \frac{\epsilon_0 A\,(V_G - \psi_s)^2}{2}\frac{\Delta k}{k^2}. \tag{6.2}$$

If Flexure-FET is biased close to pull-in ($V_G \approx V_{PI}$, $y_{dc} \approx 2/3y_0$), the non-linear Δy_s^2 term dominates the linear Δy_s term in Eq. 6.2. It is essential to bias the Flexure-FET in this nonlinear, close to pull-in regime for maximum sensitivity. Using Eqs. 6.1-6.2, we find-

$$\Delta y_s \approx \sqrt{\frac{\epsilon_0 A\,(V_G - \psi_s)^2}{2(3y_{dc} - y_0)}\frac{\Delta k}{k^2}} \approx \beta\sqrt{N_s}, \tag{6.3}$$

where $\beta = \frac{\epsilon_0 A(V_G-\psi_s)^2}{2(3y_{dc}-y_0)}\frac{A_t H_t}{Hk}$ is a bias and device dependent constant.
Since the electrostatic force in subthreshold regime is given by $\frac{1}{2}\epsilon_0 E_{air}^2 A = q\epsilon_s \psi_s N_A A$ (Eq. B.2 in appendix B), the corresponding change in the surface potential $\Delta\psi_s$ is obtained by perturbation of Eq. B.1 in appendix B, i.e.,

$$\Delta\psi_s \approx \frac{-k\Delta y_s + \Delta k(y_0 - y_{dc})}{q\epsilon_s N_A A}. \tag{6.4}$$

Using Eqs. B.3, B.4, & B.5 from appendix B, we can calculate the drain current I_{DS} in the subthreshold regime, as follows,

$$I_{DS} \approx \frac{\mu_n L\left(\frac{V_{DS}}{W}\right)\left(\frac{qn_i^2}{N_A}\right)\left(\frac{k_B T}{q}\right)}{\sqrt{\frac{2qN_A}{\epsilon_0\epsilon_s}}}\frac{e^{\frac{q\psi_s}{k_B T}}}{\sqrt{\psi_s}}. \tag{6.5}$$

Now, the ratio of the drain current before (I_{DS1}) and after (I_{DS2}) capture of biomolecules (in terms of the change in surface potential $\Delta\psi_s$) is given by-

$$\frac{I_{DS1}}{I_{DS2}} \approx \exp\left(-\frac{q\Delta\psi_s}{k_B T}\right). \tag{6.6}$$

Using Eqs. 6.4 and 6.6, the ratio $\frac{I_{DS1}}{I_{DS2}}$ is given by-

$$\frac{I_{DS1}}{I_{DS2}} \approx \exp\left(\frac{k\Delta y_s - \Delta k(y_0 - y_{dc})}{k_B T\epsilon_s N_A A}\right). \tag{6.7}$$

Therefore, if Flexure-FET is operated close to pull-in and in subthreshold regime, sensitivity S (using Eqs. 6.3 & 6.7) is given by-

$$S \equiv \frac{I_{DS1}}{I_{DS2}} \approx \exp\left(\gamma_1\sqrt{N_s} - \gamma_2 N_s\right). \tag{6.8}$$

where $\gamma_1 = \frac{k\beta}{k_B T \epsilon_s N_A A}$ and $\gamma_2 = \frac{3(y_0 - y_{dc})kA_t H_t}{k_B T \epsilon_s N_A A H}$. The sensitivity S is defined as $\frac{I_{DS1}}{I_{DS2}}$, because I_{DS} decreases after capture (see next section).

Equation 6.8 is one of the key results of this chapter and shows how nonlinear interaction between mechanical (spring-softening) and electrical (subthreshold) aspects of sensing leads to an exponential sensitivity to capture of biomolecules. Such gain in sensitivity is impossible to achieve exclusively by electrical or mechanical sensing mechanisms.

Numerical Confirmation of Flexure-FET Response

The compact analytical expression of sensitivity of the Flexure-FET sensor can be validated by the self-consistent numerical solution of Eqs. B.1-B.5. The results for the change in sensor characteristics due to the capture of biomolecules are summarized in Fig. 6.3. For example, Fig. 6.3 a shows y_{dc} vs. V_G before and after capture of target molecules. After the capture, gate moves up (for a fixed V_G) due to increased restoring spring force (because of increase in the k, Fig. 6.3 a). Interestingly, change in gate position Δy_s is maximum close to pull-in due to spring-softening effect, as shown in Fig. 6.3 b. The change in gate position Δy_s is directly reflected in change in I_{DS}. Figure 6.3 c shows I_{DS} vs. V_G before and after capture of biomolecules. Interestingly, I_{DS} decreases after capture due to increased separation between the gate and the dielectric (hence decreased capacitance). The corresponding ratio of the currents I_{DS1} (before capture) and I_{DS2} (after capture) increases exponentially with Δy_s (Fig. 6.3 d), and becomes maximum near pull-in. Note that the results from detailed numerical simulations are accurately anticipated by Eq. 6.7, thus validating the analytical model described in the previous section. Therefore, by operating the Flexure-FET close to mechanical pull-in and in electrical subthreshold regime, orders of magnitude change in I_{DS} can be easily achieved for typical surface density of $N_s = 5 * 10^{12} cm^{-2}$, projected area of the biomolecule, $A_t = \pi R_t^2$ with $R_t = 1nm$,

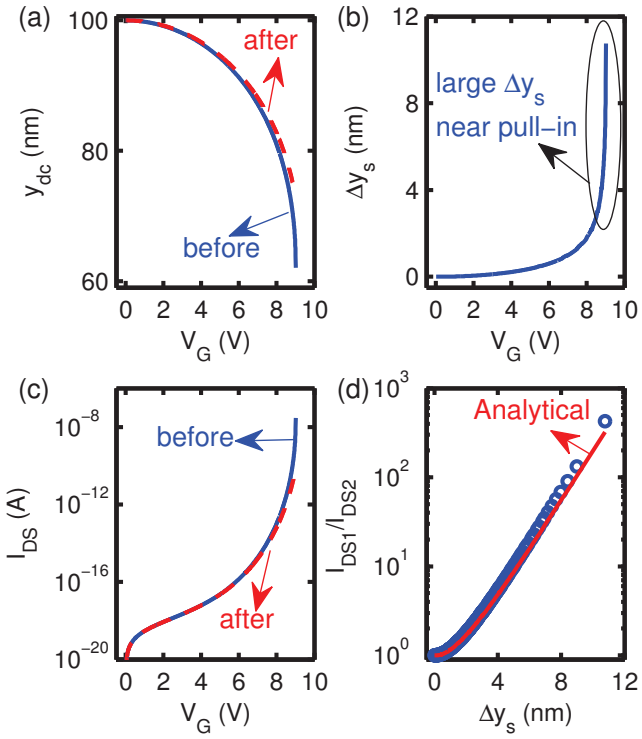

Fig. 6.3. Change in the sensor characteristics due to capture of target molecules on the surface of the gate, (a) y vs. V_G before and after capture, and (b) corresponding change in the position of gate electrode Δy_s vs. V_G. Δy_s increases rapidly near pull-in due to spring-softening effect. The capture of target molecules is directly mirrored in the change in I_{DS}. (c) I_{DS} vs. V_G before and after capture, and (d) corresponding ratio of the two currents I_{DS1} (before capture) and I_{DS2} (after capture) as a function of Δy_s. Symbols are the numerical simulation and solid line is the analytical formula (Eq. 6.7). The device considered has the following typical parameters: $L = 4\mu m, W = 1\mu m, H = 40nm, E = 200GPa, y_0 = 100nm, y_d = 5nm, \epsilon_s = 11.7, \epsilon_d = 3.9, N_A = 6e16cm^{-3}$.

and $H_t = 5.1nm$. These parameters translate to just an equivalent $\Delta k \sim 6\%$. Note that to achieve the maximum sensitivity, it is important to bias the Flexure-FET in subthreshold regime below pull-in (i.e., $V_T \approx V_{PI}$).

6.1.3 Comparison with Classical Sensors

Now, we compare the sensitivity of the proposed Flexure-FET sensors with the current nanoscale electrical/mechanical biosensors. Figure 6.4 a indicates that the Flexure-FET sensors are exponentially sensitive to change in stiffness or captured molecule density N_s (symbols: numerical simulation, solid line: analytical result, Eq. 6.8). In the following, we explain the origin of linear (or logarithmic) sensitivity for electrical and mechanical nanoscale biosensors.

Electrical Nanobiosensors

For Si-NW FET biosensors which have the optimal sensitivity in subthreshold regime [120], sensitivity S is defined to be the ratio of conductance G (after) and G_0 (before) capture of target molecules (assuming conductance increases after the capture). Therefore, using Eq. 6.5, S can be approximated as-

$$S_{SiNW} \equiv \frac{G}{G_0} \approx \exp\left(\frac{q\Delta\psi_s}{k_BT}\right). \tag{6.9}$$

Unfortunately, the detection of biomolecules in a fluidic environment involves electrostatic screening by other ions in the solution. Consequently, the surface potential scales logarithmically with biomolecule density, i.e., $(q/k_BT)\Delta\psi_s \approx \log(\delta N_S)$ [124] , where δ is a constant that depends on ionic strength and properties of dielectric/fluid interface. Therefore, optimal sensitivity of Si-NW biosensors is given by,

$$S_{SiNW} \propto \delta N_s. \tag{6.10}$$

In Fig. 6.4 b, S is plotted against volume concentration ρ, as the captured molecule density $N_s \propto \rho$ (linear regime of Langmuir isotherm [124]). Therefore, all the conclusions regarding the dependence of sensitivity on N_s also holds for ρ. It should

be noted that the reported sensitivity in the subthreshold regime [120] is actually sub-linear (Fig. 6.4 b), below the maximum sensitivity limit defined by Eq. 6.10 that can be achieved in this sensing regime. In the accumulation or the inversion regimes, $S_{SiNW} \propto \Delta\psi_s$ [124], and therefore, $S_{SiNW} \propto \log(N_S)$, as shown in Fig. 6.4 b [121, 124].

Mechanical Nanobiosensors

For nanomechanical biosensors such as resonance mode nanocantilever, the sensitivity S is defined as $\frac{\omega_0}{\omega}$, where ω is the resonance frequency after the capture of target biomolecules, and ω_0 is the resonance frequency before capture. Using the well-known fact that $\omega = \sqrt{\frac{k}{m}}$, where, k is the stiffness and m is the initial mass of the cantilever, S is given by

$$S_{Res} \equiv \frac{\omega_0}{\omega} \approx 1 + \frac{1}{2}\frac{\Delta m}{m} = 1 + \frac{1}{2}\frac{N_s W L m^*}{m}, \tag{6.11}$$

where m^* is the mass of individual biomolecule and $\Delta m = N_s W L m^*$ is the added mass of the biomolecules. Therefore, the sensitivity of mechanical biosensor can only vary linearly with N_s. This theoretical prediction is confirmed by experimental data [122] in Fig. 6.4 c. We emphasize that the nanomechanical biosensors with careful design and appropriate instrumentation can be extraordinarily sensitive; indeed, zeptogram mass detection [146] has been reported. Equation 6.11 simply suggests that the sensitivity of such sensor still varies linearly with respect to N_s.

It is also important to realize that the linear sensitivity with N_s is achieved only if the change in stiffness due to capture of molecules is negligible. In general, however, capture of target molecules increases stiffness of the membrane. If this increase in stiffness compensates the corresponding increase in the mass, there might be no change in resonance frequency at all [129, 142] and the sensitivity could be vanishingly

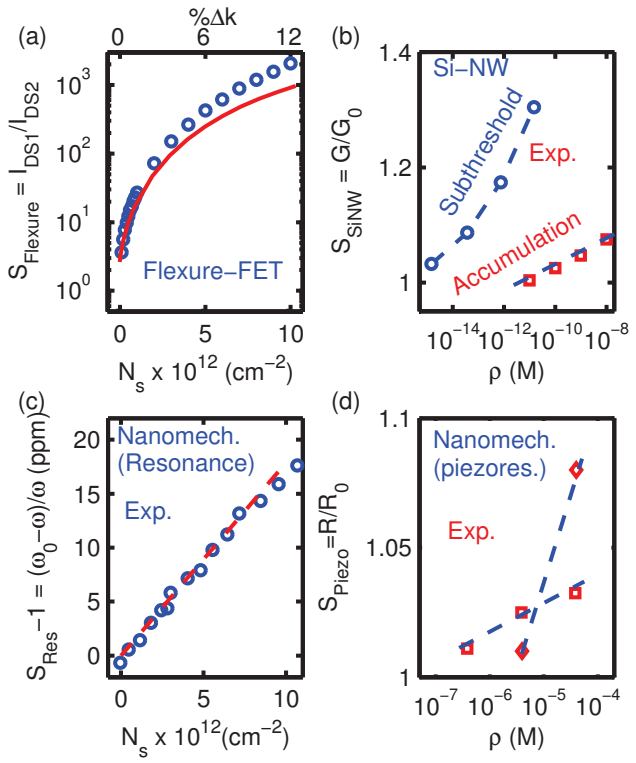

Fig. 6.4. Comparison of the sensitivity of different biosensors. Sensitivity S (a) Flexure-FET (symbols denote the numerical simulation). (b) Si-NW biosensors in subthreshold [120] and accumulation regime [121], (c) Resonance mode nanomechanical biosensors [122],(d) Surface stress change based piezoresistive nanomechanical biosensors [123], as a function of N_s or ρ. In (b)-(d), symbols are the experimental data and the line is the guide to the eye.

small. One must independently measure the change in the stiffness [143, 144] to decouple the mass-effect from stiffness-effect so that the mass of the adsorbed molecule can be correctly estimated. In contrast, the Flexure-FET relies only on the change in the stiffness and works in the static mode, and therefore, requires no more than a simple measurement of the drain current.

Another class of nanocantilever sensor involves operation in the static mode, where the capture of the target molecules introduces a surface stress, which in turn bends the cantilever. The displacement Δy_s of the tip can in principle be measured using

sophisticated optical readout methods, but a simpler approach can be used instead: One can measure the change in surface stress by measuring the change in the resistance of a piezoresistor attached to the cantilever. For these piezoresistive based cantilever biosensors, the sensitivity is defined as the ratio of resistance after (R) and before (R_0) the capture of biomolecules. Figure 6.4(d) shows a logarithmic dependence of S on ρ. Similar logarithmic dependence for surface stress change has also been reported in references [131, 132]. We, therefore, conclude that these static mode sensors do not exceed linear sensitivity limit of classical sensors.

We summarize the results discussed in this section in Fig. 6.1 a, where the sensitivity of various types of nanobiosensors have been plotted against normalized N_s, defined as the ratio of the measured quantity (either ρ or N_s) to the minimum measured ρ or N_s of the available data. Figure 6.1 a allows us to conclude that the Flexure-FET biosensor will be exponentially more sensitive compared to existing nanoscale electrical or mechanical biosensors.

6.1.4 Summary of Flexure-FET

In this section, we have demonstrated how Flexure-FET nanobiosensor achieves exponentially high sensitivity by combining two non-linear characteristics of spring-softening and subthreshold conduction. This extreme high sensitivity of Flexure-FET, therefore, breaks the fundamental limits of linear or logarithmic sensitivity of classical nanoscale electrical or mechanical biosensors. There are broad range of applications that can benefit from this sensitivity gain. For example, the current genome sequencing schemes require PCR (Polymerase chain reaction) amplification of DNA strands because of the lower sensitivity of existing biosensors. The high sensitivity of Flexure-FET can eliminate the requirement of multiplication step and hence reduce the cost of sequencing. In addition, we recall that the proposed sensing scheme (i) can detect both charged and neutral molecules and (ii) does not rely on reference electrode, (the fundamental roadblock of Si-NW type biosensors). The

sensitivity of Flexure-FET can be further enhanced by choosing a softer membrane (having low stiffness) such as some polymer with low Young's modulus or an ultra thin membrane like graphene. Finally, let us emphasize that the sensing scheme is very general which converts any change in the mechanical property of the gate electrode or change in the air-gap, to the change in the drain current of the FET channel. Therefore, the proposed idea is not necessarily restricted to biomolecules detection but should find broader applications in gas/chemical/pressure sensing as well.

6.2 Signal-to-Noise Ratio in Flexure Sensors

In the last section, we saw that operating Flexure-FET close to pull-in, can give rise to exponential sensitivity. In this section, we focus on the noise aspects of novel sensors and answer two very fundamental questions regarding Flexure sensors:

- "Does signal-to-noise ratio (SNR) and limit-of-detection (LOD) also improve close to the pull-in instability point?"
- In the previous section, we assumed that we can operate just at the boundary between stable and unstable regime i.e., at $V_G \approx V_{PI}$. We derived the analytical formula of sensitivity (Eqs. 6.3 & 6.8) based on this particular assumption. Here, we ask, "How close can we operate close to pull-in instability point, without making the system unstable?"

Without the answers to these questions, it is difficult to ascertain the technological relevance of novel Flexure sensors. Note that, in our noise analysis, we only consider the transduction noise (noise in the movable gate) and not the readout noise (channel noise) because readout noise depends on the specific readout mechanism. In general, change in the position of gate (Δy_s) can be detected using various methods such as optical methods or an integrated transistor (as shown in Flexure-FET). Therefore, we focus on the more fundamental noise sources which are present in every Flexure sensor irrespective of the readout mechanisms.

6.2.1 Flexure Sensor as a Positive Feedback System

Recall that a Flexure biosensor consists of a movable electrode (e.g., a fixed-fixed beam) and a bottom fixed electrode as shown in Fig. 6.5 a. The beam is decorated with specific receptor molecules. The movable electrode is deflected towards the bottom electrode through an applied voltage (V_G) (Fig. 6.5 a). The capture of target biomolecules increases the flexural rigidity of the beam (basis of Flexure sensors) [129, 134, 141, 142], making the beam move away from the bottom electrode as shown in Fig. 6.5 b. The change in deflection $\Delta y_s = y_{after} - y_{before}$ can be measured using either optical methods or an integrated transistor as in Flexure-FET biosensor (previous section).

The behavior of Flexure sensor in response to the capture of biomolecules or environmental noise can be understood using a simple spring-mass system in which movable electrode is suspended from a spring of stiffness k (Fig. 6.5 c). We saw in previous section that capture of target biomolecules is modeled as an increase in the stiffness from k to $k + \Delta k$ (Fig. 6.5 d). Balance of spring and electrostatic forces i.e.,

$$k\left(y_0 - y_{dc}\right) = \frac{\epsilon_0 W L}{2 y_{dc}^2} V_G^2, \tag{6.12}$$

governs the static response of the sensor (see chapter 2). To remind, y_0 is the initial air gap (at $V_G = 0$) and y_{dc} is the gap between the two electrodes at $V_G \neq 0$. Note that, $y_{dc} = y_{before}$ before capture and $y_{dc} = y_{after}$ after capture of biomolecules (Fig. 6.5). Dynamics of the movable electrode after capture of biomolecules is dictated by Newtons law i.e.,

$$m\frac{d^2\Delta y}{dt^2} + b\frac{d\Delta y}{dt} - (k + \Delta k)\left(y_0 - y_{dc} - \Delta y\right) = -\frac{\epsilon_0 W L}{2\left(y_{dc} + \Delta y\right)^2} V_G^2, \tag{6.13}$$

where Δy is change in the position from y_{dc}, m is the mass of movable electrode, b is the damping coefficient. For $\Delta y < y_{dc}$ and $\Delta k < k$, Eq. 6.13 is simplified to-

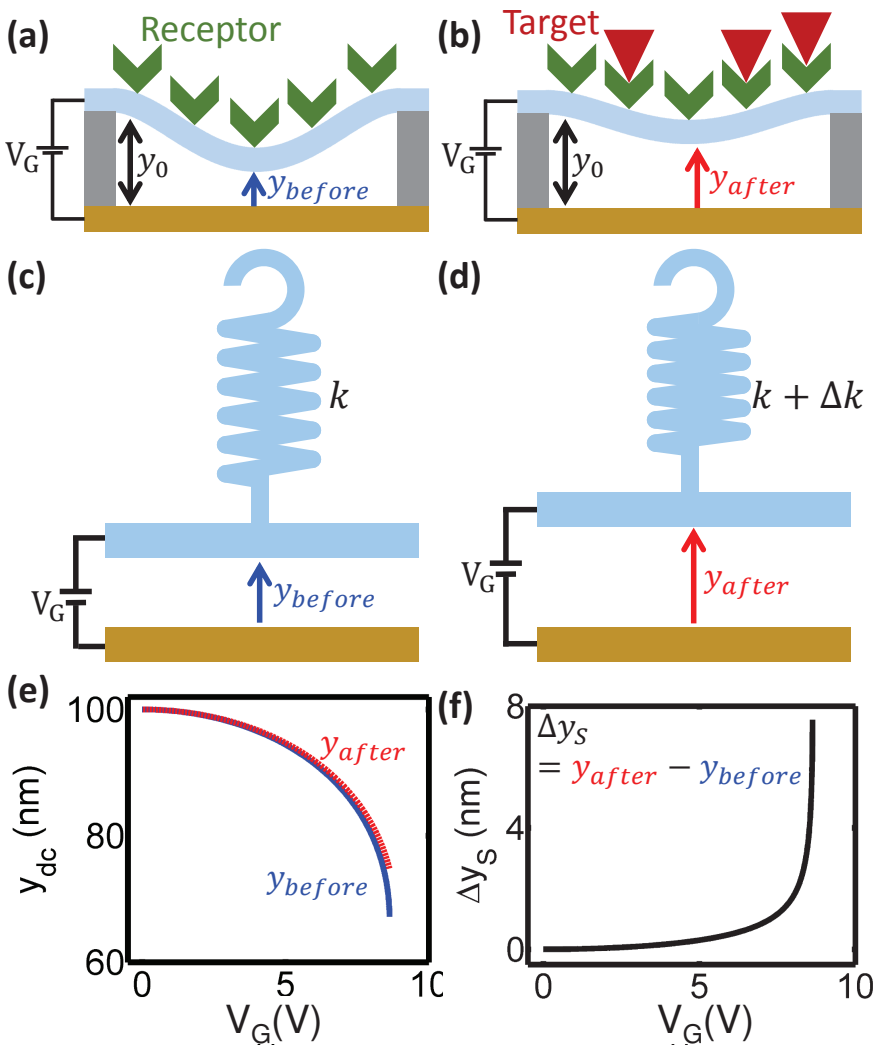

Fig. 6.5. Schematic of a Flexure biosensor (a) before and (b) after capture of biomolecules. Note the absence of integrated FET in a-b compared to Fig. 6.1. Spring-mass model of Flexure biosensor (c) before and (d) after capture of biomolecules. (e) Position of movable electrode before and after capture and (f) corresponding change in the electrode position as a function of applied bias.

$$m\frac{d^2\Delta y}{dt^2} + b\frac{d\Delta y}{dt} + \left(k - \frac{\epsilon_0 WL}{y_{dc}^3}V_G^2\right)\Delta y = \Delta k\,(y_0 - y_{dc}) \equiv \Delta F \tag{6.14}$$

Using Eq. 6.14, one can easily find the transfer function of Δy with respect to the force $\Delta F = \Delta k\,(y_0 - y_{dc})$ as follows-

$$\frac{\Delta Y(\omega)}{\Delta F(\omega)} = \frac{\frac{A}{1+A\beta}}{1 + \frac{j\omega}{\frac{k}{b}(1+A\beta)} - \frac{\omega^2}{\frac{k}{m}(1+A\beta)}} \tag{6.15}$$

Equation 6.15 is the key equation of this section and highlights several important things about Flexure sensors. For $\beta = 0$, Eq. 6.15 reduces to the well-known transfer function of a spring-mass system i.e., $T_F^{OL}(\omega) \equiv \frac{\Delta Y(\omega)}{\Delta F(\omega)} = \frac{1}{k+jb\omega-m\omega^2}$ (Fig. 6.6 a). Equation 6.15 suggests that the application of a bias V_G, provides a positive feedback with feedback gain $\beta = -\frac{\epsilon_0 WL}{y_{dc}^3}V_G^2$ (known as electrostatic stiffness) (Fig. 6.6 a). This positive feedback modifies the transfer function to $\frac{T_F^{OL}(\omega)}{1+T_F^{OL}(\omega)\beta}$ (same as Eq. 6.15). Therefore, the low frequency gain is modified from $A = 1/k$ to $A/\left(1 + A\beta\right)$ and bandwidth from $\omega_0 = \sqrt{k/m}$ to $\omega_0\sqrt{1 + A\beta}$ (assuming resonance frequency dictates the bandwidth for low values of b) (Fig. 6.8 b). We will show below that the increase of the low frequency gain and decrease of the bandwidth in a positive feedback system ($\beta < 0$), is the key for the improved SNR/LOD in Flexure sensors.

One can now use Eq. 6.15 to analyze both the signal and noise for Flexure sensors as follows. Assuming that the change in stiffness (Δk) due to capture of biomolecules is a low frequency signal i.e., $\omega \approx 0$, Δy_s can simply be obtained from Eq. 6.15

$$\Delta y_s \approx (y_0 - y_{dc})\,\frac{\Delta k}{k}\frac{1}{1 + A\beta}. \tag{6.16}$$

Equation 6.16 implies that when $A\beta \approx -1$ (equivalent to the condition of pull-in), Δy_s will be very large. This is confirmed by numerical simulations of Eq. 6.12 in Figs. 6.5 d-e. Figure 6.5 d shows y_{dc} as a function of V_G before and after capture of target molecules (similar to Fig. 6.3 a). The corresponding Δy_s is shown in Fig. 6.5 e and confirms large value of Δy_s close to pull-in (similar to Fig. 6.3 b). Intuitively, decrease in the effective stiffness ($k+\beta$) with increase in V_G (known as spring softening

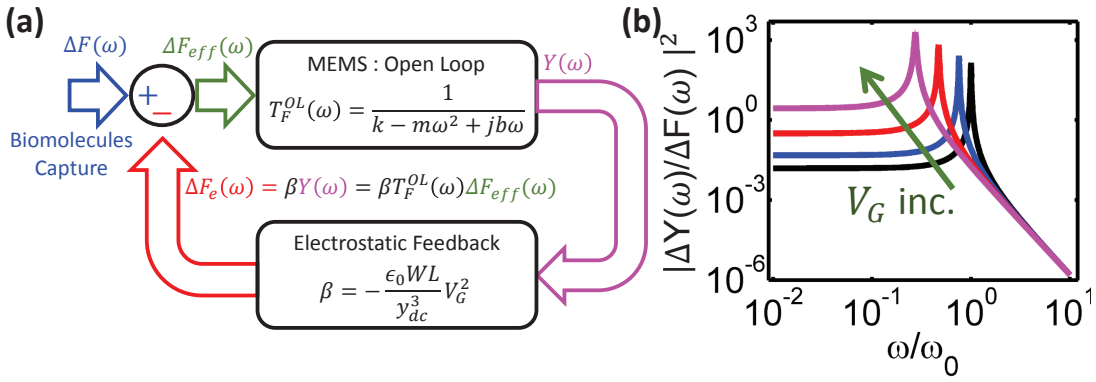

Fig. 6.6. (a) Representation of Flexure biosensor as a positive feedback system and (b)square of the magnitude of the corresponding closed loop transfer function at different voltages. As voltage increase, low frequency gain increases and resonance frequency decreases.

effect), results in large Δy_s, even for small Δk. Note that, Eq. 6.16 is valid slightly away from pull-in; whereas Eq. 6.3 is valid very close to pull-in. As we will show below, due to noise, Flexure sensors cannot be operated very close to pull-in. As a result, Eq. 6.16 will correctly estimate Δy_s.

Interestingly, closed loop system becomes unstable for $A\beta < -1$ and $A\beta = -1$ separates the stable and unstable regimes (point of pull-in instability). Note that, $A\beta = -1$ is equivalent to the condition of pull-in i.e., $k = \frac{\epsilon_0 WL}{y_{dc}^3} V_G^2$ for Flexure sensors [1].

The output noise power for Flexure sensor can also be evaluated using Eq. 6.15. We first divide the intrinsic noise of Flexure sensor in two categories namely stiffness noise and force noise. The stiffness noise will cause the stiffness to fluctuate randomly; whereas movable electrode will experience a random force due to force noise. We will below discuss the physical origin of each of these noise sources. We proceed by assuming that both force and stiffness noise are white in nature with power spectral density $S_F(\omega) = N_F$ and $S_k(\omega) = N_k$, respectively. The total noise power at the output is then given by-

$$\Delta y_N^F \equiv \sqrt{\int_0^\infty S_F(\omega) \left|\frac{\Delta Y(\omega)}{\Delta F(\omega)}\right|^2 d\omega} \approx \sqrt{\frac{N_F Q\omega_0/k^2}{1+A\beta}}, \tag{6.17}$$

$$\frac{\Delta y_N^k}{y_0 - y_{dc}} \equiv \sqrt{\int_0^\infty S_k(\omega) \left|\frac{\Delta Y(\omega)}{\Delta F(\omega)}\right|^2 d\omega} \approx \sqrt{\frac{N_k Q\omega_0/k^2}{1+A\beta}}, \tag{6.18}$$

where $Q = m\omega_0/b$ is the quality factor. Equations 6.16 - 6.17 implies that both Δy_N^F and Δy_N^k also increase when $A\beta \approx -1$. However, Δy_N^F and Δy_N^k increase at a slower rate compared to Δy_s due to different dependencies on $1 + A\beta$. Using Eqs. 6.16-6.18, SNR can be estimated as follows-

$$SNR^F \equiv \frac{\Delta y_s}{\Delta y_N^F} = \sqrt{\frac{(y_0 - y_{dc})^2 \Delta k^2}{N_F Q\omega_0 (1+A\beta)}}, \tag{6.19}$$

$$SNR^k \equiv \frac{\Delta y_s}{\Delta y_N^k} = \sqrt{\frac{\Delta k^2}{N_k Q\omega_0 (1+A\beta)}}, \tag{6.20}$$

which implies that SNR is also amplified by operating close to the point with $A\beta \approx -1$. Intuitively, this improvement in SNR can be understood as follows. First, operation close to the instability point increases the DC gain (Eq. 6.15), and thus amplifies the output signal Δy_s (Eq. 6.16). Second, had the bandwidth of the system remained constant or noise were a DC signal, the noise would have also gotten amplified in the same proportion as signal, leaving the SNR unchanged. However, the noise is AC. And, decrease in the bandwidth of the close loop system, helps reject the noise and improve SNR. Note that, the maximum value of SNR is not infinity (at $A\beta = -1$), but is governed by the value of $A\beta$ which is as close to negative one as possible, without making the system switch from stable to unstable regime due to the noise initiated transition. This simple analysis thus highlights the essence of this section. Below, we will evaluate SNR for various practical noise sources in Flexure biosensors.

Although, we have discussed SNR and LOD using the analysis based on linear transfer function, we want to point out that we have also carried full time domain analysis of noise using stochastic simulations. As discussed in the appendix E, the results obtained from the linear transfer function analysis (Eq. 6.15) are consistent with the time domain stochastic simulations (see Figs. E.1-E.2 appendix E).

6.2.2 SNR and LOD for Specific Noise Sources

We consider the following noise sources which are present in any nanoscale cantilever or beam based sensors.

(i) **Thermomechanical noise [147]** is the consequence of nanobeam being in thermal equilibrium with its surrounding at absolute temperature T. This noise exerts a random force on the beam with white power spectral density, given by-

$$S_F(\omega) = \frac{4k_B T m\omega_0}{Q}, \tag{6.21}$$

where k_B is the Boltzmann constant.

(ii) **Temperature fluctuations [148]** arises due to the small heat capacity of the nanobeam. Temperature fluctuations cause stiffness of the beam to change also. The power spectral density of corresponding fluctuations is given by-

$$S_k(\omega) = \left(\frac{\partial k}{\partial T}\right)^2 \frac{4k_B T^2}{\pi g} \frac{1}{1+(\omega\tau_T)^2} \tag{6.22}$$

where, $\partial k/\partial T$ is the rate of change of stiffness with temperature, $S_T(\omega)$ is the power spectral density of temperature fluctuations, g and τ_T are the thermal conductance and the thermal time constant associated with the nanobeam, respectively. Further details about each of the noise sources can be found in the refs. [147–150] and references therein. The goal of this section is not to discuss the origin or details of various noises sources, rather to understand how various noise sources interact with the movable gate and lead to fluctuations in the displacement. Note that, thermomechanical

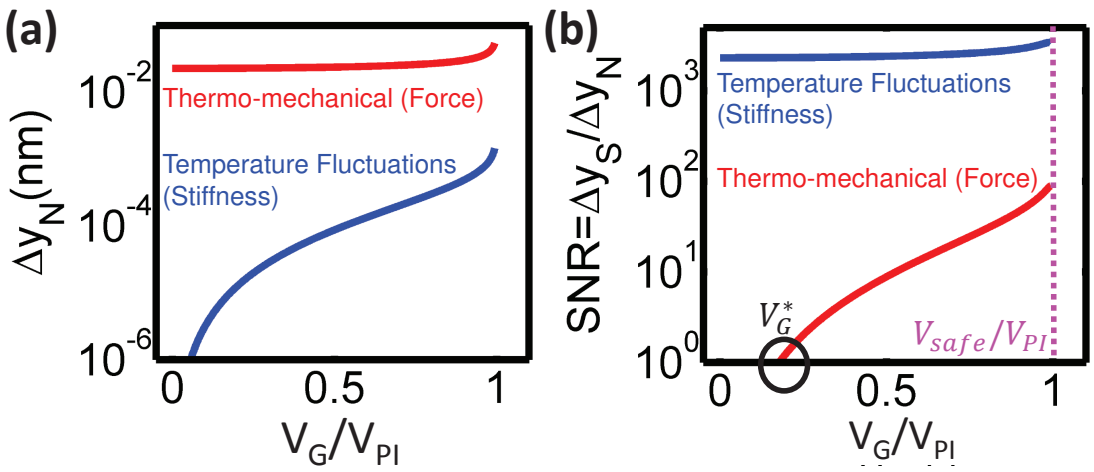

Fig. 6.7. (a) Root mean square fluctuations due to various noise sources and (b) corresponding signal-to-noise ratio as a function of applied bias for 5% change in the stiffness. The parameters used in simulations are $m = 1.26fg$,$\omega_0 = 8 \times 10^8 rad/s$, $Q = 100$, $g = 7.4 \times 10^{-6} W/K$, $\frac{1}{k}\frac{\partial k}{\partial T} = 10^{-3}/K$, and $\tau_T = 30ps$.

noise is a white force noise (no frequency dependence); whereas stiffness noise due to temperature fluctuations is also white provided $2\pi\omega_0^{-1} \gg \tau_T$, (Eq. 6.22), which is true for all practical purposes (see caption of Fig. 6.7 for various parameters). Therefore, analytical expressions of SNR will be directly relevant for both noise sources.

Figure 6.7 a shows Δy_N for both noise sources. The assumption of white noise is justified by the parameter values, $2\pi\omega_0^{-1} \approx 78ns$ which is much larger than τ_T. As expected from Eqs. 6.18 - 6.19, Δy_N increases with V_G and becomes maximum close to pull-in. The corresponding SNR for both type of noise sources is shown in Fig. 6.7 b and suggests that SNR also increases for all noise sources. The value of SNR is minimum for thermomechanical noise and this observation is consistent with the conclusions of the paper by Ekinci et al., [149]. Importantly, SNR is greater than one for stiffness noise at all values of V_G; whereas SNR$<$ 1 for $V_G < V_G^*$ for thermomechanical noise (see Fig. 6.7 b). This behavior can intuitively be understood as follows. The absence of any force on the movable electrode at $V_G = 0$, makes $\Delta y_s = 0$ irrespective of the change in the stiffness of the movable electrode; whereas

$\Delta y_N^F = \sqrt{k_B T/k}$ [151] for thermomechanical noise at $V_G = 0$, resulting in SNR= 0. Therefore, any change in the stiffness using Flexure sensors cannot be detected at $V_G = 0$. As V_G is increased, electrostatic force on the movable electrode increases and so does Δy_s (Eq. 6.16). Therefore, in order to detect a given change in the stiffness, a certain minimum V_G has to be applied. Also, note that Flexure sensor can not be operated very close to pull-in due to noise initiated pull-in (see next section). As a result, for proper functioning of the sensor, V_G should not exceed a safe operating voltage $V_{safe} < V_{PI}$. For the parameters considered in this section, $V_{safe} \approx 0.995 V_{PI}$.

Now, limit-of-detection for each type of noise source can simply be obtained by requiring SNR=3. The minimum detectable change in the stiffness (or LOD) is thus given by-

$$\Delta k_{min}^F = 3\sqrt{\frac{N_F Q \omega_0}{(y_0 - y_{dc})^2}(1 + A\beta)}, \tag{6.23}$$

$$\Delta k_{min}^k = 3\sqrt{N_k Q \omega_0 (1 + A\beta)}, \tag{6.24}$$

As expected from the increased SNR, both Δk_{min}^F and Δk_{min}^k decreases with increasing V_G (Fig. 6.8). Interestingly, Δk_{min} due to stiffness noise decreases with decreasing Q because of reduced bandwidth of the system (Fig. 6.8 b). On the other hand, Δk_{min} for thermomechanical noise is independent of Q because $N_F \propto 1/Q$ (Eqs. 6.21 & 6.23) (Fig. 6.8 a). It should be noted that the ultimate LOD is determined by the noise source with minimum SNR and that is thermomechanical noise for Flexure sensors.

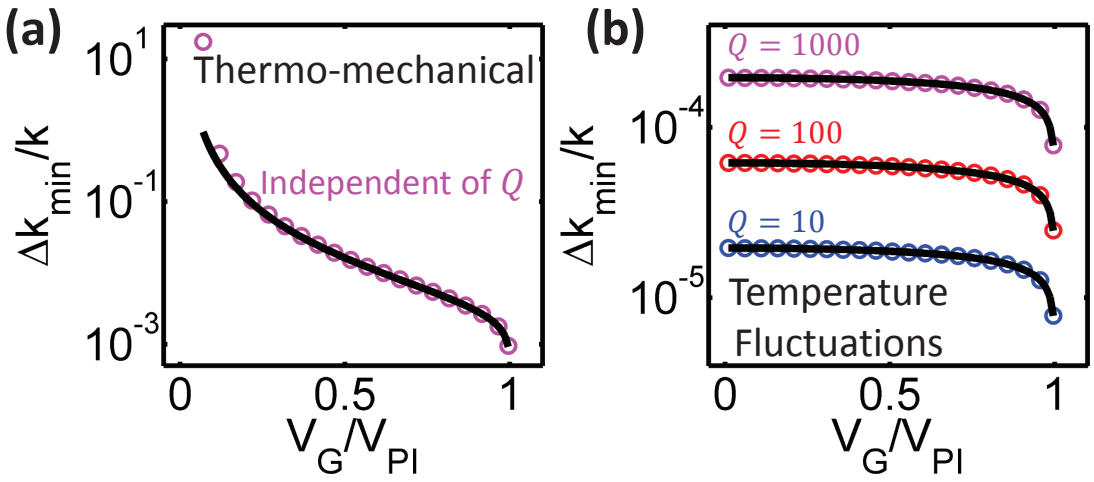

Fig. 6.8. Limit-of-Detection (LOD) for change in the stiffness limited by (a) thermomechanical noise and (b) temperature fluctuations.

6.2.3 Safe Operating Voltage to Avoid Noise Initiated Pull-in

We just saw that biasing close to pull-in improves both SNR and LOD. In this section, we answer a very important and fundamental question regarding the stability of Flexure sensors close to pull-in point. The question is "how close can we be to the pull-in point without making the sensor unstable?" Note that, in Figs. 6.7 - 6.8, V_G was swept from $V_G = 0$ to $V_G = 0.995V_{PI}$. Now, let us see, if biasing at $V_G = 0.995V_{PI}$ is practically possible or not. To answer this question, we look at the behavior of movable electrode in response to both force and stiffness noise using time domain stochastic simulations. Simulation framework has been discussed in detail in sections appendix E. Figure 6.9 a shows the potential energy ($U = \frac{1}{2}k\left(y_0 - y\right)^2 - \frac{\epsilon_0 WL}{2y}V_G^2$ landscape of Flexure sensor at $V_G = 0.995V_{PI}$. Movable electrode is stabilized at the minimum of U. In absence of noise, movable electrode should have remained at the bottom of potential energy well in Fig. 6.9 a (see the dotted line in Fig. 6.9 b also). However, thermomechanical noise exerts random force on the electrode making it fluctuate (reason for noise characterized by Δy_N^F) around its equilibrium position

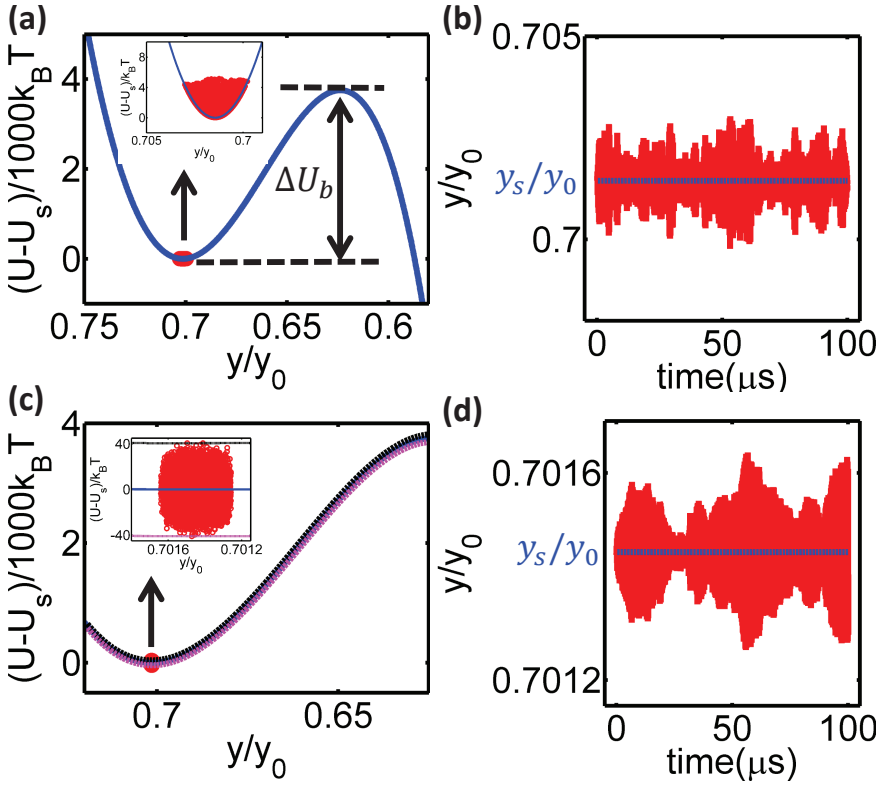

Fig. 6.9. Results of time domain stochastic simulations of a Flexure sensor at $V_G = 0.995V_{PI}$ with $\Delta U_b \approx 3.75 \times 10^3 k_B T$, due to (a)-(b) thermomechanical noise and (c)-(d) temperature fluctuations stiffness noise. U_s denote the potential energy at equilibrium position i.e., at the bottom of potential well. Symbols in Figs. a & c denote the total energy (kinetic + potential). Dotted black line in Fig. c correspond to maximum stiffness; whereas magenta line to minimum stiffness. Inset in Figs. a & c show the zoomed region around the bottom of potential well.

as shown in Figs. 6.9 a-b. Symbols in Fig. 6.9 a denote total energy (kinetic + potential) of movable electrode during fluctuations.

Due to the presence of a high energy barrier $\Delta U_b = U(y_u) - U(y_s) \approx 3.75 \times 10^3 k_B T$, ($y_s$: stable equilibrium position and y_u : unstable equilibrium position) movable electrode only fluctuates around the bottom of potential well in Fig. 6.9 a, but cannot surmount the energy barrier to make the system unstable. On the other

hand, stiffness noise due to temperature fluctuations will make the potential energy landscape fluctuate as shown in Fig. 6.9 c. Dotted black line corresponds to the potential energy profile for maximum stiffness; whereas dotted magenta for minimum stiffness. Due to the fluctuations in the stiffness, position of electrode fluctuates around its equilibrium position as shown in Figs. 6.9 c-d. However, the stiffness fluctuations are not strong enough to make the electrode pull-in. Therefore, we will classify $V_G = 0.995V_{PI}$ as the safe operating voltage.

Note that, if V_G is increased further, ΔU_b decreases and becomes $\Delta U_b \approx 5k_BT$ at $V_G = 0.99994V_{PI}$ as shown in Fig. 6.10 a. In this case, the movable electrode gets the sufficient energy from the surrounding to surmount the energy barrier and gets pulled-in as shown in Figs. 6.10 a-b. Therefore, $V_G = 0.99994V_{PI}$ cannot be classified as the safe operating voltage. Interestingly, pull-in at $V_G = 0.99994V_{PI}$ occurs due to thermomechanical noise, and not because of stiffness noise. However, if the voltage is increased even further, pull-in can occur due to stiffness noise because of temperature fluctuations as shown in Figs. 6.10 c-d. The bottom line from this section is that as we go closer and closer to pull-in point, chances of noise initiated pull-in increases. A safe operating voltage is that does not cause noise initiated pull-in or at least not in the time duration of measurement.

6.2.4 Discussions

Before we conclude this section, let us highlight some of the assumptions that were made during the analysis of SNR. First of all, we have modeled Flexure sensor using a single degree of freedom model and ignored all the details of the fixed-fixed beam [51,55]. Although, these details are important, spring-mass model captures very well the spring softening effect (positive feedback effect of a Flexure sensor) that is the sole reason of improvement in SNR. Therefore, even if we include the details of beam mechanics, it will only change the quantitative value of SNR, qualitative improvement in SNR will still remain the same. Also,we have neglected the spatial profile of

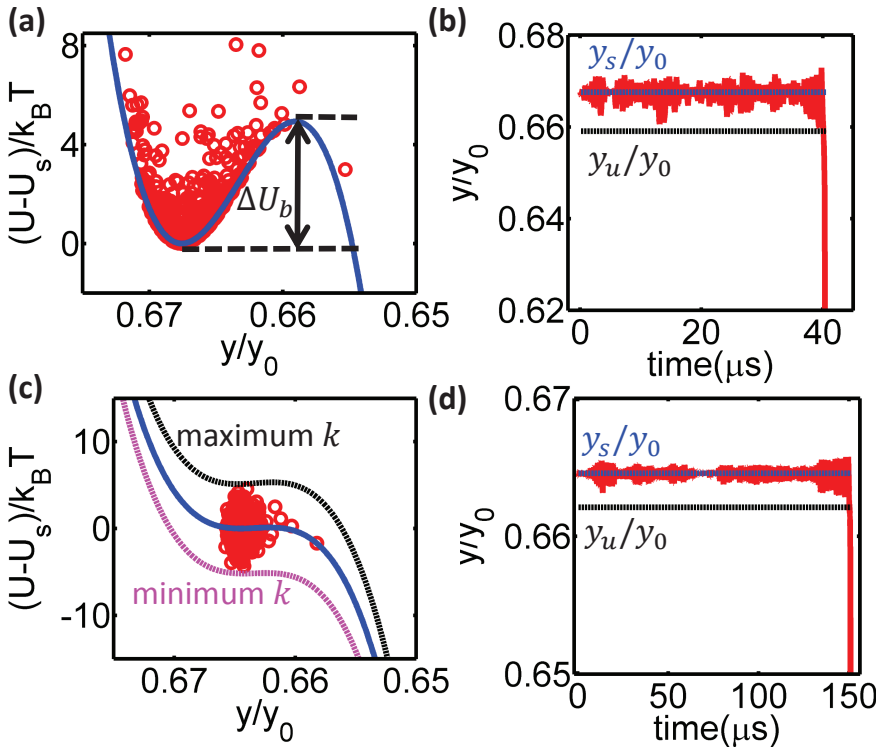

Fig. 6.10. Noise initiated pull-in due to (a)-(b) thermomechanical noise at $V_A = 0.99994V_{PI}$ with $\Delta U_b \approx 5k_BT$ and (c)-(d) stiffness noise due to temperature fluctuations at $V_A = 0.999995V_{PI}$. y_s corresponds to the stable equilibrium position; whereas y_u unstable.

adsorbed molecules on the movable electrode. The adsorption of biomolecules have been modeled assuming an effective change in the stiffness. Again, the details of the molecules adsorption on the surface are important, but will not modify the qualitative improvement in SNR due to positive feedback effect. Although, we have only considered two types of noise sources, the analysis framework and the conclusions are very general. If the input noise source is white, SNR corresponding to that source will always increase due to the reduced bandwidth close to pull-in.

6.2.5 Summary of Noise in Flexure Sensors

In this section, we have systematically analyzed the noise response of Flexure sensors using both linear transfer function analysis and time domain stochastic simulations. Surprisingly, both SNR and LOD improves close to the pull-in point. In presence of various noise sources considered, LOD is determined by thermomechanical noise. The analysis also provides the guidelines for the safe operating voltage to avoid noise initiated pull-in. We believe that the analysis presented in this section will serve as a platform for the analysis of SNR in other sensors that also operate at the boundary of stable and unstable regimes.

6.3 Conclusions

In this chapter:

- We showed another example in which instability or operation regime plays a critical role for performance enhancement. We showed that operation at the boundary between stable and unstable regimes can be advantageous for certain applications.
- We proposed a novel Flexure-FET biosensor that operate close to the pull-in instability and in subthreshold regime to achieve exponentially better sensitivity compared to the existing electronic/mechanical biosensors.
- Surprisingly, both signal-to-noise ratio and limit-of-detection improve close to the pull-in point. This improvement is the result of internal low pass filtering due to spring-softening effect, which reduces the resonance frequency close to pull-in.
- We found the voltage (called safe operating voltage) beyond which sensor will not function properly due to noise initiated pull-in. We also confirmed that

both sensitivity and signal-to-noise ratio at the safe operating voltage is higher than that of zero applied bias.

So far, we have covered many important aspects of instability starting from universal framework in chapter 3, novel solutions to the problems arising because of instability in chapter 4, and harnessing instability in this and previous chapter. In the next chapter, we will summarize all our findings and discuss the possible future directions.

7. SUMMARY AND FUTURE WORK

7.1 Summary

In this thesis, we have established fundamental design principles of Landau switches, sensors, and actuators. Landau systems such as MEMS capacitive actuators and ferroelectrics are bi-stable and their inherent instability divides the operation regime into stable and unstable. We proposed novel device solutions to the problems arising due to instability and harnessed instability for performance enhancement in novel Landau switches and Flexure sensors, respectively. The summary of the thesis is as follows:

Chapter 2 : Examples of Landau Systems

In this chapter, we illustrated the elementary physics of instability and its corresponding consequences in Landau systems.

- We discussed the origin of pull-in instability in MEMS capacitive actuators using both the evolution of energy landscapes and interaction of spring and electrostatic forces.
- We highlighted the consequences of pull-in instability on the static and dynamic response of MEMS capacitive actuators and established the concepts of spring-softening, negative capacitance, abrupt transition, hysteresis, dynamic pull-in, noise initiated pull-in, and hard-landing. Corresponding to each concept, we then pointed out applications in which the respective concept plays the critical role.

- We then discussed the origin of instability and its consequences such as negative capacitance behavior and hot-atom switching in ferroelectric materials.
- We concluded by identifying that MEMS capacitive actuators and ferroelectric materials belong to a broader class of "Landau" systems. Stable regimes are separated by an inherently unstable regime in each Landau system and that is a typical feature of all bi-stable systems.

Chapter 3 : Understanding Instability in MEMS

In this chapter, we develop a universal theory of instability of MEMS capactive actuators that works irrespective of the electrode geometry, nature of spring and/or actuation mechanisms.

- We unify the performance characteristics of electromechanical actuators through scaling relationships for pull-in instability, pull-in voltage/charge, and resonance frequency. These scaling relationships depend only on two scaling parameters, n and p, related to the electrostatic force and the nature of spring, respectively.
- We use these scaling relationships to explain a broad range of existing experimental data from literature in a single theoretical framework.
- We show how the scaling relationships can be used to characterize the electrode geometry and nature of spring for any new actuator.

Chapter 4 : Providing Solutions to the Problems due to Instability

In this chapter, we propose novel device designs to address the problems that arise due to the intrinsic instability of MEMS capacitive actuators.

- Pull-in instability limits the travel range of movable electrode to only one third of the initial air-gap in tunable-gap electromechanical actuators with planar electrodes and linear spring. To address the problem of limited travel range,

we proposed the idea of electrically reconfigurable nano-structured electrodes to extend the travel range beyond the fundamental limit of one third of the initial air-gap. The proposed electrically reconfigurable nano-structured electrodes also enable post fabrication tuning of the travel range.

- In RF-MEMS capacitive/ohmic switches or NEMS relays, during pull-in, the movable electrode hits the bottom dielectric or electrode with very high impact velocity and damages the surface. To address this problem of hard-landing, we proposed two novel strategies of dynamic soft-landing, namely resistive and capacitive braking. Resistive braking simply requires putting a resistance in series with the voltage source; whereas capacitive braking requires patterning of the bottom dielectric or electrodes. Both strategies reduce the impact velocity without affecting the pull-in voltage or time significantly.

Chapter 5 : Harnessing Negative Capacitance

This and the next chapter highlights "operation regime" as a new design variable in contrast to classical design variables such as material or geometry and focus on harnessing instability.

- Here, operation in the unstable regime leading to negative capacitance behavior of air-gap in MEMS capacitive actuators or ferroelectric materials, respectively, is utilized for the reduction of sub-threshold in field effect transistors.

- We show that Landau switches (or negative capacitance FETs) that have unstable gate insulators such as air-gap in suspended-gate FET or ferroelectric dielectric in ferroelectric-FET, typically exhibit abrupt switching characteristics ($0mV/decade$) with hysteresis.

- We discuss that stabilization of the unstable gate insulators using a series capacitor leads to hysteresis-free switching characteristics. This stabilization in the unstable regime results in the essential voltage amplification to reduce

body factor below one and sub-threshold swing below thermodynamic limit of $60mV/decade$.

- We establish that the sub-threshold swing cannot be arbitrarily reduced in NC-FETs. There is a fundamental lower limit of sub-threshold swing associated with each type of negative capacitance gate insulator or channel configuration, respectively. The existence of such a limit is the direct consequence of the stability constraints for hysteresis-free stable operation.

- We show that sub-threshold swing can be reduced in NC-FETs by improving the matching between the negative capacitance of the gate insulator and the positive series capacitance of the channel. The sub-threshold swing cannot however be reduced all the way to $0mV/decade$ in an NC-FET with single type of NC gate insulator. This is due to the presence of a point with infinite capacitance that restricts the perfect matching between the two capacitances and therefore make it impossible to achieve hysteresis-free $0mV/decade$ switching characteristics.

- We propose that the point of infinite capacitance can be bypassed in a series combination of two different types of negative capacitance gate insulators. This removal of the point of infinite capacitance will therefore enable perfect matching between the effective negative capacitance of the series combination and positive channel capacitance to realize hysteresis-free $0mV/decade$ switching characteristics.

- We illustrate the concept of hysteresis-free zero sub-threshold FET in a suspended-gate ferroelectric FET. The properly designed series combination of the air-gap and ferroelectric lead to a constant negative capacitance, which can be perfectly matched by the constant positive capacitance of the channel to achieve hysteresis-free $0mV/decade$ switching characteristics.

Chapter 6 : Harnessing Spring-Softening

In this chapter, we continue with the philosophy of harnessing instability and discuss our proposal of novel Flexure biosensors.

- We start this chapter with the proposal of a Flexure-FET biosensor in which the adsorption of biomolecules on a suspended-gate changes its stiffness. Change in the stiffness is reflected as a direct change in the drain current of the underneath FET. The operation of the proposed biosensor at the boundary between the stable and unstable regime results in maximum sensitivity towards capture of biomolecules due to spring-softening effect. At the same time, if the FET is biased in the sub-threshold regime, sensitivity of Flexure-FET biosensor becomes exponentially higher than existing electronic or mechanical biosensors.

- In order to ascertain the technological relevance of the novel biosensor, we systematically analyze its noise response to answer the fundamental question:" Does operation close to pull-in instability point also improve signal-to-noise ratio?" We find that the reduction in the resonance frequency close to the pull-in instability point due to spring-softening helps reject the high frequency noise and thus also improve the signal-to-noise ratio.

- Once we establish that Flexure sensors can also improve signal-to-noise ratio by operating close to the pull-in instability point, we ask another fundamental question:"How close can we operate close to the instability without making the system unstable?" Using the time domain stochastic simulations, we found the safe operating voltage at which the movable gate will not undergo noise initiated pull-in.

7.2 Future Work

The focus of this thesis has been to explore the fundamentals of instability in Landau systems - switches, sensors, and actuators. The contributions of the work are not only in exploring the fundamental science, but also in proposing novel device designs for several applications in the field of switching, sensing, and actuation. On the science side, the work explores the universal features of instability (chapter 3) and establishes fundamental limits of sub-threshold swing in negative capacitance field effect transistors (Chapter 5). On the applications side, the work has resulted into several novel device proposals which not only address the problems arising due to instability (chapter 4), but also harness instability for performance enhancement (chapters 5 & 6). Based on the work presented in this thesis, following directions can be explored both in experimental and theoretical fields:

7.2.1 Guidelines for Future Experiments

In this thesis, analytical modeling and numerical simulations have been used as a tool to explore the fundamentals of Landau systems. The role of simulations is not only to understand the physical phenomenon, but also to provide new directions to the experiments. Since this thesis has resulted into several novel ideas (Fig. 7.1), we believe these ideas can inspire future experiments in the following ways:

- **MEMS with Nanostructured Electrodes:** In chapter 4, we saw that the use of nanostructured electrodes (instead of classical planar) in MEMS can address the problem of travel range in tunable electromechanical actuators and hard-landing in MEMS based switches. One can focus on fabrication/characterization of MEMS devices with novel patterned electrodes and demonstrate the concept of extended travel range and soft-landing. MEMS with patterned electrodes will help verify the scaling relationships developed in chapter 3. The fabricated devices can also be used to generalize the scaling relationships to account for

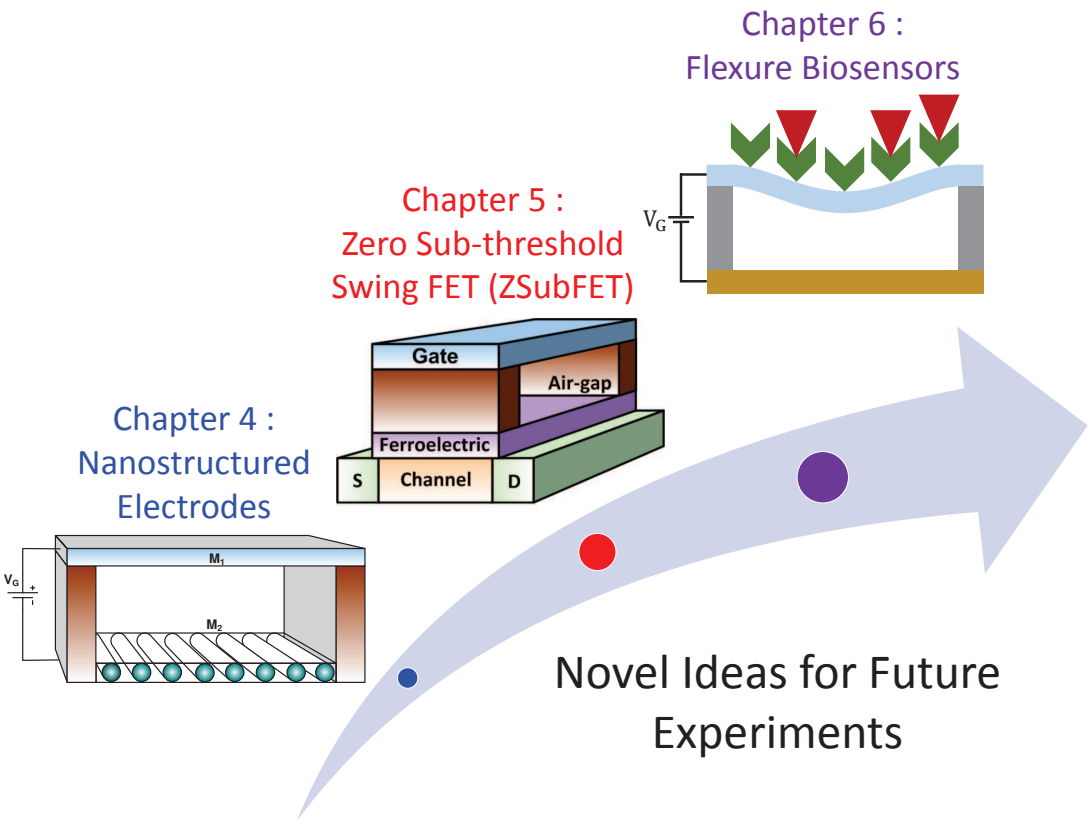

Fig. 7.1. Several novel devices proposals are the outcome of this thesis and should inspire future experiments in the field of switching, sensing, and actuation.

the non ideal effect such as residual stress [55] that may be present in a practical device.

- **Hysteresis-Free Suspended-Gate FET:** Since the proposal of negative capacitance field effect transistor in 2008 [19], there has been only one experimental demonstration of the concept on a ferroelectric capacitor structure [104] and one on a ferroelectric FET [103]. The field however lacks sufficient experimental data to clearly validate the concept and several related predictions e.g., minimum sub-threshold swing. In this direction, one can focus on the fabrication/characterization of suspended-gate FET (instead of ferroelectric FET)

and demonstrate (i) hysteresis-free sub-$60mV/decade$ switching characteristics and (ii) associated minimum sub-threshold swing. Although, SG-FET does not require fabrication of any specific material, it will have its own set of challenges such as creating air-gap above the semiconductor channel, suspending the gate, and controlling doping in the channel so that channel capacitance can stabilize the gate throughout the air-gap.

- **Hysteresis-Free Zero Sub-threshold Swing FET:** In chapter 5, we proposed the concept of hysteresis-free zero sub-threshold swing FET (ZSubFET) and demonstrated that suspended-gate ferroelectric FET can lower the sub-threshold swing all the way to $0mV/decade$. The fabrication/characterization of ZSubFET will not only validate the proposed concept, but can also help us explore fundamental questions regarding ideal switching characteristics. Since concept of ZSubFET requires a specific set of parameters as discussed in chapter 5, the challenge will be to achieve exact matching between ferroelectric and suspended-gate (needed for $0mV/decade$ switching) in presence of process variations.

- **Flexure Biosensors:** In chapter 6, we proposed novel Flexure sensors that utilize spring-softening effect to improve both the sensitivity and signal-to-noise ratio. Although, individual pieces of Flexure biosensors such as stiffness increase due to capture of biomolecules and maximum change in the displacement close to pull-in, have been experimentally demonstrated [118], complete demonstration of the novel sensor awaits. Along these lines, one can focus on the fabrication of Flexure sensor to establish the fundamental fact that both signal and signal-to-noise ratio increase at the boundary of stable and unstable regime. Like SG-FET challenge in the fabrication of Flexure biosensors will be creating the air-gap and suspending the gate. Moreover, if the measurements are performed in liquid environment, the biggest challenge will be to keep the

air-gap isolated from liquid. If liquid goes inside the air-gap, it may lead to malfunctioning of the device.

7.2.2 Analyzing the Available Experimental Data on Negative Capacitance

In chapter 5, we discussed negative capacitance behavior of MEMS and ferroelectric materials to achieve sub-$60mV/decade$ switching characteristics in FETs. Since 2008, when Salahuddin et al., [19] proposed negative capacitance (NC) for the first time, there have been couple of experimental works [103, 104, 152–155] on the proof-of-concept of NC. However, there are several puzzles in the available experimental data, which needs to be resolved before one confirms the presence of NC in an experiment. Below we lay down the key features of the available experiments and point out various puzzles, which needs to be resolved.

Historically, the temperature dependent hysteresis and it's disappearance above the curie temperature can be considered as a signature of the negative capacitor [156]. In the recent literature [103, 104, 152–155], when negative capacitor is being considered for voltage amplification in transistors, there have been experiments on two types of structures, namely, *capacitor* and *transistor* to experimentally demonstrate the concept of negative capacitance (NC). A capacitor structure consists of a series combination of a negative (a ferroelectric) and a positive capacitor; whereas a transistor structure employs a negative capacitor as the gate insulator. Before we discuss any specific experiments, let us highlight the key points that one should look to confirm the presence of an NC in an experiment.

1. In a capacitor structure, total capacitance of the series combination of a negative and positive capacitor should be higher than that of the positive capacitor. Since, the negative capacitance regime of a ferroelectric material is temperature dependent, one can use temperature as a variable to observe negative capacitance.

2. In a transistor structure, sub-threshold swing should be less than $60mV/decade$ *without* any hysteresis for low power applications. If there is any hysteresis associated with negative capacitor, the hysteresis window should not depend on the range as well as rate of voltage sweep.

3. If negative capacitor cannot be stabilized in the entirety of the unstable regime, there will be a hysteresis in the output characteristics characterized by branches with abrupt transition. The hysteresis window will however not depend on the range as well as rate of the voltage sweep.

It is also important to emphasize that the mere presence of any NC does not guarantee an improved transistor with lower sub-threshold swing. Other effects such as short channel effects and self-heating needs to be considered as well. Also, inability to observe NC does not mean that NC is impossible in principle. It is possible that the presence of domains in a ferroelectric and other non-idealities may be preventing from clear observations. With this background let us look at the available experimental data in literature-

Capacitor Structure

First, let us revisit the physics of negative capacitance in a series combination of a negative and positive capacitor. The total capacitance of the series combination of a ferroelectric and a regular series capacitor is given by (Fig. 7.2 a)-

$$C_G^{-1} = C_{FE}^{-1} + C_s^{-1}, \tag{7.1}$$

$$C_G^{-1} = \left(\alpha_0 + 3\beta_0 Q^2\right) y_{FE} + C_s^{-1}, \tag{7.2}$$

where C_{FE} is the capacitance of the ferroelectric, C_s is the capacitance of the series positive capacitor, α_0 and $\beta_0 > 0$ are material constant of ferroelectric material. Note

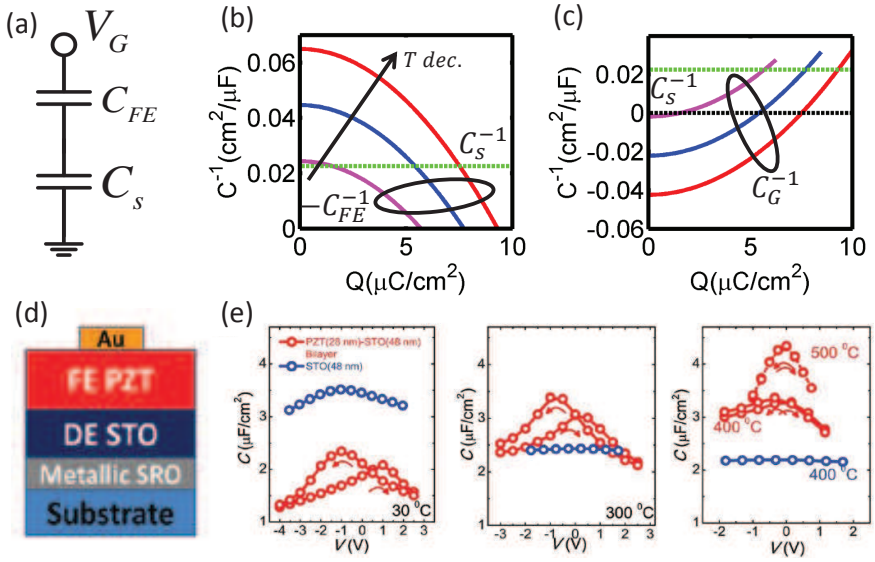

Fig. 7.2. (a) Capacitive divider model of the series combination of ferroelectric and regular capacitor and (b)-(c) Simulated capacitance of the ferroelectric highlighting the increase in the capacitance in the region when ferroelectric is stabilized in the unstable regime. (d) Schematic of the structure fabricated by Khan et al., [104] and (e) Corresponding experimental data (taken from [104]) of total capacitance at three different temperatures.

that, $\alpha_0 = \alpha\,(T - T_c)$ and is negative for $T < T_c$, where α is a material constant and T_c is curie temperature. Figure 7.2 b shows C_{FE} (< 0) for three different temperatures below T_c. C_s is a constant and is assumed to be independent of temperature. Note that, the negative capacitance of ferroelectric cannot be observed in isolation since ferroelectric is unstable in that regime. However, when it is in series with C_s, it can be stabilized in the negative capacitance regime provided total capacitance $C_G > 0$ [19]. Figure 7.2 c shows the corresponding total capacitance for constant C_s, which is positive at low T in a very limited range. However, as T is increased, α_0 decreases, and C_G becomes positive in a large range. Note that, whenever $C_G > 0$ with $C_{FE} < 0$, C_G is larger than C_s (signature of negative capacitance and point 1 mentioned above). However, if C_G becomes negative, the structure will become unstable once again, leading to hysteresis.

With this background, let us look at the experimental data by Khan et al., [104] in Figs. 7.2 d-e. They fabricated a stack of STO (regular positive capacitor) and PZT (temperature dependent negative capacitor) as shown in Fig. 7.2 a. Using temperature as the tuning parameter (ranging from $30°C - 500°C$), they showed that the capacitance of the series combination (Fig. 7.2 d) was larger than the capacitance of STO (Fig. 7.2 e). They observed this increase in the capacitance over large range of frequencies (ranging from $100KHz - 1MHz$), various thicknesses of PZT ($28nm$, $29nm$, and $64nm$) and STO ($48nm$, $46nm$,$54nm$), and over wide temperature range [104]. Based on these observations, they attributed the increase in the capacitance to the negative capacitance of PZT and thus providing a proof-of-concept of negative capacitance of ferroelectric materials. Since temperature dependence of total capacitance is consistent with the theory discussed above, negative capacitance observed in capacitor structure can be attributed to the real negative capacitance of ferroelectric materials. Since Khan et al., [104] observed negative capacitance at very high temperature ($300°C - 500°C$), which may not be relevant for room temperature applications, a proof-of-concept of negative capacitance at room temperature (27°) was recently provided by Appleby et al., [154], again in a capacitor structure with $BaTiO_3$ (thickness $20nm$, $30nm$, $50nm$) as the ferroelectric material and STO as the regular positive capacitor (thickness $25nm$).

Transistor Structure

We have so far seen that the experiments done on the capacitor structures provide a reasonable proof-of-concept of negative capacitance of ferroelectric materials. We now look at the other set of experiments performed on the transistor structures with ferroelectric [103, 152, 155] material or a polarization layer [153] as the gate insulator. The summary of the experimental observations is as follows-

- Experimental data shows sub-$60mV/decade$ switching characteristics *with* hysteresis (Fig. 7.3). In some cases, sub-$60mV/decade$ is observed along one branch

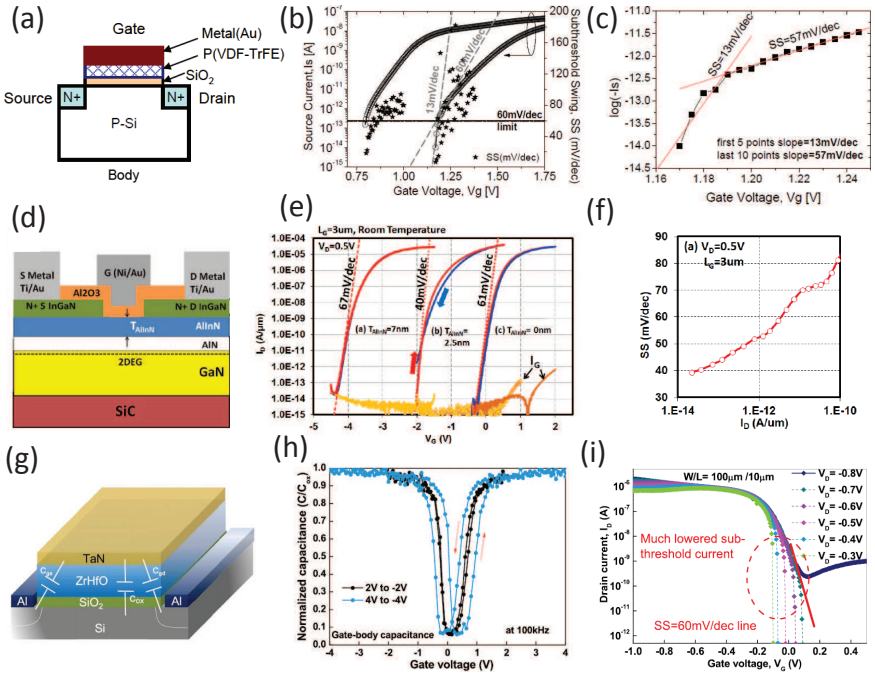

Fig. 7.3. Hysteretic sub-60mV/decade switching characteristics observed in experiments. (a) Schematic of a ferroelectric FET with a polymer ferroelectric as the gate insulator [103], (b) current-voltage characteristics showing sub-60mV/decade switching with hysteresis, and (c) sub-threshold swing as a function of gate voltage. (Data taken from [103]) (d) Schematic of a HEMT with AlInN as the polarization layer [153], (e) corresponding thickness dependent current-voltage characteristics showing sub-60mV/decade switching, and (f) sub-threshold swing as a function of the drain current. (Data taken from [153]) (g) Schematic of a transistor with ZrHfO as the ferroelectric material [155], (h) range of voltage sweep dependent hysteretic capacitance voltage characteristics, and (i) corresponding hysteretic sub-60mV/decade current-voltage characteristics. (Data taken from [155])

only [153] (Figs. 7.3 d-f), while in other cases sub-60$mV/decade$ switching occurs along both branches [103, 152, 155] (Figs. 7.3 a-c & g-i).

- Sub-threshold swing in Figs. 7.3 b-c is less than 60mV/decade only at five points at very low current values. For majority of the experimental data points, sub-threshold swing is close to 60$mV/decade$.

- Hysteresis window depends upon the range of sweep voltages [152, 153, 155]. As the range of sweep voltage increases, hysteresis window increases as well (Fig. 7.3 h).

In the literature, this hysteretic sub-60$mV/decade$ switching characteristics along one or both branches has been attributed to the negative capacitance of the underlying gate insulator. First, the hysteresis loop defeats the main purpose of NC-FETs, namely, to reduce the power supply voltage. Second, although one cannot deny the experimental hysteretic sub-60$mV/decade$ switching characteristics, one should be very careful before correlating it with the negative capacitance of the ferroelectric material due to following reasons. Both the experimental observations are not in accordance with the points (two and three mentioned previously), namely, (i) sub-60$mV/decade$ switching due to negative capacitor should be hysteresis-free for low power applications and (ii) if there is any hysteresis associated with the negative capacitor, it should be independent of the range as well as the rate of voltage sweep. Without addressing the origin of hysteresis in these transistor structures, it will not be reasonable to associate sub-60$mV/decade$ switching with negative capacitance.

In general, hysteretic sub-60$mV/decade$ switching characteristics may also arise in one of the following two ways. First, if the internal charges inside the gate insulator (which is ferroelectric in this case) move slowly compared to the voltage sweep rate, one may observe hysteresis in the output current-voltage characteristics. Also, sub-threshold swing could be lower than 60$mV/decade$ during the downward voltage sweep. Moreover, the hysteresis window will also depend on the range of voltage sweep since larger voltage will induce more internal charges. Some of these features of charging appears to be present in Fig. 7.3.

Second, hysteretic sub-60$mV/decade$ switching characteristics may also arise because of the poly-crystalline nature of the ferroelectric. A poly-crystalline material will have several grains and each grain will switch at a different voltage. We can view a transistor with poly-crystalline ferroelectric as gate insulator as several transistors connected in parallel with single crystalline ferroelectric as gate insulators (each with

different switching voltage). The current voltage characteristics for each of such parallel transistors will be hysteretic with abrupt transition. The total current will be sum of the individual currents and can in principle exhibit sub-$60mV/decade$ switching. Although, both of these hypothesis will require detailed analysis, they highlight that hysteretic sub-$60mV/decade$ switching may arise because of other reasons also, which one should carefully consider while interpreting the experimental data.

One of the key goals of the future work will be to isolate these parasitic effects from negative capacitance phenomena.

7.2.3 Minimum Power Supply Voltage

In chapter 5, we proposed a switch that in principle can achieve ideal switching characteristics i.e., $0mV/decade$ sub-threshold swing without any hysteresis. This proposal of ideal switch raises a question of fundamental interest:" What is the corresponding power supply voltage and energy dissipation?" Without the answer to this question, it is difficult to ascertain the relevance of an ideal switch. As briefly mentioned in chapter 5, the answer to this question will fundamentally be determined by noise considerations and error probabilities. The work will require identifying various noise sources associated with movable gate, ferroelectric dielectric, and semiconductor channel in ZSubFET. Based on the analysis of various noise sources, one would require to calculate the power supply voltage corresponding to an allowed error probability (for accidental switching from one state to another) [102].

7.2.4 Single Molecule Detection

In chapter 6, we proposed novel Flexure sensors, which amplify both the signal and signal-to-noise ratio (SNR) close to the instability point. The extreme sensitivity of these sensors raises a very important and technologically relevant question: "Can novel Flexure biosensors detect single molecule and enable early stage detection of fatal diseases?" First of all, the answer to this question will require modeling of

Flexure sensors using Euler-Bernoulli (EB) framework (section A.1.1) (as opposed to lumped parameter spring-mass model in chapter 6). EB framework will help understand how does the position of molecule on the movable gate affect the signal. Second, in order to evaluate the corresponding SNR, one would require noise analysis of the beam (again as opposed to spring-mass system in chapter 6). Based on the analysis of position dependent signal and SNR, one can find out the molecules which can be detected using Flexure sensor.

7.2.5 Exploring Other Instabilities

In this thesis, we have explored the fundamentals of instability by using pull-in instability of MEMS capacitive actuators as an illustrative example. In the future, one can explore other kind of instabilities, which may be present in a MEMS capacitive actuator.

Buckling Instability

In this thesis throughout, we did not consider any axial load in the movable electrode, i.e., $P = 0$ in Eq. 2.1. If a compressive axial load ($P > 0$ by definition) is present and is above a critical load, the movable electrode may be buckled up or down. As a part of the future work, one can explore the effect of this buckling on the negative capacitance and sub-threshold swing in chapter 5. The work will require exploring how does drain current change as a function of P and how does buckling transition affect switching characteristics of suspended-gate FET.

One can also use buckling of the movable gate for stress based sensing. Change in the stress of a movable electrode has previously been used for vapor, pH and/or biomolecules [139, 157, 158], but with limited sensitivity. Inspired from the idea of operating close to an instability point for better sensitivity and SNR, one can explore novel sensors operating close to the buckling instability point. One can also explore

the extra advantages that can be obtained through exploitation of both pull-in and buckling instability.

Ferroelastic Materials

In chapter 2-6, we focused on MEMS actuators in which the material of movable electrode was presumed to be linear elastic. Linear elastic materials have a parabolic energy dispersion such that $U = \frac{1}{2}E\epsilon^2$, where U is the energy per unit volume, E is the Young's modulus and ϵ is the strain. Therefore, they follow a linear $\sigma = E\epsilon$ stress (σ)-strain (ϵ) relationship. As mentioned in appendix A, the modeling framework developed in this thesis, is applicable to only linear elastic materials. However, there are ferroelastic materials [159], which do not follow linear stress-strain relationship. Like other ferroics e.g., ferromagnets and ferroelectric, they have two well potential energy landscape and are characterized by an intrinsic instability. As a part of the future work, one can explore MEMS capacitive actuators in which movable electrode is made of a ferroelastic material. One can try to answer the questions such as:(i) how will the pull-in instability change?, (ii) can one get additional advantages in a suspended-gate FET, (iii) will the sensitivity of Flexure sensors with ferroelastic membrane be better than conventional sensors?

7.3 Conclusions

To conclude, this thesis advances the field of MEMS by proposing electrode geometry as a new design variable and the field of electronic devices such as transistors by proposing operation regime as a new design variable. We believe that the novel device proposals will provide new directions to researchers working in both theoretical and experimental fields. Since this thesis introduces several new concepts regarding instability, we hope that the work may find applications in other fields beyond MEMS and FETs as well.

LIST OF REFERENCES

LIST OF REFERENCES

[1] H. C. Nathanson, W. E. Newell, R. A. Wickstrom, and J. R. Davis, "The Resonant Gate Transistor," *Transactions on Electron Devices*, vol. 14, no. 3, pp. 117–133, 1967.

[2] R. Bogue, "MEMS sensors: Past, Present and Future," *Sensor Review*, vol. 27, no. 1, 2007.

[3] W. S. N. Trimmer, "Microrobots and Micromechanical Systems," *Sensors and Actuators*, vol. 19, 1989.

[4] F. Chollet and H. Liu, *A (not so) short introduction to MEMS*. Creative Commons, 2011.

[5] B. Vigna, "Physical Sensors drive MEMS Consumerization Wave," in *Proceedings of the International Micromachine/Nanotech Symposium*, 2007.

[6] ITRS, "Micro-Electro-Mechanical-Systems (MEMS)," tech. rep., International Technology Roadmap for Semiconductors, 2011.

[7] W. Josh, "www.forbes.com."

[8] D. Dudley, W. Duncan, and J. Slaughter, "Emerging Digital Micromirror Device (DMD) Applications," tech. rep., Texas Instruments, Inc., 2008.

[9] Y. Development, "MEMS for Cell Phones and Tablets," tech. rep., Yole Development, 2012.

[10] P. Jeff, "MEMS Everywhere Marker Update," tech. rep., Yole Development, 2012.

[11] B. Vigna, "More than Moore: micro-machined products enable new applications and open new markets," in *IEDM*, 2005.

[12] W. Arden, M. Brillouët, P. Cogez, M. Graef, B. Huizing, and R. Mahnkopf, "More than Moore," tech. rep., International Roadmap Committee, 2012.

[13] M. Bohr, "The Evolution of Scaling from the Homogeneous Era to the Heterogeneous Era," in *IEDM*, pp. 1–6, 2011.

[14] I. Ferain, C. a. Colinge, and J.-P. Colinge, "Multigate transistors as the future of classical metal-oxide-semiconductor field-effect transistors.," *Nature*, vol. 479, pp. 310–6, Nov. 2011.

[15] N. Singh, A. Agarwal, L. Bera, T. Liow, R. Yang, S. Rustagi, C. Tung, R. Kumar, G. Lo, N. Balasubramanian, and D.-L. Kwong, "High-performance fully depleted silicon nanowire (diameter /spl les/ 5 nm) gate-all-around CMOS devices," *IEEE Electron Device Letters*, vol. 27, pp. 383–386, May 2006.

[16] T. Dürkop, S. A. Getty, E. Cobas, and M. S. Fuhrer, "Extraordinary Mobility in Semiconducting Carbon Nanotubes," *Nano Letters*, vol. 4, pp. 35–39, Jan. 2004.

[17] S. Z. Butler, S. M. Hollen, L. Cao, Y. Cui, J. A. Gupta, H. R. Gutiérrez, T. F. Heinz, S. S. Hong, J. Huang, A. F. Ismach, E. Johnston-Halperin, M. Kuno, V. V. Plashnitsa, R. D. Robinson, R. S. Ruoff, S. Salahuddin, J. Shan, L. Shi, M. G. Spencer, M. Terrones, W. Windl, and J. E. Goldberger, "Progress, challenges, and opportunities in two-dimensional materials beyond graphene.," *ACS nano*, vol. 7, pp. 2898–926, Apr. 2013.

[18] A. M. Ionescu and H. Riel, "Tunnel field-effect transistors as energy-efficient electronic switches.," *Nature*, vol. 479, pp. 329–37, Nov. 2011.

[19] S. Salahuddin and S. Datta, "Use of negative capacitance to provide voltage amplification for low power nanoscale devices.," *Nano letters*, vol. 8, pp. 405–10, Feb. 2008.

[20] V. Pott, H. Kam, R. Nathanael, J. Jeon, E. Alon, and T.-J. King Liu, "Mechanical Computing Redux: Relays for Integrated Circuit Applications," *Proceedings of the IEEE*, vol. 98, pp. 2076–2094, Dec. 2010.

[21] N. Abele, R. Fritschi, K. Boucart, F. Casset, P. Ancey, and A. M. Ionescu, "Suspended-Gate MOSFET: bringing new MEMS functionality into solid-state MOS transistor," in *IEDM*, 2005.

[22] K. E. Petersen, "Silicon as a Mechanical Material," *Proceedings of The IEEE*, vol. 70, no. 5, 1982.

[23] F. Battiston, J.-P. Ramseyer, H. Lang, M. Baller, C. Gerber, J. Gimzewski, E. Meyer, and H.-J. Güntherodt, "A chemical sensor based on a microfabricated cantilever array with simultaneous resonance-frequency and bending readout," *Sensors and Actuators B: Chemical*, vol. 77, pp. 122–131, June 2001.

[24] J. L. Arlett, E. B. Myers, and M. L. Roukes, "Comparative advantages of mechanical biosensors," *Nature Nanotechnology*, vol. 6, pp. 203–215, 2011.

[25] T. Bifano, "Adaptive imaging: MEMS deformable mirrors," *Nature Photonics*, vol. 5, pp. 21–23, Jan. 2011.

[26] Q. M. Technologies, "Value Proposition of mirasol Displays," tech. rep., Qualcomm Technologies, 2011.

[27] D. J. Young and B. E. Boser, "A Micromachine-Based RF Low-Noise Voltage-Controlled Oscillator," in *Custom Integrated Circuits Conference*, 1997.

[28] G. M. Rebeiz and J. B. Muldavin, "RF MEMS switches and switch circuits," *IEEE Microwave Magazine*, vol. 2, pp. 59–71, 2001.

[29] T. Bifano, J. Perreault, R. Krishnamoorthy Mali, and M. Horenstein, "Microelectromechanical deformable mirrors," *IEEE Journal of Selected Topics in Quantum Electronics*, vol. 5, no. 1, pp. 83–89, 1999.

[30] J. J. Yao, "RF MEMS from a device perspective," *Journal of Micromechanics and Microengineering*, vol. 10, pp. R9–R38, 2000.

[31] H. J. De Los Santos, G. Fischer, H. A. C. Tilmans, and J. T. M. van Beek, "RF MEMS for ubiquitous wireless connectivity: Part 2 - Application," *IEEE Microwave Magazine*, vol. 5, pp. 50–65, 2004.

[32] F. Chen, H. Kam, D. Markovic, T.-J. K. Liu, V. Stojanovic, and E. Alon, "Integrated circuit design with NEM relays," in *2008 IEEE/ACM International Conference on Computer-Aided Design*, pp. 750–757, IEEE, Nov. 2008.

[33] S. Pamidighantam, R. Puers, K. Baert, and H. A. C. Tilmans, "Pull-in voltage analysis of electrostatically actuated beam structures with fixed-fixed and fixed-free end conditions," *Journal of Micromechanics and Microengineering*, vol. 12, pp. 458–464, July 2002.

[34] S. Sze and J. Irvin, "Resistivity, mobility and impurity levels in GaAs, Ge, and Si at 300K," *Solid-State Electronics*, vol. 11, pp. 599–602, June 1968.

[35] D. H. Werner and S. Ganguly, "An overview of fractal antenna engineering research," *IEEE Antennas and Propagation Magazine*, vol. 45, pp. 38–57, 2003.

[36] P. R. Nair and M. A. Alam, "Performance limits of nanobiosensors," *Applied Physics Letters*, vol. 88, p. 233120, June 2006.

[37] G. M. Rebeiz, *RF MEMS: Theory, Design, and Technology*. John Wiley & Sons, 2003.

[38] E. K. Chan, E. C. Kan, and R. W. Dutton, "Nonlinear Dynamic Modeling of Micromachined Switches," *IEEE MTT-S Digest*, vol. 3, pp. 1511–1514, 1997.

[39] X. H. Guo and A. Alexeenko, "Compact model of squeeze-film damping based on rarefied flow simulations," *Journal of Micromechanics and Microengineering*, vol. 19, 2009.

[40] R. H. Rand, "Lecture Notes on Nonlinear Vibrations," 2004.

[41] S. H. Strogatz, *Nonlinear Dynamics And Chaos: With Applications To Physics, Biology, Chemistry, And Engineering*. Westview Press, 2001.

[42] K. M. Rabe, C. H. Ahn, and J.-M. Triscone, eds., *Physics of Ferroelectrics: A Modern Perspective*. Springer-Verlag, 2007.

[43] M. Masuduzzaman and M. A. Alam, "Hot atom damage (HAD) limited TDDB lifetime of ferroelectric memories," in *2013 IEEE International Electron Devices Meeting*, pp. 21.4.1–21.4.4, IEEE, Dec. 2013.

[44] S. Krylov, B. R. Ilic, D. Schreiber, S. Seretensky, and H. Craighead, "The pull-in behavior of electrostatically actuated bistable microstructures," *Journal of Micromechanics and Microengineering*, vol. 18, p. 055026, May 2008.

[45] A. Jain and M. A. Alam, "Universal Resonant and Pull-in Characteristics of Tunable-Gap Electromechanical Actuators," *IEEE Transactions on Electron Devices*, vol. 60, pp. 4240–4247, Dec. 2013.

[46] V. Sazonova, Y. Yaish, H. Ustunel, D. Roundy, T. A. Arias, and P. L. McEuen, "A tunable carbon nanotube electromechanical oscillator," *Nature*, vol. 431, pp. 284–287, 2004.

[47] R. R. He, X. L. Feng, M. L. Roukes, and P. D. Yang, "Self-transducing silicon nanowire electromechanical systems at room temperature," *Nano Letters*, vol. 8, pp. 1756–1761, 2008.

[48] A. Arun, S. Campidelli, A. Filoramo, V. Derycke, P. Salet, A. M. Ionescu, and M. F. Goffman, "SWNT array resonant gate MOS transistor," *Nanotechnology*, vol. 22, 2011.

[49] L. Midolo, P. J. van Veldhoven, M. A. Dundar, R. Notzel, and A. Fiore, "Electromechanical wavelength tuning of double-membrane photonic crystal cavities," *Applied Physics Letters*, vol. 98, no. 21, 2011.

[50] J. S. Bunch, A. M. van der Zande, S. S. Verbridge, I. W. Frank, D. M. Tanenbaum, J. M. Parpia, H. G. Craighead, and P. L. McEuen, "Electromechanical resonators from graphene sheets.," *Science*, vol. 315, pp. 490–3, Jan. 2007.

[51] M. I. Younis, E. M. Abdel-Rahman, and A. Nayfeh, "A reduced-order model for electrically actuated microbeam-based MEMS," *Journal of Microelectromechanical Systems*, vol. 12, pp. 672–680, 2003.

[52] M. Dequesnes, S. V. Rotkin, and N. R. C. P. I. I. S.-.-. Aluru, "Calculation of pull-in voltages for carbon-nanotube-based nanoelectromechanical switches," *Nanotechnology*, vol. 13, pp. 120–131, 2002.

[53] H. Ustünel, D. Roundy, and T. A. Arias, "Modeling a suspended nanotube oscillator.," *Nano letters*, vol. 5, pp. 523–6, Mar. 2005.

[54] S. Sapmaz, Y. Blanter, L. Gurevich, and H. van der Zant, "Carbon nanotubes as nanoelectromechanical systems," *Physical Review B*, vol. 67, June 2003.

[55] E. M. Abdel-Rahman, M. I. Younis, and A. H. Nayfeh, "Characterization of the mechanical behavior of an electrically actuated microbeam," *Journal of Micromechanics and Microengineering*, vol. 12, pp. 759–766, 2002.

[56] B. Witkamp, M. Poot, and H. S. J. van der Zant, "Bending-mode vibration of a suspended nanotube resonator," *Nano Letters*, vol. 6, pp. 2904–2908, 2006.

[57] H. M. Ouakad and M. I. C. A. . Younis, "Nonlinear Dynamics of Electrically Actuated Carbon Nanotube Resonators," *Journal of Computational and Nonlinear Dynamics*, vol. 5, 2010.

[58] A. Dehé, R. Aigner, and L. M. Castañer, "Current Drive Methods to Extend the Range of Travel of Electrostatic Microactuators Beyond the Voltage Pull-In Point," *Journal of Microelectromechanical Systems*, vol. 11, no. 3, pp. 255–263, 2002.

[59] J. I. Seeger and B. E. Boser, "Charge Control of Parallel-Plate , Electrostatic Actuators and the Tip-In Instability," *Journal of Microelectromechanical Systems*, vol. 12, no. 5, pp. 656–671, 2003.

[60] E. Hung and S. Senturia, "Extending the travel range of analog-tuned electrostatic actuators," *Journal of Microelectromechanical Systems*, vol. 8, no. 4, pp. 497–505, 1999.

[61] S. Palit, A. Jain, and M. Ashraful Alam, "Universal scaling and intrinsic classification of electro-mechanical actuators," *Journal of Applied Physics*, vol. 113, p. 144906, Apr. 2013.

[62] J. I. Seeger and B. E. Boser, "Dynamics and Control of Parallel-Plate Actuators Beyond the Electrostatic Instability," in *Transducers*, pp. 474–477, 1999.

[63] E. K. Chan and R. W. Dutton, "Electrostatic Micromechanical Actuator with Extended Range of Travel," *Journal of Microelectromechanical Systems*, vol. 9, no. 3, pp. 321–328, 2000.

[64] S. Akita, Y. Nakayama, S. Mizooka, Y. Takano, T. Okawa, Y. Miyatake, S. Yamanaka, M. Tsuji, and T. Nosaka, "Nanotweezers consisting of carbon nanotubes operating in an atomic force microscope," *Applied Physics Letters*, vol. 79, no. 11, p. 1691, 2001.

[65] E. R. Deutsh, *Achieving Large Stable Vertical Displacement in Surface Micro-Machined Microelectromechanical Systems (MEMS)*. PhD thesis, Massachusetts Institute of Technology, 2002.

[66] O. Bochobza-Degani, D. Elata, and Y. Nemirovsky, "A general relation between the ranges of stability of electrostatic actuators under charge or voltage control," *Applied Physics Letters*, vol. 82, no. 2, p. 302, 2003.

[67] H. A. C. Tilmans and R. Legtenberg, "Electrostatically driven vacuum-encapsulated polysilicon resonators part II. theory and performance," *Sensors and Actuators a-Physical*, vol. 45, pp. 67–84, 1994.

[68] W. Y. Fung, E. N. Dattoli, and W. Lu, "Radio frequency nanowire resonators and in situ frequency tuning," *Applied Physics Letters*, vol. 94, p. 203104, May 2009.

[69] Y. Dong-xu, H. Hong, and Y. Wei-min, "Nonlinear Dynamic Characterization of Electro-statically Actuated Sub-micro Beam Resonator," *Proc. of SPIE*, vol. 7381, 2009.

[70] N. Olofsson, J. Ek-Weis, A. Eriksson, T. Idda, and E. E. B. Campbell, "Determination of the effective Young's modulus of vertically aligned carbon nanotube arrays: a simple nanotube-based varactor.," *Nanotechnology*, vol. 20, p. 385710, Sept. 2009.

[71] O. Bochobza-Degani, D. Elata, and Y. Nemirovsky, "A general relation between the ranges of stability of electrostatic actuators under charge or voltage control," *Applied Physics Letters*, vol. 82, no. 2, p. 302, 2003.

[72] K. C.-H., P. N., P. B., and E. H.D., "Experiments and modeling of carbon nanotube-based NEMS devices," *Journal of the Mechanics and Physics of solids*, vol. 53, pp. 1314–1333, 2005.

[73] A. Jain, P. R. Nair, and M. a. Alam, "Strategies for dynamic soft-landing in capacitive microelectromechanical switches," *Applied Physics Letters*, vol. 98, no. 23, p. 234104, 2011.

[74] A. Jain and M. A. Alam, "Extending and Tuning the Travel Range of Microelectromechanical Actuators Using Electrically Reconfigurable Nano-Structured Electrodes," *Journal of Microelectromechanical Systems*, vol. 22, pp. 1001–1003, Oct. 2013.

[75] F. Sugihwo, M. Larson, and J. Harris, "Micromachined widely tunable vertical cavity laser diodes," *Journal of Microelectromechanical Systems*, vol. 7, pp. 48–55, Mar. 1998.

[76] R. Zengerle, A. Richter, and H. Sandmaier, "A micro membrane pump with electrostatic actuation," in *Proceedings of IEEE Micro Electro Mechanical Systems*, pp. 19–24, Ieee, 1992.

[77] P. B. Chu and K. S. J. Pister, "Analysis of Closed-loop Control of Parallel-Plate Electrostatic MicroGrippers," in *IEEE International Conference on Robotics and Automation*, pp. 3–8, 1994.

[78] D. Piyabongkarn, Y. Sun, R. Rajamani, A. Sezen, and B. Nelson, "Travel range extension of a MEMS electrostatic microactuator," *IEEE Transactions on Control Systems Technology*, vol. 13, pp. 138–145, Jan. 2005.

[79] J. I. Seeger and S. B. Crary, "Stabilization of electrostatically actuated mechanical devices," in *Transducers*, pp. 1133–1136, 1997.

[80] C. H. Lee, D. R. Kim, and X. L. Zheng, "Fabricating nanowire devices on diverse substrates by simple transfer-printing methods," *Proceedings of the National Academy of Sciences of the United States of America*, pp. 9950–9955, 2010.

[81] M. W. Li, R. B. Bhiladvala, T. J. Morrow, J. A. Sioss, K. K. Lew, J. M. Redwing, C. D. Keating, and T. S. Mayer, "Bottom-up assembly of large-area nanowire resonator arrays," *Nature Nanotechnology*, pp. 88–92, 2008.

[82] H. J. Kim, C. Son, and B. Ziaie, "A multiaxial stretchable interconnect using liquid-alloy-filled elastomeric microchannels," *Applied Physics Letters*, vol. 92, p. 011904, 2008.

[83] D. M. Burns and V. M. Bright, "Nonlinear flexures for stable deflection of an electrostatically actuated micromirror," in *Proc. SPIE: Microelectronics Structures and MEMS for Optical Processing III*, vol. 3226, pp. 125–135., 1997.

[84] K. Akarvardar, D. Elata, R. Parsa, G. C. Wan, K. Yoo, J. Provine, P. Peumans, R. T. Howe, and H. S. P. Wong, "Design Considerations for Complementary Nanoelectromechanical Logic Gates," 2007.

[85] M. A. Philippine, S. J. Timpe, and K. Komvopoulos, "Evolution of interfacial adhesion force in dynamic micromachines due to repetitive impact loading," *Applied Physics Letters*, vol. 91, 2007.

[86] K. Komvopoulos, "Surface engineering and microtribology for microelectromechanical systems," *Wear*, vol. 200, pp. 305–327, 1996.

[87] B. Borovic, A. Q. Liu, D. Popa, H. Cai, and F. L. Lewis, "Open-loop versus closed-loop control of MEMS devices: choices and issues," *Journal of Micromechanics and Microengineering*, vol. 15, pp. 1917–1924, 2005.

[88] H. Sumali, J. E. Massad, D. A. Czaplewski, and C. W. Dyck, "Waveform design for pulse-and-hold electrostatic actuation in MEMS," *Sensors and Actuators A: Physical*, vol. 134, pp. 213–220, 2007.

[89] M. S. Allen, J. E. Massad, R. V. Field, and C. W. Dyck, "Input and design optimization under uncertainty to minimize the impact velocity of an electrostatically actuated MEMS switch," *Journal of Vibration and Acoustics*, vol. 130, 2008.

[90] J. C. Blecke, D. S. Epp, H. Sumali, and G. G. Parker, "A Simple Learning Control to Eliminate RF-MEMS Switch Bounce," *Journal of Microelectromechanical Systems*, vol. 18, pp. 458–465, 2009.

[91] D. A. Czaplewski, C. W. Dyck, H. Sumali, J. E. Massad, J. D. Kuppers, I. Reines, W. D. Cowan, and C. P. Tigges, "A soft-landing waveform for actuation of a single-pole single-throw ohmic RF MEMS switch," *Journal of Microelectromechanical Systems*, pp. 1586–1594, 2006.

[92] A. Jain and M. A. Alam, "Prospects of Hysteresis-Free Abrupt Switching (0 mV/decade) in Landau Switches," *IEEE Transactions on Electron Devices*, vol. 60, pp. 4269–4276, Dec. 2013.

[93] A. Jain and M. A. Alam, "Stability Constraints Define the Minimum Subthreshold Swing of a Negative Capacitance Field-Effect Transistor," *IEEE Transactions on Electron Devices*, vol. 61, no. 7, pp. 2235–2242, 2014.

[94] T. Yuan and N. T. H., *Fundamentals of Modern VLSI Devices*. Cambridge University Press, 1998.

[95] T. N. Theis and P. M. Solomon, "It's time to reinvent the transistor!," *Science*, vol. 327, pp. 1600–1601, Mar. 2010.

[96] T. N. Theis and P. M. Solomon, "In Quest of the Next Switch: Prospects for Greatly Reduced Power Dissipation in a Successor to the Silicon Field-Effect Transistor," *Proceedings of the IEEE*, vol. 98, no. 12, 2010.

[97] K. Jeon, W.-Y. Loh, P. Patel, C. Y. Kang, J. Oh, A. Bowonder, C. Park, C. S. Park, C. Smith, P. Majhi, H.-H. Tseng, R. Jammy, T.-J. K. Liu, and C. Hu, "Si tunnel transistors with a novel silicided source and 46mV/dec swing," in *2010 Symposium on VLSI Technology*, pp. 121–122, IEEE, June 2010.

[98] P. B. G. Kailash Gopalakrishnan and J. D. Plummer, "I-MOS: A Novel Semiconductor Device with a Subthreshold Slope lower than kT/q," in *IEEE IEDM*, 2002.

[99] J.-C. Tolédano and P. Tolédano, *The Landau theory of phase transitions*. Singapore: World Scientific, 1987.

[100] W. Shu-Yau, "A New Ferroelectric Memory Device, Metal-Ferroelectric-Semiconductor Transistor," *Transactions on Electron Devices*, vol. ED-201, no. 8, pp. 499–504, 1974.

[101] H. Kam, D. T. Lee, R. T. Howe, and T.-J. King, "A new nano-electromechanical field effect transistor (NEMFET) design for low-power electronics," in *IEDM*, (Washington, DC), pp. 463–466, 2005.

[102] V. Zhirnov, R. Cavin, J. Hutchby, and G. Bourianoff, "Limits to binary logic switch scaling-a gedanken model," *Proceedings of the IEEE*, vol. 9, pp. 1934–1939, Nov. 2003.

[103] D. Salvatore, Giovanni A. Bouvet and A. M. Ionescu, "Demonstration of Subthrehold Swing Smaller Than 60mV/decade in Fe-FET with P(VDF-TrFE)/SiO2 Gate Stack," in *IEDM*, 2008.

[104] A. Islam Khan, D. Bhowmik, P. Yu, S. Joo Kim, X. Pan, R. Ramesh, and S. Salahuddin, "Experimental evidence of ferroelectric negative capacitance in nanoscale heterostructures," *Applied Physics Letters*, vol. 99, p. 113501, Sept. 2011.

[105] G. A. Salvatore, A. Rusu, and A. M. Ionescu, "Experimental confirmation of temperature dependent negative capacitance in ferroelectric field effect transistor," *Applied Physics Letters*, vol. 100, p. 163504, Apr. 2012.

[106] J. I. Seeger and S.B. Crary, "Analysis and simulation of MOS capacitor feedback for stabilizing electrostatically actuated mechanical devices," *Transactions on Built Environment*, vol. 31, 1997.

[107] A. Jain and M. A. Alam, "Prospects of Hysteresis-Free Abrupt Switching (0 mV/decade) in Landau Switches," *IEEE Transactions on Electron Devices*, vol. 60, no. 12, pp. 1–1, 2013.

[108] A. I. Khan, C. W. Yeung, C. Hu, and S. Salahuddin, "Ferroelectric Negative Capacitance MOSFET : Capacitance Tuning & Antiferroelectric Operation," in *IEDM*, pp. 255–258, 2011.

[109] D. Jimenez, E. Miranda, and A. Godoy, "Analytic Model for the Surface Potential and Drain Current in Negative Capacitance Field-Effect Transistors," *IEEE Transactions on Electron Devices*, vol. 57, pp. 2405–2409, Oct. 2010.

[110] D. Lam, F. Yang, A. Chong, J. Wang, and P. Tong, "Experiments and theory in strain gradient elasticity," *Journal of the Mechanics and Physics of Solids*, vol. 51, no. 8, pp. 1477–1508, 2003.

[111] B. Wang, J. Zhao, and S. Zhou, "A micro scale Timoshenko beam model based on strain gradient elasticity theory," *European Journal of Mechanics - A/Solids*, vol. 29, no. 4, pp. 591–599, 2010.

[112] Y. P. Zhao, L. S. Wang, and T. X. Yu, "Mechanics of adhesion in MEMSa review," *Journal of Adhesion Science and Technology*, vol. 17, pp. 519–546, Jan. 2003.

[113] J. Knapp and M. de Boer, "Mechanics of microcantilever beams subject to combined electrostatic and adhesive forces," *Journal of Microelectromechanical Systems*, vol. 11, pp. 754–764, Dec. 2002.

[114] N. Abele, A. Villaret, A. Gangadharaiah, C. Gabioud, P. Ancey, and A. Ionescu, "1T MEMS Memory Based on Suspended Gate MOSFET," in *International Electron Devices Meeting*, pp. 1–4, IEEE, 2006.

[115] G. A. Salvatore, L. Lattanzio, D. Bouvet, I. Stolichnov, N. Setter, and A. M. Ionescu, "Ferroelectric transistors with improved characteristics at high temperature," *Applied Physics Letters*, vol. 97, p. 053503, Aug. 2010.

[116] A. Cano and D. Jimenez, "Multidomain ferroelectricity as a limiting factor for voltage amplification in ferroelectric field-effect transistors," *Applied Physics Letters*, vol. 97, p. 133509, Sept. 2010.

[117] A. Jain and M. A. Alam, "Stability-Constraints Define the Minimum Subthreshold Swing of a Negative Capacitance Field Effect Transistor," *IEEE, Transactions on Electron Devices*, vol. Accepted, 2014.

[118] A. Jain, P. R. Nair, and M. a. Alam, "Flexure-FET biosensor to break the fundamental sensitivity limits of nanobiosensors using nonlinear electromechanical coupling.," *Proceedings of the National Academy of Sciences of the United States of America*, vol. 109, no. 24, pp. 9304–8, 2012.

[119] P. Bergveld, "Thirty years of ISFETOLOGY - What happened in the past 30 years and what may happen in the next 30 years," *Sensors and Actuators B-Chemical*, vol. 88, pp. 1–20, 2003.

[120] X. P. A. Gao, G. F. Zheng, and C. M. Lieber, "Subthreshold Regime has the Optimal Sensitivity for Nanowire FET Biosensors," *Nano Letters*, vol. 10, pp. 547–552, 2010.

[121] Y. L. Bunimovich, Y. S. Shin, W. S. Yeo, M. Amori, G. Kwong, and J. R. Heath, "Quantitative real-time measurements of DNA hybridization with alkylated nonoxidized silicon nanowires in electrolyte solution," *Journal of the American Chemical Society*, vol. 128, pp. 16323–16331, 2006.

[122] K. L. Ekinci and M. L. Roukes, "Nanoelectromechanical systems," *Review of Scientific Instruments*, vol. 76, 2005.

[123] K. W. Wee, G. Y. Kang, J. Park, J. Y. Kang, D. S. Yoon, J. H. Park, and T. S. Kim, "Novel electrical detection of label-free disease marker proteins using piezoresistive self-sensing micro-cantilevers," *Biosensors and Bioelectronics*, vol. 20, pp. 1932–1938, 2005.

[124] P. R. Nair and M. A. Alam, "Screening-limited response of nanobiosensors," *Nano Letters*, vol. 8, pp. 1281–1285, 2008.

[125] M. M. C. Cheng, G. Cuda, Y. L. Bunimovich, M. Gaspari, J. R. Heath, H. D. Hill, C. A. Mirkin, A. J. Nijdam, R. Terracciano, T. Thundat, and M. Ferrari, "Nanotechnologies for biomolecular detection and medical diagnostics," *Current Opinion in Chemical Biology*, vol. 10, pp. 11–19, 2006.

[126] G. F. Zheng, F. Patolsky, Y. Cui, W. U. Wang, and C. M. Lieber, "Multiplexed electrical detection of cancer markers with nanowire sensor arrays," *Nature Biotechnology*, vol. 23, pp. 1294–1301, 2005.

[127] N. V. Lavrik, M. J. Sepaniak, and P. G. Datskos, "Cantilever transducers as a platform for chemical and biological sensors," *Review of Scientific Instruments*, vol. 75, pp. 2229–2253, 2004.

[128] K. S. Hwang, S. M. Lee, S. K. Kim, J. H. Lee, and T. S. Kim, "Micro- and Nanocantilever Devices and Systems for Biomolecule Detection," *Annual Review of Analytical Chemistry*, vol. 2, pp. 77–98, 2009.

[129] A. K. Gupta, P. R. Nair, D. Akin, M. R. Ladisch, S. Broyles, M. A. Alam, and R. Bashir, "Anomalous resonance in a nanomechanical biosensor," *Proceedings of the National Academy of Sciences of the United States of America*, vol. 103, pp. 13362–13367, 2006.

[130] A. Boisen and T. Thundat, "Design & fabrication of cantilever array biosensors," *Materials Today*, vol. 12, pp. 32–38, 2009.

[131] G. H. Wu, R. H. Datar, K. M. Hansen, T. Thundat, R. J. Cote, and A. Majumdar, "Bioassay of prostate-specific antigen (PSA) using microcantilevers," *Nature Biotechnology*, vol. 19, pp. 856–860, 2001.

[132] J. Zhang, H. P. Lang, F. Huber, A. Bietsch, W. Grange, U. Certa, R. McKendry, H. J. Guntgerodt, M. Hegner, and C. Gerber, "Rapid and label-free nanomechanical detection of biomarker transcripts in human RNA," *Nature Nanotechnology*, vol. 1, pp. 214–220, 2006.

[133] H. Torun, K. K. Sarangapani, and F. L. Degertekin, "Spring constant tuning of active atomic force microscope probes using electrostatic spring softening effect," *Applied Physics Letters*, vol. 91, 2007.

[134] J. Tamayo, D. Ramos, J. Mertens, and M. Calleja, "Effect of the adsorbate stiffness on the resonance response of microcantilever sensors," *Applied Physics Letters*, vol. 89, 2006.

[135] P. S. Waggoner and H. G. Craighead, "The relationship between material properties, device design, and the sensitivity of resonant mechanical sensors," *Journal of Applied Physics*, vol. 105, 2009.

[136] W. Zhang, R. Baskaran, and K. L. Turner, "Effect of cubic nonlinearity on auto-parametrically amplified resonant MEMS mass sensor," *Sensors and Actuators A: Physical*, vol. 102, pp. 139–150, Dec. 2002.

[137] W. Zhang and K. L. Turner, "Application of parametric resonance amplification in a single-crystal silicon micro-oscillator based mass sensor," *Sensors and Actuators A: Physical*, vol. 122, pp. 23–30, July 2005.

[138] M. I. Younis and F. Alsaleem, "Exploration of New Concepts for Mass Detection in Electrostatically-Actuated Structures Based on Nonlinear Phenomena," *Journal of Computational and Nonlinear Dynamics*, vol. 4, p. 021010, Apr. 2009.

[139] D. R. Southworth, L. M. Bellan, Y. Linzon, H. G. Craighead, and J. M. C. A. . Parpia, "Stress-based vapor sensing using resonant microbridges," *Applied Physics Letters*, vol. 96, 2010.

[140] V. Kumar, J. W. Boley, Y. Yang, H. Ekowaluyo, J. K. Miller, G. T. C. Chiu, and J. F. C. A. . Rhoads, "Bifurcation-based mass sensing using piezoelectrically-actuated microcantilevers," *Applied Physics Letters*, vol. 98, 2011.

[141] H. Craighead, "Nanomechanical systems - Measuring more than mass," *Nature Nanotechnology*, vol. 2, pp. 18–19, 2007.

[142] D. Ramos, J. Tamayo, J. Mertens, M. Calleja, and A. Zaballos, "Origin of the response of nanomechanical resonators to bacteria adsorption," *Journal of Applied Physics*, vol. 100, 2006.

[143] E. Gil-Santos, D. Ramos, J. Martinez, M. Fernandez-Regulez, R. Garcia, A. San Paulo, M. Calleja, and J. Tamayo, "Nanomechanical mass sensing and stiffness spectrometry based on two-dimensional vibrations of resonant nanowires," *Nature Nanotechnology*, vol. 5, pp. 641–645, 2010.

[144] F. Sadeghian, H. Goosen, A. Bossche, and F. van Keulen, "Application of electrostatic pull-in instability on sensing adsorbate stiffness in nanomechanical resonators," *Thin Solid Films*, vol. 518, pp. 5018–5021, 2010.

[145] P. R. Nair and M. A. Alam, "Theory of Selectivity of label-free nanobiosensors: A geometro-physical perspective," *Journal of Applied Physics*, vol. 107, 2010.

[146] Y. T. Yang, C. Callegari, X. L. Feng, K. L. Ekinci, and M. L. Roukes, "Zeptogram-scale nanomechanical mass sensing," *Nano Letters*, vol. 6, pp. 583–586, 2006.

[147] P. Saulson, "Thermal noise in mechanical experiments," *Physical Review D*, vol. 42, pp. 2437–2445, Oct. 1990.

[148] A. N. Cleland and M. L. Roukes, "Noise processes in nanomechanical resonators," *Journal of Applied Physics*, vol. 92, p. 2758, Aug. 2002.

[149] K. L. Ekinci, "Ultimate limits to inertial mass sensing based upon nanoelectromechanical systems," *Journal of Applied Physics*, vol. 95, p. 2682, Mar. 2004.

[150] Y. Yong and J. Vig, "Resonator surface contamination-a cause of frequency fluctuations?," in *Proceedings of the 42nd Annual Frequency Control Symposium, 1988.*, pp. 397–403, IEEE, 1988.

[151] H. J. Butt and M. Jaschke, "Calculation of thermal noise in atomic force microscopy," *Nanotechnology*, vol. 6, pp. 1–7, Jan. 1995.

[152] A. Rusu, G. A. Salvatore, D. Jimenez, and A. M. Ionescu, "Metal-Ferroelectric-Meta-Oxide-semiconductor field effect transistor with sub-60mV/decade subthreshold swing and internal voltage amplification," in *2010 International Electron Devices Meeting*, pp. 16.3.1–16.3.4, IEEE, Dec. 2010.

[153] H. W. Then, S. Dasgupta, M. Radosavljevic, L. Chow, B. Chu-Kung, G. Dewey, S. Gardner, X. Gao, J. Kavalieros, N. Mukherjee, M. Metz, M. Oliver, R. Pillarisetty, V. Rao, S. H. Sung, G. Yang, and R. Chau, "Experimental observation and physics of negative capacitance and steeper than 40mV/decade subthreshold swing in Al¡inf¿0.83¡/inf¿In¡inf¿0.17¡/inf¿N/AlN/GaN MOS-HEMT on SiC substrate," in *2013 IEEE International Electron Devices Meeting*, pp. 28.3.1–28.3.4, IEEE, Dec. 2013.

[154] D. J. R. Appleby, N. K. Ponon, K. S. K. Kwa, B. Zou, P. K. Petrov, T. Wang, N. M. Alford, and A. O'Neill, "Experimental observation of negative capacitance in ferroelectrics at room temperature.," *Nano letters*, vol. 14, pp. 3864–8, July 2014.

[155] C. H. Cheng and A. Chin, "Low-Voltage Steep Turn-On pMOSFET Using Ferroelectric High-κ Gate Dielectric," *IEEE Electron Device Letters*, vol. 35, pp. 274–276, Feb. 2014.

[156] W. Merz, "Double Hysteresis Loop of BaTiO3 at the Curie Point," *Physical Review*, vol. 91, pp. 513–517, Aug. 1953.

[157] Q. Thong Trinh, G. Gerlach, J. Sorber, and K.-F. Arndt, "Hydrogel-based piezoresistive pH sensors: Design, simulation and output characteristics," *Sensors and Actuators B: Chemical*, vol. 117, pp. 17–26, Sept. 2006.

[158] K. Gruber, T. Horlacher, R. Castelli, A. Mader, P. H. Seeberger, and B. A. Hermann, "Cantilever array sensors detect specific carbohydrate-protein interactions with picomolar sensitivity.," *ACS nano*, vol. 5, pp. 3670–8, May 2011.

[159] S. C. Abrahams, "Ferroelasticity," *Material Research Bulletin*, vol. 6, pp. 881–890, 1971.

[160] S. A. Emam, *A Theoretical and Experimental Study of Nonlinear Dynamics of Buckled Beams*. PhD thesis, Virginia Polytechnic Institute and State University, 2002.

[161] P. Osterberg, H. Yie, X. Cai, J. White, and S. Senturia, "Self-consistent simulation and modelling of electrostatically deformed diaphragms," in *IEEE, MEMS*, 1994.

[162] L. X. Zhang and Y. P. Zhao, "Electromechanical model of RF MEMS switches," *Microsystem Technologies*, vol. 9, pp. 420–426, 2003.

[163] H. Kam, S. Member, and T.-j. K. Liu, "Pull-In and Release Voltage Design for Nanoelectromechanical Field-Effect Transistors," *IEEE Transactions on Electron Devices*, vol. 56, no. 12, pp. 3072–3082, 2009.

[164] W.-H. Lin and Y.-P. Zhao, "Casimir effect on the pull-in parameters of nanometer switches," *Microsystem Technologies*, vol. 11, pp. 80–85, 2005.

[165] A. Jain, S. Palit, and M. A. Alam, "A physics based predictive modeling framework for dielectric charging and creep in RF MEMS capacitive switches and varactors," *Journal of Microelectromechanical Systems*, vol. 21, no. 2, pp. 420–429, 2012.

[166] C. Goldsmith, J. Ehmke, A. Malczewski, B. Pillans, S. Eshelman, Z. Yao, J. Brank, and M. Eberly, "Lifetime characterization of capacitive RF MEMS switches," in *IEEE Microwave Symposium Digest*, vol. 1, pp. 227–230 ST – Lifetime characterization of capacit, 2001.

[167] X. Yuan, S. Cherepko, J. Hwang, C. L. Goldsmith, C. Nordqusit, and C. Dyck, "Initial observation and analysis of dielectric-charging effects on RF MEMS capacitive switches," in *IEEE Microwave Symposium Digest*, vol. 3, pp. 1943–1946, 2004.

[168] X. Yuan, J. C. M. Hwang, D. Forehand, and C. L. Goldsmith, "Modeling and characterization of dielectric-charging effects in RF MEMS capacitive switches," in *IEEE Microwave Symposium Digest*, pp. 753–756, 2005.

[169] W. M. van Spengen, R. Puers, R. Mertens, and I. De Wolf, "A comprehensive model to predict the charging and reliability of capacitive RF MEMS switches," *Journal of Micromechanics and Microengineering*, vol. 14, pp. 514–521, 2004.

[170] X. B. Yuan, Z. Peng, J. C. M. Hwang, D. Forehand, and C. L. Goldsmith, "Acceleration of dielectric charging in RF MEMS capacitive switches," *IEEE Transactions on Device and Materials Reliability*, vol. 6, pp. 556–563 ST – Acceleration of dielectric charging, 2006.

[171] X. Rottenberg, B. Nauwelaers, W. Raedt, and H. A. C. Tilman, "Distributed Dielectric charging and its impact on RF MEMS devices," in *European Microwave Conference*, vol. 1, pp. 77–80, 2004.

[172] X. Rottenberg, I. De Wolf, B. Nauwelaers, W. De Raedt, and H. A. C. Tilmans, "Analytical model of the DC actuation of electrostatic MEMS devices with distributed dielectric charging and nonplanar electrodes," *Journal of Microelectromechanical Systems*, vol. 16, pp. 1243–1253, 2007.

[173] C. L. Goldsmith, D. I. Forehand, Z. Peng, J. C. M. Hwang, and I. L. Ebel, "High-Cycle Life Testing of RF MEMS Switches," in *IEEE Microwave Symposium Digest*, pp. 1805–1808, 2007.

[174] S. Melle, D. De Conto, D. Dubuc, K. Grenier, O. Vendier, J. L. Muraro, J. L. Cazaux, and R. Plana, "Reliability modeling of capacitive RF MEMS," *IEEE Transactions on Microwave Theory and Techniques*, vol. 53, pp. 3482–3488, 2005.

[175] P. Mark and T. E. Hartman, "On Distinguishing Between Schottky and Poole-Frenkel Effects in Insulators," *Journal of Applied Physics*, vol. 39, p. 2163, 1968.

[176] C. A. and W. C. L. A. E. R., "The role of bulk traps in metal-insulator contact charging," *Journal of Physics D: Applied Physics*, vol. 7, pp. 713–725, 1974.

[177] B. D.A., A. R.A., and M. M.J., "Charge trapping in silicon-rich Si3N4 thin films," *Solid-State Electronics*, vol. 30, pp. 1295–1301, 1987.

[178] R. R., "Phenomenological theory to model leakage currents in metalinsulatormetal capacitor systems," *Phys. Stat. Sol.*, vol. 239, pp. 59–70, 2003.

[179] M. Exarchos, V. Theonas, P. Pons, G. J. Papaioannou, S. Melle, D. Dubuc, F. Cocetti, and R. Plana, "Investigation of charging mechanisms in Metal-Insulator-Metal structures," *Microelectronics Reliability*, vol. 45, pp. 1782–1785, 2005.

[180] P. C. Arnett and B. H. L. A. E. Yun, "Silicon nitride trap properties as revealed by charge-centroid measurements on MNOS devices," *Applied Physics Letters*, vol. 26, pp. 94–96, 1975.

[181] S. Palit and M. A. Alam, "Theory of charging and charge transport in "intermediate" thickness dielectrics and its implications for characterization and reliability," *Journal of Applied Physics*, vol. 111, pp. 54110–54112, Mar. 2012.

[182] X. Yuan, Z. Peng, J. C. M. Hwang, D. Forehand, and C. L. Goldsmith, "Temperature Acceleration of Dielectric Charging in RF MEMS Capacitive Switches," in *IEEE Microwave Symposium Digest*, pp. 47–50, 2006.

[183] R. W. Herfst, P. G. Steeneken, and J. Schmitz, "Time and voltage dependence of dielectric charging in RF MEMS capacitive switches," in *IEEE Int. Reliability Physics Symposium*, pp. 417–421, 2007.

[184] H. H. Hsu and D. Peroulis, "A Viscoelastic-aware experimentally derived model for analog RF-MEMS varactors," in *IEEE MEMS*, pp. 783–786, 2010.

[185] M. V. Gils, J. Bielen, and G. McDonald, "Evaluation of Creep in RF MEMS Devices," in *EuroSime*, pp. 1–6, 2007.

[186] X. Yan, W. L. Brown, Y. Li, J. Papapolymerou, C. Palego, J. C. M. Hwang, and R. P. Vinci, "Anelastic Stress Relaxation in Gold Films and Its Impact on Restoring Forces in MEMS Devices," *Journal of Microelectromechanical Systems*, vol. 18, pp. 570–576, 2009.

[187] D. Roylance, "Engineering Viscoelasticity," tech. rep., Department of Materials Science and Engineering, Massachusetts Institute of Technology, Cambridge, MA, 2001.

[188] H.-H. Hsu and D. Peroulis, "A CAD Model for Creep Behavior of RF-MEMS Varactors and Circuits," *IEEE Transactions on Microwave Theory and Techniques*, vol. 59, no. 7, pp. 1761–1768, 2011.

[189] A. Jain, A. E. Islam, and M. A. Alam, "A Theoretical Study of Negative Bias Temperature Instability in p-type NEMFET," in *IEEE, University/Government/Industry Micro/Nano SymposiumUniversity/Government/Industry Micro/Nano Symposium*, 2010.

[190] A. Jain, A. E. Islam, and M. A. Alam, "On the electro-mechanical reliability of NEMFET as an analog/digital switch," in *2012 IEEE International Reliability Physics Symposium (IRPS)*, IEEE, Apr. 2012.

[191] M. A. Alam, H. Kufluoglu, D. Varghese, and S. Mahapatra, "A comprehensive model for PMOS NBTI degradation: Recent progress," *Microelectronics Reliability*, vol. 47, pp. 853–862, 2007.

[192] C. Hu, S. C. Tam, F.-C. Hsu, P.-K. Ko, T.-Y. Chan, and K. W. Terrill, "Hot-electron-induced MOSFET degradation-Model, monitor, and improvement," *IEEE Transactions on Electron Devices*, vol. 32, pp. 375–385, 1985.

[193] M. A. Alam, "A critical examination of the mechanics of dynamic NBTI for PMOSFETs," in *IEEE International Electron Device Meeting*, 2003.

[194] M. A. Alam, J. Bude, and A. Ghetti, "Field acceleration for oxide breakdown-can an accurate anode hole injection model resolve the E vs. 1/E controversy?," in *International Reliability Physics Symposium*, pp. 21–26, 2000.

[195] J. Li and A. Dasgupta, "Failure-mechanism models for creep and creep rupture," *IEEE Transactions on Reliability*, vol. 42, pp. 339–353, 1993.

[196] H. Kufluoglu and M. A. Alam, "A generalized reaction-diffusion model with explicit H-H2 dynamics for negative-bias temperature-instability (NBTI) degradation," *IEEE Transactions on Electron Devices*, vol. 54, pp. 1101–1107, 2007.

APPENDICES

A. EULER-BERNOULLI BEAM FRAMEWORK FOR MEMS

Here, we discuss Euler-Bernoulli (EB) beam framework for the modeling and simulation of MEMS actuators (sec. A.1). We will illustrate that the physics of instability studied using simple spring-mass model in chapter 2 is consistent with the detailed numerical simulations (sec. A.2). The difference between the spring-mass model of chapter 2 and EB framework is the following. In spring-mass model, all the points on the movable electrode M_1 are assumed to move together. In EB framework, position resolved deflection of M_1 is considered to account for the bending of M_1.

A.1 Model System

Figure A.1 shows the schematic of capacitive and FET actuators and highlights that different points on M_1 have different deflection. As explained in chapter 1, capacitive actuator consists of a movable electrode M_1 and a fixed electrode M_2, separated by an air-gap and a thin dielectric (Fig. A.1 A); whereas FET actuator (Fig. A.1 B) consists of a movable gate suspended above a semiconductor channel which is connected between source and drain. Both actuators are actuated by applying a voltage between the movable electrode M_1 or gate and the fixed electrode M_2 or the semiconductor channel. Note that, in capacitive actuators, application of voltage only changes the capacitance; whereas in FET actuators, it changes the drain current I_{DS} also. The operation of both actuators is dictated by the interaction between mechanical energy (or force) and electrostatic energy (or force), which are discussed below-

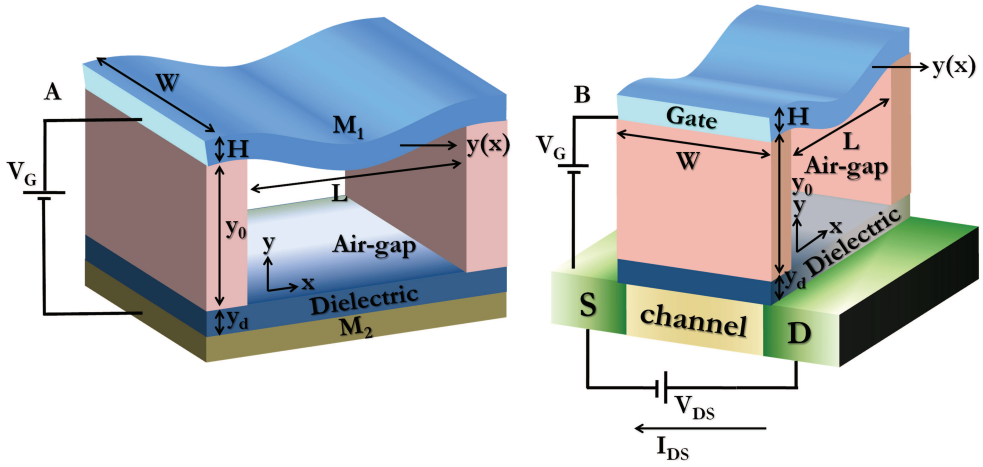

Fig. A.1. Schematic of MEMS Actuators. (A) Capacitive actuators represent RF-MEMS capacitive switches, varactors, deformable mirrors, and Mirasol displays. (B) FET actuators represent suspended-gate FET, resonant gate transistor, and SG-FET.

A.1.1 Euler-Bernoulli Beam Framework

Mechanical Energy

From the mechanical perspective, we treat movable electrode (M_1 or gate) as a fixed-fixed beam, albeit cantilever or some other configuration are also possible. Fixed-fixed beam satisfies the following boundary conditions-

$$y(0) = y(L) = y_0, \tag{A.1}$$

$$\frac{\partial y}{\partial x}(0) = \frac{\partial y}{\partial x}(L) = 0, \tag{A.2}$$

where $y(x)$ defines the shape of the beam, L is the length, and y_0 is the initial air-gap. Equation A.1 suggests that both ends of the beam are fixed at y_0. The slope of beam shape $y(x)$ at both ends is zero and Eq. A.2 reflects that. The mechanical energy of the beam consists of three parts: (i) bending energy ($U_{Bending}$), (ii) stretching energy ($U_{Stretching}$), and (iii) stress energy (U_{Stress}) [160] i.e.,

$$U_{Bending} = \frac{1}{2} EI \int_0^L \left(\frac{\partial^2 y}{\partial x^2} \right)^2 dx, \tag{A.3}$$

$$U_{Stretching} = \frac{EWH}{8L} \left[\int_0^L \left(\frac{\partial y}{\partial x} \right)^2 dx \right]^2, \tag{A.4}$$

$$U_{Stress} = -\frac{P}{4} \int_0^L \left(\frac{\partial y}{\partial x} \right)^2 dx, \tag{A.5}$$

where E is the Young's modulus of the beam's material, I is the second moment of area, W is the width, H is the thickness, x is along the length of the beam, and P is the axial load in the beam. For a rectangular cross-sectional beam, second moment of area is $I = \frac{WH^3}{12}$. Equations A.3-A.5 govern the mechanical aspect of the actuator. The electrostatic aspect of the actuator is discussed below.

Electrostatic Energy

The electrostatic energy of a MEMS actuator is given by-

$$U_{elec} = -\frac{1}{2} W \int_0^L \int_{-\infty}^{y(x)} \epsilon_0 E^2(x,u) du dx = -\frac{1}{2} \int_0^L C(y(x)) V_G^2 dx, \tag{A.6}$$

where ϵ_0 is the permittivity of free space, $E(x,y)$ is the electric field at the point (x,y), $C(y(x))$ is the capacitance per unit length, and V_G is the applied voltage, Now, knowing both the mechanical and electrostatic energy component, we obtain the governing equations of MEMS actuation below.

Euler-Bernoulli Equation

The steady state behavior of the MEMS actuator is dictated by the minimization of the total energy U, which consists of mechanical energy (Eqs. A.3-A.5) and electrostatic energy (Eq. A.6). Since, $U = U_{Bending} + U_{Stretching} + U_{Stress} + U_{elec}$, minimization of U with respect to $y(x)$ (i.e., $dU = 0$) yields Euler-Bernoulli equation [161,162] i.e.,

$$EI\frac{\partial^4 y}{\partial x^4} + \left(P - \frac{EWH}{2L}\int_0^L \left(\frac{\partial y}{\partial x}\right)^2 dx\right)\frac{\partial^2 y}{\partial x^2} = F_{elec}, \tag{A.7}$$

where the first term on left hand side corresponds to $U_{Bending}$, term with P to U_{Stress}, and the other term to $U_{Stretching}$. F_{elec} is the electrostatic force per unit length and is given by [161]-

Electrostatic Force

$$F_{elec} = \frac{1}{2}\epsilon_0 E_{air}^2 W = -\frac{1}{2}\frac{dC}{dy}V_G^2, \tag{A.8}$$

where E_{air} is the electric field in air. Now, steady state behavior of the actuator can be obtained from the solutions of Eqs. A.7-A.8. Note that, electrostatic force for a parallel-plate capacitive actuator (Fig. A.1 A) is solely governed by its capacitance $C = \frac{\epsilon_0 W}{y+\frac{y_d}{\epsilon_d}}$, where y_d is the dielectric thickness and ϵ_d is the dielectric constant. Therefore, $F_{elec} = \frac{1}{2}\frac{\epsilon_0 W}{\left(y+\frac{y_d}{\epsilon_d}\right)^2}V_G^2$ for parallel-plate capacitive actuators . In case of FET actuators, we need to consider the physics of semiconductor channel to calculate F_{elec}, which is discussed below.

Electrostatic Force in FET Actuators

In case of FET actuators, F_{elec} for a given $y(x)$ is given by the coupled solution of the following equations [163]-

$$V_G = \left(y + \frac{y_d}{\epsilon_d}\right)\epsilon_s E_s(\psi_s) + \psi_s, \tag{A.9}$$

$$E_s(\psi_s) = \sqrt{\frac{2qN_A}{\epsilon_0\epsilon_s}}\left[\psi_s + \left(e^{-\frac{q\psi_s}{k_B T}} - 1\right)\frac{k_B T}{q} - \left(\frac{n_i}{N_A}\right)^2\left(\psi_s - \left(e^{\frac{q\psi_s}{k_B T}} - 1\right)\frac{k_B T}{q}\right)\right]^{\frac{1}{2}}, \tag{A.10}$$

where ψ_s is the surface potential in the semiconductor channel, ϵ_s is the dielectric constant of the channel material, q is the charge on an electron, k_B is the Boltzmann constant, T is the absolute temperature, n_i is the intrinsic carrier concentration in the channel, and N_A is the doping concentration. Note that, $E_s(\psi_s)$ is the electric field at semiconductor-dielectric interface and $E_{air} = \epsilon_s E_s(\psi_s)$ is the electric field in air which dictates F_{elec} (Eq. A.8). Equation A.9 suggests that sum of voltage drop in air ($yE_{air} = y\epsilon_s E_s(\psi_s)$), dielectric ($\frac{y_d}{\epsilon_d}\epsilon_s E_s(\psi_s)$), semiconductor ($\psi_s$) must be equal to the applied gate voltage V_G. y_d is the thickness of thin dielectric layer and ϵ_d is the dielectric constant. Now, the coupled solutions of Eqs. A.7-A.10 governs the steady state response of FET actuators.

The corresponding drain current I_{DS} in response to the applied gate voltage V_G is given by-

$$Q_i = \frac{qn_i^2}{N_A}\int_0^{\psi_s} \frac{e^{\frac{q\psi}{k_B T}}}{E_s(\psi)} d\psi, \tag{A.11}$$

$$I_{DS} = \mu \frac{V_{DS}}{W}\int_0^L Q_i dx, \tag{A.12}$$

where Q_i is the inversion charge density, μ is the mobility of mobile charge carriers in the channel, and V_{DS} is the drain to source voltage.

Equations A.7-A.10 describe the steady state response of MEMS actuators. The transient response or the dynamics of M_1 or gate, when V_G is applied and removed is governed by [51, 55]-

Beam Dynamics

$$\rho WH\frac{\partial^2 y}{\partial t^2} + b\frac{\partial y}{\partial t} + \left[EI\frac{\partial^4 y}{\partial x^4} + \left(P - \frac{EWH}{2L}\int_0^L \left(\frac{\partial y}{\partial x}\right)^2 dx\right)\frac{\partial^2 y}{\partial x^2}\right] = F_{elec}, \tag{A.13}$$

where ρ is the density of the M_1 or gate's material, b is the damping coefficient and t is the time. The first term on the left hand side is the inertia term and the second

terms corresponds to the dissipation due to damping. In MEMS actuators, damping is dominated by squeeze-film gas damping [39] which depends on the pressure of surrounding gas. Note that, Equation A.13 in steady state (all time derivative equated to zero) reduces to equation A.7.

A.1.2 Limitations and Approach

Limitations

Although the modeling framework developed above is sufficiently general for our purpose, it is only applicable to linear elastic materials following $\sigma = E\epsilon$, where σ is the stress and ϵ is the strain. The models do not apply to other materials following nonlinear stress-strain relationship e.g., ferroelastic materials [159]. Moreover, the modeling framework only accounts for the mechanical and electrostatic forces and does not account for the other forces like casimir forces [164], which may be present at very small air-gap (y_0). It should also be stressed, that the nonlinearity arising because of the stretching (i.e., cubic nonlinearity in spring) is only the consequence of large deflection and not any specific material behavior.

Approach

Although we have discussed both Euler-Bernoulli framework and spring-mass model (chapter 2), we have relied on Euler-Bernoulli framework for the reliability study of MEMS actuators (appendix G and H) and used spring-mass model to propose new device proposals (chapters 3-6). Specifically:

- Implications of degradation mechanisms e.g., (i) dielectric charging and creep in context of RF-MEMS capacitive switches in appendix G and (ii) NBTI, HCI and creep in context of SG-FET in appendix H are studied using Euler-Bernoulli framework.

- Problem of travel range (chapter 4), hard-landing (chapter 4), hysteresis (chapter 5), and new proposal of Flexure biosensor (chapter 6) have been analyzed using the spring-mass model.

Our reliance on spring-mass model is justified because it captures all the essential features of instability and this thesis advocates instability as a design variable. Also note that, we have not considered the effect of $U_{Stretching}$ (Eq. A.4) and U_{Stress} (i.e., $P = 0$, Eq. A.5) unless otherwise specified. Similarly, the nonlinear component of spring force has not been considered without any specific mention. These additional effects are important in a practical device, but here our focus is on the fundamentals of an idealized device free from non ideal effects arising from $U_{Stretching}$ and U_{Stress}.

A.2 Results and Discussions

A.2.1 Operation of MEMS Actuator

Static Behavior of Capacitive Actuator: CV Characteristics and Beam Shapes

We numerically solve Eqs. A.7-A.8 for the static behavior of a parallel-plate MEMS actuator and the results are summarized in Fig. A.2. The steady state shapes of the beam, during voltage sweep from $0V$ to $60V$ and then back to $0V$, are shown in Figs. A.2(a)-(b). In response, the beam bends symmetrically towards the dielectric (Fig. A.2(a)), with a corresponding increase in the capacitance (Fig. A.2(c), bottom branch). When $V_G > V_{PI}$, F_{elec} exceeds spring-like restoring force (fourth order derivative term in Eq. A.7), and beam is pulled-in abruptly to rest on the dielectric (Fig. A.2(a)). Note that, this pull-in (for a thin dielectric) occurs when beam crosses two third of the air-gap (Fig. A.2 (a)). Therefore, beam shapes such that $0 < y_{center} < 2/3y_0$, where y_{center} is the position of the center of the beam, are fundamentally not accessible which is equivalent of having a band-gap in semiconductors (Figs. A.2 (a)-(b)). This pull-in behavior causes the capacitance (C)

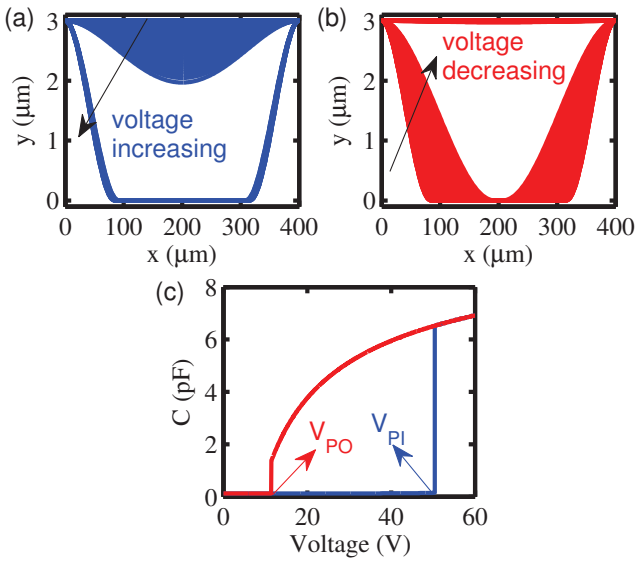

Fig. A.2. (a)-(b) Steady state shapes of the beam when the voltage is increasing (a) and when it is decreasing (b). (c) The capacitance vs. voltage (CV) curve of a capacitive actuator e.g., RF-MEMS capacitive switch. Abrupt jump in capacitance at V_{PI} (when voltage is increasing) is due to pull-in behavior of the device.

to jump discontinuously from the lower to the upper branch (Fig. A.2(c)). Any further increase in V_G, increases the contact area (Fig. A.2(a)), and hence, the capacitance of the device (Fig. A.2(c)). In the reverse cycle, when voltage is ramped down, the contact area reduces gradually (Fig. A.2(b)), and so does the capacitance (Fig. A.2(c)). At $V_G = V_{PO}$, the beam barely touches the dielectric at a single point, which is shown in Fig. A.2(b). When $V_G < V_{PO}$, beam is released from the dielectric and comes back in air (Fig. A.2(b)).

Pull-in Dynamics of Capacitive Actuator: Effect of Voltage and Pressure

For pull-in dynamics of the switch, we solve Eq. A.13 in response to a step voltage. The corresponding shapes of the beam, displacement and velocity of the center of the beam as a function of time are shown in Figs. A.3(a) and A.3(b),

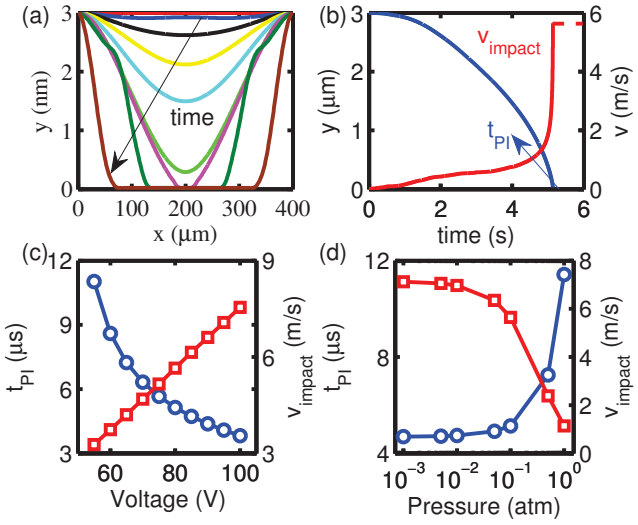

Fig. A.3. Pull-in dynamics of capacitive MEMS actuator. (a) Shape of the fixed-fixed beam at different instants of the time during pull-in. Time is increasing in the direction of arrow. (b) Displacement (left axis) and velocity (right axis) of the center of beam during pull-in showing t_{PI} and v_{impact} (c) Effect of voltage on pull-in dynamics of the switch. t_{PI} (left axis, $\circ$) decreases and v_{impact} (right axis,$\triangle$) increases with voltage due to increase in the electrostatic force. (d) Effect of pressure on pull-in dynamics of the switch. When pressure is low, dynamics is inertia dominated and hence t_{PI} (left axis, $\circ$) and v_{impact} (right axis,$\triangle$) are almost constant. Above a certain pressure (in our case ~ 0.1 atm), pull-in dynamics becomes damping dominated, therefore, t_{PI} and v_{impact} changes rapidly as a function of pressure.

respectively. We define t_{PI} as the pull-in time needed for the upper electrode to reach the dielectric from its up state position, and v_{impact} as the impact velocity with which the upper electrode lands on the dielectric. The rapid increase in the velocity near the contact (Fig. A.3(b)) reflects the rapid increase in $F_{elec} = \frac{1}{2}\frac{\epsilon_0 W}{\left(y+\frac{y_d}{\epsilon_d}\right)^2}V_G^2$ close to the contact (when $y \approx 0$). Figure A.3(c) shows t_{PI} and v_{impact} as a function of the applied voltage V_G. As V_G increases, F_{elec} increases as $\sim V_G^2$ thereby decreasing t_{PI} and increasing v_{impact}. Our numerical simulation shows that v_{impact} increases almost linearly with voltage ($v_{impact} \propto V_G$), and t_{PI} decreases as $t_{PI} \propto 1/V_G$ (Fig.

A.3(c)). Another important factor in determining t_{PI} and v_{impact} is the squeeze film gas damping, which is dictated by the pressure p of the ambient gas [39]. As p decreases, mean free path of gas molecules ($\lambda \propto 1/p$) increases, which then reduces the squeeze film gas damping [39]. This reduction in damping decreases t_{PI} (Fig. A.3(d)), and increases v_{impact} (Fig. A.3(d)). Figure A.3(d) also shows that t_{PI} and v_{impact} are insensitive to pressure when p is low (dynamics is dominated by inertia i.e., $\rho W H d^2y/dt^2 > bdy/dt$ in Eq. A.13); whereas t_{PI} increases and v_{impact} decreases rapidly above a critical pressure (in this case 0.1 atm), and dynamics become damping dominated i.e., $bdy/dt > \rho W H d^2y/dt^2$ in Eq. A.13.

Static and Dynamic Behavior of FET Actuator

Figure A.4 shows the static and dynamic behavior of a FET actuator e.g., SG-FET obtained from self consistent numerical simulations of Eqs. A.7-A.10 & A.13 . The application of gate voltage (V_G) bends down the beam symmetrically as shown in Fig. A.4(a) (like in Fig. A.2). Such bending of the beam increases the gate capacitance and the drain current (I_{DS})(Fig. A.4(c)). For $V_G > V_{PI}$, the beam is abruptly pulled-in giving rise to abrupt switching equivalent to subthreshold swing of $0mV/dec$ (Fig. A.4(c) and Fig. A.4 (d) for pull-in dynamics). Further increase in V_G beyond V_{PI} increases the contact area of the beam with the dielectric (Fig. A.4(a)) and thereby increases the capacitance. Increase in V_G also increases the inversion charge in the channel. As a consequence of this increase in the inversion charge, drain current continuously increases beyond V_{PI}. During pull-out, V_G must be reduced below V_{PO} to restore the beam into its original shape. During this release phase (Fig. A.4(b)), first the contact area of the beam reduces, and then at $V_G = V_{PO}$, the beam touches the dielectric only at a single point (Fig. A.4(b)). Finally, for $V_G < V_{PO}$, beam comes back in air (Fig. A.4 (d) for release dynamics).

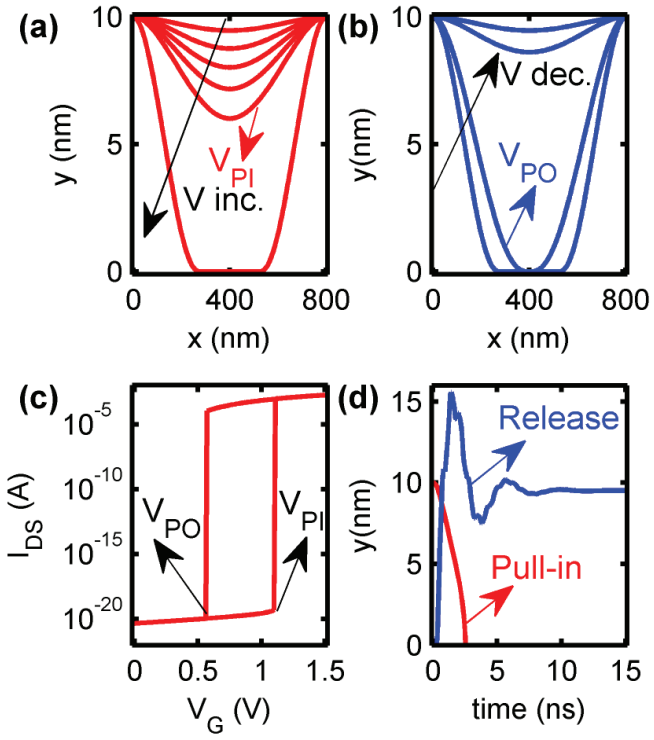

Fig. A.4. Device operation of a SG-FET. The shapes of the beam when gate voltage is (a) increasing, and (b) decreasing. (c) Drain current (I_{DS}) vs. V_G characteristic showing the pull-in voltage (V_{PI}), pull-out voltage (V_{PO}), and arbitrarily low subthreshold swing due to abrupt pull-in behavior. (e) Pull-in and release dynamics of SG-FET suggests response of the system within $\sim 10ns$ during the on (pull-in) and off (release) transition.

A.3 Conclusions

To conclude, we have provided the Euler-Bernoulli equation based modeling framework for MEMS actuators. We also highlighted the limitations and discussed our approach. The operation of MEMS actuators have been illustrated using detailed numerical simulations. Most importantly, this chapter confirms that the spring-mass system in chapter 2, captures all the essential features of instability very well.

B. SPRING-MASS MODEL OF SUSPENDED-GATE FET

The operating principle of Suspended gate FET can be understood using the lumped parameter spring-mass model (Fig. 5.3 a). With the application of gate bias V_G, the gate moves downward towards the dielectric and the corresponding increase in gate capacitance is reflected in the increased drain current I_{DS}. The static behavior of the device is dictated by the balance of spring and electrostatic forces, i.e.,

$$k(y_0 - y) = \frac{1}{2}\epsilon_0 E_{air}^2 A, \tag{B.1}$$

where $k = \frac{\alpha W H^3}{12 L^3}$ is the stiffness, α is a geometrical factor, E is the Young's modulus, W is the width, H is the thickness, L is the length of the gate electrode, y_0 is the air-gap, y is the position of the gate electrode, ϵ_0 is the permittivity of free space, E_{air} is the electric field in the air, and $A = WL$ is the area of the gate electrode. The electric field below the membrane E_{air} is equal to $\epsilon_s E_s(\psi_s)$, where, ϵ_s is the dielectric constant of the substrate and,

$$E_s(\psi_s) = \sqrt{\frac{2qN_A}{\epsilon_0 \epsilon_s}} \left[\psi_s + \left(e^{-\frac{q\psi_s}{k_B T}} - 1 \right) \frac{k_B T}{q} - \left(\frac{n_i}{N_A} \right)^2 \left(\psi_s - \left(e^{\frac{q\psi_s}{k_B T}} - 1 \right) \frac{k_B T}{q} \right) \right]^{\frac{1}{2}}, \tag{B.2}$$

where $E_s(\psi_s)$ is the electric field at the substrate-dielectric interface (see Ref. [94] page 64 for a detailed derivation of Eq. B.2), ψ_s is the surface potential, q is the charge of an electron, N_A is the substrate doping, k_B is the Boltzmann constant, T is the absolute temperature, and n_i is the intrinsic carrier concentration in the substrate. The voltage drop in air ($y\epsilon_s E_s(\psi_s)$), dielectric $\left(\frac{y_d}{\epsilon_d}\epsilon_s E_s(\psi_s)\right)$, and substrate($\psi_s$) can be related to the applied gate bias V_G as follows-

$$V_G = \left(y + \frac{y_d}{\epsilon_d} \right) \epsilon_s E_s(\psi_s) + \psi_s, \tag{B.3}$$

where y_d is the dielectric thickness. Equations B.1-B.3 are solved self-consistently for y and ψ_s at each V_G. The corresponding inversion charge density (Q_i)in the channel and drain current (I_{DS}) are given by,

$$Q_i = \frac{qn_i^2}{N_A} \int_0^{\psi_s} \frac{e^{\frac{q\psi}{k_B T}}}{E_s(\psi)} d\psi, \tag{B.4}$$

$$I_{DS} = \mu_n L Q_i \frac{V_{DS}}{W}, \tag{B.5}$$

where μ_n is the channel mobility for electrons, V_{DS} is the applied drain to source voltage.

C. SIMULATION FRAMEWORK FOR FERROELECTRIC FET

For FE-FET, the static behavior is governed by the minimization of total systems energy and that results in the voltage drop across the ferroelectric (V_{FE}) given by:

$$\frac{V_{FE}}{y_{FE}} = \alpha_0 Q + \beta_0 Q^3 + \gamma_0 Q^5, \tag{C.1}$$

where Q is the total charge, y_{FE} is the insulator thickness, and α_0,β_0,γ_0 are material's constant. Equation C.1 is same as Eq. 2.27 discussed in chapter 2. In an FE-FET, the total charge Q is same as the total charge in the channel ($Q_s(\psi_s)$), which is given by:

$$\begin{aligned} Q &= Q_s\left(\psi_s\right) = \epsilon_0 \epsilon_s E_s\left(\psi_s\right) \\ &= \sqrt{2q\epsilon_0\epsilon_s N_A}\left[\psi_s + \left(e^{-\frac{q\psi_s}{k_B T}} - 1\right)\frac{k_B T}{q} - \left(\frac{n_i}{N_A}\right)^2\left(\psi_s - \left(e^{\frac{q\psi_s}{k_B T}} - 1\right)\frac{k_B T}{q}\right)\right]^{\frac{1}{2}}, \end{aligned} \tag{C.2}$$

where $E_s\left(\psi_s\right)$ is the electric field at semiconductor dielectric interface (Eq. B.2 in appendix B). ψ_s is the surface potential and is related to gate voltage (V_G) as follows:

$$V_G = V_{FB} + \left(\alpha_0 Q + \beta_0 Q^3 + \gamma_0 Q^5\right) y_{FE} + \psi_s. \tag{C.3}$$

Now, Eqs. C.2-C.3 are solved self consistently at each V_G to find ψ_s and Q. The corresponding inversion charge density and drain current are given by Eq. B.4 & Eq. B.5, respectively.

D. NUMERICAL SIMULATIONS FOR CALCULATION OF RESONANCE FREQUENCY

In the previous appendix section, we disucseed the Euler-Bernoulli framework and numerical simulations. Here, we discuss the numerical simulations of spring-mass system to obtain voltage dependent resonance frequency for various actuators considered in chapter 3. For all the actuators, the static response (i.e. y vs.V_G/Q_G) has been obtained by iteratively solving the equation of force balance Eq. 2.5 with F_{elec} given in Table 3.1. Figure A1(a) shows the response (i.e., y vs. V_G/Q_G) of one such simulation for parallel-plate actuator. The simulations for the static response are straightforward; however, dynamic response (i.e., ω vs. V_G/Q_G) requires time consuming iterative simulations. Specifically, in order to obtain ω vs. V_G/Q_G characteristics for any actuator, we first obtain its y vs. V_G/Q_G characteristics as shown in Fig. D.1 a. Then, at each V_G/Q_G, we perturb the system from its steady state equilibrium position and observe the small oscillation behavior. For example, Fig. D.1 b shows the displacement vs. time sequence for small oscillation at $V_G = 40V$. The phase plot for the same is shown in Fig. D.1 c. We then take the FFT (Fast Fourier Transform) of the displacement (Fig. D.1 d). The peak in the amplitude corresponds to the resonance frequency. For small oscillations there is only one dominant frequency as expected. Now, we perform these dynamic simulations at each V_G/Q_G to obtain ω vs. V_G/Q_G characteristics discussed in chapter 3.

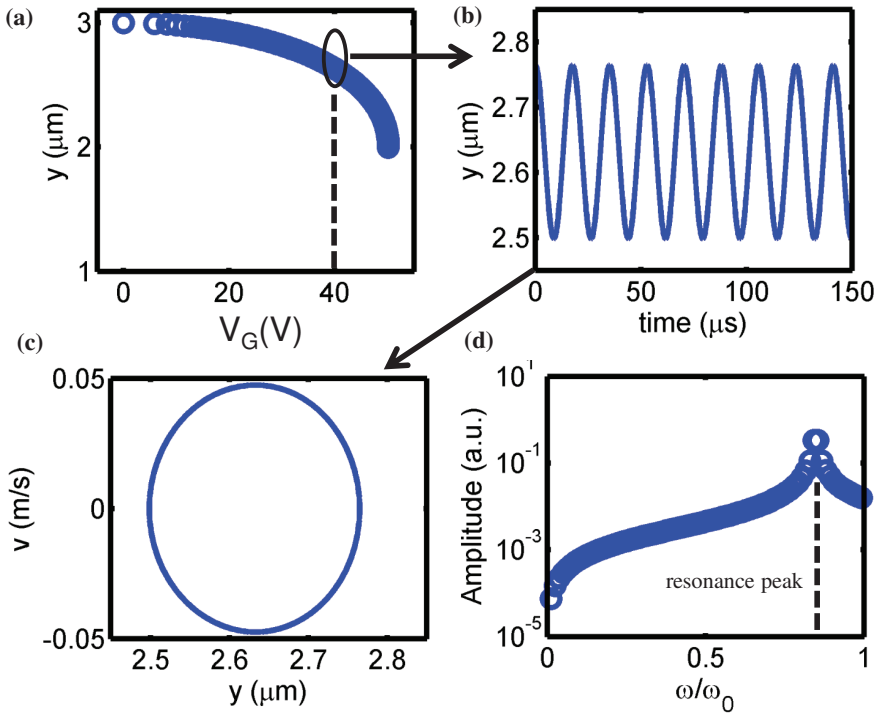

Fig. D.1. Dynamic behavior of a parallel-plate actuator for a linear spring (a) steady state y vs. V_G characteristics, (b) displacement vs. time for small oscillation at $V_G = 40V$ around the steady state equilibrium position, (c) phase plot for the same with v being the velocity of M_1, and (d) amplitude of Fast Fourier Transform of displacement as a function of ω/ω_0. Frequency corresponding to peak denotes the resonance frequency at $V_G = 40V$. ω_0 is the resonance frequency at $V_G = 0$.

E. TIME DOMAIN STOCHASTIC SIMULATIONS FOR NOISE IN FLEXURE SENSORS

E.1 Time Domain Simulation Framework for Force Noise

The time domain response of Flexure sensor in presence of white thermo-mechanical force noise is modeled using Newton's law, given by-

$$m\frac{dv}{dt} + bv = k\left(y_0 - y\right) - \frac{\epsilon_0 WL}{2y^2}V_G^2 + F_N(t), \tag{E.1}$$

$$\frac{dy}{dt} = v. \tag{E.2}$$

Here, m is mass of the movable electrode, v is the velocity, t is time, $b = m\omega_0/Q$ is the damping coefficient. $F_N(t)$ is the random noise force with autocorrelation function $\left\langle F_N(t)F_N(t^{'})\right\rangle = 2k_BTb\delta(t-t^{'})$ and one sided power spectral density $S_F(\omega) = 4k_BTb$. It is also important to note that, white Gaussian noise force is $F_N(t) = \sqrt{2k_BTb}\frac{dW(t)}{dt}$, where $W(t)$ is the Brownian process.

Using the definition $\frac{dv}{dt} = \frac{v(t+\Delta t)-v(t)}{\Delta t}$ and $\frac{dy}{dt} = \frac{y(t+\Delta t)-y(t)}{\Delta t}$, Eqs. E.1 - E.2 can be written as follows-

$$\left(1 + \frac{b\Delta t}{m}\right)v\left(t+\Delta t\right) = v(t) + \frac{k\Delta t}{m}\left(y_0 - y(t)\right) - \frac{\epsilon_0 WL}{2my^2}V_G^2\Delta t + \sqrt{2k_BTb}\frac{dW_{\Delta t}(t)}{m} \tag{E.3}$$

$$y(t+\Delta t) = y(t) + v(t+\Delta t)\Delta t, \tag{E.4}$$

where $v(t)$ and $v(t+t)$ are the values of velocity, at time t and $t+\Delta t$, respectively. Similarly, $y(t)$ and $y(t+\Delta t)$ are the values of electrode position, at time t and $t+\Delta t$, respectively. Δt is the time step. Most importantly, $dW_{\Delta t}(t)$ is a random variable that is normal distributed with mean zero and standard deviation $\sqrt{\Delta t}$. Knowing the initial condition i.e., $y(0)$ and $v(0)$, Eqs. E.3 - E.4 can be solved for any V_G. At every instant t, a new random variable $dW_{\Delta t}(t)$ is generated to evaluate Eqs. E.3 - E.4.

E.2 Time Domain Simulation Framework for Stiffness Noise

The time domain response of Flexure sensor in presence of white stiffness noise is also modeled using Newton's law, given by-

$$m\frac{dv}{dt} + bv = \left(k + \Delta k_N(t)\right)(y_0 - y) - \frac{\epsilon_0 WL}{2y^2}V_G^2 + F_N(t), \tag{E.5}$$

$$\frac{dy}{dt} = v. \tag{E.6}$$

where $\Delta k_N(t)$ is the random noise due to stiffness fluctuations with autocorrelation $\left\langle \Delta k_N(t)\, \Delta k_N\left(t'\right)\right\rangle = 0.5N_k\left(t-t'\right)$ and one sided power spectral density $S_{\Delta k}(\omega) = N_k$. It is also important to note that white stiffness fluctuations are $\Delta k_N(t) = \sqrt{0.5N_k}\frac{dW(t)}{dt}$. For numerical simulations, Eqs. E.5 - E.6 can be written as follows-

$$\left(1 + \frac{b\Delta t}{m}\right)v(t+\Delta t) = v(t) + \frac{k\Delta t}{m}(y_0 - y(t)) - \frac{\epsilon_0 WL}{2my^2}V_G^2\Delta t + (y_0 - y(t))\sqrt{0.5N_{\Delta k}}\frac{dW_{dW_{\Delta t}}(t)}{m} \tag{E.7}$$

$$y(t + \Delta t) = y(t) + v(t + \Delta t)\Delta t, \tag{E.8}$$

Equations E.7-E.8 can be now solved for any V_G to evaluate the noise response due to stiffness fluctuations.

E.3 Numerical Simulations

Figures E.1-E.2 show the results of time domain stochastic simulations (for same parameters as used in chapter 6) for thermo-mechanical noise and stiffness noise due to temperature fluctuations, respectively. We simulated the noise response at different voltages. For one voltage $V_G = 0.9V_{PI}$, results are summarized in Figs. E.1 a-d and Figs. E.2 a-d, respectively. Figures E.1 a-b show the fluctuations in the position of electrode on the potential energy landscape. Each symbol denote the total energy during fluctuations. As expected, electrode does random thermal vibration around its equilibrium position as shown in Fig. E.1 c. Figure E.1 d shows the corresponding sample average of root mean square fluctuations i.e.,

$$\Delta y_N(t) = \sqrt{\frac{1}{N_s}\sum_{i=1}^{i=N_s}\left(y_i(t) - y^i_{mean}(t)\right)^2} \tag{E.9}$$

$$y^i_{mean}(t) = \frac{1}{N_s}\sum_{i=1}^{i=N_s} y_i(t). \tag{E.10}$$

Here, $y_i(t)$ denote the position of electrode during i^{th} simulation at time t and $y^i_{mean}(t)$ is the corresponding mean position. N_s (1000 in this thesis) is the number of simulations performed to do the averaging. Interestingly, $\Delta y_N(t)$ starts from zero

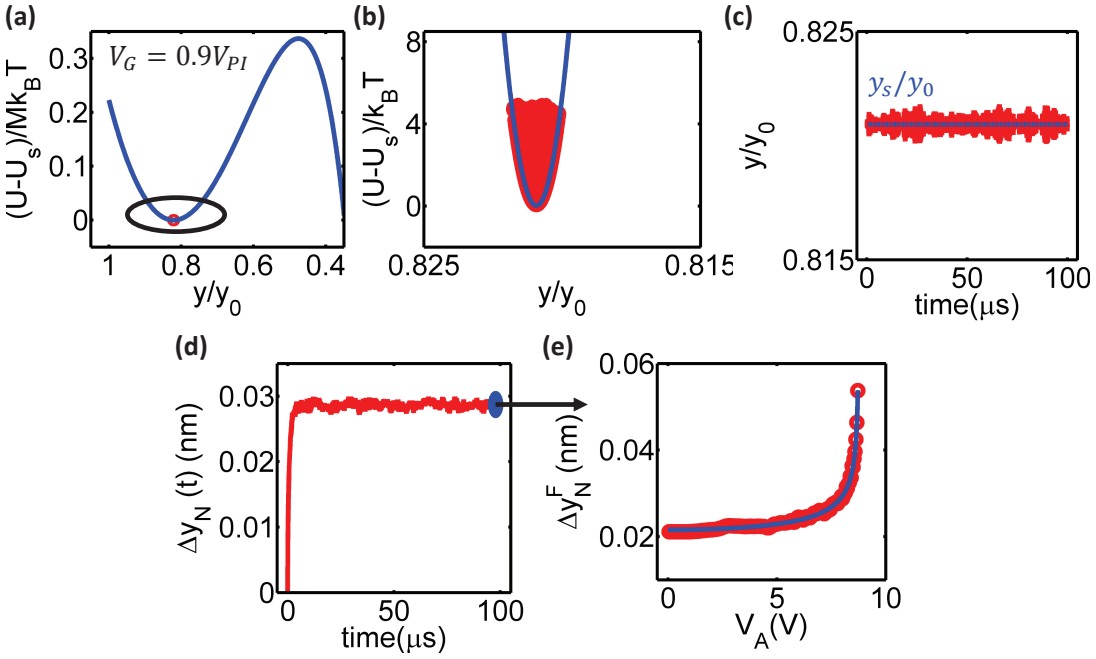

Fig. E.1. Time domain stochastic numerical simulations of thermo-mechanical noise. (a)-(b) Fluctuations of movable electrode position shown on the potential energy landscape. The region in the oval has been zoomed. Symbols denote the total energy (kinetic + potential) of the electrode. (c) Position of electrode as a function of time. y_s denote the equilibrium position. (d) Root mean square fluctuations as a function of time. (e) Equilibrium value of root mean square fluctuations is the average noise power. Symbols denote the results from time domain numerical simulations; whereas solid line denote the calculations from linear transfer function based analysis (Eq. 6.17 in chapter 6).

and then saturates to an equilibrium value (solid dot in Fig. E.1 d), which is nothing but the average noise power. Figure E.1 e compares the results obtained from time domain simulations (symbols) with the ones obtained from transfer function based analysis (solid line). In spite of the presence of highly nonlinear electrostatic force, the results match due to small values of fluctuations (Fig. E.1 d and Fig. E.2 d), thus justifying linearization around the equilibrium value (Eq. 6.14 & Eq. 6.15 in chapter 6) for transfer function based analysis. Having said that, as we go closer to the pull-

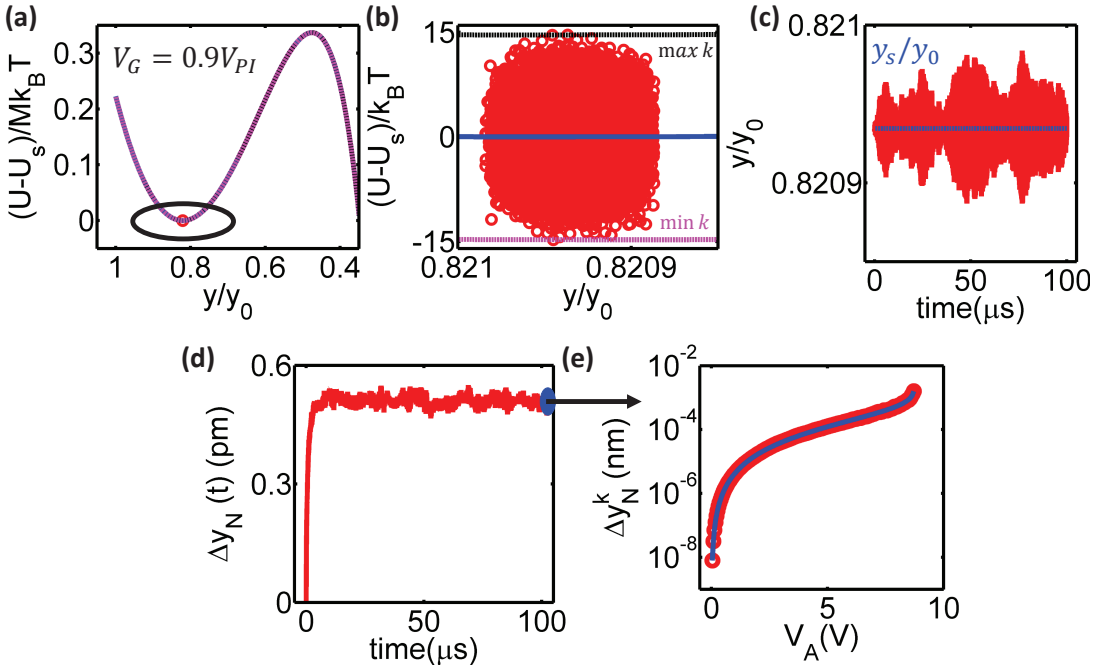

Fig. E.2. Time domain stochastic numerical simulations of stiffness noise due to temperature fluctuations. (a)-(b) Fluctuations of movable electrode position shown on the potential energy landscape. The region in the oval has been zoomed. Dotted black curve corresponds to the maximum stiffness; whereas magenta dotted to minimum stiffness. Symbols denote the total energy (kinetic + potential) of the electrode. (c) Position of electrode as a function of time. y_s denote the equilibrium position. (d) Root mean square fluctuations as a function of time. (e) Equilibrium value of root mean square fluctuations is the average noise power. Symbols denote the results from time domain numerical simulations; whereas solid line denote the calculations from linear transfer function based analysis (Eq. 6.18 in chapter 6).

in voltage, fluctuations increase eventually leading to noise initiated pull-in. So, the linear transfer function based analysis is valid so long as we are below safe operating voltage. Note that, similar results and similar matching between time domain and transfer function analysis is achieved for stiffness noise also (Fig. E.2).

F. ANALYTICAL FORMULA OF TRAVEL RANGE

Here, we derive the analytical formula (Eqs. 4.2-4.3) of travel range for array of nano- wires/tubes (example of cylinders). The static operation of microactuator (as discussed in chapters 2-3) is governed by the balance of spring and electrostatic force (Eq. F.1). Equation F.2 is the condition for pull-in instability-

$$k\,(y_0 - y) = -\frac{1}{2}\frac{dC}{dy}V^2, \tag{F.1}$$

$$k = -\frac{1}{2}\frac{d^2C}{dy^2}V^2, \tag{F.2}$$

where k is the spring constant, y_0 is the initial air-gap, y is the gap between the two electrodes, C is the capacitance and V is the applied voltage. The solution of Eqs. F.1-F.2 yields-

$$\frac{y_c}{y_0} = \frac{1}{1+\alpha}, \tag{F.3}$$

where $y_c = y_0 - t_r^V$ is the critical gap at which pull-in instability occurs, t_r^V is the travel range, and-

$$\alpha = -\frac{\frac{dC}{dy}}{y_c\frac{d^2C}{dy^2}} \tag{F.4}$$

For an array of cylinders with $C_{array} = (2\pi\epsilon_0 L)/\log(\sinh(2\pi(y+R)/g)/(\pi R/g)$, expression for α is given by-

$$\alpha = \frac{g}{4\pi y_c}\frac{\sinh\left(\frac{4\pi(y_c+R)}{g}\right)\log\left(\frac{\sinh\left(\frac{2\pi(y_c+R)}{g}\right)}{\frac{\pi R}{g}}\right)}{\left(1+\cosh\left(\frac{4\pi(y_c+R)}{g}\right)+\log\left(\frac{\sinh\left(\frac{2\pi(y_c+R)}{g}\right)}{\frac{\pi R}{g}}\right)\right)} \tag{F.5}$$

where ϵ_0 is the permittivity of free space, L is the length of individual cylinder and g is the separation between the individual cylinders. This complex looking expression for α (Eq. F.4) can be simplified in the two regimes (left of the peak and right of the peak in Fig. 4.4, chapter 4). For small values of g (left of the peak), using the fact that, $\cosh\left(\frac{4\pi(y_c+R)}{g}\right) \gg \log\left(\frac{\sinh\left(\frac{2\pi(y_c+R)}{g}\right)}{\frac{\pi R}{g}}\right)$, $\frac{\sinh\left(\frac{4\pi(y_c+R)}{g}\right)}{\cosh\left(\frac{4\pi(y_c+R)}{g}\right)} \sim 1$, and $\sinh\left(\frac{4\pi(y_c+R)}{g}\right) \approx \frac{1}{2}\exp\left(\frac{2\pi(y_c+R)}{g}\right)$, α reduces to

$$\alpha \approx \frac{g}{4\pi y_c}\log\left(\frac{\exp\left(\frac{2\pi(y_c+R)}{g}\right)}{\frac{2\pi R}{g}}\right). \tag{F.6}$$

On further simplification of Eq. F.6, we get-

$$\exp(ax) = 2bx\exp(cx) \tag{F.7}$$

where $a = 2\pi(y_c + R)$, $b = 2\pi R$, $c = 4\pi y_c\alpha$, and $x = 1/g$. Interestingly, Eq. F.7 has an analytical solution which when combined with Eq. F.3 gives us the result shown in Eq. 4.2 in chapter 4.

In contrast, for large values of g (right of the peak in Fig. 4.4, chapter 4), $\log\left(\frac{\sinh\left(\frac{2\pi(y_c+R)}{g}\right)}{\frac{\pi R}{g}}\right) \approx \log\left(\frac{2\pi(y_c+R)}{g}\right)$. This logarithmic dependence allows us to assume $\log\left(\frac{2\pi(y_c+R)}{g}\right) \approx \log\left(\frac{2\pi(y_0+R)}{g}\right) \equiv \lambda$. Moreover, using the fact that $\sinh(z) \approx z + \frac{z^3}{6}$, and $\cosh(z) \approx 1 + \frac{z^2}{2}$, where $z = 4\pi(y_c + R)/g$, value of α reduces to -

$$\alpha \approx \frac{g}{4\pi y_c}\frac{\lambda\left(z + \frac{z^3}{6}\right)}{\lambda + 2 + \frac{z^2}{2}}. \tag{F.8}$$

Simplifying Eq. F.8, we get-

$$ax + \frac{(ax)^3}{6} = bx\left(\lambda + 2 + \frac{(ax)^2}{2}\right). \tag{F.9}$$

where $a = 4\pi(y_c + R)$, $b = (4\pi y_c\alpha)/\lambda$, and $x = 1/g$. Solving Eq. F.9 in conjunction with Eq. F.3, we get back the equation 4.3 in chapter 4.

G. RELIABILITY OF RF-MEMS : DIELECTRIC CHARGING AND CREEP

In chapter 4, we discussed one of the reliability issues of RF-MEMS capacitive switches, namely hard-landing. Here[1], we focus on other electromechanical reliability issues of RF-MEMS capacitive switches and varactors. We specifically address the reliability issues of dielectric charging in capacitive switches (sec. G.1) and creep (sec. G.2) in varactors.

G.1 Capacitive Switches : Dielectric Charging

G.1.1 Background and Goals

Another key reliability issue of RF-MEMS capacitive switches is dielectric charging [166, 167]. When the movable electrode M_1 is pulled-in (down state, Fig. G.1 (a)), charges are injected into the traps/defects inside the dielectric. These trapped charges modify the electrostatic force acting on M_1, and cause the CV curve to shift, and the V_{PI} and V_{PO} to change over time. This parametric degradation eventually leads to catastrophic failure by stiction i.e., the electrode M_1 can no longer be restored to up state even at zero voltage (i.e.,$V_{PO} < 0$), because the restoring spring force can no longer overcome the downward electrostatic force exerted by the accumulated charges within the dielectric. We define the lifetime (t_{life}) of the device due to dielectric charging by the condition $V_{PO}(t_{life}) = 0$. In order to predict t_{life}, three key factors should be considered: (1) physical mechanism of time-dependent charge injection into the dielectric, (2) modification of electrostatic force due to injected charges, and (3) evolution of V_{PO} as a function of time.

[1]The content (text and figures) in this section have been adapted from [165] ©IEEE 2012.

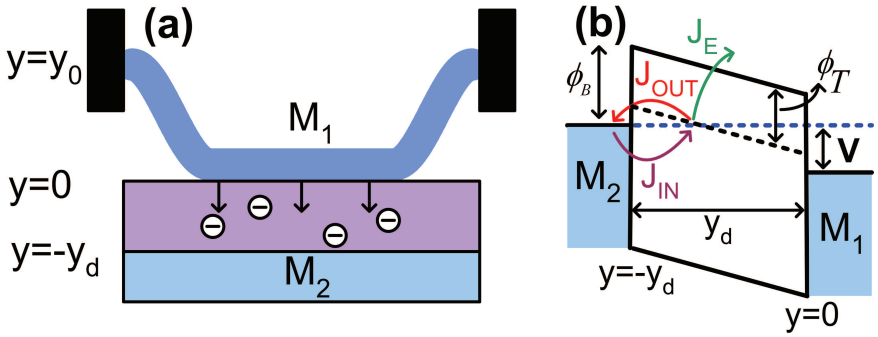

Fig. G.1. Problem of dielectric charging in RF-MEMS capacitive switches. (a) Schematic of the capacitive switch when M_1 is pulled-in, showing charge injection into the bulk traps inside the dielectric. (b) The band diagram of a metal-insulator-metal system defining the barrier heights and current components into and out of the traps. Voltage V has been applied between the electrode M_1 and M_2.

In the literature, time dynamics of V_{PO} is modeled either by a simple resistor-capacitor model, with its time constants fitted to experimental data [168–170], or by considering the injected charge simply as an input parameter [171, 172]. Therefore, it is difficult to know if the predictions from these empirical models are reliable, or how sensitive the model is to the changes in physical parameters such as trap density and barrier height, arising from changes in the fabrication conditions. Similarly, the dependence of t_{life} on the stress voltage V has been studied experimentally, and a basic model $t_{life} \sim \exp(-\gamma V)$ has been observed to fit the data [167, 173, 174], where γ is the voltage-acceleration factor. This "exponential" model has been derived by assuming Frenkel-Poole (FP) charge injection [166, 174], but the applicability of FP conduction to the dielectrics used in RF-MEMS ($\sim 100-500nm$) is questionable [175]. The field lacks a physics-based theoretical model/framework, which can anticipate time evolution of V_{PI}/V_{PO} and predict t_{life}. In this section, we first develop a model for time-dependent charge injection inside the dielectric and couple it with the Euler-Bernoulli (EB) framework of MEMS actuation (sec. A.1.1) to achieve the following goals-

- establish a scaling relationship for time-dynamics of pull-out voltage, i.e., $\Delta V_{PO}(t) = g(t/t_{life}) \sim (t/(t_{life}(V)))^{\beta}$, where β is device-specific constant,
- show that the number of cycles of reliable operation of a capacitive switch is given by $N_{life} = (t_{life}(V))/(d_c T - t_{PI}(V))$, where d_c is the duty-cycle, t_{PI} is the pull-in time, and $f = 1/T$ is the frequency of operation of actuation voltage,
- demonstrate that the lifetime predicted by the empirical "exponential model" is unduly pessimistic; physics of charge injection within the dielectric anticipates a more optimistic super-exponential voltage scaling, (i.e., $t_{life} \gg \exp(-\gamma V)$),
- show that the dynamic charge injection within the dielectric increases the impact velocity v_{impact}, which may further degrade surface morphology of the dielectric.

G.1.2 Dielectric Charging Model

There is a long history of modeling and experiments related to charge injection into the dielectric, details of which can be found in references [176–179]. Here we only highlight the key features/equations of dielectric charging related to RF-MEMS capacitive switches. During the pulled-in state, the switch can be modeled as a metal-insulator-metal (MIM) system. Figure G.1(b) shows the band diagram of the MIM system, showing the location of a trap in energy, barrier height Φ_B, and three trapping/de-trapping (J_{IN}, J_{OUT}, and J_E) fluxes into and out of the traps. The traps are assumed electrically neutral (before charge injection from the contact), uniformly distributed within the dielectric with density N_T, with a tunneling capture cross section σ, and located at an energy level Φ_T below the dielectric conduction band [180]. The three trapping/de-trapping fluxes are based on the following processes: (1) electrons injected from the metal contacts into traps by tunneling (J_{IN}), (2) electrons tunneling out from the traps back into the contact (J_{OUT}), and/or (3) electrons emitted out of the traps into the dielectric conduction band by a field-assisted, temperature activated FP emission process (J_E). The expressions for $J_{IN}(y)$, $J_{OUT}(y)$ and $J_E(y)$ in terms of trapped electron density $n_T(y,t)$ and device-specific

constants $A_{IN}(y)$, $A_{OUT}(y)$, and $A_E(y)$, (details of which can be found in [165, 181]) are given by Eqs. G.1-G.3.

$$J_{IN}(y) = A_{IN}(y)(N_T - n_T(y,t)), \tag{G.1}$$

$$J_{OUT}(y) = A_{OUT}(y)n_T(y,t), \tag{G.2}$$

$$J_E(y) = A_E(y)n_T(y,t). \tag{G.3}$$

The rate of change of $n_T(y,t)$ is given by the balance of current fluxes going into and coming out of the traps i.e.,

$$q\Delta y\frac{dn_T(y,t)}{dt} = J_{IN}(y) - J_{OUT}(y) - J_E(y). \tag{G.4}$$

The solution of Eq. G.4 provides the time dynamics of $n_T(y,t)$. These trapped charges modify the electrostatic force (Eqs. G.5-G.6) acting on the electrode M_1 as follows:-

$$F_{elec} = \frac{W\epsilon_0(V - \Delta V(t))^2}{2(y + \frac{y_d}{\epsilon_d})^2}, \tag{G.5}$$

$$\Delta V(t) = -\frac{1}{\epsilon_0\epsilon_d}\int_{-y_d}^{0} y n_T(y,t)dy. \tag{G.6}$$

Equation A.7 & A.13can now be solved with the modified electrostatic force (Eqs. G.5-G.6) to study the effect of dielectric charging on V_{PI}/V_{PO}, t_{PI}, v_{impact}, and t_{life}.

G.1.3 Results and Discussions

Figure G.2 summarizes the predictions regarding the lifetime of the capacitive switch due to dielectric charging. Figure G.2(a) shows the evolution of electron number density (n_T) inside the dielectric as a function of stress time when actuated by $80V$. The peak value of n_T increases rapidly, and the centroid of n_T profile moves

away from the M_1-dielectric interface deeper into the dielectric as a function of contact duration. These negative charges within the dielectric increases the electrostatic force on the upper membrane (Eqs. G.5-G.6), which makes the pull-in of the device easier (smaller V_{PI}) and the pull-out difficult (smaller V_{PO}). This reduction in V_{PI}/V_{PO} shifts the CV curve to the left (Fig. G.2(b)). Figure G.2(c) shows V_{PO} as a function of stress time at different stress voltages. When V_{PO} crosses zero, electrode M_1 can not be pulled-out even at zero applied voltage. As a result, the device fails due to stiction. The corresponding lifetime of the switch is shown in Fig. G.2(e). Interestingly, if we plot ΔV_{PO} against a new variable $t/t_{life}(V)$, all the curves associated with different stress voltages overlap, i.e., $\Delta V_{PO} \sim g(t/t_{life})$, (Fig. G.2(d)). Although, we cannot offer an analytical derivation, our numerical simulations of fixed-fixed beam strongly suggests that-

$$\Delta V_{PO} \sim g\left(\frac{t}{t_{life}}\right) \approx 1 - \exp\left(-\left(\frac{t}{t_{life}}\right)^{\beta}\right), \tag{G.7}$$

which reduces to a power-law of the form, $\Delta V_{PO} \sim (t/t_{life})^{\beta}$, at short times. Here β is constant that depends on material parameters and device geometry. Based on some initial results, we speculate that $\Delta V_{PO} = g(t/t_{life})$ might apply to any MEMS geometry, where the functional form of g can be obtained from experimental data for arbitrarily complex MEMS switches. If so, this scaling function offers a new algorithm for accelerated lifetime testing and would allow the device designer to determine t_{life} at reduced V_{stress} based on the failure kinetics at higher applied biases.

We now explore the voltage dependence of $t_{life}(V)$ and $N_{life}(V)$, related to the voltage acceleration model. Figures G.2(e)-(f) suggest that an empirical exponential model $t_{life}(V) \sim \exp(-\gamma V)$, based on voltage acceleration coefficient γ determined from the accelerated tests, might severely underestimate the lifetime of RF-MEMS capacitive switches at operating voltages. Therefore, a more physics based model like the one discussed in this section is needed to correctly predict t_{life}/N_{life} of the switch.

In an operational circuit, RF-MEMS switch is repeatedly turned on (pulled-in) and off (pulled-out). Therefore, we need to look into how repeated switching affects

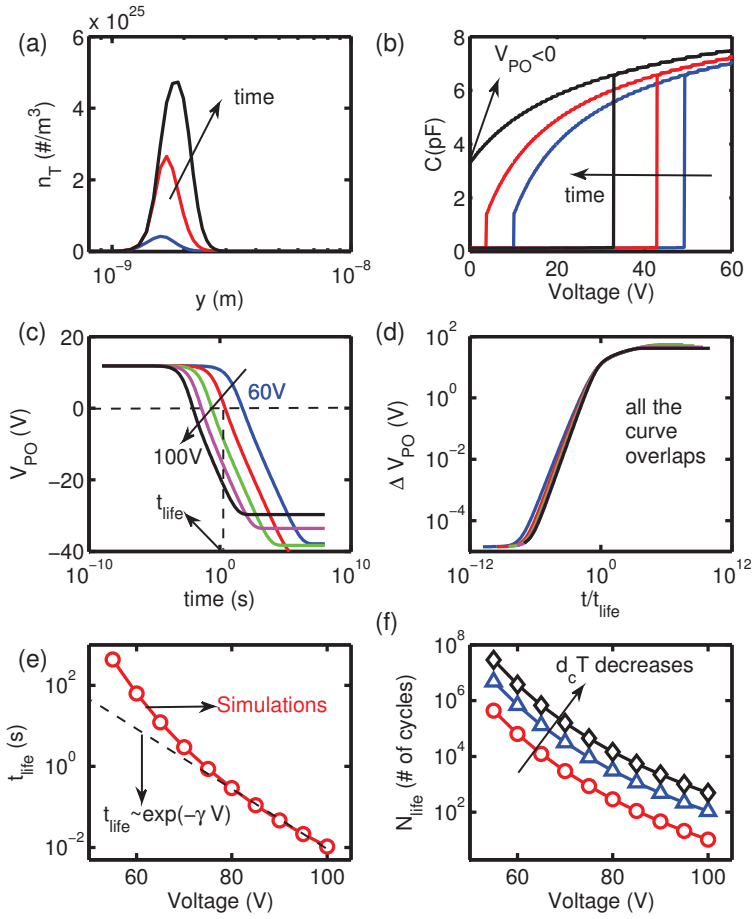

Fig. G.2. Effect of dielectric charging on the performance and lifetime of a capacitive switch. (a) Electron number density (n_T) inside the dielectric at different instants of the time, when stressed at $80V$. (b) CV curve shifts to the left because of the accumulation of negative charges inside the dielectric (time increases in the direction of arrow). (c) V_{PO} plotted against stress time at various stress voltages. Stress voltage increases in the direction of arrow with an increment of $10V$. (d) When ΔV_{PO} is plotted against t/t_{life}, all the curves at different stress voltage overlap. (e) t_{life} of the device at different stress voltages. (f) The lifetime of the device defined by the number of cycles (N_{life}) plotted as a function voltage for $d_cT = 1000\mu s(\circ)$, $d_cT = 100\mu s(\triangle)$, $d_cT = 25\mu s(\diamond)$, respectively.

the lifetime. The DC t_{life} can be viewed as a sum of the contact times during AC

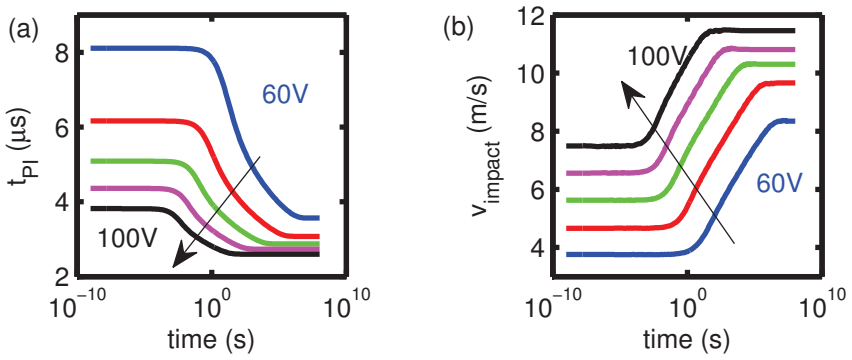

Fig. G.3. Effect of dielectric charging on pull-in dynamics of the switch. (a) t_{PI} decreases and (b) v_{impact} increases with stress time due to accumulation of negative charges inside the dielectric. Actuation voltage increases in the direction of arrow with an increment of $10V$.

stress. Therefore, the number of cycles of safe operation (N_{life}) of the switch under AC stress can be deduced from DC t_{life}, as follows:-

$$N_{life} = \frac{t_{life}}{d_c T - t_{PI}}, \tag{G.8}$$

where d_c is the duty cycle, and $f = 1/T$ is the frequency of the operation of actuation voltage. Equation G.8 assumes that there is no relaxation of trapped charges during the time when voltage is removed because of the very low electric field in dielectric [165]. It implies that during AC stress when voltage is removed, ΔV_{PO} does not recover. Hence, an AC stress that toggles between 0 and V, does not improve integrated lifetime (t_{life}) of the switch, but it can only improve N_{life} depending upon d_c and T. Figure G.2(f) shows N_{life} for different values of $d_c T$. N_{life} increases as $d_c T$ decreases, because lower $d_c T$ implies shorter contact time per cycle. Moreover, since $d_c T - t_{PI}$ is the contact time for dielectric charging, N_{life} increases significantly as $d_c T \rightarrow t_{PI}$.

Dielectric charging not only affects the static behavior (V_{PI}, V_{PO}, and CV curve) of the device, but also affects the pull-in dynamics (t_{PI} and v_{impact}) and the understanding of this phenomenon is essential for correct operation of the switch. Figures

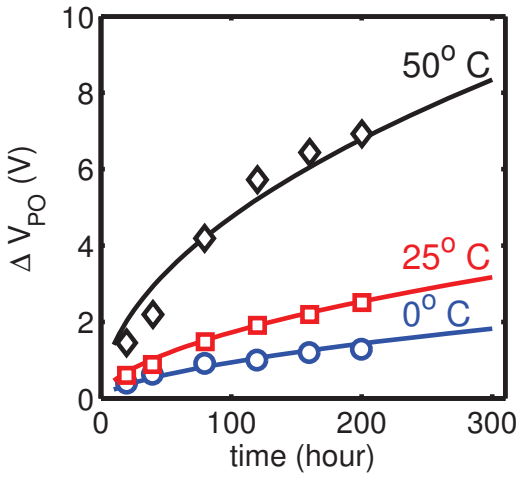

Fig. G.4. Comparison of our theoretical model with the experimental data [182]. ΔV_{PO} as a function of stress time for different temperatures. Symbols are the experimental data and solid lines are predictions of our model

G.3(a)-(b) show t_{PI} and v_{impact} as a function of the total integrated stress time at different actuation voltages. The trapped charges inside the dielectric increase the electrostatic force, and therefore, decreases t_{PI} (Fig. G.3(a)), and increases v_{impact} (Fig. G.3(b)). Therefore, techniques of soft landing discussed in section 4.2 in chapter 4 will help lessen this problem.

Finally, to validate the model just developed, we interpret the data from the literature through two non-trivial predictions of our model. Figure G.4 shows ΔV_{PO} as a function of stress time for different temperatures [182]. Our simulation matches very well with the experimental data [182] and suggests that the model is physically justified. The temperature dependence in our model comes from temperature activated FP emission current $J_E(y)$ [165, 181].

As a second validation, we explore the validity of the novel scaling relationship proposed in Fig. G.2(d) by using the experimental data from Ref. [183]. Figure G.5(a) shows ΔV_{PO} as a function of time for four different stress voltages. When this

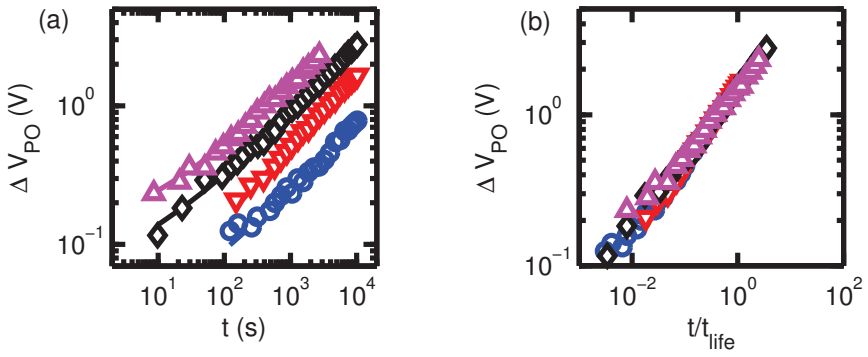

Fig. G.5. Validation of scaling relationship against experimental data [183] (a) ΔV_{PO} as a function of t for four different stress voltages: $30V(\circ)$, $35V(\bigtriangledown)$, $40V(\diamond)$, $45V(\bigtriangleup)$. (b) When ΔV_{PO} is plotted against t/t_{life} assuming $V_{PO} = 1.5V$, all the curves overlap. This confirms the scaling behavior as anticipated in Fig. G.2(d).

ΔV_{PO} is plotted against t/t_{life}, assuming $V_{PO} = 1.5V$, all the curves overlap (Fig. G.5(b)), which is consistent with Eq. G.7 and anticipated by our numerical model.

G.1.4 Summary

To summarize this section on dielectric charging, we have provided a theoretical framework for lifetime prediction and parametric degradation of V_{PI}, V_{PO}, t_{PI}, and v_{impact} due to dynamic charge injection inside the dielectric. These results confirm that the physical model may help interpret many features of the experimental data that could not be analyzed by simpler empirical models.

G.2 Varactors : Creep

G.2.1 Background and Goals

RF-MEMS varactors operate below V_{PI}, and are therefore safe from the problem of dielectric charging and hard-landing. It has however been observed that a sustained DC bias causes electrode M_1 to continuously sag from its steady state equilibrium

position, resulting in the steady increase in the capacitance [184, 185]. This change in the capacitance degrades the tuning range of the varactor. This phenomenon has been attributed to creep [184, 185]. In literature, experimentally derived dynamic spring-constant was used to study the resonator's (using an RF-MEMS varactor) frequency degradation over time [184]. When generalized to a CAD model, it allows us to explore "creep compliance" as a function of time and interpret the characteristics of resonators and phase shifters [23]. Unfortunately, this empirical lumped-parameter spring-mass model can neither account for the position-resolved bending of the movable electrode as a function of time, nor does it address the "creep-limited lifetime" of the varactors. We define "creep-limited lifetime" as the time needed to cross a certain predefined (and circuit specific) threshold of capacitance degradation due to creep. In this section, we generalize the EB equation (Eq. A.7) to include a spring-dashpot model of viscoelasticity to predict the shape of the movable electrode as a function of time and voltage. This model allows us to predict parametric degradation of varactor performance and the associated creep-limited lifetime. Specifically, we achieve the following goals in this section-

- generalize the EB equation (Eq. A.7) to include a spring-dashpot model of viscoelasticity to predict the effect of creep on the time-dependent capacitance change under DC/AC bias,
- predict the creep-limited t_{life} of a varactor, and finally,
- study the effect of AC bias on creep induced capacitance change.

G.2.2 Creep Model

Creep in RF-MEMS varactors has been studied using theory of viscoelasticity [184, 186]. A viscoelastic material can be represented as a combination of linear spring (elastic element) and a dashpot (viscous element) (Fig. G.6) [187]. The linear spring follows the Hooke's law, $\sigma = E\epsilon$, where σ is the stress, ϵ is the strain, and E is the Young's modulus; whereas the dashpot follows the Newton's law $\sigma = \eta d\epsilon/dt$,

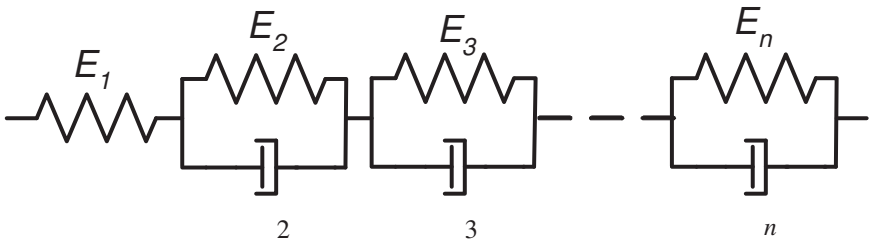

Fig. G.6. A spring-dashpot model of a viscoelastic material. We use this model in conjunction with EB equation to account for the creep behavior observed in RF-MEMS varactors.

where, η is the viscosity of material. The elastic and viscous components experience the same strain when they are in parallel, but the total strain is the sum of the two strains when they are in series. A model of creep with multiple time constants, as shown in Fig. G.6, can be defined by the following stress-strain relationship:-

$$\frac{\sigma}{E_i} = \frac{\eta_i}{E_i}\frac{d\epsilon_i}{dt} + \epsilon_i, i = 2, ...n, \tag{G.9}$$

$$\epsilon = \frac{\sigma}{E_1} + \sum_{i=2}^{n} \epsilon_i, \tag{G.10}$$

where, E_i, is the Young's modulus, η_i is the viscosity, ϵ_i is the strain of the i^th branch of the model, σ is the total stress, and ϵ is the total strain.

The steady-state EB equation (Eq. A.7) describes the steady state elastic response ($\sigma = E\epsilon$) of the beam. It is, however, necessary to use a time-dependent stress-strain relationship (Eqs. G.9-G.10) for modeling the creep behavior of the varactors. The following generalized EB equation accounts for the "spring-dashpot" response of the beam (Eqs.G.9-G.10), and allows us to interpret the time-dependent creep phenomena observed experimentally (see the published report [165] by us for derivation).

$$E_1 I \frac{\partial^4 y}{\partial x^4} = F_{elec} + E_1 I \sum_{i=2}^{n} \epsilon_i^m, \tag{G.11}$$

$$\frac{F_{elec}}{E_i I} = \frac{\eta_i}{E_i}\frac{d\epsilon_i^m}{dt} + \epsilon_i^m, i = 2, ...n, \tag{G.12}$$

where, ϵ_i^m is an intermediate strain of the beam.

G.2.3 Results and Discussions

Now, we explore the creep-limited lifetime of RF-MEMS varactors using the numerical simulations of Eqs. G.11-G.12. Figures G.7-G.8 summarize the results of time-dependent creep. We first validate the theoretical model by comparing against experimental data [188] based on nickel (Ni) membrane. Figure G.7(b) shows the capacitance of the device at $V = 20V$ as a function of stress time. Using a three branch model of viscoelasticity, our model predictions reproduces the experimental features of creep degradation reasonably well [188]. The corresponding shapes of the beam at different instants of time are shown in Fig. G.7(a).

The experimentally validated model offers us an opportunity to explore the creep behavior of varactor at different voltages. The time-dependent change in capacitance for two different operating voltages are shown in Fig. G.7(c). This change in capacitance degrades circuit performance, that is, an oscillator circuit will no longer remain tuned at the desired frequency due to the creep induced capacitance change and an external feedback circuit that compensates for the capacitance change will be necessary for the correct operation of the circuit. To quantify the capacitance degradation, we define the creep-limited lifetime as being the time in which capacitance changes by a fixed percentage of the capacitance at $t = 0$, i.e., $\left(\frac{C(t_{life})-C(0)}{C(0)} = r\right)$, where $C(t_{life})$ is the capacitance at $t = t_{life}$, $C(0)$ is the capacitance at $t = 0$ at the operating voltage V, and r is the tolerance limit for degradation. For example, Fig. G.7(d) shows creep-limited lifetime for $r = 0.05$ as a function of stress voltage. As operating voltage increases, the lifetime reduces exponentially. The voltage acceleration observed here is mainly due to spring-softening effect (see chapter 2), which effectively weakens the spring as a function of stress voltage.

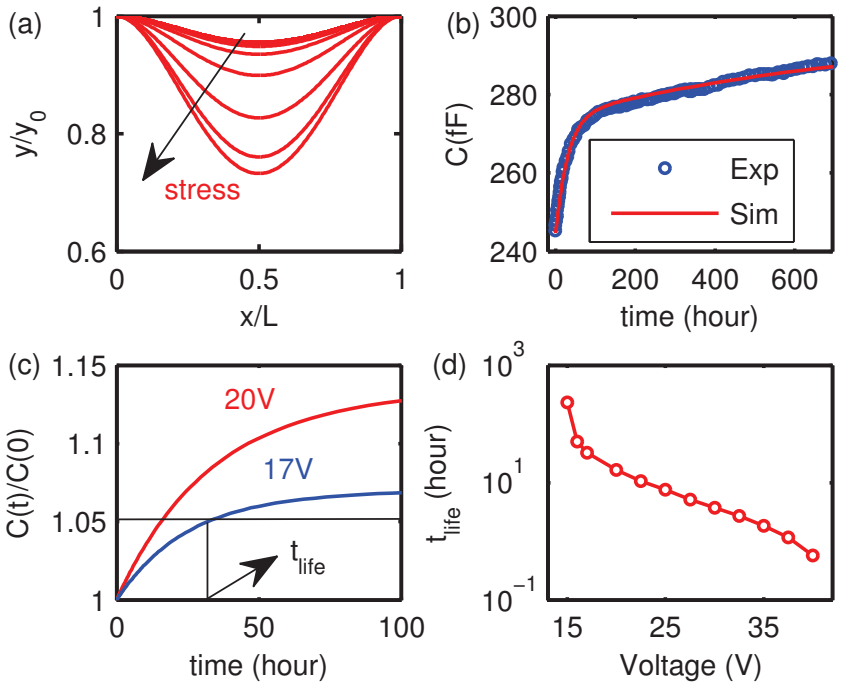

Fig. G.7. Creep behavior of RF-MEMS varactors under DC stress. (a) shape of the fixed-fixed beam during DC stress. Beam moves further down from its steady state position due to creep causing (b) capacitance of the device to increase as a function of time. Our theoretical model predicts very well the experimentally observed capacitance change [188]. (c) Capacitance change as a function of time for two different applied voltages. (d) t_{life} as a function of applied voltage due to creep. t_{life} increases rapidly at low stress voltages.

When the voltage is removed, the beam should ideally be restored to the initial position of zero deflection, but creep prevents this instant restoration of the pristine beam shape (Fig. G.8(a)). Instead the beam (and the capacitance) is restored asymptotically to the original shape over a long period of time (Fig. G.8(b)). In practice however, device is operated continuously and voltage is applied repeatedly. For such an AC stress, Figs. G.8(c)-(d) show the capacitance of the device at stress voltage and at zero voltage. When the voltage is applied, the capacitance continues to increase due to creep, and when voltage is removed, it recovers slowly. If the time

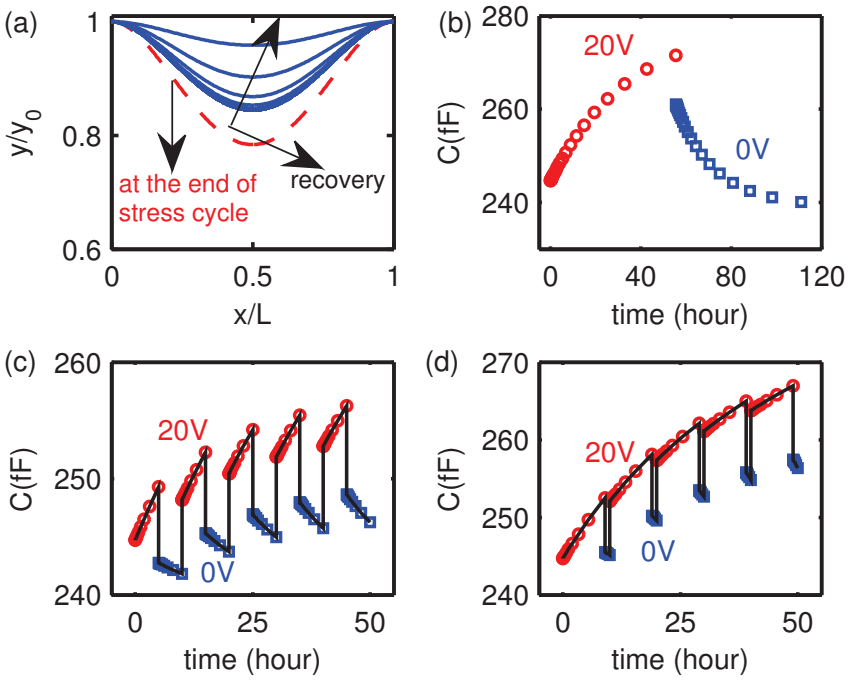

Fig. G.8. Creep behavior of RF-MEMS varactors under AC stress. (a) Shape of the fixed-fixed beam during stress-recovery. When voltage is removed, beam does not go all the way up, it goes up to a certain amount and then it recovers slowly which is reflected in (b) the capacitance of the device as a function of time. (c)-(d) Capacitance of the device as a function of time during AC stress. When a square voltage waveform of period 10 hour is applied, then at high voltage capacitance goes up due to creep, and when voltage is removed capacitance slowly recovers. Recovery depends on the duty cycle of the waveform. At (c) duty cycle of 50%, recovery is more as compared to (d) duty cycle of 90%.

allowed for recovery is insufficient, residual capacitance at zero voltage increases with number of cycles (Fig. G.8(c)-(d)). This increase in the capacitance at zero voltage is higher for higher duty cycle (Fig. G.8(c)-(d)), because less time is available for recovery.

G.2.4 Summary

To summarize this section on creep, our analysis shows that creep can be incorporated in the EB equation framework using viscoelastic theory. The framework presented can explain the experimentally observed time-dependent capacitance change and offers the possibility to predict creep-limited lifetime for arbitrary voltages.

G.3 Conclusions

To conclude, we have discussed the electromechanical reliability issues of RF-MEMS capacitive switches and varactors with the following contributions-

1. In the context of dielectric charging for capacitive switches, we developed a physics based predictive modeling framework to predict the time evolution of pull-in/pull-out voltage, pull-in dynamics (pull-in time and impact velocity) and eventually DC and AC life-time of the switch.
2. For varactors, we provided a modified Euler-Bernoulli equation to predict creep limited life-time.

H. ELECTROMECHANICAL RELIABILITY ISSUES OF SG-FET

In chapter 5, we discussed switching characteristics of SG-FET in detail. Here[1], we look into the reliability issues that may possibly arise when SG-FET is used as an analog/digital switch. We explore how does the classical reliability of FET or MEMS e.g., Negative Bias Temperature Instability (NBTI) [191], Hot Carrier Initiated Degradation (HCI) [192], and creep affect the SG-FET's long term operation.

H.1 Background and Goals

SG-FET, apart from its use in logic applications, can also be used as (i) a sleep transistor and (ii) resonant gate transistor [1]. In spite of this wide range of applications of SG-FET, there has not been any systematic study on the reliability of SG-FET to assess its promise for becoming a viable digital/analog technology.

SG-FET is analogous to a classical MOSFET in terms of the electrical performance, except for its behavior in off state. Therefore, many of the reliability concerns for MOSFET are also relevant for SG-FET. For classical digital technology based on MOSFET switches, Negative Bias Temperature Instability (NBTI) [191, 193], Hot Carrier Initiated Degradation (HCI) [192], and gate dielectric breakdown (TDDB) [194] are the major reliability concerns. One wonders how these reliability concerns would change if SG-FET were to replace the CMOSFET technology. Moreover, the mechanical nature of SG-FET may introduce additional reliability concerns such as creep [195], which is yet to be discussed in literature, but may have important con-

[1]The content (text and figures) in this section have been adapted from [189] ©IEEE 2010 and [190] ©IEEE 2012.

sequences for qualification of a technology that includes sleep transistor or resonant gate transistor.

Therefore, we develop a systematic theory of electromechanical reliability of SG-FET related to NBTI, HCI, and Creep. We show that these reliability concerns have dramatically different implications for SG-FET compared to CMOS switches.

H.2 Hot Carrier Initiated Degradation

H.2.1 Theory of HCI

Hot carrier injection is a persistent reliability concern for CMOS technology incorporating p- and n-type MOSFETs. HCI causes degradation of the gate dielectric near the drain side of a MOSFET (Fig. H.1 (a)). According to the classical theory of HCI [192], it occurs when the product of number and energy of the channel carriers is maximum. For long channel classical MOS transistors, it typically occurs near the drain side when the gate voltage is about half the drain voltage. Below this critical bias condition (i.e., at $V_G << V_{DS}/2$), there are not enough carriers near the drain side of the channel to do any damage, whereas at higher bias (i.e., at $V_G >> V_{DS}/2$), the carriers near the drain are not hot enough to cause any significant degradation. In simple CMOS circuit like inverter (Fig. H.1 (b), such $V_G \sim V_{DS}/2$ occurs when both p- and n-type FETs are ON during switching of input signal. We will show below that in a SG-FET inverter, during high to low switching of input, no current flows through n-type SG-FET making it immune to the problem of HCI.

H.2.2 Results : HCI Immune SG-FET Inverter

In order to explore the response of SG-FET to HCI, we simulate switching behavior of SG-FET inverter accounting for gate's pull-in and release dynamics. The switching behavior of SG-FET inverter is then compared with that of a classical MOSFET inverter. Figures H.2-H.3 summarize the results of MOSFET and SG-FET inverter

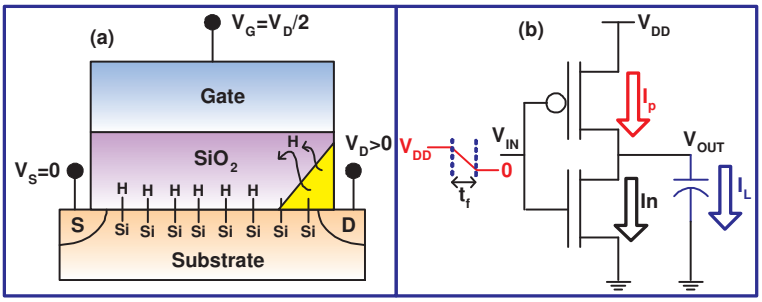

Fig. H.1. (a) Classical theory of HCI suggests oxide defect creation near the drain side of a MOSFET when gate voltage is about half the drain voltage. (b) Schematic of the inverter, where HCI situation is simulated during $1 \rightarrow 0$ switching of input signal. I_p, I_n and I_L are different current components flowing through PMOS, NMOS and load capacitor respectively. I_n is responsible for the HCI degradation.

respectively during high to low switching of the input signal. Figure H.2 (a) shows input and output voltage during switching. Various current components in Fig. H.2 (b) suggest that non zero current flows through n-type MOS (current I_n) (Fig. H.2(b)) implying that there is a direct current path from V_{DD} to ground. Note that, I_n is the major cause of HCI in n-type MOS. Moreover, direct current path from V_{DD} to ground increases the power dissipation (also known as short circuit power) of the switching.

In SG-FET inverter, when input voltage is switched from high to low, n-type SG-FET turns off as soon as the input voltage goes below the threshold voltage. This suggests that n-type SG-FET turns off within the fall time (t_f) of the input signal. Moreover, it springs back in the air and its release dynamics is shown in Fig. H.3 (a). In contrast, p-type SG-FET does not turn on even after the input voltage has reached zero (i.e., $|V_{GS}| = V_{DD}$). This is because, it starts from the up state and sees a high threshold voltage in the beginning. As it starts to move, threshold voltage decreases and it turns on as soon as threshold voltage goes below V_{DD}; which occurs close to pull-in (Fig. H.3(a)). Therefore, p-type SG-FET sees the delay of pull-in time during turn-on which is dictated by the intrinsic pull-in dynamics of SG-FET. The input and

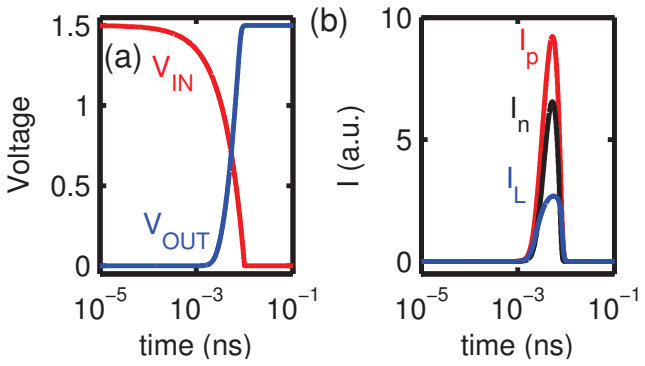

Fig. H.2. Simulation results of MOSFET inverter during high to low switching of the input. (a) Input and output voltage and (b) various current components during switching.

output voltage in Fig. H.3 (b) reflects that there is an intrinsic delay of pull-in time between the input going low and output going high. Because of this intrinsic delay, p- and n-type SG-FET are never simultaneously on. Interestingly, no current flows through n-type SG-FET as expected as it turns off before p-type SG-FET is turned on (Fig. H.3 (c)). Therefore, n-type SG-FET does not see the condition of HCI during this transition. Hence, the logic family associated with complementary SG-FET will be intrinsically immune to HCI degradation! Moreover, in SG-FET inverter there is no direct current path from V_{DD} to ground; all the current flowing through p-type SG-FET directly flows through the load capacitor (Fig. H.3(c)). Therefore, SG-FET inverter does not have the problem of short-circuit power dissipation and dissipates only $1/2C_LV_{DD}^2$ during the switching.

H.3 Negative Bias Temperature Instability

H.3.1 Theory of NBTI

Now, we discuss Negative Bias Temperature Instability which is one of the major reliability problems in classical p-type MOSFET biased in inversion, i.e., when the

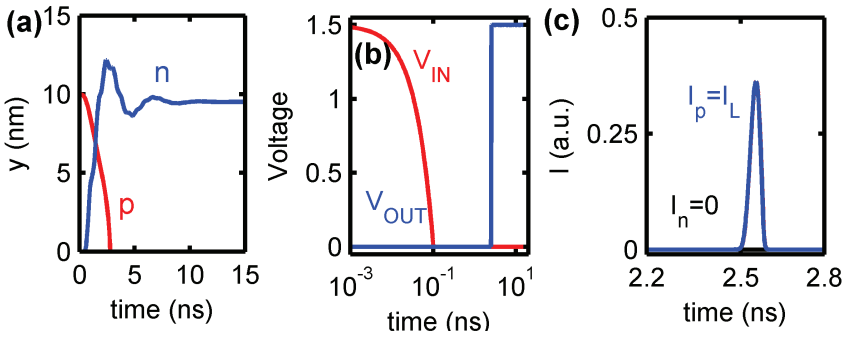

Fig. H.3. Simulation results of SG-FET inverter during high to low switching of the input. This simulation accounts for the pull-in/release dynamics of the beam. (a) Displacement of the center of the beam of p-and n-type SG-FET. p-type SG-FET is pulled-in and n-type SG-FET is pulled-out during this switching. (b) Input and out voltage and (c) various current components flowing through different elements during switching.

gate is negatively biased with respect to source and drain. This phenomenon is attributed to interface defect formation ($Si-H \rightarrow Si^{-}+H$) at the Si/SiO_2 interface of a PMOS transistor and is consistently modeled using the Reaction-Diffusion (R-D) framework [191, 193, 196]. During ON state (when $|V_G| > |V_{PI}|$), inversion charges (holes) populate near the Si/SiO_2 interface. These holes are captured by the interfacial Si-H bonds and dissociate the bond creating interface defect or dangling Si-bonds (Fig. H.4(a)). The rate of such defect generation is given by,

$$\frac{dN_{IT}}{dt} = k_f(N_0 - N_{IT}(t)) - k_r N_{IT}(t) N_H^0, \tag{H.1}$$

where N_0 is the initial number of $Si-H$ bond at Si/SiO_2 interface, $N_{IT}(t)$ is the fraction of these $Si-H$ bonds broken at time t due to NBTI stress, k_f is the dissociation constant of $Si-H$ bond breaking process, k_r is the constant for reverse reaction, and N_H^0 is the concentration of H atoms at the Si/SiO_2 interface. The H atom released in this process can anneal the broken bonds described by second term

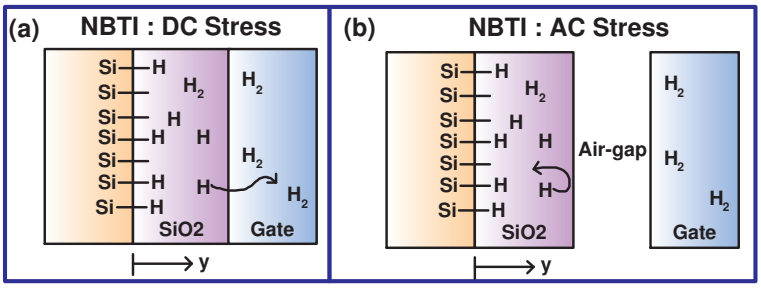

Fig. H.4. Negative Bias Temperature Instability (NBTI) in SG-FET under (a) DC stress when gate has been pulled-down (b) Off state during AC stress. Gate is separated from the dielectric by an air-gap when the gate voltage is removed under AC stress.

of the equation H.1 or may diffuse away from the interface, according to the following diffusion equation, i.e.,

$$\frac{\partial N_X}{\partial t} = D_X \frac{\partial^2 N_X}{\partial y^2} \tag{H.2}$$

where N_X is the concentration of diffusion species and D_X is their diffusion coefficient, which can be both H and H_2 [191]. Equations H.1 and H.2 are solved self-consistently to calculate the concentration of interface defect $N_{IT}(t)$. Now, this build up of $N_{IT}(t)$ modify the electrostatic force (Eq. A.8) acting on the gate due to the modification of electric field in air ($E_{air} = \epsilon_s E_s(\psi_s) + \frac{qN_{IT}}{\epsilon_0}$, see Eq. A.10 for $E_s(\psi_s)$). Therefore, we now solve Eq. A.7 with the modified electrostatic force to study the effect of NBTI on SG-FET's long term operation.

H.3.2 Results : NBTI - DC Stress

Figure H.5 shows the results of NBTI under DC stress. During the DC stress in SG-FET, dissociation of $Si-H$ bonds increases the dangling bond density $N_{IT}(t) \sim t^n, n = 1/6$ (Fig. H.5(a)), just like a classical MOSFET [191]. Increase in $N_{IT}(t)$, increases the electric field in air E_{air} and hence the electrostatic force (Eq. A.8) acting on the beam, which results in reduction of V_{PI} and V_{PO} (Fig. H.5(b)). Figure

H.5 (c) shows the time evolution of ΔV_{PO} for different stress voltages V_s. Eventually, when $\Delta V_{PO}(t_{life}) = V_{PO}(0)$, ($V_{PO}(0)$ is the initial pull-out voltage) the beam sticks irreversibly with the dielectric (catastrophic failure due to stiction) and can not be pulled-out even at zero applied bias. This stiction is a similar to the failure mechanism of RF-MEMS capacitive switches due to dielectric charging (chapter 4) and unfortunately, SG-FET will not be immune to it. Using $\Delta V_{PO} = V_{PO}(0)$ as the lifetime criteria, we calculate lifetime (t_{life}) of SG-FET as a function of stress voltage (V_s) in Fig. H.5(d). Lifetime decreases exponentially with V_s. Therefore, even though time evolution of N_{IT} in MOSFET and SG-FET is same, NBTI in MOSFET remains a parametric degradation (only changes the threshold voltage), whereas it can lead to catastrophic failure in SG-FET.

H.3.3 Results : NBTI - AC Stress

Now, we compare NBTI induced degradation of SG-FET and MOSFET under AC stress condition. When gate bias is removed for classical MOSFET, N_{IT} relaxes due to repassivation of dangling Si bonds [191,193]. In SG-FET, however, N_{IT} relaxation is much smaller compared to classical MOSFET (Fig. H.6(a)), because the gate is physically separated from the dielectric in off-state of SG-FET (Fig. H.4(b)). Therefore, the hydrogen trapped within the gate can not diffuse back to repassivate dangling Si bonds (Fig. H.4(b)). The hydrogen contained in the movable gate is lost forever to the gate interconnect. Instead, only the residual hydrogen species contained within the thin dielectric at the moment of electrode separation contributes to N_{IT} relaxation. As a result, SG-FET degrades faster than MOSFET at low frequencies (Figs. H.6(b)). At high enough frequency ($f > 2D_{H_2}/y_d^2$, where D_{H_2} is the diffusion coefficient of H_2), when SG-FET switching speed exceeds the hopping rate of H_2, hydrogen profile becomes insensitive to repeated opening/closing of the switch, and N_{IT} degradation of SG-FET and MOSFET becomes indistinguishable (Figs. H.6(c)).

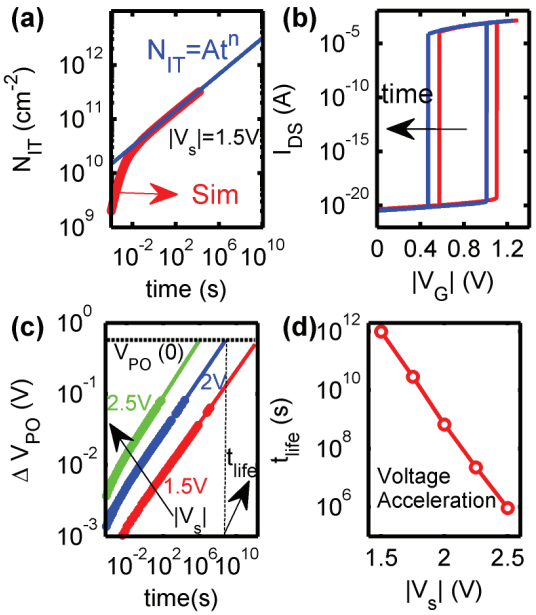

Fig. H.5. Simulation results for NBTI in SG-FET under DC stress. (a) At the pulledin state of a p-SG-FET with stress voltage $V_s = -1.5V$, $Si-H$ bonds dissociate, and increases $N_{IT} \sim t^n, n = 1/6$ just like classical MOSFET. (b) N_{IT} increases the electrostatic force acting on the beam and decreases V_{PI}/V_{PO} by left-shifting the $I_{DS} - V_G$ characteristics. (c) Change in pull-out voltage for different stress voltages. (d) t_{life} decreases exponentially at higher V_s.

Figure H.6(d) shows the AC-DC ratio as a function of frequency, which summarizes the discussions of Figs. H.6(b-c).

H.4 Creep

Now, we discuss the issue of creep in context of sleep transistor and resonant gate transistor which operate below pull-in. To analyze the effect of creep, we use modified Euler-Bernoulli framework developed in section G.2.2 in context of RF-MEMS varactors, and the results are summarized below:

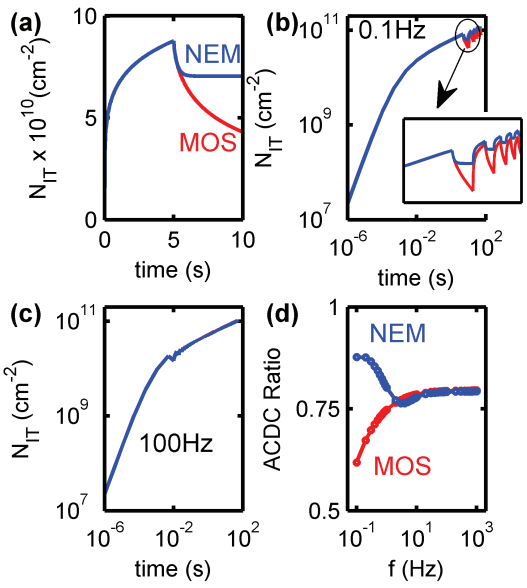

Fig. H.6. Simulation results for NBTI in SG-FET after (a) one cycle and (b) multiple cycles of low-frequency AC stress suggesting less relaxation in SG-FET compared to classical MOSFET. (c) At high frequency, degradation in SG-FET and MOSFET becomes indistinguishable. (d) AC/DC ratio for SG-FET and MOSFET as a function of frequency for fixed stress time of 100 seconds suggesting that at high frequency SG-FET and MOSFET degradation is indistinguishable.

H.4.1 Results : Creep

Creep will be a reliability problem in SG-FET when it is operated below pull-in as in sleep transistor and resonant gate transistor. Even at $V_G = 0$, there will be a residual force acting on the gate, because of non-zero flat-band voltage, and the gate will be deflected. This residual force will weaken the gate by creep (as in case of RF-MEMS varactors in appendix G), and the gate will continue to move down over time (Fig. H.7 (a)) and will cause air-gap to decrease. As a result of this, capacitance of the device will increase (Fig. H.7 (b)). This increase in the off-state capacitance will increase the off-state leakage over time. Eventually, the advantage of low-power

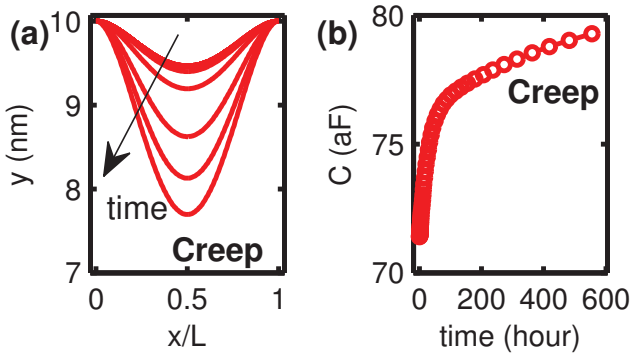

Fig. H.7. Identifying creep as one of the reliability problem in SG-FET. (a) For $V_{FB} \neq 0$, gate will be deflected even for $V_G = 0$, and will continue to move down because of creep. (b) Movement of gate will increase the capacitance with time, and hence the leakage current (and off-state power consumption) of the device.

consumption will be diminished. Therefore, creep will be parametric degradation for SG-FET circuits operating below pull-in.

H.5 Conclusions

To conclude, we find that SG-FET based logic family will be immune to reliability issues associated with HCI due to intrinsic pull-in and release dynamics of SG-FET. We also establish that NBTI may lead to catastrophic failure due to stiction in p-SG-FET. And, finally creep is identified to be a reliability problem for below pull-in operation in sleep transistors and resonant gate transistors.

VITA

VITA

Ankit Jain received his B.Tech degree from the Indian Institute of Technology (IIT) Kanpur, India in 2008. He received academic excellence award from IIT Kanpur for the academic year 2006-2007. He is currently working towards his PhD degree in Electrical and Computer Engineering at Purdue University under the guidance of Prof. M. A. Alam. His research interests include modeling, simulation, and design of emerging electronic devices such as novel nonlinear biosensors for health-care applications, steep sub-threshold switches for low power computation, and low power MEMS based displays for 21^{st} century electronics. He has received "Five Students Who Move the World Forward" award from Purdue University for his dissertation. His research on the proposal of Flexure-FET biosensor has been widely discussed in many newspapers, scientific blogs, and websites.